High-efficiency GaN-based light-emitting diodes : light extraction by photonic crystals and microcavities.

Aurélien David

To cite this version:

Aurélien David. High-efficiency GaN-based light-emitting diodes : light extraction by photonic crystals and microcavities.. Physics [physics]. Ecole Polytechnique X, 2006. English. NNT : . pastel-00002956

HAL Id: pastel-00002956
https://pastel.hal.science/pastel-00002956v1
Submitted on 23 Jul 2010

Thèse présentée pour obtenir le grade de

DOCTEUR DE L'ECOLE POLYTECHNIQUE

Discipline: Physique
par

Aurélien DAVID

High-efficiency GaN-based light-emitting diodes: Light extraction by photonic crystals and microcavities

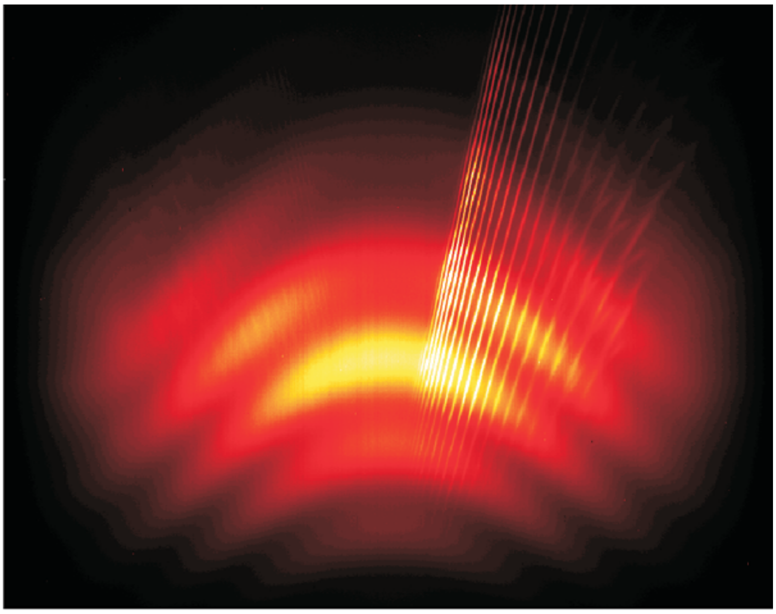

Soutenue le 3 Juillet 2006 devant le jury composé de:

Lucio Claudio ANDREANI (Université de Pavie)	Rapporteur
Jean-Yves DUBOZ (CHREA, Valbonne)	Rapporteur
Henri BENISTY (IOTA, Orsay)	
Vincent BERGER (Université Paris VII)	
Steven DENBAARS (UCSB, Santa Barbara)	
Didier PRIBAT (PICM, Ecole Polytechnique, Palaiseau)	
Invité: Claude WEISBUCH (UCSB, Santa Barbara)	

Remerciements

Arrivé au moment de remercier tous ceux qui m'ont aidé et soutenu durant cette thèse, je suis surpris de constater combien ces trois ans ont pu passer si vite. Pourtant, que de chemin parcouru !

Je me dois de commencer par Claude et Henri, grâce à qui j'ai passé trois merveilleuses années toujours intéressantes et pleines de surprises. Infaillibles lorsque j'avais besoin d'aide et prêts à me laisser libre quand je le voulais, ils ont toujours fait preuve d'un soutien moral sans faille : on dit souvent qu'une thèse comporte des moments difficiles, mais ça n'est qu'à moitié vrai avec eux ! Si ces trois années ont été si agréables, c'est bien sûr grâce à eux, ainsi qu'au reste de l'équipe à l'X-IOTA : Emilie, Jérôme, Omer et Cyrille... et mon compagnon de voyage Lucio-San, avec qui j'espère encore arpenter les quatre coins de la planète !

Je voudrais aussi dire un grand merci à l'ensemble du PMC pour la bonne ambiance qui règne toujours dans les couloirs, et particulièrement à François Ozanam pour avoir su me pousser sur la route de la physique.

A Santa Barbara, j'ai pu bénéficier de conditions de travail exceptionnelles : j'ai profité d'un accès sans limites aux moyens nécessaires pour produire et mesurer de multiples échantillons. Je tiens donc à remercier chaleureusement Steve Denbaars pour m'avoir toujours soutenu sans hésiter et ouvert grand les portes d'UCSB. Mes remerciements vont aussi à Jim Speck et Shuji Nakamura pour leur bienveillance et leurs conseils. Enfin, j'ai une pensée toute particulière pour Pierre Petroff : sa générosité et sa bonne humeur ont éclairé mes séjours à UCSB – sans parler d'un accueil chaleureux dans son laboratoire de mesures !

Je dois également beaucoup à quelques personnes pour leur aide précieuse à UCSB. Je pense tout d'abord à Tetsuo, mon *sensei* de salle blanche, qui m'a tant aidé dans l'élaboration des premiers échantillons et m'a transmis ses précieux " secrets " de fabrication : sans lui, cette thèse en serait probablement resté au niveau du calcul ! Merci aussi à Fred, pour son aide infaillible –pratique comme morale– dans les moments difficiles et pour tous les précieux coups de mains lors des longues journées de mesures... Un grand merci aussi à Elison pour son aide sur les mesures, et pour tous les bon moments, sur les vagues et ailleurs.

Je tiens enfin à saluer tous ceux avec qui j'ai travaillé à UCSB et sans qui la partie expérimentale de cette thèse n'aurait pas été possible : Rajat bien sûr, ainsi que toute l'équipe des épitaxieurs, mais aussi l'ensemble du personnel de la salle blanche, toujours prompt à réagir et d'une efficacité redoutable – même le week-end ! Tout cela produit des conditions de travail idéales et sans doute uniques.

Je voudrais également remercier la DGA pour ma bourse de thèse, ainsi que le SSLDC pour le financement du travail à Santa Barbara.

Enfin, mes ultimes remerciements vont à mes proches : mes amis en France et aux Etats-Unis, et bien sûr ma famille et Claire, toujours présents quand il le fallait. A vous tous, merci d'exister !

Contents

Table of symbols

a	lattice constant of a photonic crystal
d	depth of a photonic crystal
f	filling factor of a photonic crystal
DBR	distributed Bragg reflector
DOS	photonic density of states
$\mathbf{E}$	Electric field
$\mathbf{E}_G^x$	Harmonic $\mathbf{G}$ of the x-component of the electric field
EL	Electroluminescence
FBZ	first Brillouin zone
$\mathbf{G}$	reciprocal lattice vector
G_0	Norm of the basis vectors of the reciprocal lattice
F_p	Purcell factor
$\mathbf{H}$	Magnetic field
$\mathbf{H}_G^x$	Harmonic $\mathbf{G}$ of the x-component of the magnetic field
k_0	wavevector of a wave in vacuum, defined as $k_0 = \omega/c = 2\pi/\lambda$
$k_{//}$	in-plane wavevector
k”	imaginary part of the in-plane wavevector
k_z	vertical component of the wavevector
L_{decay}	exponential decay length of a decaying wave
M	plane wave cutoff, related to the number N of plane waves by $N = 2M + 1$
n_{eff}	effective index of a wave
$\mathcal{P}$	power radiated by a wave
PhC	Photonic crystal
PL	Photoluminescence
PW	plane wave
φ	azimuthal angle in spherical coordinates
QGM	quasi-guided mode
QW	quantum well
RL	reciprocal lattice
t	thickness of the core (unetched region) of a waveguide
θ	polar angle in spherical coordinates
θ_c	critical angle
u	normalized frequency, defined as $u = a/\lambda$

Introduction

Thanks to the appearance of efficient blue and white light-emitting diodes, solid-state lighting is in a position to replace conventional lighting sources within years. However, for LEDs to be competitive with the best current sources such as fluorescence lamps, ultimate optimization of all aspects of LEDs' efficiency is necessary.

Several processes are likely to limit the efficiency of LEDs. One may naively think that the main limiting factor is internal light generation. However, this is not the case in a variety of materials, where the conversion from carriers to photons reaches 50% to 90% if the material's quality is high enough. In this case, the strongest limiting factor is that of light extraction, i.e. the ability for photons generated inside the semiconductor to escape into air.

Unfortunately, most of the light emitted inside the LED turns out to be trapped by total internal reflection at the interface with air. Although many efficient light extraction strategies have already made their way to commercial applications, they are mostly based on the principle of randomizing the paths followed by light, which gives limited control on the emission pattern of LEDs. Typical examples of such methods are shaping of the LED (for instance in a pyramid form) or surface roughening. These structures sometimes suffer from complex fabrication processes which are not compatible with a fully planar fabrication.

The case of blue InGaN LEDs is somewhat special because their material and growth constraints differ from that of other III-V compounds. In particular, their refractive index is rather low (~ 2.5), they benefit from the presence of a transparent substrate, and they require thick layers to be grown for sufficient material quality. Owing to its comparatively recent availability, the issue of light extraction has not yet been fully explored in this material: this is currently a topic of active research, which has seen a flurry of interest and of publications recently. As in other semiconductors, light extraction based on randomization is currently the preferred choice in commercial products. This is partly due to the simpler conceptual framework of such approaches which makes them reasonably easy to implement.

During this thesis, I explored several alternative strategies to obtain high-efficiency LEDs in GaN-based materials. The basic objective was to consider light extraction methods which would avoid randomizing the paths followed by light, in order to keep a better control on the radiation properties of the LEDs. To this effect, I used light extraction strategies which rely on the *wave nature* of light rather than a geometric approach. The two methods explored in this thesis are:

- Microcavity LEDs (MCLEDs), where the presence of close mirrors around the LED modifies the radiation pattern of the light source due to interference effects, and increases light emission in directions where it can escape the LED
- Photonic crystal LEDs, where a periodic dielectric structure is used as a diffraction grating to scatter out-of-plane the light guided in the LED. Most of the work of this thesis focused on this second approach, which presents greater theoretical and fabrication challenges but also offers a vast space of parameters to finely control the emission properties of a light source.

Both of these approaches have been extensively studied in the 90's, notably at EPFL, Ecole Polytechnique and the University of Glasgow. These studies focused on more conventional III-V semiconductors such as GaAs, and demonstrated the soundness of both methods for efficient light extraction. Generalization to address the case of GaN structure presented the main objective of this thesis.

An important advantage of both these methods is their *deterministic* approach: the phenomena responsible for light extraction can be described exactly. Therefore, suitable design enables one to *tune* the emission properties of the light source by varying its parameters.

Besides, from a practical point of view, both methods are well adapted to planar processes and are thus reasonable candidates for integration in actual mass-produced devices.

The first Chapter of this thesis is devoted to Microcavity LEDs. Chapter 2 introduces the theoretical concepts and first experiments on light extraction by photonic crystals. Chapter 3 presents results on several implementations of LEDs with photonic-crystal-assisted light extraction, which aim at adressing the specific limitations of GaN photonic crystals. Finally, Chapters 4 and 5 describe the theoretical tools used for the design and modeling of photonic structures, and report on advances in 2D and 3D modeling.

Chapter 0

Resumé en français

0.1 Contexte

Une diode électroluminescente (LED), c'est-à-dire une jonction *pn* où les porteurs électriques sont convertis en lumière au niveau de la jonction, constitue en principe un convertisseur idéal d'énergie électrique en énergie lumineuse. Depuis la découverte, dans les années 1990, des LEDs à base de GaN émettant dans le bleu, tout le spectre visible est couvert par les LEDs. Elles constituent donc une technologie prometteuse pour remplacer les sources de lumière conventionnelles: des LEDs de haute efficacité permettraient des économies d'énergie considérables, tout en apportant d'autres avantages (robustesse et grande durée de vie, compacité, rapidité, contrôle du rendu des couleurs et de l'intensité lumineuse...).

Toutefois, de nombreux facteurs limitent en pratique l'efficacité des LEDs. Outre la qualité du matériau, qui conditionne l'efficacité de la conversion interne de l'électricité en lumière, la question de l'extraction de la lumière est un obstacle majeur à l'obtention de LEDs à haute efficacité. En effet, la lumière étant générée dans un matériau de haut indice ($\sim 2.5 - 3.5$), la plus grande partie de celle-ci reste piégée dans la LED par réflexion totale interne. Seuls 4 à 5% de la lumière peuvent s'échapper par une face d'une LED cubique.

De nombreuses stratégies ont été proposées au cours des décennies passées pour remédier à ce problème et augmenter l'extraction lumineuse. Dans leur grande majorité, les solutions actuellement appliquées dans les produits commerciaux emploient une approche dite géométrique, qui consiste à faire varier l'angle de propagation des rayons lumineux dans la LED (idéalement, à le rendre *aléatoire*) pour que la lumière s'échappe de la LED après quelques rebonds. Ceci peut être obtenu en modifiant la forme de la LED (c'est de cas des pyramides tronquées inversées de Lumileds), ou encore en texturant la surface de la LED a l'échelle microscopique pour briser la conservation de l'angle à la réflexion. Aujourd'hui, ces solutions s'avèrent efficaces et l'efficacité totale d'une bonne LED est de plusieurs dizaines de %. Toutefois, les approches géométriques ne sont pas forcément idéales. Les trajectoires suivies par les rayons lumineux ne sont en général pas (ou mal) contrôlées, ce qui rend certaines pertes par absorption inévitables (par exemple lors de la réflexion sur les contacts métalliques). En outre, le diagramme de rayonnement de telles sources est peu directionnel (en l'absence d'optiques collimatrices supplémentaires).

A l'opposé, les approches dites ondulatoires reposent sur les propriétés ondulatoires de la lumière. Ainsi, les LEDs à microcavités (MCLEDs) permettent de modifier le diagramme angulaire d'émission de la LED, et d'augmenter ainsi la fraction de lumière qui pourra être extraite directement. Les LEDs à cristaux photoniques (PhC) emploient des structures périodiques (réseaux bidimensionnels) pour extraire par diffraction la lumière piégée dans le semi-conducteur. Ces approches sont conceptuellement plus complexes, ce qui explique sans doute qu'elles n'aient que rarement été retenues à l'échelle industrielle. Toutefois, au prix de cette complexité, elles offrent un plus grand contrôle sur les trajectoires de la lumière, et permettent donc en principe d'obtenir des sources 'déterministes' dont le diagramme d'émission est directionnel.

Le travail de ma thèse a porté sur l'application des stratégies ondulatoires d'extraction de la lumière, aux diodes à base de GaN. La plus grande partie du travail s'est concentrée sur l'exploration (théorique et expérimentale) des LEDs à cristaux photoniques.

0.2 LEDs à microcavité

0.2.1 Principe

Une MCLED est formée d'une couche mince (quelques longueurs d'onde optiques) placée entre deux miroirs. Les réflexions multiples causées par ces miroirs produisent des interférences (constructives ou destructives, selon l'angle d'émission de la lumière), ce qui modifie le diagramme d'émission: la lumière est répartie dans des modes appelés *modes Fabry-Pérot*. Idéalement, une plus grande partie de la lumière est alors émise à des angles où elle est extraite (le *cône de lumière*). Pour obtenir une bonne MCLED, les miroirs doivent réfléchir avec de basses pertes.

Intuitivement, il est clair que dans le cas d'une LED épaisse, les directions d'interférences constructives et destructives sont très nombreux : l'extraction de la lumière est ainsi moyennée et peu sensible à L. Les écarts à cette statistique ne peuvent être atteints que pour une LED suffisamment mince, où seuls quelques modes Fabry-Pérot subsistent. Dans ce régime, l'efficacité d'extraction lumineuse est approximativement donnée par:

$$\eta = \frac{\lambda}{nL} \tag{1}$$

Où λ est la longueur d'onde de la lumière, n l'indice du matériau et L l'épaisseur de la cavité. Il apparaît donc que pour être efficace, une MCLED doit être mince (quelques longueurs d'onde).

En outre, on peut montrer pour une efficacité d'extraction optimale, l'épaisseur de la cavité doit être contrôlée avec une précision d'une dizaine de nm (le 'désaccord' de la cavité). De même, pour un couplage optimal entre les modes optiques extraits et les puits quantiques, ces derniers doivent être placés aux ventres des modes – donc encore une fois avec une précision de quelques nm.

On voit donc que les contraintes de fabrication sont considérables : miroirs efficaces et sans pertes, épitaxie et fabrication avec une haute précision.

0.2.2 Application aux LEDs GaN

En pratique, peu de bons miroirs existent dans le GaN. De bons miroirs diélectriques (injectables électriquement) n'étant aujourd'hui pas disponibles, on doit se tourner vers les miroirs métalliques en Ag. La fabrication de MCLEDs nécessite alors le report sur un substrat métallique, l'ablation laser du substrat saphir initial, et l'amincissement chemico-mécanique de la cavité GaN. Ce processus est complexe et ne permet pas un bon contrôle de l'épaisseur finale de la cavité.

De nombreuses MCLEDs ont ainsi été fabriquées, et étudiées à l'aide d'une mesure de luminescence résolue en angle. Les mesures donnent accès au diagramme d'émission en champ lointain, et permettent d'étudier la modification de sa dépendance angulaire avec l'épaisseur de la cavité. On peut ainsi observer le passage au régime de microcavité lorsque cette épaisseur diminue. En revanche, les propriétés électriques de la LED sont altérées lors de la fabrication et il est impossible de mettre en évidence une augmentation de l'extraction de lumière. Ce résultat semble hélas inhérent à la méthode de fabrication, et nous pousse à conclure que les MCLEDs GaN nécessiteraient un processus de fabrication plus contrôlé.

0.3 Extraction de la lumière par cristaux photoniques

Face aux insuffisances des MCLEDs GaN, une autre stratégie d'extraction de la lumière a ensuite été explorée: la diffraction par des cristaux photoniques (PhCs). Plutôt que de tenter de modifier le diagramme d'émission de la source, on accepte qu'une partie importante de la lumière soit émise dans des modes guidés, mais on intègre un réseau de diffraction à la LED pour diffracter ces modes vers l'air.

Le principe de l'extraction de lumière par PhC a d'abord été testé en photoluminescence. Des PhC à réseau triangulaire, avec un pas de $a = 200$ nm et une profondeur ~ 200 nm, ont été formés dans des échantillons à puits quantiques. Les échantillons ont été excités par un laser HeCd, et la luminescence collectée avec une mesure résolue en angle. En plus du signal de luminescence directe des puits quantiques, la diffraction des modes guidés par le PhC apparaît comme un signal additionnel sur les spectres.

En isolant le signal de diffraction de la luminescence directe, et en transformant les axes du spectre (angle → vecteur d'onde, longueur d'onde → fréquence), on obtient la *relation de dispersion* du PhC.

Cette relation de dispersion peut être expliquée qualitativement en convoluant la relation de dispersion d'un guide d'onde GaN épais (plusieurs μm, correspondant à des dizaines de modes guidés) avec la relation de dispersion d'un PhC bidimensionnel de faible force photonique. Cette interprétation qualitative est confirmée par un calcul rigoureux (résolution des équations de Maxwell à 3 dimensions), qui reproduit précisément la mesure sans paramètre ajustable. Les mesures effectuées dans différentes directions cristallographiques et polarisations confirment les propriétés théoriques des bandes d'un PhC.

En outre, le calcul numérique révèle l'existence d'un grand nombre de bandes photoniques qui n'apparaissent pas sur la mesure. Ces bandes correspondent aux modes de *bas ordre* du guide d'onde GaN (le mode fondamental et les modes peu excités). En effet, ces modes de haut indice effectif ont une faible pénétration dans le PhC, et sont donc faiblement diffractés. Ils se propagent à travers la zone de PhC sans être extraits, et n'apparaissent pas dans la mesure expérimentale. Or, 40% environ de la lumière guidée dans le GaN est émise dans ces modes de bas ordre. Il convient donc de proposer une stratégie permettant l'extraction de ces modes.

0.4 Diodes à cristaux photoniques

Plusieurs types de LEDs à cristaux photoniques ont été proposées et testées.

0.4.1 Modification de la distribution de modes guidés

La première implémentation vise à résoudre le problème des modes de bas ordres non extraits. A cet effet, la structure épitaxiale de la LED est légèrement modifiée: une couche d'AlGaN de bas indice ($n = 2.4$, contre $n = 2.5$ dans le cas du GaN) est insérée sous la zone active. La LED est alors constituée de trois régions optiques : une couche épaisse ('buffer') de GaN, une couche d'AlGaN (1 μm) servant de barrière optique, et un mince guide d'onde ($\sim$ 300 nm) contenant la jonction *pn*. Le guide d'onde est conçu pour qu'un mode guidé, dit *mode de surface*, puisse s'y propager.

Les puits quantiques étant situés dans le guide d'onde, leur couplage avec le mode de surface est bon: ainsi, une grande partie de la lumière y est émise. En revanche, les modes de bas ordres localisés dans le buffer de GaN sont évanescents dans la barrière d'AlGaN et se couplent donc peu à l'émission des puits. En outre, le mode de surface interagit bien avec les PhC, situés eux aussi en surface, et est donc extrait efficacement. Ainsi, tous les modes guidés recevant de la lumière sont susceptibles d'être bien extraits par le PhC.

Après vérification de cette approche par des calculs numériques, des LEDs à PhC incorporant cette couche de bas indice ont été fabriquées. Comme précédemment, des mesures résolues en angle ont été effectuées pour étudier la structure de bande correspondante. Sur cette structure de bande, on voit apparaître les bandes photoniques déjà observées en photoluminescence (correspondant aux modes de haut ordre), mais aussi un nouveau mode apparaissant de façon très intense sur les spectres. Le haut indice effectif de ce mode confirme qu'il s'agit du mode de surface attendu. Son intensité indique qu'une grande partie de la lumière est bien émise dans ce mode, et justifie la validité de l'approche.

Des comparaisons de puissance ont ensuite été réalisées entre ces LEDs et des LEDs classiques. L'augmentation de puissance n'est que de +70%, ce qui est assez modeste en vue de la grande quantité de lumière guidée dans la LED. Néanmoins, ces performances peuvent en partie être imputées au manque d'optimisation de la structure, et les mesures constituent au moins une bonne preuve de concept.

0.4.2 Pavages d'Archimède

On s'intéresse ici au choix du réseau cristallin du PhC. Une approche cinématique bidimensionnelle est d'abord utilisée pour comparer différents réseaux cristallins. Deux phénomènes opposés entrent en jeu : d'une part l'augmentation du nombre de points du réseau réciproque augmente les canaux de diffraction vers l'air, mais d'un autre côté les diffractions (pertes) vers le substrat sont également augmentées. En outre, un réseau simple n'est efficace qu'autour du second ordre de Bragg ($a \sim \lambda/n$), ce qui contraint fortement le régime de fonctionnement du PhC. Dans ces conditions, il apparaît que le réseau simple le plus efficace (pour une structure GaN sur saphir) est un réseau triangulaire : bien que certains angles de propagation (autour de la direction ΓK du PhC) ne soient pas extraits vers l'air, les pertes vers le substrat sont limitées et ce compromis est optimal.

Cependant, on peut également concevoir des structures plus complexes où les pertes vers le substrat sont limitées par un autre mécanisme (ablation laser du substrat ou ajout d'un DBR par exemple). Dans ce cas, la limitation liée aux pertes dans le substrat est levée et on peut utiliser un réseau *omnidirectionnel*, c'est-à-dire tel que tous les angles azimutaux de propagation soient diffractables vers l'air. Cette propriété est vérifiée par les *pavages d'Archimède A7*, réseaux cristallins complexes (réseau triangulaire, 7 trous par maille) qui possèdent 12 directions de diffraction forte dans l'espace réciproque (contre 6 seulement pour un réseau triangulaire simple).

Des LEDs à PhC comportant un réseau A7 ont donc été fabriquées. Leur structure de bande photonique, étudiée grâce à la mesure résolue en angle, confirme les propriétés attendues de ce réseau cristallin. La dispersion des bandes photoniques est conforme à la théorie; de plus, l'ensemble de la structure de bandes se trouve dans le cône de lumière, ce qui confirme que le réseau extrait de façon omnidirectionnelle. Enfin, on peut identifier les bandes photoniques avec le point du réseau réciproque responsable de leur diffraction : on s'aperçoit alors que les bandes observées correspondent bien aux 12 points de forte diffraction. Ceci confirme que l'extraction de lumière est réalisée de façon efficace, c'est-à-dire sur une échelle comparable à celle d'un réseau triangulaire simple (en d'autres termes, l'omnidirectionnalité n'a pas été obtenue au prix d'une distance d'extraction excessive).

0.4.3 PhC-LEDs à report sur substrat

On s'intéresse ensuite à des LEDs combinant les propriétés des MCLEDs avec les cristaux photoniques. Ces LEDs sont obtenues en fabriquant des MCLEDs (report sur substrat métallique et ablation laser du substrat saphir, amincissement de la LED) puis en y ajoutant des PhC pour l'extraction de la lumière guidée. On peut espérer que de telles LEDs soient particulièrement efficaces : l'absence de substrat diélectrique évite les pertes dans le substrat ; et l'utilisation d'une couche mince ramène à un guide d'onde faiblement multimode où tous les modes peuvent bien interagir avec le PhC (on évite le problème des modes de bas ordre).

En contrepartie, la fabrication de telles LEDs est particulièrement délicate, car l'ajout d'un PhC augmente les possibilités de dommages à la LED (court-circuit causé par le PhC par exemple). De fait, la plupart des LEDs fabriquées ne fonctionnaient pas, et les quelques LEDs restantes possédaient de forts courants de fuite et de très mauvaises propriétés électriques. Elles ont toutefois été analysées avec la mesure résolue en angle pour caractériser leurs propriétés photoniques.

Ces mesures, effectuées sur des LEDs de différentes épaisseurs (400 nm à 1 μm), confirment la raréfaction des modes guidés lorsque de la couche de GaN est amincie. Elles indiquent en outre que le phénomène d'absorption des modes guidés est important dans ces LEDs : les bandes photoniques semblent disparaître à certaines fréquences, correspondant à une forte absorption dans le substrat métallique.

Un calcul numérique confirme cette observation : dans les LEDs fabriquées, le miroir en or absorbe une grande partie de l'énergie des modes guidés. En revanche, l'emploi d'un miroir à faible absorption (comme de l'argent) limiterait fortement ce phénomène.

0.4.4 PhC-LEDs à recroissance latérale

Les implémentations précédentes de PhC-LEDs (couche de bas indice, PhC LED à report sur substrat) mettent en évidence la nécessité de structurer la LED dans la direction verticale pour s'assurer que la lumière guidée interagit bien avec le PhC. Une nouvelle approche est étudiée ici: l'insertion d'un réseau de diffraction en SiO_2 *dans* la structure épitaxiale, puis la recroissance de la jonction *pn* sur ce réseau.

De telles structures permettent un contrôle de la distribution de modes guidés (car la couche contenant le PhC agit comme une couche de bas indice) et possèdent une géométrie avantageuse : le PhC étant intégré dans la LED, sa surface est plane et peut entièrement être recouverte par un contact électrique, ce qui n'était pas le cas avec les PhC creusés en surface des LEDs.

Les calculs numériques révèlent que pour être efficace, ces structures doivent êtres minces (plus précisément, la jonction *pn* crûe sur le PhC ne doit pas dépasser 300 nm d'épaisseur). Cela rend l'épitaxie délicate, car la coalescence au-dessus du PhC peut nécessiter une certaine épaisseur.

Les premiers échantillons, réalisés avec des PhC unidimensionnels, répondent à cette exigence. S'ils ne permettent pas d'être quantitatif quant à l'efficacité de l'extraction de lumière (un PhC bidimensionnel serait nécessaire pour de bonnes performances), leur structure de bande photonique confirme la double action du PhC : diffraction des modes guidés et barrière optique modifiant la distribution des modes guidés.

0.4.5 Emission dans le PhC

Enfin, on s'intéresse à des structures atypiques où le PhC traverse les puits quantiques (en photoluminescence). On pourrait s'attendre à ce que la présence du PhC induise d'importantes recombinaisons non-radiatives et diminue fortement la luminescence. Pourtant, comme l'ont démontré Keller *et. al*, un recuit du matériau à haute température semble 'guérir' le matériau et restaure la luminescence. On a donc affaire à des structure à grande force photonique, où l'émission spontanée a lieu directement dans une couche périodique où la densité d'états photoniques est fortement modifiée – ceci est en contraste avec les structures précédentes, où le PhC ne servait que comme réseau de diffraction et où l'émission spontanée était très peu altérée.

On s'intéresse donc aux propriétés théoriques de l'émission spontanée dans de telles structures. On peut en effet craindre qu'un effet Purcell (modification du taux d'émission spontanée) négatif n'ait lieu, en raison de la diminution de la densité d'états photonique. Les calculs révèlent que l'effet

Purcell reste heureusement modéré (notamment si les puits quantiques sont placés adéquatement). En outre, ils indiquent que si la source est située au coeur du PhC, l'émission se distribue sur des modes localisés dans la couche du PhC. L'existence de ces modes est a priori surprenante, car ils parviennent à se localiser dans une couche de bas indice malgré l'existence d'un buffer GaN de plus haut indice. On peut toutefois expliquer la présence de ces modes, et montrer qu'il s'agit d'une généralisation de modes quasi-guidés unidimensionnels. L'existence de ces modes permet de comprendre les propriétés d'émission spontanée (effet Purcell) de façon intuitive.

0.5 Modélisation 2D de cristaux photoniques

Ce chapitre et le suivant concernent la modélisation numérique des structures à base de cristaux photoniques. On s'intéresse ici aux structures bidimensionnelles, modélisées par la méthode de l'expansion en ondes planes (PWE). On rappelle tout d'abord la formulation générale de cette méthode. On présente ensuite la factorisation de Fourier rapide (FFF), méthode qui permet d'améliorer la convergence numérique de l'algorithme en modifiant le calcul de la transformée de Fourier de la carte diélectrique $\epsilon(r)$. La FFF est appliquée à différents types de PhC, et les gains en convergence sont confirmés dans chaque cas. Enfin, la PWE est formulée dans le cas d'une propagation hors du plan.

0.6 Modélisation 3D de cristaux photoniques

Ce dernier chapitre traite de la modélisation rigoureuse de cristaux photoniques en 3 dimensions. Après un passage en revue rapide des différentes méthodes trouvées dans la littérature, deux méthodes sont développées en détail.

La première, dite méthode hybride, est une méthode originale mise au point durant cette thèse. Elle permet de calculer les modes de Bloch d'une structure multicouche contenant des PhC. Elle s'appuie sur une discrétisation à 3 dimensions (développement en ondes planes avec FFF dans les deux directions horizontales, et en différences finies dans la direction verticale). Grâce à des *conditions aux limites transparentes*, le taux de perte du mode peut être calculé par une procédure itérative : on résout ainsi rigoureusement les équations de Maxwell. Bien que coûteuse numériquement du fait de la discrétisation 3D, cette méthode s'avère bien adaptée aux calculs sur des structures GaN multimodes, car il est possible de calculer approximativement la dispersion de plusieurs modes simultanément.

La seconde méthode est une méthode de matrice de diffusion ($\mathbb{S}$-matrix, ou RCWA) classique. Son implémentation est rappelée, y compris lorsque la FFF est appliquée. Cette méthode permet de calculer les propriétés diffractives (réflexion, transmission) d'une structure périodique, ainsi que d'en calculer les modes de Bloch. Enfin, l'ajout d'une discontinuité électromagnétique dans la structure permet de calculer le diagramme d'émission d'un dipôle émetteur. Le calcul des modes de Bloch est plus rapide avec cette méthode qu'avec la méthode hybride, mais seul un mode peut être calculé à la fois, ce qui rend les structures GaN épaisses pénibles à traiter.

0.7 Conclusion

De nombreuses structures ont été proposées et réalisées durant cette thèse pour augmenter l'extraction de la lumière des LEDs GaN, en employant des approches ondulatoires. Les LEDs à microcavités se sont avéré délicates à fabriquer, et le manque de contrôle du processus de fabrication n'a pas permis d'en tirer des résultats quantitatifs convaincants. La plus grande partie du travail s'est ensuite concentrée sur les LEDs à cristaux photoniques. L'aller-retour entre modélisation numérique et réalisations expérimentales a permis de comprendre les propriétés optiques des PhC sur GaN et de proposer des stratégies d'optimisation pour les LEDs à PhC. La principale difficulté consiste à structurer la LED dans la direction verticale pour s'assurer que tous les modes guidés interagissent bien avec le PhC. En général, les structures de grande force photoniques permettent un meilleur contrôle des propriétés photoniques mais sont plus délicates à mettre en oeuvre (tant du point de vue de la fabrication que de la compréhension et de l'optimisation). Malgré les performances modestes obtenues jusqu'ici, le grand contrôle offert par les PhC-LEDs permet raisonnablement d'espérer qu'elles pourraient trouver une application industrielle dans les années à venir, une fois les problèmes d'optimisation surmontés.

Chapter 1

Light-emitting diodes

This chapter outlines the basic theory of light-emitting diodes and introduces the issue of light extraction, as well as strategies commonly adopted in order to enhance the latter. Readers familiar with these concepts may skip the following and resume their reading at Chapter 2, where the first results of the thesis work itself are presented. For a complete treatment of *pn* junctions, the reader is referred to [1].

1.1 Basics on light-emitting diodes

1.1.1 Luminescence from a semiconductor

A semiconductor is characterized by an electronic band structure with a small energy gap between the last filled band (valence band) and the first empty band (conduction band). Electrons can be excited from the valence to the conduction band, for instance by thermal energy (at nonzero temperature), or absorption of an incoming photon. The vacancy left by such an electron in the Fermi sea of the valence band can be treated as a particle, and is called a *hole*. Alternately, electrons and holes can be injected by applying a current through a semiconductor.

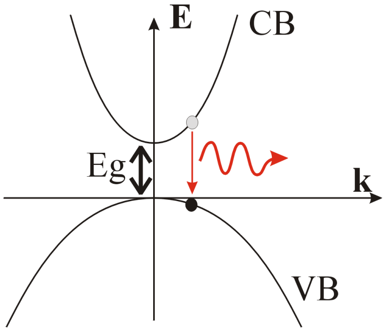

Figure 1.1: Luminescence in a semiconductor. E_g is the band gap, and $\mathbf{k}$ the wavevector of the electrons. The dispersion of the bands is parabolic close to the Γ point.

Once an electron is in the conduction band, it can return to the valence band (thus ’filling the hole’) by emitting a photon. Light-emitting diodes (LEDs) rely on this phenomenon, called spontaneous emission. Spontaneous emission is characterized by conservation of energy and momentum between the electron-hole pair and the emitted photon. Notably, energy conservation implies that the photon is emitted with an energy close to the band gap of the semiconductor: light emitted by a semiconductor is thus nearly monochromatic, in contrast with the emission of a blackbody radiator which spreads over a wide frequency range.

A *quantum well* (QW) is formed by a double heterostructure where a thin layer of a semiconductor (the well) is sandwiched between to thick layers of a semiconductor with a larger gap (the barriers). If the well is thin enough (typically one to a few nm), the separation between quantized electronic energy levels (in the direction of the well) is much larger than the thermal energy $k_B T$ and only the lowest-energy levels are populated. Since electrons are still free in the plane perpendicular to the well, they still possess a dispersion relation in this direction. As can be seen on Fig. 1.2, this results in luminescence at a higher energy than the gap of the well material, because of the quantum confinement energy.

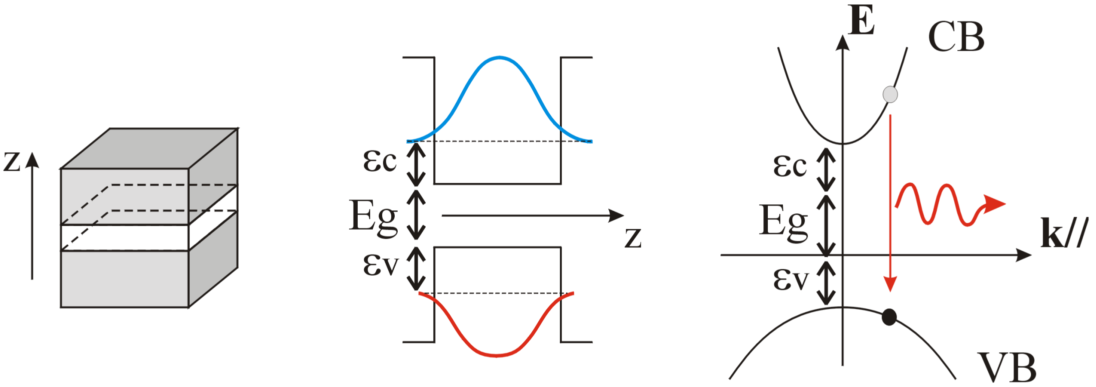

Figure 1.2: (Left) Geometry of a quantum well (grown along z) (Middle) First energy levels in a quantum well, and associated wavefunctions along z (i.e. density probabilities of electrons and holes). (Right) Dispersion in a quantum well. $\mathbf{k}_{||}$ is the electron's wavevector in the plane of the QW. The luminescence energy is shifted with respect to the well material's band gap.

1.1.2 The p-n junction

Electroluminescence from a semiconductor was first documented in 1907 by H. J. Round, when he observed a visible glow from a SiC crystal upon imposing an electrical bias.[2] However, the theory of the $p-n$ junction was not understood until Shockley's article in 1949 [3], which led Lehovec *et. al* in 1951 to interpret the electroluminescence of SiC as the radiative recombination of electron-hole pairs in a $p-n$ junction.[4].

The most simple form of $p-n$ junction, called *homojunction*, is depicted on Fig. 1.3. It consists of a junction between a piece of p-doped semiconductor (where the holes concentration is higher than the electrons concentration) and a piece of n-doped semiconductor. At the interface between both regions, the conduction and valence bands bend so that the bulk values of the Fermi level (i.e. far away from the junction) are aligned. Microscopically, this band bending is due to the diffusion of carriers in the opposite region (e.g. electrons in the p-region and vice-versa), which in turns yields an electric field between the carriers and the vacancies they left behind them. This electric field in turn produces a conduction current, which exactly balances the diffusion current in equilibrium conditions.

When an external voltage $V > 0$ is applied on the junction, the equilibrium between both currents is broken and a net diffusion of carriers is favored. It can be shown (Shockley's law) that the current flowing through the $p-n$ junction varies exponentially with V:

$$I(V) \sim exp\left(\frac{eV}{k_B T}\right) \tag{1.1}$$

This results in an excess of minority carriers on both sides of the junction. These carriers recombine radiatively, producing *electroluminescence*.

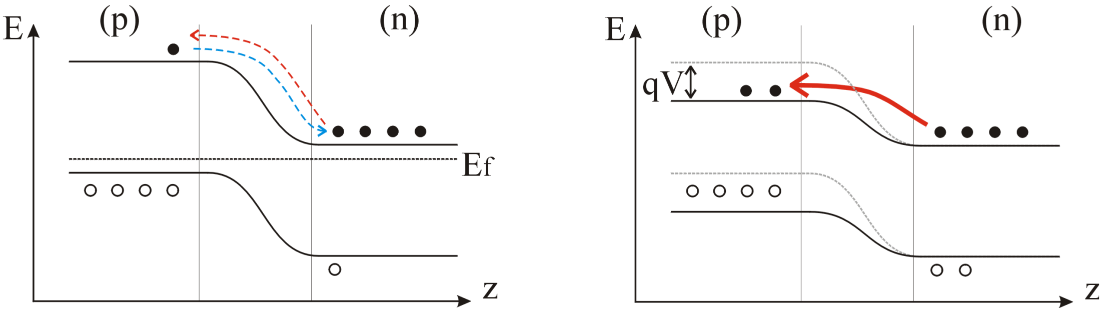

Figure 1.3: (Left) Zero-biased homojunction. The diffusion current and the conduction current created by the electric field in the junction balance each other (dashed arrows). (Right) When a positive bias V is applied, the bands bending decreases and the diffusion of carriers increases. More minority carriers are present in the opposite region where they can recombine and emit light.

However, the efficiency of the phenomenon is limited by absorption of the emitted light (re-absorption at the junction, and free-carrier absorption in the p and n regions). To avoid this, one resorts to *heterostructures* where the energy gap at the $p-n$ junction is smaller than in the p and n regions, thus decreasing light reabsorption in these regions (Fig. 1.4). When the thickness of the central region decreases below the De Broglie wavelength of carriers, it becomes a quantum well. Quantum well structures are more efficient than simple heterostructures, because they enable higher carrier density in the active region (and hence a lower recombination time) at a given current density, and because they efficiently decrease re-absorption in the host material. Besides, they offer more control on the wavelength of emission thanks to the controlled quantum confinement energy shift.

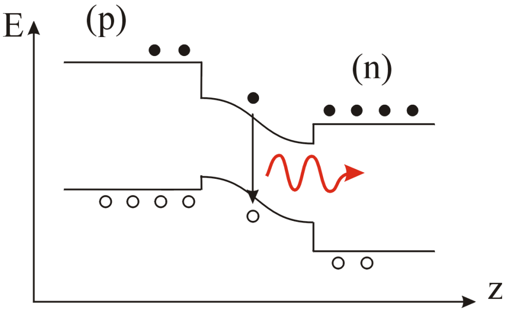

Figure 1.4: Heterostructure $p-n$ junction: the gap is lower in the central region, avoiding re-absorption of photons in the p and n regions.

Thus, in an ideal $p-n$ junction, all the injected carriers are converted into light at a given wavelength: this constitutes a perfectly efficient conversion of electricity into light. Unfortunately, a number of factors limit the efficiency in actual light-emitting diodes, as will be seen below.

1.2 Solid-state lighting

1.2.1 Uses of LEDs

Until a decade ago, the only available materials for visible light emission were AlGaAs and AlGaInP compounds. LEDs were mostly used for cheap alpha-numeric displays (red to green LEDs), and for telecommunications (infrared LEDs). The only blue-emitting devices were based on SiC and possessed very poor efficiency.

In 1993, Shuji Nakamura's work at Nichia led to the development of the first high-brightness InGaN blue LEDs.[1][6] This achievement completed the range of primary color, greatly extending the possible applications toward the field of solid-state lighting. Solid-state sources with various colors can be obtained either by combining several LEDs, or by down-converting part of the light emission of an UV or blue-emitting LED with phosphors. The latter is typically used to obtain white LEDs: a blue-emitting LED is coated by phosphors which absorb part of its emission and re-emit yellow light.

The greatest potential market of visible LEDs is that of general lighting, although the development of high-efficiency white LEDs is still in progress (see below) and it is likely that LEDs will not replace conventional light sources before a decade. It should be noted that general lighting is a major market: according to the US department of Energy, the sales of lighting products represent 60 billions $ each year worldwide.

Besides the economic potential of this market, opportunities are also huge in terms of energy savings. Indeed, in the US lighting represents 8% of the total energy consumption and 22% of the electricity energy consumption. The inefficient incandescent bulbs remain the most widespread sources so far: they consume 40% of the lighting energy to produce only 15% of the light ouptut! A penetration of LEDs of 50% in the general lighting market would yield considerable energy savings of more than 350 TWh, or the equivalent of the continuous energy production of 100 nuclear plants.

Meanwhile, along its development, solid-state lighting has unlocked a number of niche markets. Let us quote the automotive market (LEDs are now integrated in headlamps in a number of car models), backlighting of display screens (including TVs), display projectors, street signals, and most recently the important market of cell phones (screens, keyboards and camera flashes).

Currently, the LED market represents 3.7 billions $ each year globally. 58% of this figure corresponds to the cell phone market, while illumination only represents 5% of the market.

1.2.2 Performance of an LED

External quantum efficiency

In general the performance of a lighting device is characterized by its *external quantum efficiency* or *wall-plug efficiency* η, defined as the ratio of emitted (optical) power to injected (electrical) power:

$$\eta = \frac{\mathcal{P}_{opt}}{\mathcal{P}_{el}} \tag{1.2}$$

Several factors contribute to η, which may be decomposed as follows:

$$\eta = \eta_{inj} \times \eta_{int} \times \eta_f \times \eta_{extract} \tag{1.3}$$

The *injection efficiency* η_{inj} is the fraction of electron-hole pairs injected into the LED which reaches the $p-n$ junction. This value is for instance limited by leakage of the current in the LED and by Joule losses in the electrical contacts of the LED.

---

[1] More precisely, Nakamura demonstrated how GaN could be p-doped and thus injected electrically. This was obtained by Mg doping of p-GaN, followed by a thermal annealing to activate the Mg donors.[5]

The *internal quantum efficiency* η_{int} is the fraction of electron-hole pairs reaching the $p-n$ junction which recombine radiatively. It is limited by nonradiative recombinations of electron-hole pairs.

The *feeding efficiency* η_f is the ratio of the energy of an emitted photon[2] $\hbar\omega$ to the energy of an electron-hole pair injected in the LED:

$$\eta_f = \frac{\hbar\omega}{qV} \tag{1.4}$$

Where V is the voltage drop across the LED and q the elementary charge. In general, part of the electrons'energy can be lost to phonons and $\eta_f < 1$.

Finally, the *light extraction efficiency* $\eta_{extract}$ is the fraction of the photons emitted at the $p-n$ junction which actually escape the LED. Its value is limited by light reflection which traps photons inside the LED where it is eventually absorbed (either by the semiconductor or by the metal contacts).

It should be noted that, in the case of a white LED where phosphors are used for down-conversion (for instance, by absorbing blue light and re-emitting yellow light) the efficiency of this process also has to be taken into account in the overall LED's efficiency.

Fig. 1.5 summarizes the state of the art in LEDs' external quantum efficiency in 2005.

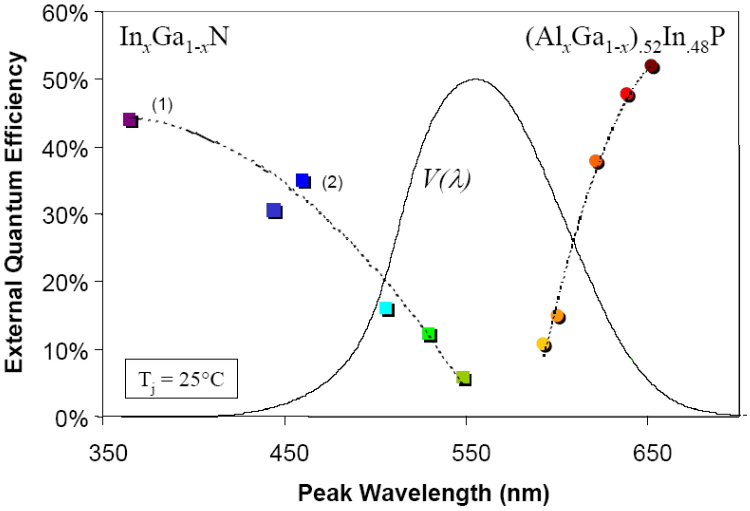

Figure 1.5: [After Lumileds' presentation] Best external quantum efficiency obtained in LEDs in 2005. Note the collapse of η in the yellow-green region: AlGaInP compounds are limited by band structure effects (the gap becomes indirect, and the barriers of heterostructures too small, leading to carriers leakage) while InGaN compounds with high In contents suffer from higher dislocation densities, and hence low internal quantum efficiency.

Photometry

Power output

Besides the wall-plug efficiency of an LED, other figures of merit may be used to characterize its efficiency. In the case of a visible-light LED, on may consider the luminous power $\mathcal{P}_{lum}$ of the LED (expressed in *lumens per watts*), which takes into account the response of the human eye to light and is defined as:

$$\mathcal{P}_{lum} = 683 V_{CIE} \times \mathcal{P}_{opt} \tag{1.5}$$

---

[2] In the realistic case of a polychromatic source, the *average* energy of the emitted photons should be considered.

V_{CIE} is the photoptic response curve of the human eye adopted by the Commission Internationale d'Éclairage (CIE), as shown on Fig. 1.6. The maximal value of V_{CIE} is 1, at $\lambda = 555$ nm.

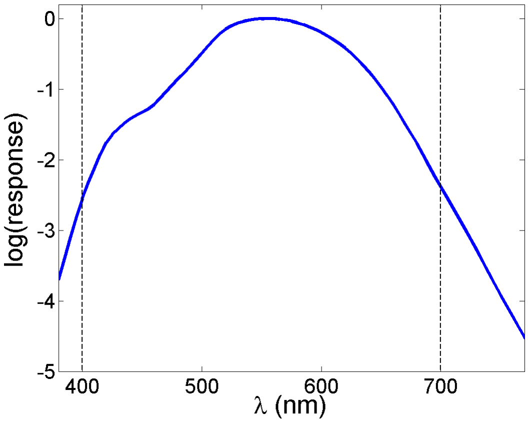

Figure 1.6: CIE response curve V_{CIE}. It reaches unity at $\lambda = 555$ nm. The visible spectrum is conventionally defined as the wavelength range between 400 nm and 700 nm.

The *luminous efficiency* of the LED is then defined as:

$$\eta_{lum} = \frac{\mathcal{P}_{lum}}{\mathcal{P}_{el}} \tag{1.6}$$

We also have $\eta_{lum} = 683 V_{CIE} \times \eta_{ext}$, so that the maximal possible luminous efficiency is 683 lm/W and can only be obtained for a green-emitting light source.

Currently, high-power white LEDs are routinely in the 30-50 lm/W range. The US Department of Energy's objective of 100 lm/W for a white-emitting LED in 2010 has already been reached by several companies at the laboratory level (Cree announced a record efficiency of 130 lm/W in the summer of 2006), and should be available in commercial products by the end of 2006. This is to be compared to 10-20 lm/W for good incandescent sources, and 50-100 lm/W for good fluorescent sources. Obtaining LEDs with efficiency of 150 lm/W is generally considered a target for competitiveness against conventional sources.

Of course, if LEDs are to supplement other white light sources, plain efficiency is not enough: they must also be available at a competitive price. In this context, light sources are then described in terms of lm/\$ or even lm/W/\$. Currently, high-power LEDs are still more expensive by a factor 25-100 than conventional light sources if only the initial (buying) cost is considered. However, considering their far longer lifetime and higher robustness, they are already competitive with incandescent sources if costs are considered over time (although still 10 times more expensive than the best fluorescent sources).

Considering the various aspects in which LEDs can still be optimized, it is quite reasonable to expect that this factor of 25-100 in efficiency will be reached within one decade. Besides, LEDs offer additional potential advantages such as small size, fast response time, control of the output intensity, good color rendering and high brightness (see below).

Brightness

Another important figure of merit is the *brightness* (or *luminance*) of an LED:

$$\mathcal{L} = \frac{d\mathcal{P}_{opt}}{d\Omega dA} \tag{1.7}$$

Here, $d\Omega$ is the solid angle of light emission and dA is the area of the light source (Fig. 1.7). The total optical power emitted by the LED can be obtained by integrating $\mathcal{L}$ over solid angles and over the LED's surface.

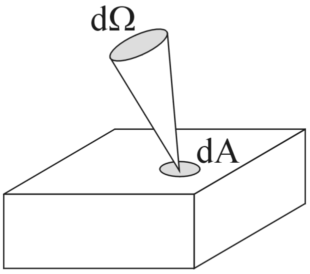

Figure 1.7: Brightness corresponds to the optical power emitted per unit surface and solid angle.

Brightness is a meaningful quantity because under common imaging conditions, the human eye is sensitive to the light emitted by unit surface, rather than to the total emitted light. Therefore, a light source with a high brightness (such as an LED where all the light is emitted in a given direction directly from the chip) will appear brighter to an observer than a lower-brightness source (for instance, an LED emitting the same intensity in the same direction, but through additional redirecting optics which make the light source seem larger).

Besides, light emission can be strongly angle-dependent, and for some applications (such as video projectors, screens backlighting or coupling to an optical fiber), a directional emission within a given angular range can be desirable feature: the directionality of emission can be evaluated by integrating brightness over the desired solid angle.

Color rendering

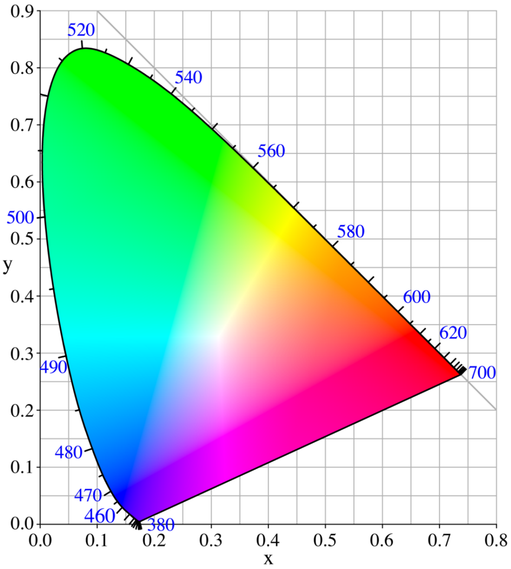

Figure 1.8: CIE chromaticity diagram: colors can be described as a mix of red, green and blue, and can be characterized by tow chromaticity coordinates x and y.

The concept of color rendering describes the ability of a light source at illuminating objects with satisfying colors to the human eye. Unfortunately, perception of colors is much harder to define than concepts such as brightness.

Most colors can be reproduced as a suitable superposition of three basic colors, such as red, green and blue. This is represented in the CIE's chromaticity diagram of Fig. 1.8.

As can be seen on Fig. 1.8, a given color can be obtained by several mixes of other colors, and hence by several light sources (called metameric sources). However, if these metameric sources are used to light a same object, they do not produce the same effect because the object's reflectivity depends on the detailed spectrum of a light source, not only on its overall color. Therefore, one has to introduce the *color rendering index* (CRI) of a light source, which describes its ability at rendering objects' colors.

To measure the CRI of a light source, several test samples are illuminated by the light source and by a reference source (usually a blackbody because a color seems 'natural' when seen under the sun's light). The color of the object illuminated by both sources is then compared, and the tested source obtains a high CRI if it closely matches the reference source. The maximal CRI is 100. Typical cool white fluorescent lamps have a CRI of 62, but more expensive and sophisticate lamps with phosphors have a higher CRI (~ 80). Sources like low pressure sodium lamps can have a negative CRI. Good white LEDs currently have a CRI of $\sim 85-90$ but use expensive phosphors, and do not always have the best external quantum efficiency. On the other hand, cheap white LEDs made of a blue LED with yellow phosphors, usually offer poor and non-uniform color rendering. This tradeoff between high CRI and high efficiency is a general feature, which may be improved by future, more efficient phosphors.

Fig. 1.9 summarizes the US Department of Energy's expectations for LED performances for the next decade.

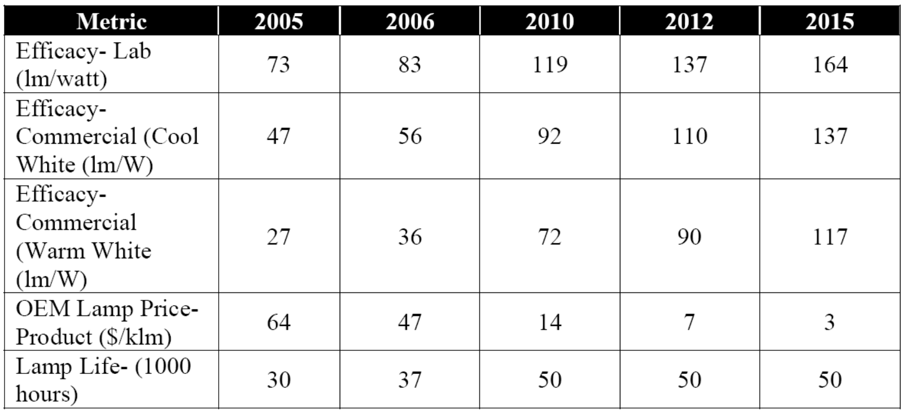

Metric	2005	2006	2010	2012	2015
Efficacy- Lab (lm/watt)	73	83	119	137	164
Efficacy- Commercial (Cool White (lm/W)	47	56	92	110	137
Efficacy- Commercial (Warm White (lm/W)	27	36	72	90	117
OEM Lamp Price- Product ($/klm)	64	47	14	7	3
Lamp Life- (1000 hours)	30	37	50	50	50

Figure 1.9: Prospective evolution of LED performances according to the US DOE (while keeping a high CRI $\sim 85-90$).

1.3 Light extraction from an LED

1.3.1 The issue of light extraction

As can be seen, the efficiency of an LED is limited by several factors which are to a large extent decoupled. Better contacts and optimized doping profile of the semiconductor lead to higher injection efficiency, while higher semiconductor quality increases the internal quantum efficiency. In order to obtain a very high external efficiency (dozens of %), each of these factors needs to be optimized. The work of this thesis focuses on the optimization of light extraction efficiency, but one should keep in mind that an ultimate high-efficiency LED must address all other limitations.

Most of the light emitted inside an LED is unable to escape the LED and to reach the outside medium (air) because of the refractive index contrast between the semiconductor (typically $n_1 \sim 2.5 - 3.5$) and air ($n_2 = 1$). According to Snell-Descartes' law at the semiconductor/air interface $n_1 \sin\theta_1 = n_2 \sin\theta_2$, light can escape to air only if it propagates in the semiconductor with an angle smaller than the *critical angle* θ_c:

$$\theta_c = \sin^{-1}\left(\frac{n2}{n1}\right) \tag{1.8}$$

The range of angles $\theta < \theta_c$ is called the *extraction cone.* Light impinging on the interface beyond the extraction cone is reflected (*total internal reflection*) and eventually re-absorbed in the semiconductor or in the metallic contacts (Fig. 1.10).

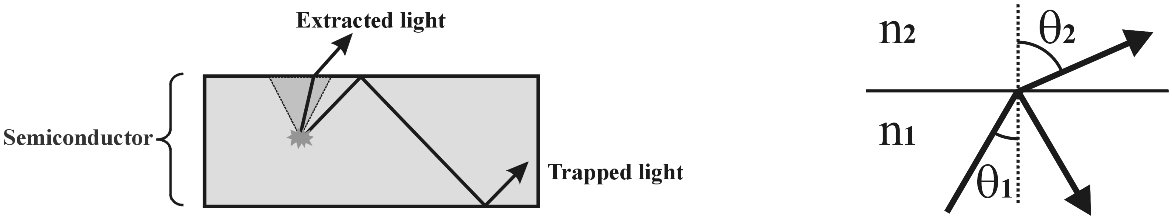

Figure 1.10: (Left) Trajectories of extracted and trapped light emitted in a semiconductor: only light emitted within the extraction cone (dotted lines) can escape. (Right) Illustration of Snell-Descartes'law $n_1 \sin\theta_1 = n_2 \sin\theta_2$.

Of course, it may be argued that part of this trapped light will eventually reach the side of the LED and be extracted (Fig. 1.11). However, this phenomenon is limited by re-absorption in the semiconductor layer. Besides, even if six extraction cones (one per side) are considered, most of the light is still trapped: the solid angle spanned by each extraction cone corresponds to 4% of the total solid angle (in the case of GaN with $n = 2.5$), limiting the light extraction to 24% at best.[3]

1.3.2 Epoxy encapsulation

The easiest way to enhance light extraction is to encapsulate the LED in an large epoxy dome, which also protects the LED mechanically (Fig. 1.12). In this case, light first escapes to the epoxy, of index $n \sim 1.5$.[4] Because the LED chip is small compared to the dome, all the emitted light then impinges

---

[3] This holds for an LED with a transparent substrate, as is the case for GaN-on-sapphire. Other materials, such as InGaAsP, possess opaque substrates which further limit light extraction.

[4] Unfortunately, materials with higher refractive index can not be used. This is mainly due to the unavailability of high-index materials sustaining high temperatures over a long period of time: degradation of the encapsulant because of heat causes strain on the contacts and eventually destroys the LED. This is a major issue regarding the lifetime of LEDs.

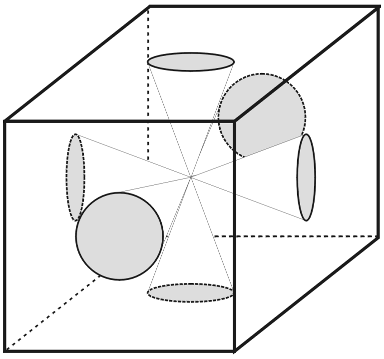

Figure 1.11: Six extraction cones are available for light extraction (if re-absorption is neglected).

on the epoxy/air interface near normal incidence and is extracted.[5] Besides, brightness is conserved under certain angles where the dome adequately images the chip surface.

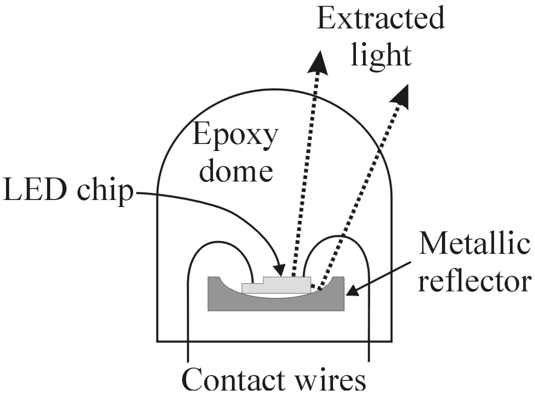

Figure 1.12: LED chip encapsulated in an epoxy dome.

The extraction cone for a GaN/epoxy interface represents 10% of the total solid angle (against 4% only in the case of GaN/air). In the most optimistic case, the total light extraction efficiency is then 6 × 10% = 60%. However, this value is actually never reached because of re-absorption of laterally travelling light in the GaN layer, and of absorption by the metallic contacts − notably by the semi-transparent Ni/Au *p*-contact. Although it is difficult to find accurate figures for such 'simple' GaN LEDs as that of Fig. 1.12, an extraction efficiency of 20% at best seems realistic, and is substantiated by Monte-Carlo simulations.[7]

1.3.3 Advanced light extraction schemes

In the following, we briefly present the main strategies for efficient light extraction. The first two schemes can be classified as 'geometric' approaches, while the latter rely on the wave nature of light. For a review and a comparison of these different schemes applied to a 'classic' material (AlGaInP) the reader is referred to Ref. [8].

---

[5] The Fresnel reflection coefficient near normal incidence is only 4%.

Shaped LED chip

In order to further enhance light extraction, a straightforward idea consists in modifying the shape of the LED chip, in order to avoid trapped trajectories. Ideally, light rays then span all possible angles inside the LED, and are able to escape after a few bounces. An implementation of this concept is Hewlett-Packard's truncated-inverted pyramid (Fig. 1.13), which in 1999 reached a record external quantum efficiency $\eta = 60.9\%$ at $\lambda = 650$ nm (under pulsed operation).[9]

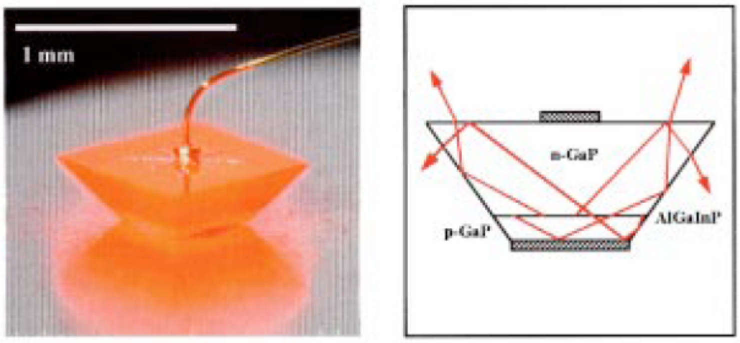

Figure 1.13: (After Ref. [9]) Hewlett-Packard's high-efficiency truncated-inverted pyramid LED.

This solution is efficient in terms of light extraction, but does not necessarily yield high brightness (the whole surface of the chip emits light) and above all it can be costly because the chips have to be shaped individually.

Small-scale structuration

Rather than modifying the overall shape of the LED, one may also consider altering its surfaces on a smaller scale (for instance by texturing or roughening it) in order to avoid total internal reflection. This idea was first introduced in Ref. [10], leading to $\eta = 30\%$. Since then, numerous implementations of surface-textured LEDs have been introduced. Let us quote for instance OSRAM's buried micro-reflector LEDs.[8] As regards GaN-based LEDs, a clever fabrication scheme for substrate-less roughened LEDs was introduced by Fujii *et. al* (Ref. [11]), leading to a demonstration of $\eta = 38\%$ at $\lambda = 440nm$ by Lumileds.[12] Likewise, the sapphire substrate is textured in Nichia's GaN-based LEDs.

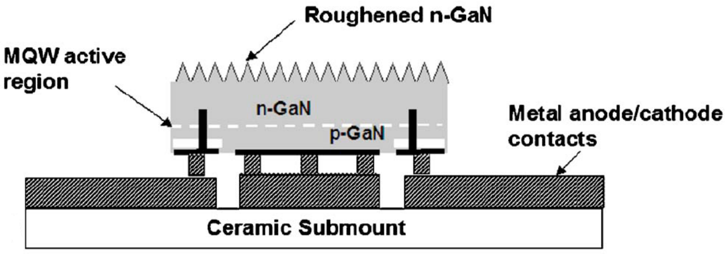

Figure 1.14: (After Ref. [12]) Lumileds' flip-chip, laser-lift-off roughened GaN LED.

An advantage of small-scale structuration over the global shaping of the LED chip is that light can be extracted after traveling a short distance (especially in the case of thin-film LEDs). This avoids re-absorption of trapped light and reduces the emitting area, which can increase the LED's brightness.

Microcavity LEDs

Micro-cavity LEDs (MCLEDs) will be studied in Chapter 2. In a MCLED, light is emitted inside a thin planar cavity where multiple reflections lead to Fabry-Pérot interferences. The angular emission pattern of the LED is then modified, so that a larger fraction of the emitted light can fall within the extraction cone.

Photonic Crystals

Light extraction by photonic crystals (PhCs) will be studied in the rest of this thesis. More precisely, we will focus on the possibility of diffracting guided lights thanks to a photonic crystal grating. For the sake of completeness, let us quote another approach often found in the literature, which consists in preventing emission of guided light by producing a band gap for guided modes.[13] This second approach, which implies 'stronger' photonic structurations, will be addressed shortly at the end of Chapter 4.

Geometric vs. wave optics

Clearly, the two first solutions presented above rely on geometric optics: they aim at modifying (ideally, *randomizing*) the propagation direction of light rays. Such approaches typically result in a nearly isotropic light emission pattern. Besides, the trajectories followed by light in the semiconductor are likely to be ergodic, and hence to bounce several times on the lossy metal contacts.

The two latter approaches, on the other hand, explicitly use wave properties of light. While they rely on more complex concepts, they also give greater control on the emission properties of a light source, and notably on its emission pattern. This is useful for two reasons. First, the external far-field pattern of the LED can be manipulated to obtain a directional source, without using any additional optics. Second, and more subtly, the path followed by light *inside the LED* before extraction can also be controlled. In a sophisticated stucture, one could thus consider taloring the trajectory of guided light so that it propagates in dielectric until it is extracted, in order to avoid excessive losses (in the metallic contacts for instance).

1.4 A few words on GaN LEDs

To close this chapter, let us give a few details on the specifics of GaN-based LEDs. Two major difficulties characterize this material: the choice of the substrate and the doping (especially p-doping).

1.4.1 Choice of the substrate, material defects

Unlike many other semiconductors, bulk wafers of GaN are currently not available (at least, not at a price compatible with lighting objectives) and other possible substrates generally suffer from a large lattice mismatch. The most common substrate is sapphire (Al_2O_3) because it is very cheap − although the lattice mismatch is as large as $\Delta a = 16\%$. Sapphire is transparent and has a refractive index $n \sim 1.7$ in the blue region. It is also perfectly insulating. Another possible substrate is 6H-SiC: although much more expensive, the lattice mismatch is only 3.5%. Companies like Cree use SiC as a substrate for high-power LEDs, whose high retail price make the cost of this substrate acceptable. Unfortunately SiC is partially absorbing in the blue region (absorption coefficient $\alpha \sim 10$ to 20 cm^{-1} at $\lambda = 400$ nm [14]), which is not ideal for light extraction. Finally, ZnO is seen as a promising substrate with a lattice mismatch of only 2%, although this material is still being explored.

In general, a high lattice constant mismatch implies a high density of dislocations, caused by the strain in GaN. Dislocations act as sites for non-radiative recombinations, decreasing the internal quantum efficiency of GaN compounds. Indeed, substrates with a better lattice matching generally result in higher internal efficiency. In order to reduce dislocations, a thick (several μm) GaN buffer layer is usually grown over the substrate in order to accommodate strain, before the $p - n$ junction itself is grown.

However, it must be pointed out that the mechanisms responsible for recombinations (both radiative and non-radiative) in GaN compounds are not well understood, especially in the presence of InGaN quantum wells. Notably, the dislocations density in GaN-on-sapphire is typically $\sim 10^{10}$ cm^{-2}: at such a density, luminescence would be quenched in any typical III-V semiconductors. Surprisingly, the internal efficiency reaches several dozens of % in InGaN. Several hypotheses have been introduced to account for this high efficiency. The most popular scenario involves the existence of small-scale In-rich clusters, forming 'quantum dots' where carriers are localized and can recombine radiatively without feeling the effect of dislocations. While TEM images of InGaN quantum wells initially seemed to support this thesis, it is not fully accepted yet and it seems that more recent measurements put it in question. Numerous other experiments, such as time-resolved photomuminescence and micro-cathodoluminescence, led to other possible explanations of the properties of InGaN, but there is so far no consensus. Let us note that indium-related carriers localization may take place even in the absence of indium-rich clusters (for instance, because of monolayer fluctuations at the quantum well's interfaces, or because of indium potential barriers forming around the dislocations [15]). One of the difficulties in this matter may be the variety of growth conditions between different groups, which probably lead to GaN with rather different microscopic properties: in the end, it is not certain that one single explanation will prove definitive for all groups.

In any case, the high density of dislocations undoubtedly degrades the optical properties of GaN compounds, prompting numerous efforts in order to reduce it, such as lateral epitaxial overgrowth (see Chapter 4, Section 4.4) or growth of GaN on alternate substrates.

1.4.2 Doping of GaN

In addition to the growth of GaN itself, doping also proves challenging and has constituted a hurdle to GaN injection for decades. Si is used for n-doping and is usually not an issue. On the other hand, the best p-donor is Mg and is still quite a poor donor: the formation of Mg-H complex degrades the electrical properties of p-GaN. In the 1990's, the demonstration by Shuji Nakamura of a thermal annealing process which activates this complex finally yielded GaN LEDs with acceptable electrical properties. However, p-GaN remains problematic even today: its lateral resistivity is still very high, so that holes tend to flow 'vertically' below the p-contacts rather than to spread laterally. Besides, Mg tends to contaminate MOCVD reactors so that p-GaN is always grown as the *last* layer in a structure.

As a consequence, GaN LEDs are topped with p-contacts under which luminescence occurs. Unfortunately, the optical properties of p-contacts are usually rather poor. The most frequent p-contact is made of a thin (a few nm) 'semi-transparent' NiAu layer, whose absorption is $\sim 25\%$ after a suitable annealling process. Another option is the use of a transparent material such as ITO (indium tin oxide). Although absorption in ITO is low, it suffers from other drawbacks. Notably, its lifetime is limited, and a GaN/ITO interface forms a Schottly barrier so that a thin Ni layer usually has to be placed at the interface to make the contact ohmic, thus increasing optical losses.

As a conclusion, there is a clear need for p-contacts with good optical properties (or of an injection scheme which limits contact losses) for efficient light extraction from GaN LEDs.

Fig. 1.15 presents a sketch of a typical GaN-on-sapphire LED, and illustrates some of the constraints mentioned above.

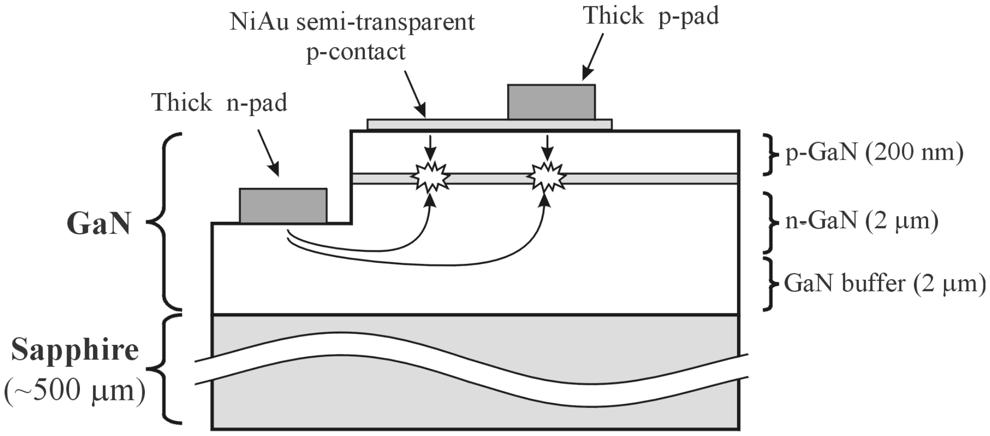

Figure 1.15: Simple GaN-based LED on a sapphire substrate. The arrows indicate the flow of carriers: light is only generated below the p-contact, so that absorption losses are difficult to avoid.

1.4.3 Guided light in GaN

As has already been pointed out, most light generated in a high-index material is trapped by total internal reflection, prompting the need for an efficient light extraction strategy. More specifically, roughly two thirds of the emitted light remain trapped in the GaN layer. Due to the dimensions of this thin-film GaN layer (a few μm high and hundreds of μm wide) it behaves as a waveguide: light is distributed in a series of so-called *guided modes*, which will be studied in Chapter 3. Without anticipating the following chapters, let us point out that due to the thin-film nature of GaN, wave optics properties can be applied and light extraction strategies based on these properties (e.g. microcavities and photonic crystals) seem naturally suited to GaN structures.

1.5 Conclusion

In principle, light-emitting diodes constitute an efficient means of converting electrical power to visible light because photons are only generated around a desired visible energy, in contrast to incandescent sources. However, several factors limit their ultimate efficiency, among which the difficulty to extract the generated light outside of the semiconductor.

While this fact has been known and addressed for years, most technical solutions found on the market are based on the principle of *randomizing* the directions accessible to light, so that it eventually escapes the LED. This approach is efficient but yields little control over the far-field pattern of the LED (which is essentially isotropic). Solutions relying on wave optics, on the other hand, are based on more complex principle but should allow a better control of the LED's directionality, while keeping a planar fabrication process. The work of this thesis is focused on the study of two such strategies for GaN-based LEDs, namely micro-cavity LEDs and photonic crystal LEDs.

Bibliography

[1] H. C. Casey and M. B. Panish. *Heterostructure lasers Part A: fundamental principles.* Academic Press, 1978.

[2] H. J. Round. A note on carborundum. *Electrical World*, page 309, 1907.

[3] W. Shockley. The theory of p-n junctions in semiconductors and p-n junction transistors. *Bell System Technical Journal*, 28(3):435–489, 1949.

[4] K. Lehovec, C. A. Accardo, and E. Jamgochian. Injected light emission of silicon carbide crystals. *Physical Review*, 83(3):603–607, 1951.

[5] S. Nakamura, N. Iwasa, M. Senoh, and T. Mukai. Hole compensation mechanism of p-type GaN films. *Japanese Journal of Applied Physics Part 1-Regular Papers Short Notes and Review Papers*, 31(5A):1258–1266, 1992.

[6] S. Nakamura, S. Pearton, and G. Fasol. *The Blue Laser Diode: The Complete Story.* Springer, Berlin, 2000.

[7] T. X. Lee, C. Y. Lin, S. H. Ma, and C. C. Sun. Analysis of position-dependent light extraction of GaN-based LEDs. *Optics Express*, 13(11):4175–4179, 2005.

[8] K. Streubel, N. Linder, R. Wirth, and A. Jaeger. High brightness AlGaInP light-emitting diodes. *IEEE Journal of Selected Topics in Quantum Electronics*, 8(2):321–332, 2002.

[9] M. R. Krames, M. Ochiai-Holcomb, G. E. Hofler, C. Carter-Coman, E. I. Chen, I. H. Tan, P. Grillot, N. F. Gardner, H. C. Chui, J. W. Huang, S. A. Stockman, F. A. Kish, M. G. Craford, T. S. Tan, C. P. Kocot, M. Hueschen, J. Posselt, B. Loh, G. Sasser, and D. Collins. High-power truncated-inverted-pyramid (AlxGa1-x)(0.5)In0.5P/GaP light-emitting diodes exhibiting $>$ 50 percent external quantum efficiency. *Applied Physics Letters*, 75(16):2365–2367, 1999.

[10] I. Schnitzer, E. Yablonovitch, C. Caneau, T. J. Gmitter, and A. Scherer. 30-percent external quantum efficiency from surface textured, thin-film light-emitting-diodes. *Applied Physics Letters*, 63(16):2174–2176, 1993.

[11] T. Fujii, Y. Gao, R. Sharma, E. L. Hu, S. P. DenBaars, and S. Nakamura. Increase in the extraction efficiency of GaN-based light-emitting diodes via surface roughening. *Applied Physics Letters*, 84(6):855–857, 2004.

[12] O. B. Shchekin, J. E. Epler, T. A. Trottier, T. Margalith, D. A. Steigerwald, M. O. Holcomb, P. S. Martin, and M. R. Krames. High performance thin-film flip-chip InGaN-GaN light-emitting diodes. *Applied Physics Letters*, 89(7), 2006. 071109.

[13] S. H. Fan, P. R. Villeneuve, J. D. Joannopoulos, and E. F. Schubert. High extraction efficiency of spontaneous emission from slabs of photonic crystals. *Physical Review Letters*, 78(17):3294–3297, 1997.

[14] R. Groth and E. Kauer. Absorption freier ladungstrager in alpha-SiC-kristallen. *Physica Status Solidi*, 1(5):445–450, 1961.

[15] A. Hangleiter, F. Hitzel, C. Netzel, D. Fuhrmann, U. Rossow, G. Ade, and P. Hinze. Suppression of nonradiative recombination by v-shaped pits in GaInN/GaN quantum wells produces a large increase in the light emission efficiency. *Physical Review Letters*, 95(12), 2005. 127402.

Chapter 2

Micro-Cavity LEDs

As has been seen in the previous chapter, only $\sim 5\%$ of the light emitted by an LED naturally escapes the semiconductor by one face. In order to enhance this value, one may consider altering the emission pattern of the quantum wells, so that a greater fraction of the emitted light is directly directed in the extraction cone. This leads to the concept of MicroCavity LED (MCLED), where a thin LED is embedded between two mirrors.[1] The resulting multiple interferences modify the pattern of emitted light, thus enhancing light extraction (Fig. 2.1). In this chapter, we present theoretical results and experimental measurements on GaN-based MCLEDs.

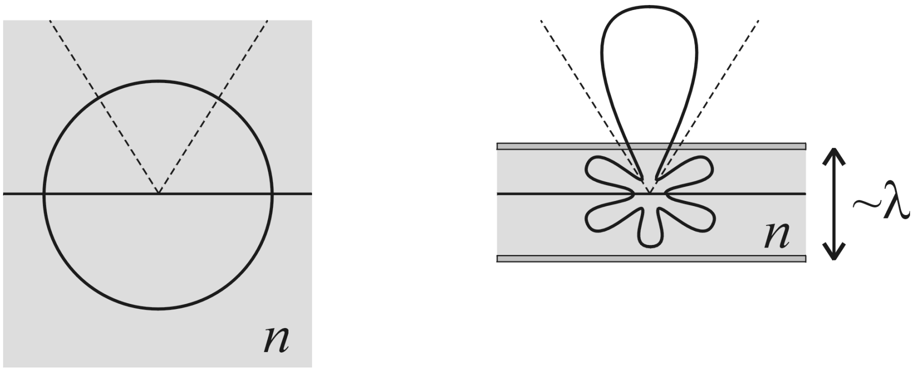

Figure 2.1: Principle of a microcavity LED. (Left) In a bulk medium, light emission is isotropic. Only a few % of the total emission fall above the critical angle (dashed line). (Right) The presence of mirrors modifies the emission pattern of the source, yielding preferential emission above the light cone.

2.1 MCLEDs: Theory

2.1.1 Principle of MCLEDs

To introduce the principle of microcavity LEDs, let us first explore semi-quantitatively the behavior of a light source in a Fabry-Pérot cavity, following the tutorial description of Ref. [2]. We will then resort to exact simulations in order to quantify the potential of this approach in the case of GaN LEDs. A more thorough treatment of the theory of MCLEDs can be found in Refs. [3, 4].

Fabry-Pérot cavity

We consider a plane wave whose wavelength in the vacuum is λ_0. In a medium of index n, the wavevector of this wave is:

$$k = nk_0 = n\frac{2\pi}{\lambda_0} \tag{2.1}$$

Where k_0 is the wavevector of light in the vacuum. If we take the convention $c = 1$, the frequency of light is:

$$\omega = \frac{2\pi}{\lambda_0} = k_0 \tag{2.2}$$

Let us now consider a Fabry-Pérot cavity made of a dielectric of index n and thickness L placed between two mirrors, as depicted on Fig. 2.2. We assume that this structure is illuminated from top by an incident plane wave of intensity $I_0 = E_0^2$, impinging at an angle θ.

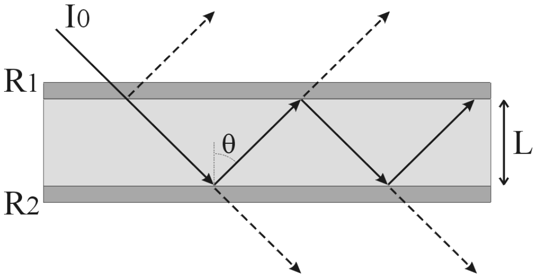

Figure 2.2: Sketch of a Fabry-Pérot cavity.

Let us denote as r_1 and R_1 (respectively r_2 and R_2) the field and intensity reflection coefficients of mirror 1 (resp. 2). We also introduce the corresponding transmission coefficients t_1, T_1, t_2 and T_2. The plane wave transmitted by the structure has an amplitude:

$$\begin{aligned} E_t &= E_0 t_1 t_2 \left(1 + r_1 r_2 e^{2i\phi} + \left(r_1 r_2 e^{2i\phi}\right)^2 + \dots\right) \\ &= E_0 \frac{t_1 t_2}{1 - r_1 r_2 e^{2i\phi}} \end{aligned} \tag{2.3}$$

Here, 2ϕ is the phase shift of the wave during a round-trip in the cavity, given by:

$$2\phi = 2nk_0 L cos(\theta) \tag{2.4}$$

Therefore, the transmission (in intensity) of the Fabry-Pérot is:

$$\begin{aligned} T_{FP} = \frac{|E_t|^2}{|E_0|^2} &= \frac{T_1 T_2}{1 + R_1 R_2 - 2r_1 r_2 \cos 2\phi} \\ &= \frac{T_1 T_2}{(1 - r_1 r_2)^2}\mathcal{A}(\phi) \end{aligned} \tag{2.5}$$

Where $\mathcal{A}$ is the Airy function:

$$\mathcal{A}(\phi) = \frac{1}{1 + C\sin^2\phi} \quad \text{with} \quad C = \frac{4r_1 r_2}{(1 - r_1 r_2)^2} \tag{2.6}$$

The Airy function is thus characteristic of the transmittive behavior of a Fabry-Pérot.

Fabry-Pérot with embedded light source

Let us now consider the same structure, with a light-emitting source located at a position z inside the cavity (Fig. 2.3). We assume that this source emits plane waves isotropically in all directions θ.

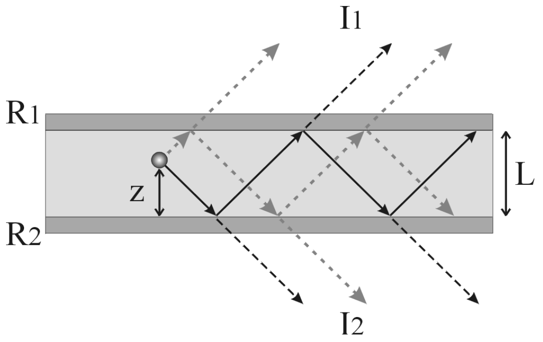

Figure 2.3: Fabry-Pérot cavity with an embedded source.

We now introduce two phase shifts:

$$\phi = nk_0Lcos(\theta)$$
$$\phi' = nk_0zcos(\theta) \tag{2.7}$$

As before, ϕ is the phase shift of a plane wave going through the cavity of size L, and ϕ' is the analogous for propagation on a vertical distance z. We can now express the amplitude of the field above the cavity in direction θ:

$$\begin{aligned} E_1 &= E_0e^{i(\phi-\phi')}t_1\left(1+r_1r_2e^{2i\phi}+\dots\right)+E_0e^{i(\phi+\phi')}r_2t_1\left(1+r_1r_2e^{2i\phi}+\dots\right) \\ &= E_0t_1\frac{1+r_2e^{2i\phi'}}{1-r_1r_2e^{2i\phi}} \end{aligned} \tag{2.8}$$

We define the so-called *antinode factor*, which describes the density of the electromagnetic field inside the cavity:

$$\zeta(\phi') = 1 + R_2 + 2r_2cos2\phi' \tag{2.9}$$

We can thus express the intensity emitted above the cavity:

$$I_1 = |E_1|^2 = I_0\frac{T_1}{(1-r_1r_2)^2}\mathcal{A}(\phi)\zeta(\phi') \tag{2.10}$$

Likewise, the intensity emitted below the cavity is:

$$I_2 = I_0\frac{T_2}{(1-r_1r_2)^2}\mathcal{A}(\phi)\zeta(\phi') \tag{2.11}$$

Thus, it appears that the emission intensity in a given direction is a product of two factors: the Airy function, which indicates the resonant behavior of the bare Fabry-Pérot cavity, and the antinode factor, which governs the coupling efficiency of the light source to the Fabry-Pérot modes. Indeed, ζ is maximal when the source is located at an antinode of a given mode: in this case, emission in the mode is favored.

For instance, when $z = L/2$ (source at the middle of the cavity), $\mathcal{A}$ is maximal whenever $\phi = m\pi$, corresponding to constructive interferences of the Fabry-Pérot. However, when m is odd, $\zeta = 0$ because the corresponding Fabry-Pérot mode is odd and has a node in the middle of the cavity, at the position of the source.

Light extraction, cavity order

So far, we have only considered that both the cavity and the outer media had the same index n, and thus neglected the possibility of total internal reflection. We now turn to a case where the upper medium has an index n_{ext}. Thus, light emitted in the cavity beyond the critical angle θ_c can not propagate in this medium. The critical angle is given by:

$$\theta_c = asin\left(\frac{n_{ext}}{n}\right) \tag{2.12}$$

Moreover, we make several simplifying assumptions. The lower mirror is assumed to be perfect, so that $r_2 = 1$. The reflectivity of the upper interface is still taken as constant and equal to r_1. Finally, we assume that the source is located at the center of the cavity, e.g. $z = L/2$.

With all these assumptions, the intensity emitted upward simplifies to:

$$I_1 = 2I_0T_1\frac{1+\cos\phi}{1+R_1-2r_1cos2\phi} \tag{2.13}$$

Of course, this simple form should no longer hold when $\theta > \theta_c$ because then r_1 jumps to unity. However, we disregard this fact for now and assume that this expression still gives a fair estimate of the power emitted beyond the critical angle. We consider a model case where $n = 2.5$ (a typical value for GaN), $n_{ext} = 1$ and $R_1 = 0.2$.[1] The cavity thickness is taken so that the so-called *cavity order* m_c is integer, where:

$$m_c = \frac{nL}{\lambda} \tag{2.14}$$

This condition simply corresponds to requesting that I_1 be maximal at $\theta = 0$. Fig. 2.4 shows several examples of I_1 as a function of θ, for $m_c = 15$, 3 and 1 respectively

I_1 consists of peaks corresponding to the Fabry-Pérot modes excited by the source. The modes falling above θ_c are extracted. As can be seen, m_c governs the number of peaks in I_1, e.g. the number of Fabry-Pérot modes supported by the cavity. The power carried by each of these peaks is constant. Indeed, integration of I_0 over peak p, taking solid angles into account, is best carried out by integrating over ϕ and yields:

$$\int_p I_0 \sin\theta d\theta \sim \int_{(2p-1)\pi}^{(2p+1)\pi} I_0 d\phi = 2\pi I_0 \tag{2.15}$$

We are now ready to draw conclusions on the effect of L on the light extraction efficiency. It is given by the ratio of light emitted above θ_c and the total emission:

$$\eta = \frac{\displaystyle\int_{\theta=0}^{\theta_c} I_1 sin\theta d\theta}{\displaystyle\int_{\theta=0}^{\pi/2} I_1 sin\theta d\theta} \tag{2.16}$$

---

[1] This corresponds to the Fresnel reflection coefficient at normal incidence for an interface between $n = 2.5$ and $n = 1$.

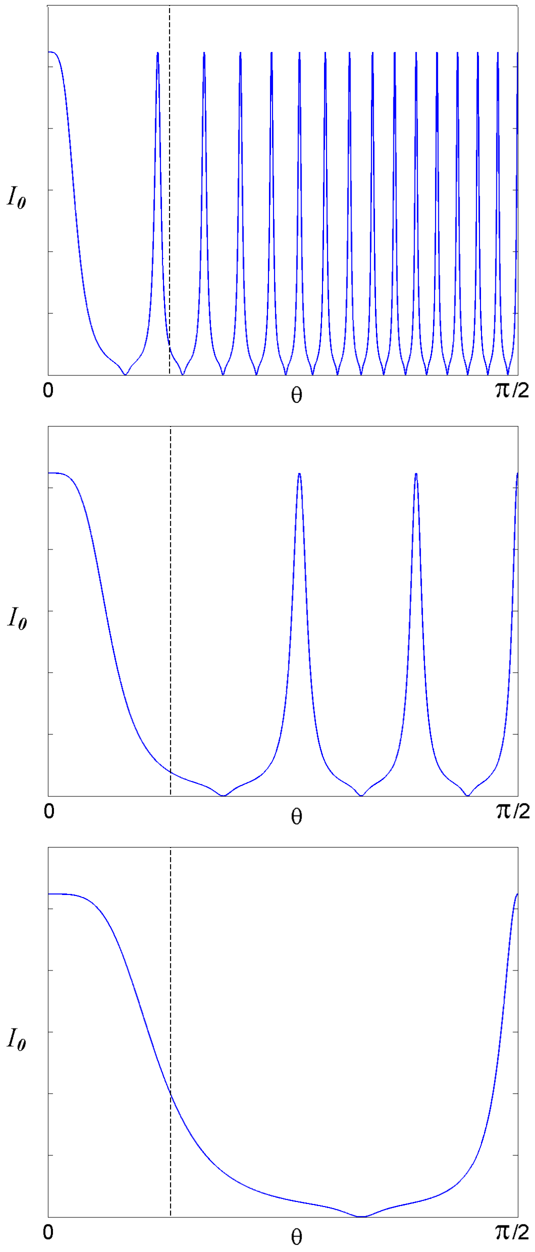

Figure 2.4: Intensity emitted by a source in a GaN Fabry-Pérot cavity, with cavity orders m_c = 15, 3 and 1 from top to bottom. Thinner cavities feature less emission peaks. Light emitted above θ_c (dashed vertical line) is extracted to air.

When $L >> \lambda$, in the thick cavity regime, I_1 features many peaks both above and below θ_c, and η is simply the ratio of the solid angles of integration:

$$\eta \sim \frac{2\pi(1 - cos\theta_c)}{2\pi} \sim \frac{n_{ext}^2}{2n^2} \tag{2.17}$$

When $L \sim \lambda$, we depart from this statistical limit. When L is small enough that only one peak is in the escape cone, we reach the so-called *microcavity regime*. Since the intensity is equally shared between peaks, the extraction efficiency is then simply:

$$\eta = \frac{1}{m_c} \tag{2.18}$$

This relation shows that high-efficiency MCLEDs should have a low cavity order, e.g. be *as thin as possible.* As will be seen, the relation is only approximate and no longer holds for very thin cavities ($m_c \sim 1$) where the extraction efficiency saturates around 50% at best.

The crossover between the thick cavity and microcavity regimes, when η becomes higher than the thick cavity limit, corresponds to:

$$m_c = \frac{2n^2}{n_{ext}^2} \tag{2.19}$$

In the case of GaN, this yields $m_c \sim 12$ or a thickness $\sim 2\mu$m.

Finesse

A useful quantity in the description of a cavity is its *finesse*, which describes the relative width of the Fabry-Pérot peaks. It is defined as:

$$F = \frac{\Delta\phi}{\phi} \approx \frac{\pi\sqrt{r_1 r_2}}{1 - r_1 r_2} \tag{2.20}$$

Where $\Delta\phi$ is the full width at half maximum of the cavity's Airy function (Eq. 2.6). The last part of Eq. 2.20 is valid when r_1 and r_2 are large enough. Fig. 2.5 compares emissions of two cavities (as given by Eq. 2.13) with $R_1 = 0.1$ and $R_1 = 0.5$ respectively (and $R_2 = 1$), corresponding to finesses of ~ 2.6 and 9. For the cavity of higher finesse, most of the extracted peak falls in the extraction cone, while a larger part of this peak lies beyond the critical angle for the cavity of lesser finesse. However, this effect is seen to be quite modest in our case: thanks to its low refractive index (2.5), GaN has a rather large critical angle which can easily accommodate a Fabry-Pérot mode.

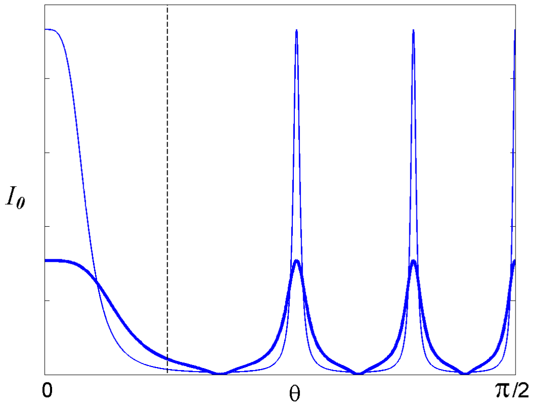

Figure 2.5: Intensity emitted by a source in a cavity with $m_c = 3$, and a finesse $F = 2.6$ (thick line) and $F = 9$ (thin line) respectively. For the cavity of lower finesse, a larger part of the extracted mode leaks beyond the critical angle, but this effect is small.

Detuning

The efficiency of Eq. 2.18 can easily be enhanced if the cavity thickness slightly departs from the value $\lambda m_c/n$. More precisely, we define the detuning δ by:

$$\delta = \lambda - \frac{Ln}{m_c} \tag{2.21}$$

It can then be shown (Ref. [5]) that the extraction efficiency is roughly maximal for an optimal value:

$$\delta_{opt} = -\lambda \frac{n_{ext}^2}{4n^2} \tag{2.22}$$

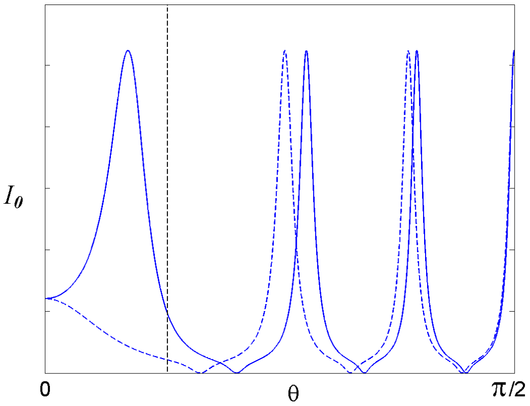

Figure 2.6: Detuned emission for the same cavity as $m_c = 3$ above. Full line: optimal detuning, the extracted peak is entirely in the extraction window. Dashed line: worst case, the peak is nearly entirely outside of the extraction window.

Indeed in this case, as can be seen on Fig. 2.6, the extracted peak is *fully* located in $\theta \in [0; \theta_c]$, and the extracted intensity is doubled. Another consequence is that maximum emission now occurs for $\theta > 0$; in terms of external angle, the maximum is close to $\theta = 45^o$. The resulting far-field pattern of such an LED is sometimes described as 'rabbit's ears' because of its appearance (see Fig. 2.12 for examples).

On the other hand, a detuning with the inverse sign has the opposite effect: the mode is pushed outside of the extraction window, and the efficiency is spoiled. This implies that L should be controlled with a good accuracy, because the optimal and worst detunings are separated by a short distance, only ~ 30 nm in the case of GaN.

In summary, the microcavity regime corresponds to thin cavities, where the extraction efficiency departs from the average value of thick cavities because only a few Fabry-Pérot modes are present. If the cavity thickness is correctly tuned, one of these peaks is fully extracted, and the extraction efficiency is $\sim 2/m_c$: it is highest for very thin cavities. For optimal light extraction, the thickness of the cavity has to be controlled with accuracy: a 30 nm error completely spoils its efficiency.

2.1.2 Application to the case of GaN

So far, we have accounted for the microcavity effect with a simplistic model: all reflectivities were kept constant and absorption and polarization effects were neglected, as well as possible modifications of the radiative lifetime of the light emitter.

To treat the case of GaN structures, we now turn to exact electromagnetic simulations. We model the emission of a quantum well in a multilayer structure with the method of the transfer matrix with a dipole source, introduced in Ref. [6]. In this method, described in more details in Chapter 6, Maxwell's equations are solved exactly in the presence of a light source, and yield its emission pattern as well as its extraction efficiency. More specifically, here and in all the remainder of the thesis, we model InGaN quantum wells as a superposition of *horizontal* dipoles with random orientation.[2]

Emission in a typical GaN structure

As a comparison basis, let us first study the emission diagram of a typical GaN LED. Our test structure is made of a sapphire substrate (of index $n_{sapphire} = 1.7$), a 3μm thick GaN layer (of index $n_{GaN} = 2.5$) with a quantum well located 150 nm below the GaN surface, and an air superstrate. Fig. 2.7 displays the emission diagram of the quantum well.

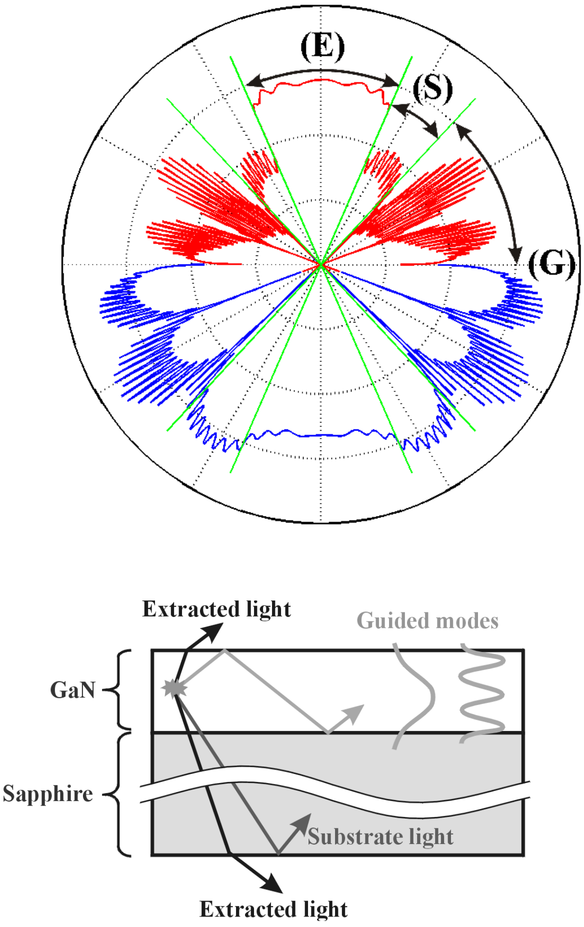

Figure 2.7: Emission diagram of a quantum well in a GaN structure, representing the power emitted per solid angle as a function of polar angle of emission θ (on a logarithmic scale). The horizontal axis corresponds to the position of the quantum well. E = directly extracted light, S = substrate light, G = guided light. The radial lines represent the critical angles θ_c^{air} and θ_c^s.

---

[2] This is consistent with the Hamiltonian of wurtzite InGaN grown along the c-axis, where the spin-orbit valence band is splitted from the heavy and light holes bands by the anisotropy of the crystal along the *c*-axis. [7] In this case, the emission is expected to correspond mostly to that of horizontal dipoles, as shown in Apppendix B. However, to my knowledge, no experimental verification of this property has been published yet.

Let us analyze this diagram. We define the critical angles of air and sapphire as:

$$\theta_c^{air} = asin\left(\frac{1}{n_{GaN}}\right) \quad \theta_c^s = asin\left(\frac{n_{sapphire}}{n_{GaN}}\right) \tag{2.23}$$

Light emitted close to the vertical ($\theta \in [0, \theta_c^{air}]$) is in the escape cone of air and can thus exit the LED. Of course, part of this light is emitted downward in the sapphire substrate. However, sapphire is transparent to visible light and this light can simply be redirected upward by placing a metallic mirror under the substrate. Alternately, one may place a metallic mirror on top of the LED and emit light through the substrate side, as is commonly done for basic GaN LEDs. We call this light *extracted light*. It amounts to 12% of the total emitted light.[3] This value neglects the possible absorption in metallic contacts, which can be quite high (40% in a simple NiAu semitransparent contact).

Light emitted at angles $\theta \in [\theta_c^{air}, \theta_c^s]$ is propagative in sapphire but not in air. This light is called *substrate light*,[4] and carries away 25% of the total light emission. Because of the thickness of the substrate ($\sim 500\mu$m), this light propagates mostly in sapphire and suffers very little absorption. Thus, it can propagate for several cm and is usually observed at the cleaved edge of the sample. Part of it can usually be redirected upward by a geometric approach (such as mirrors on the sides of the LED), and actually accounts for most of the light emission in a basic mounted LED.

Finally, light emitted at angles $\theta > \theta_c^s$ is only propagative in GaN. This light forms so-called guided modes in the GaN layer, which acts as a thick waveguide. The properties of guided modes will be explored in the following chapters. Here, this *guided light* carries away 66% of the total light emission: this is the light we aim at extracting!

GaN MCLEDs: choice of the materials

Let us now discuss possible structures for GaN microcavity LEDs. In general, two kinds of mirrors can be considered: dielectric and metallic mirrors.

Dielectric mirrors, also called Distributed Bragg Reflectors (DBRs), are made of stacks of two dielectrics of different indices n_1 and n_2. Light is reflected by the constructive interference of the multiple reflexions occurring at the dielectric interfaces (Fig. 2.8). In principle, reflexion can be arbitrarily high in a given direction provided the DBR has a sufficient number of layers. Good reflectivity is obtained with fewer layers if the index contrast $\Delta n = n_2 - n_1$ is high. Likewise, a high Δn ensures high reflectivity in a large angular range. An important advantage of DBRs is that conductive DBRs can be grown epitaxially and thus embedded in the LED.

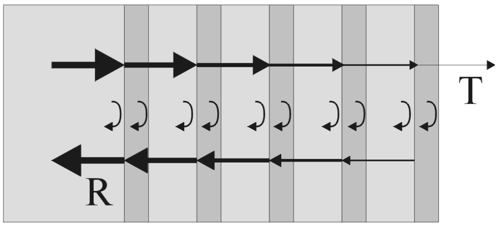

Figure 2.8: Principle of a Distributed Bragg reflector: alternated layers of indices n_1 and n_2 produce multiple reflections of an incoming wave. If all reflections interfere constructively, the reflexion coefficient (R) can be arbitrarily high for a sufficient number of layers. The optimal layer thicknesses of the layers for reflection at a wavelength λ are λ/n_1 and λ/n_2, respectively.

---

[3] One must be careful to take solid angles into account when evaluating light emission: glancing polar angles ($\theta \sim 90^o$) correspond to a large solid angle and thus carry away a large fraction of the light emission.

[4] The name *leaky light* is also found in the literature, but we avoid it here because of a possible confusion with the leaky modes of photonic crystals which will be studied in the next chapters.

In the case of GaN unfortunately, good conductive DBRs are very difficult to grow. The available compounds are AlGaN and InGaN. AlGaN has a higher gap (and therefore a lower index) and InGaN a lower gap.

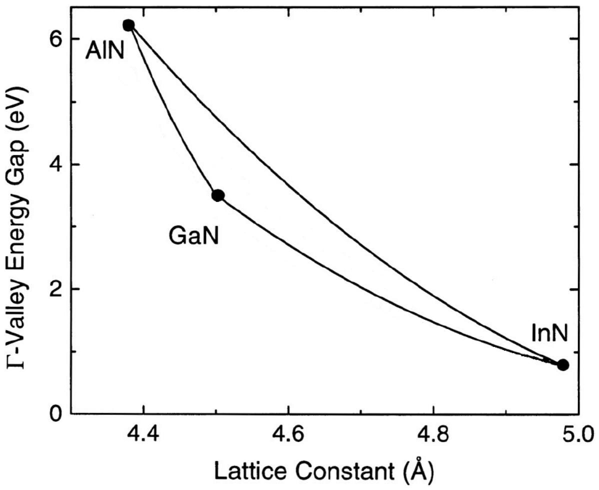

Figure 2.9: (After Ref. [7]) Band parameters of AlInGaN compounds in wurtzite form.

However, the crystal lattice mismatch increases rapidly with the Al or In content, leading to strain and to cracks in the epitaxial layers. One has to maintain low contents of Al and In in order to avoid this: the index contrast in this case is quite limited, $\Delta n \sim 0.2$ being a typical value. This implies that even if a high number of pairs is used, leading to good reflectivity at normal incidence, the angular width of the reflectivity plateau is limited. Besides, the *penetration length* (the distance of penetration of evanescent light in the DBR) goes up, leading to a higher cavity order m_c.

It should be mentioned however that excellent results have been reported recently at EPFL. These are based on the use of AlInGaN compounds, where the strain is mitigated and overall higher index contrasts can be obtained.[8]

Metallic mirrors have the advantage of offering high reflectivity at all angles. They usually have very small penetration lengths (the skin depth in a good metal is of a few nm), making small cavity orders accessible. On the other hand, they can absorb light and can not be embedded in the LED during growth. The effect of absorption is especially strong if the active region is too close to the mirror (a few tens of nm): in this case, surface plasmons can be efficiently excited by the electron-hole pairs of the quantum well and non-radiative loss becomes very strong.[9]

On the side of metallic mirrors, Ag and Al are reasonable choices. They both have high reflectivity ($\sim$ 90%) in the visible, down to 400 nm. Surface plasmons are still a possible concern, so that the quantum wells should be kept at least 50 nm away from the metal.

Overall, the choice of a material system is not straightforward, because of the relative advantages of DBRs and metallic mirrors. As a consequence, we consider in the following several kinds of structures, which combine both kinds of mirrors.

Simulation of GaN MCLEDs

To determine the optimal structure, we take various combinations of mirrors, and consider extraction both in air and epoxy. For the top mirrors, we compare a DBR with $N = 13$ pairs (indices $n = 2$ and 2.5, leading to an optimistic index contrast $\Delta n = 0.5$), and an Ag mirror ($n = 0.05 + 2.5i$). For the bottom mirrors we compare a DBR with N=3[5] and a simple interface between GaN and air/epoxy. The emitting wavelength is $\lambda = 405$ nm. Both the cavity thickness and the position of the quantum well are varied in order to determine the optimal extraction in each structure. We obtain optimization diagrams as shown on Fig. 2.10.

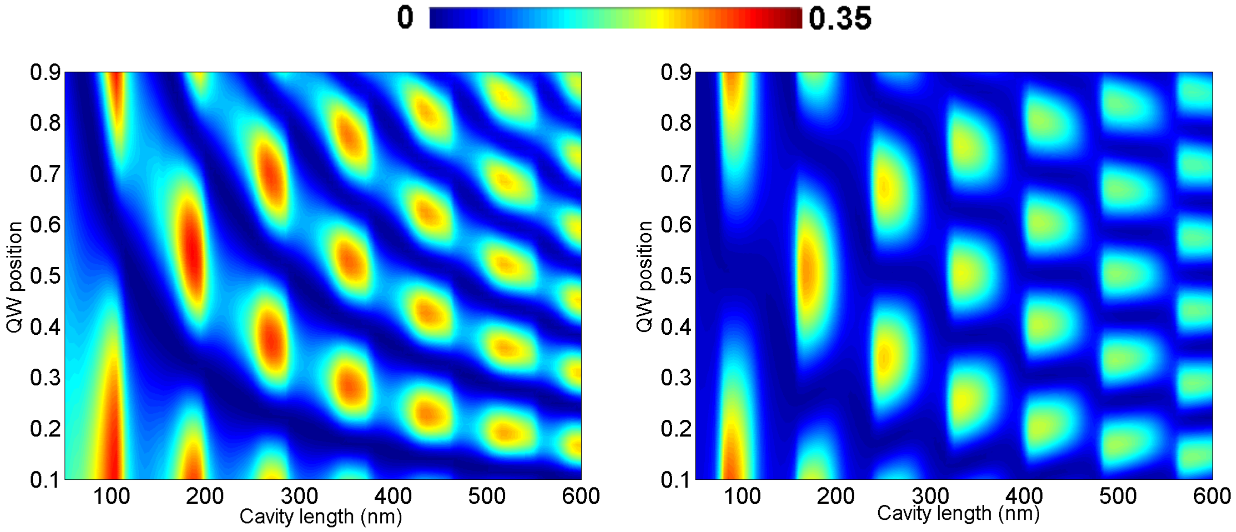

Figure 2.10: Optimization diagrams of GaN MCLEDs. (Left) Ag bottom mirror and simple air/GaN interface on top. (Right) DBRs on both sides (with $N = 15$ for the bottom and $N = 4$ for the top mirror), and extraction to air. 'QW position' refers to the relative position of the quantum well in the cavity, 0 corresponding to the bottom and 1 to the top. As can be seen, the windows of optimal extraction are quite narrow (a few dozens of nm), especially in the presence of DBRs which increase the finesse of the MCLED and hence produce sharper resonances.

Notably, it appears that the extraction efficiency does not rise to 1 for very thin LEDs, as could be expected from the approximate expression of Eq. 2.18. Indeed, the simplified treatment used to obtain this equation no longer holds in this regime: a large fraction of the light (at least 50%) always remains trapped as guided modes in the GaN layer. Strategies to extract this light will be adressed in the following chapters.

The optimal extraction efficiency of each structure is then taken as the maximum of the diagram (disregarding cavity thicknesses below 100 nm, which are not realistic). Fig. 2.11 summarizes the results.

	DBR (N=3)	Interface
DBR (N=13)	23	24
Ag	31	31

	DBR (N=3)	Interface
DBR (N=13)	27	27
Ag	43	44

Figure 2.11: Optimal extraction efficiencies (in % of total emission) for various MCLED geometries (rows=bottom mirror, columns=top mirror). Left table: extration in air, right table: extraction in epoxy. N is the number of pairs of the DBR. 'Interface' refers to a simple GaN/outer medium interface.

As can be seen, the optimal values are always found using a metal bottom mirror: the penetration length in a DBR is too detrimental in terms of cavity order. Extraction to epoxy is of course favorable

---

[5] Indeed, a modest reflectivity is sufficient for the top DBR, which should always be less reflective than the bottom mirror.

because it leads to a larger critical angle. In general, use of a top DBR does not enhance efficiency. This is simply because for very thin MCLEDs with cavity orders $m_c \sim 2$, the escape cone of a GaN/air (resp. GaN/epoxy) interface is naturally large enough to accommodate most of the extracted peak: increasing the finesse of the cavity has no strong beneficial effect. This feature is already visible on the approximate treatment of Fig. 2.6, where it is apparent that the extracted mode fits well within the extraction cone. Besides, the effective cavity length increases when a DBR is present (the modes can leak in the dielectric more than in air), which leads to more emission in guided modes: this turns out to outbalance the positive effect of the top DBR in the case of epoxy, leading to an overall lower extraction.

On the other hand, a top DBR has a direct impact on the far-field pattern of the LED, as shown on Fig. 2.12: because of the higher finesse of the cavity, the extracted peak has a much narrower angular aperture. This can be useful for some applications, especially if one wants to couple the emitted light to an optical fiber, or to obtain a spectral selectivity (indeed, the angle of the ears shifts with λ).

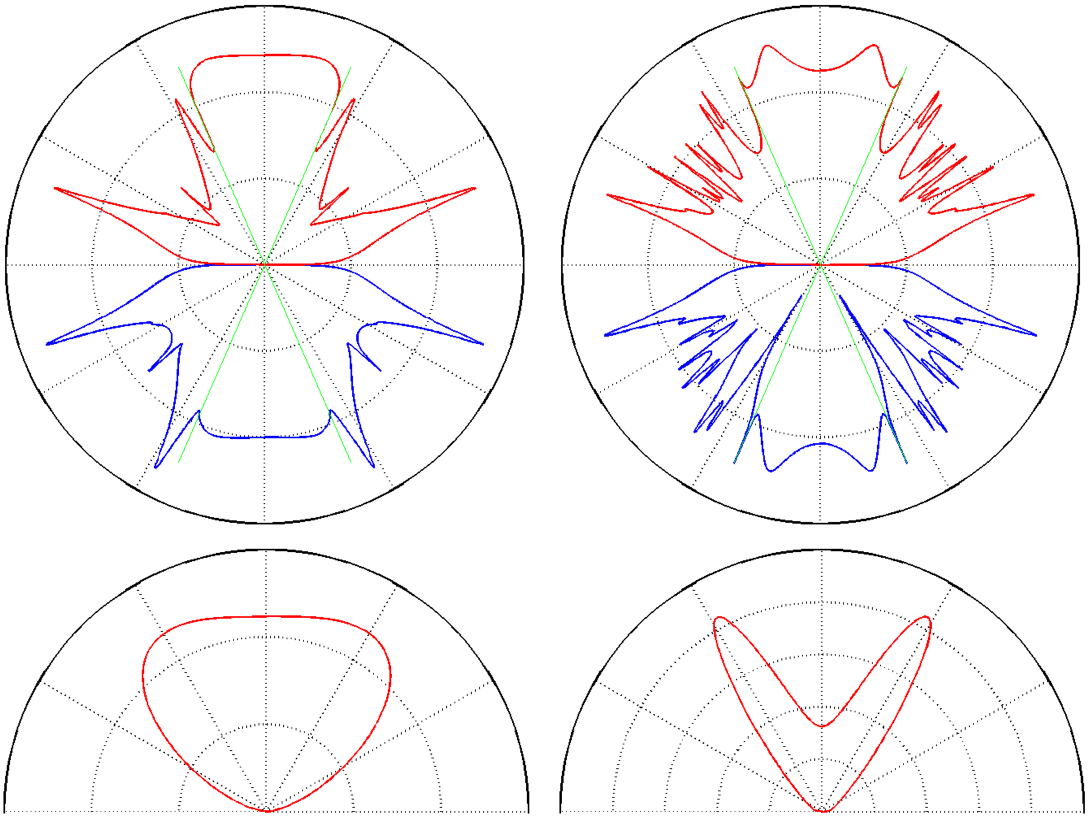

Figure 2.12: Emission diagrams (λ = 405 nm) of GaN MCLEDs with an Ag bottom mirror, a 185 nm thick cavity and a relative quantum well position 0.55. (Top) Internal emission of the source, logarithmic scale. (Bottom) External emission through the top surface, linear scale. (Left) GaN/air interface. (Right) DBR (N=3) on top of the GaN layer. In the presence of the top DBR, notice the more numerous guided mode peaks (internal emission) and the sharper extracted peak.

In accordance with these simulations, experimental efforts at UCSB have been directed toward MCLEDs made of a metallic mirror and a simple GaN/air interface. These are reported in the next section.

Microcavity LEDs constitute a simple approach to enhancing light extraction. Their potential is well assessed in usual III-V materials. In the case of GaN however, unlike in GaAs, the material characteristics are not favorable to an efficient implementation. Good conductive DBRs are not available. The best structures are made of a thin GaN layer reported on a metallic substrate. For these structures, calculations predict an optimal extraction efficiency of 31% in air and 44% in epoxy.

2.2 Fabrication and measurement of GaN MCLEDs

This section presents experimental results on MCLEDs obtained at UCSB. All the following were measured on structures fabricated by Tetsuo Fujii. A first report on these efforts can also be found in Ref. [10].

2.2.1 GaN MCLEDs: fabrication process

The fabrication process of these LEDs is complex: one has to bond the GaN layer on a metallic substrate (Ref. [11]) and get rid of the sapphire substrate. This is done by a laser lift-off process where the sample is illuminated through the sapphire by a pulsed 245 nm KrF excimer laser. This laser is strongly absorbed at the sapphire/GaN interface, the heat shock leading to separation of the substrate from the GaN layer. The resulting structure, made of a $\sim 4\mu$m GaN layer on a metal submount, is then thinned down by chemical-mechanical polishing (CMP) to obtain the desired GaN thickness.

Table 2.13 details the fabrication process.

p-contact	p-type activation p-contact area definition p-contact formation	RTA SiO2 deposition Lithographic patterning SiO2 etching Metal deposition Lift-off
Wafer bonding	Thick metal deposition Bonding to submount	e-beam 1
Laser lift-off	Laser rastering on whole surface Ga metal removal	Krf Eximer laser HCl dip
GaN thinning	Coarse Gan etching Polishing	RIE 5 (Cl2) Chemico-mechanical polishing
Device separation	Mesa definition	Lithographic patterning SiO2 deposition SiO2 etching Mesa etching by RIE 5 (Cl2)
n-contact	n-contact definition n-contact formation	Lithographic patterning Metal deposition Lift-off

Figure 2.13: MCLED fabrication process.

An advantage of the CMP is that is naturally non-uniform: different mesa thicknesses can be obtained on the same sample. This wedge effect is very useful to characterize different cavity orders at the same time. Moreover, owing to the difficulty to obtain an accurate thickness (as already mentioned, the desired precision is on the order of 10 nm), it is hoped that at least some of the mesas will be close to the desired thickness.

In practice, Ni/Ag is usually chosen as a *p*-electrode. Ag provides good reflectivity, while a thin Ni layer (a few nm) ensures good electrical injection. The bonding metal is Au, which has a low melting point and efficiently sticks the GaN to the submount. The submount can be Si or a ceramic. Fig. 2.14 depicts the cross-section of the resulting device.

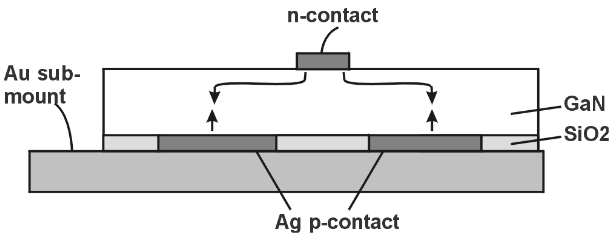

Figure 2.14: Cross-section of a laser-lift-off MCLED. Arrows depict carriers flow. Due to good current spreading in n-GaN and poor current spreading in p-GaN, light is generated only above the highly reflective p-contacts.

2.2.2 Characterization of GaN MCLEDs

Angle-resolved luminescence setup

The micro-cavity effect should significantly modify the far-field emission pattern of LEDs. Therefore, in order to characterize MCLEDs, I resorted to an angle-resolved luminescence setup, whose installation at UCSB was initiated by Carole Schwach (Fig. 2.15). This setup consists of an optical fiber mounted on a rotating arm, which collects luminescence spectra at various polar angles around the measured sample. A polarizer is placed before the fiber, to distinguish between TE and TM-polarized light. The signal is then analyzed by a spectrometer. The distance between the sample and the fiber is $\sim$ 15 cm, and the collection is limited by an aperture with 1 mm diameter, leading to an angular aperture 0.5^o. Since most light sources are at most 1 mm large, they can be considered punctual.[6]

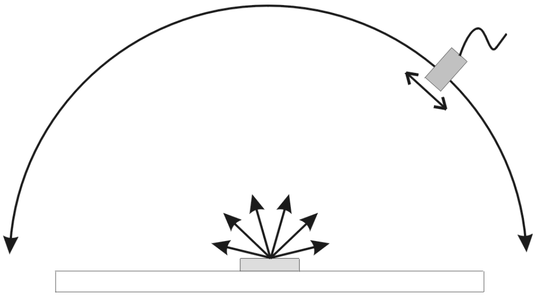

Figure 2.15: Angle-resolved luminescence setup: the luminescence is collected at all polar angles around the source.

Thinning of GaN LEDs: the onset of the micro-cavity regime

The criterion usually considered to characterize the micro-cavity regime is that of Eq. 2.19. This condition just amounts to reaching a thickness where the extraction efficiency departs significantly from the thick-LED regime. Due to the non-uniform thinning process of the MCLEDs, a wide range of thicknesses is naturally obtained on the same sample. This proves useful to observe the evolution of the LED far-field pattern with decreasing thickness.

---

[6] The area of collection by the optical fiber is larger, on the order of 1cm^2, but this is not a problem if the emitting surface is small.

Fig. 2.16 presents spectra obtained at various angles on a thick laser-lift off GaN LED, and the collection of several of these spectra in a 2-dimensional plot of emission versus wavelength and angle of emission. Such plots fully characterize the far-field emission pattern of an LED[7] and will frequently be used in the remainder of this thesis as an analysis tool.

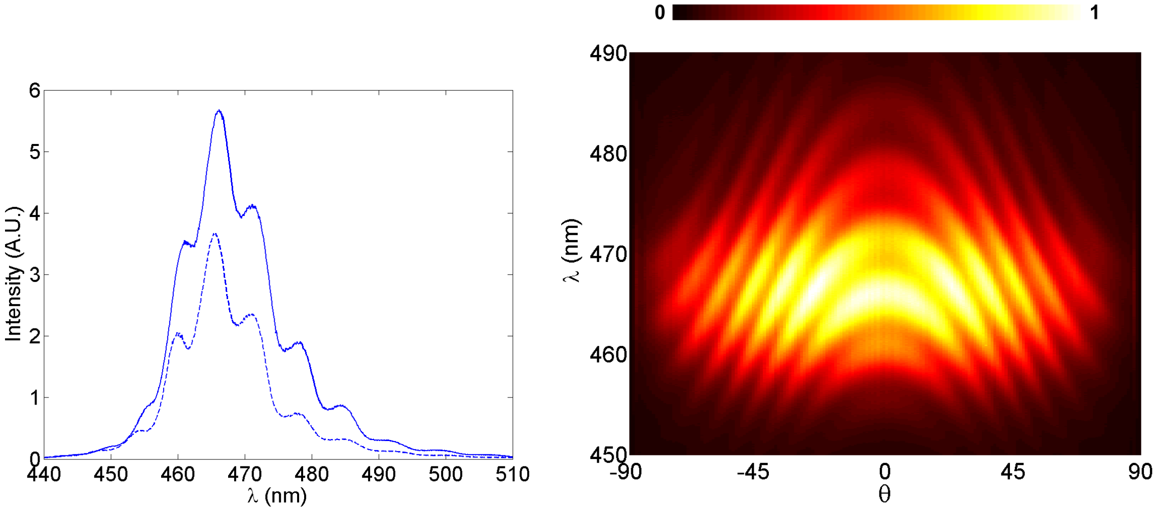

Figure 2.16: (Left) Angle-resolved spectra of a thick laser-lift-off LED, taken at $\theta = 0^o$ (full line) $\theta = -60^o$ (dashed line). (Right) 2D Angular spectrum of a flip-chipped and laser lift off LED with regular thickness (several μm). This plot is obtained by collecting spectra taken at various angles between $\theta = -90^o$ and 90^o.

The LED of Fig. 2.16 was not thinned down after the LLO process, and the GaN layer remains thick ($\sim 3\mu$m). Thus, it displays Fabry-Pérot interferences with an short fringe spacing ($\sim 5nm$). The resulting spectrum is quite similar to typical luminescence spectra of GaN-on-sapphire structures (although the contrast of the Fabry-Pérot fringes is modified because sapphire is replaced by a metal mirror).

Fig. 2.17 presents angular spectra obtained on thinned-down MCLEDs. All spectra come from the same sample, processed by Tetsuo Fujii. As can be seen, the number of Fabry-Perot fringes varies from LED to LED, evidencing non-uniform mechanical polishing of the sample.

To determine accurately the thickness of the LEDs, we need to deconvolve the intrinsic Fabry-Pérot effect from other factors such as the emission lineshape of the quantum wells. The spectral and angular dependence of the spectra is of the general form:

$$I(\lambda, \theta) = f(\lambda) g(\lambda, \theta) F(\theta) cos(\theta) \tag{2.24}$$

Here, $f(\lambda)$ is the emission lineshape of the quantum well (e.g. how much light is emitted at each wavelength); $g(\lambda, \theta)$ is the emission per unit solid angle of the Fabry-Perot cavity; $F(\theta)$ is the Fresnel reflection coefficient at angle θ; and the term $cos(\theta)$ is a solid angle correction.[8] Of course, $g(\lambda, \theta)$ and $F(\theta)$ are both part of the cavity's response and there is no formal reason for distinguishing them. However, it is convenient in practice to remove the Fresnel contribution and keep only $g(\lambda, \theta)$ which does not vanish at glancing angles.

---

[7] At least in a given azimuthal direction

[8] More precisely, the surface of collection of the angular setup is always orthogonal to the radial direction. On the other hand, the emission of a Fabry-Perot cavity is usually expressed as a flow across a horizontal cross-section, so that a $\cos\theta$ projection appears.

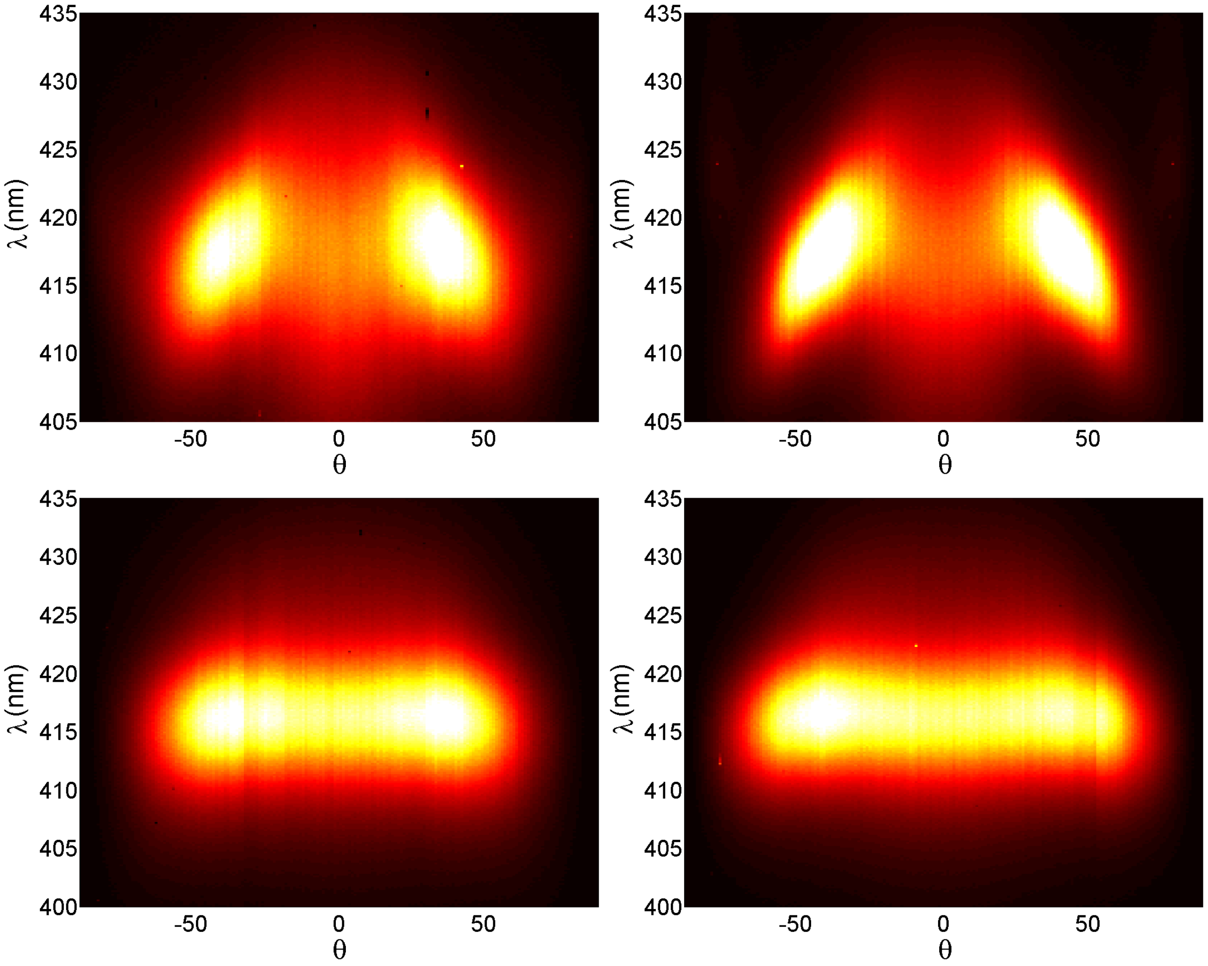

Figure 2.17: Angular spectra of thinned-down MCLEDs processed on the same wafer, both with nearly-optimal detuning (Left: collection in TE polarization, right: in TM polarization). (Top) Rather thick MCLED ($t \sim 900$ nm). The dispersion of the extracted Fabry-Pérot mode (curvature with varying angles) is still visible. (Bottom) Thinner MCLED ($t \sim 500$ nm): because the layer is very thin, the dispersion of the extracted mode is now barely visible over the spectral width of the LED.

The thickness of each LED can be determined from the *spectral* distance between two Fabry-Perot fringes. In order to do this, the angular spectra first need to be renormalized to remove the effect of the emission lineshape of the quantum wells $f(\lambda)$. This lineshape can be obtained by measuring the emission of a regular LED made from the same sample, using an objective with a large enough numerical aperture to average the Fabry-Perot fringes. An equivalent method consists in simply summing the angle-resolved spectrum over all angles, thus averaging the Fabry-Perot fringes. It may be argued that in the case of thin MCLEDs, this averaging is no longer efficient because there are too few modes in the air cone (ultimately, only one mode). However in practice, this method turns out to be suitable even for thin LEDs – even though the actual quantum well lineshape is not exactly recovered, the fringe spacing can usually be estimated with good accuracy.

Likewise, the cavity thickness can also be determined from the *angular* distance between two Fabry-Perot modes. Again, one first has to normalize the spectra by the factor $F(\theta)cos(\theta)$ in order to measure the true fringe spacing of the Fabry-Perot cavity. This justifies the collection of polarized spectra, because $F(\theta)$ depends on polarization.

In practice, one can thus normalize the initial spectra by the factor $f(\lambda)F(\theta)cos(\theta)$ to obtain $g(\lambda,\theta)$ and determine the thickness with both approaches. Clearly, for the thinnest MCLEDs, this normalization procedure is crucial in order to recover the Fabry-Perot fringes and estimate the fringe spacing.

For a given angle, if two maxima (or minima) of the Fabry-Perot fringes occur at wavelengths λ_1 and λ_2, those are linked to the cavity thickness L by:

$$L = \frac{1}{2\left(n/\lambda - n'/\lambda'\right)} \tag{2.25}$$

Here n and n' are the refractive indices of GaN at wavelengths λ and λ'. This simple formula comes from neglecting the penetration length of the modes in the bottom metallic mirror and in the top air mirror. This is a good approximation since both lengths are on the order of a few nm. On the other hand, inclusion of refractive index dispersion $n(\lambda)$ (taken from Ref. [12]) is essential for good accuracy, especially for thinner cavities, where the correction can be larger than 20%.

At a given wavelength, if two maxima occur at angles θ_1 and θ_2, the cavity thickness can be deduced from:

$$L = \frac{\lambda}{2n\left(cos\theta_1 - cos\theta_2\right)} \tag{2.26}$$

Usually, values obtained by both methods agree well (within 10-20 nm).

As an example, Fig. 2.18 displays the normalized spectra at normal incidence corresponding to the two LEDs of Fig. 2.17.

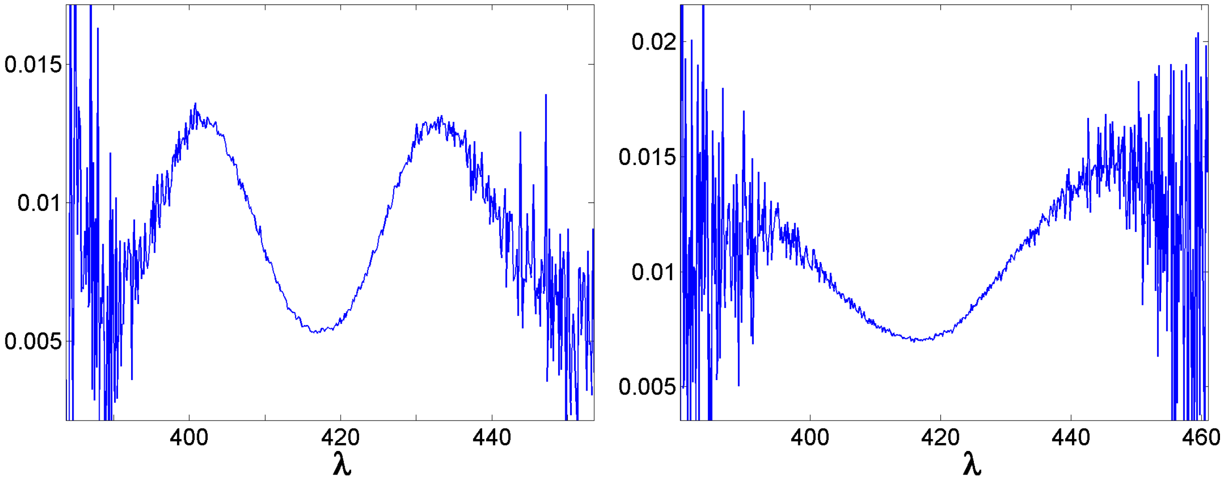

Figure 2.18: Determination of MCLED thickness on normalized spectra, for the two LEDs of Fig. 2.17 (left: thicker LED, right: thinner LED). The normalization restores the intrinsic fringe spacing of the cavity.

Application of Eq. 2.25 to these LEDs yields respective thicknesses : 900 nm and 500 nm. The position of the rabbit's ears for both LEDs indicate that they are well detuned, so that the extracted mode is fully inside the extraction cone. In principle, this should correspond to a large extraction efficiency.

Unfortunately, the epitaxial wafers used in these LEDs contained a multi-quantum well layer made of 5 InGaN quantum wells with 12-nm-thick GaN barriers between the quantum wells. Therefore, the active region spreads over 50 nm: if some quantum wells are optimally placed (at the antinode of the extracted mode), others are placed at the node of this same mode and degrade the efficiency of the device.

Optimally detuned MCLEDs

In order to prevent this effect, additional generations of MCLEDs were processed using a single quantum well grown by Rajat Sharma at UCSB. Interestingly, although it is generally considered that multi-quantum wells are necessary for efficient LEDs, very good luminescence performances were obtained on these wafers.

As previously, very thin LEDs (down to $\sim 350 - 400$ nm) with good detuning could be obtained. In principle, this should correspond to fairly large light extraction, although the uncertainty on the LEDs' thickness makes theoretical estimations uncertain.

Unfortunately, light extraction enhancement could not be quantified on these samples. This is mainly due to the fact that, in general, the electrical properties of thin MCLEDs are poor, with unstable contacts and sometimes high sheet resistivity. Therefore, no safe comparison with thick laser-lift-off LEDs could be obtained.

This difficulty was encountered over several generations of MCLEDs. Considering the complexity and the modest yield of the process, and the fact that only a few of the fabricated devices possess the proper thickness, the chances of evidencing optimal light extraction seem dim at this point. It leads us to conclude that a new, more robust fabrication process is desirable in order to obtain MCLEDs with well-controlled thickness and good electrical injection. A very selective dry etch, stopping at the required thickness with an accuracy $\sim 10nm$, may be an acceptable solution as regards thickness control.

High finesse MCLEDs

According to calculations, the optimal extraction efficiency of GaN MCLEDs is reached for a combination of a metallic mirror and a simple GaN/air (or epoxy/air) interface. However, these LEDs are also characterized by a poor finesse, because of the weak reflectivity of this interface. For some applications, it may be interesting to compromise somewhat the extraction efficiency to achieve a higher finesse – for instance if light has to be coupled at a more specific angle, as in the case of coupling to an optical fiber.

This can best be obtained by increasing the reflectivity of the top mirror. To this effect, some of the LEDs studied above were coated with a dielectric mirror composed of SiO_2 ($n \sim 1.5$) and Ta_2O_5 ($n \sim 1.95$). Since these dielectrics are insulating, the top p-contact had to be protected before deposition. The DBRs were characterized and deposited by Tetsuo Fujii. The optical indices of both dielectrics were estimated by ellipsometry and by fitting a reflectivity curve at normal incidence (Fig. 2.19).

The DBR-coated LEDs were again analyzed by angle-resolved measurements. The spectra, displayed on Fig. 2.21, reveal a peculiar emission. The spectra are very strongly TM-polarized (by a factor 30) and with maximal TM emission around 55^o.

The unusual TM-polarized emission of these LEDs is sketched on Fig. 2.21.

In order to understand this behavior, the angle-dependent reflectivity of the DBR was investigated (Fig. 2.22). It turns out that there is indeed a strong dip in TM reflectivity around 65^o (angle in air). This reflectivity dip is linked to the Brewster angles of SiO_2 and Ta_2O_5: all partial reflections are weak around the same angle, which yields an overall poor reflectivity. On the other hand, the TE reflectivity remains rather high at all times. Moreover, the experimental fact that barely any TE light escapes from the LED tends to indicate that there is some loss in the LED (possibly in the metal layer), so that the excessive TE reflectivity prevents light from escaping before being absorbed. This phenomenon depends quite critically on the accurate values of the optical indices: here, the indices obtained from ellipsometry lead to a high TE reflectivity at all angles which is compatible with the

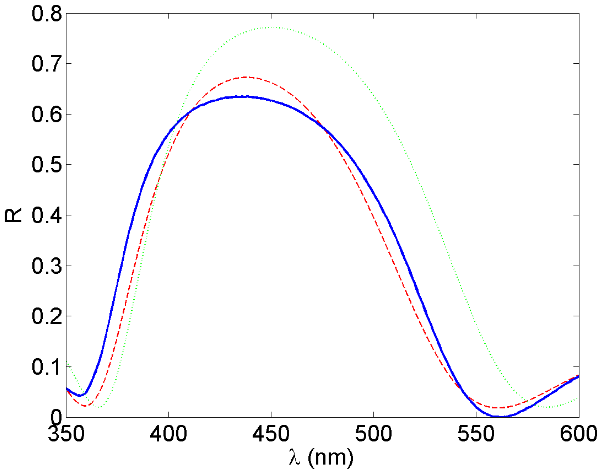

Figure 2.19: Reflectivity of a 4 pairs SiO_2/Ta_2O_5 DBR, with respective thicknesses 76 nm and 58 nm. (Full) Measured data. (Dotted) Theoretical calculation with indices $n_{SiO2} = 1.48$ and $n_{Ta2O5} = 1.95$ (values obtained by ellipsometry). (Dashed) Best theoretical fit obtained by varying n_{Ta2O5} (obtained for $n_{Ta2O5} = 1.85$).

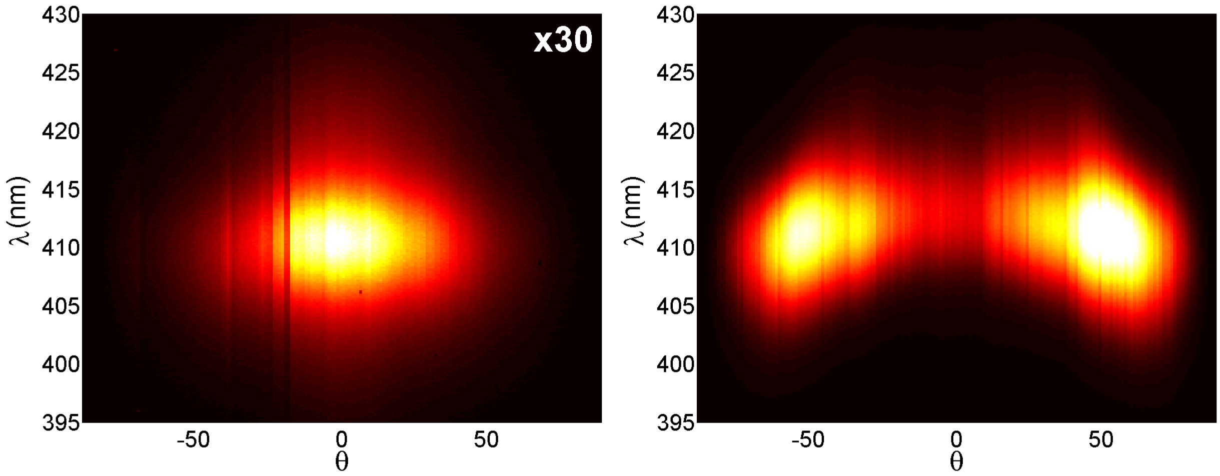

Figure 2.20: Angular spectra of MCLEDs with a 4 pairs SiO_2/Ta_2O_5 DBR. The scale of the TE spectrum is 30 times smaller than that of the TM spectrum. Note that TM emission is maximal around 55°.

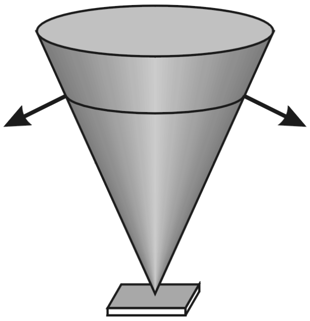

Figure 2.21: TM-polarized emission from a MCLED with a DBR.

experimental observation. On the other hand, the fitted index of Ta_2O_5 yields a lower TE reflectivity which can not account for the measurement.

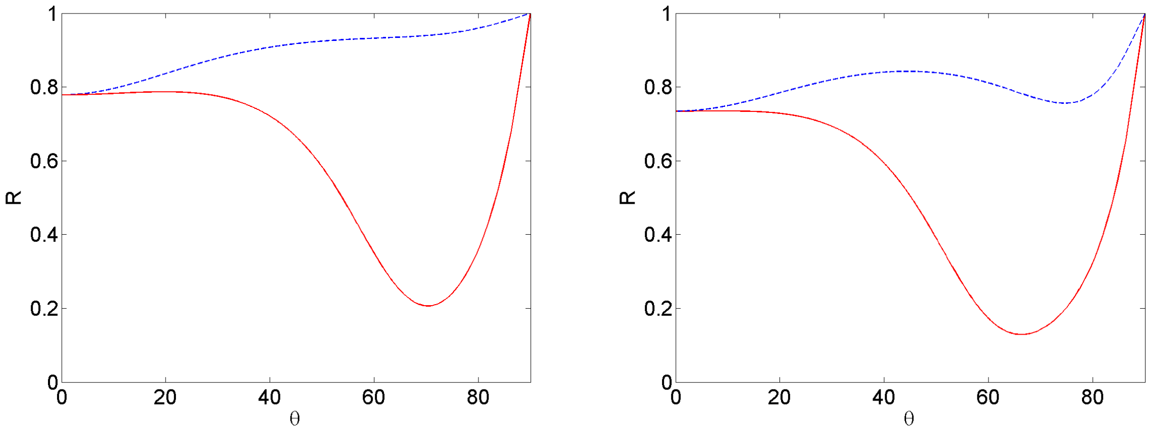

Figure 2.22: Calculated reflectivity spectra of the deposited DBR as a function of the angle in air (for light coming from the GaN side). Dashed line: TE, full line: TM. Left: optical indices taken from ellipsometry measurements. Right: indices best fitting a normal-incidence reflectivity measurement.

In summary, these LEDs suffer from an excessive DBR reflectivity which prevents TE light from escaping the LEDs and spoils their efficiency. Still, they possess uncommon polarization properties.

2.3 Conclusion

Microcavity LEDs are an efficient approach to enhance light extraction by redistributing the emission pattern of the LED. Their potential is well assessed in conventional III-V materials. However, implementation of MCLEDs in GaN proves challenging. The fabricated structures, obtained by bonding to a metallic submount and laser lift-off of the sapphire substrate, require complex processing. The microcavity effect was clearly observed with GaN cavities as thin as 500 nm, and the peculiar emission properties of hybrid metal/DBR MCLEDs were investigated. On the other hand, enhanced light extraction could not be quantified. The very demanding accuracy of the fabrication process – notably as concerns the GaN thickness – lead us to conclude that a more controlled process is necessary. Besides, guided modes are present even in the thinnest structures and limit their ultimate efficiencies.

Bibliography

[1] N. E. J. Hunt, E. F. Schubert, R. A. Logan, and G. J. Zydzik. Enhanced spectral power-density and reduced linewidth at 1.3-mu-m in an InGaAsP quantum-well resonant-cavity light-emitting diode. *Applied Physics Letters*, 61(19):2287–2289, 1992.

[2] D. Ochoa. *Diodes electroluminescentes planaires a haut rendement d'extraction lumineuse.* PhD thesis, EPFL, 2001.

[3] H. Benisty, H. De Neve, and C. Weisbuch. Impact of planar microcavity effects on light extraction - part I: Basic concepts and analytical trends. *IEEE Journal of Quantum Electronics*, 34(9):1612–1631, 1998.

[4] H. Benisty, H. De Neve, and C. Weisbuch. Impact of planar microcavity effects on light extraction - part II: Selected exact simulations and role of photon recycling. *IEEE Journal of Quantum Electronics*, 34(9):1632–1643, 1998.

[5] D. Ochoa, R. Houdre, R. P. Stanley, C. Dill, U. Oesterle, and M. Ilegems. Device simultaneous determination of the source and cavity parameters of a microcavity light-emitting diode. *Journal of Applied Physics*, 85(5):2994–2996, 1999.

[6] H. Benisty, R. Stanley, and M. Mayer. Method of source terms for dipole emission modification in modes of arbitrary planar structures. *Journal of the Optical Society of America a-Optics Image Science and Vision*, 15(5):1192–1201, 1998.

[7] I. Vurgaftman and J. R. Meyer. Band parameters for nitrogen-containing semiconductors. *Journal of Applied Physics*, 94(6):3675–3696, 2003.

[8] J. F. Carlin, J. Dorsaz, E. Feltin, R. Butte, N. Grandjean, M. Ilegems, and M. Laugt. Crack-free fully epitaxial nitride microcavity using highly reflective AllnN/GaN Bragg mirrors. *Applied Physics Letters*, 86(3), 2005. 031107.

[9] Z. Huang, C. C. Lin, and D. G. Deppe. Spontaneous lifetime and quantum efficiency in light-emitting-diodes affected by a close metal mirror. *IEEE Journal of Quantum Electronics*, 29(12):2940–2949, 1993.

[10] T. Fujii, A. David, C. Schwach, P. M. Pattison, R. Sharma, K. Fujito, T. Margalith, S. P. Denbaars, C. Weisbuch, and S. Nakamura. Micro cavity effect in GaN-based light-emitting diodes formed by laser lift-off and etch-back technique. *Japanese Journal of Applied Physics Part 2-Letters*, 43(3B):L411–L413, 2004.

[11] J. J. Wierer, D. A. Steigerwald, M. R. Krames, J. J. O'Shea, M. J. Ludowise, G. Christenson, Y. C. Shen, C. Lowery, P. S. Martin, S. Subramanya, W. Gotz, N. F. Gardner, R. S. Kern, and S. A. Stockman. High-power AlGaInN flip-chip light-emitting diodes. *Applied Physics Letters*, 78(22):3379–3381, 2001.

[12] H. Y. Zhang, X. H. He, Y. H. Shih, M. Schurman, Z. C. Feng, and R. A. Stall. Waveguide study and refractive indices of GaN:Mg epitaxial film. *Optics Letters*, 21(19):1529–1531, 1996.

Chapter 3

Photonic crystals and light extraction

The previous chapter evidenced the detrimental role of guided modes for light extraction: even in the most optimistic cases, more that 50% of the light is emitted in these. In this chapter, we introduce and explore the concept of light extraction of guided modes by photonic crystals (PhCs). After a qualitative justification of the phenomenon of light extraction by a periodic medium, we give more quantitative trends based on electromagnetic calculations. We then present the first photoluminescence experiments performed at UCSB, which give us insight on the specific features of light extraction in GaN structures.

3.1 Basics of light extraction by periodic structures

In this part, we present a qualitative justification of how periodic structures can extract guided light. Our discussion begins with a description of guided modes in a dielectric layer. Then, we discuss how introduction of a periodic index modulation modifies the structure of guided modes. Finally, we discuss how stronger modulations modify the overall dispersion of light and how they impact extraction.

3.1.1 Guided modes

The Fabry-Pérot model presented in the previous chapter allows us to understand the origin of fringes in the reflectivity (or emission) spectra of a thin-film layer: these arise from multiple reflexions at the interfaces of the dielectric layer, which interfere constructively or destructively depending on their angle and modulate the far-field intensity in the corresponding direction.

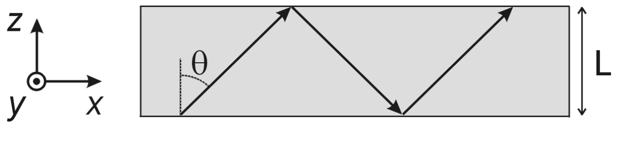

Figure 3.1: Bouncing ray inside a waveguide.

Let us now see what happens when we consider a plane wave (of wavelength λ) which propagates inside the dielectric layer (thickness L, index n), at an angle θ *larger* than the critical angle (Fig. 3.1). This wave can not propagate in air. It bounces at the dielectric/air interface, where it is reflected (total internal reflection). Hence, it interferes with itself, just as Fabry-Pérot modes do. However, in the case of a Fabry-Pérot mode, the successive bouncing rays have decreasing amplitude because part of the energy is transmitted outside of the dielectric each time it bounces. Here, in contrast, reflectivity reaches unity and all interfering rays have the same amplitude, leading to a singular summation:

$$E(\theta) = E_0 \sum_{p=1}^{\infty} e^{i2p\phi} \quad , \quad \phi = nk_0Lcos(\theta) \tag{3.1}$$

Where $k_0 = 2\pi/\lambda = \omega$.[1] In general, all terms of the series average out and it is equal to zero, except when $\phi = p\pi$, in which case the series diverges. In summary, we obtain a comb for phases:

$$E(\theta) \sim \sum_{p=1}^{\infty} \delta(\phi = p\pi) \tag{3.2}$$

Where the δ are Dirac functions. The angles corresponding to $\phi = p\pi$ are those where the field interferes constructively with itself and can thus propagate inside the dielectric layer, without attenuation. Such propagating light is called a *guided mode.*

Of course, the condition $\phi = p\pi$ is only approximate because, to establish it, we neglected the fact that light can penetrate (albeit with an exponential decay) in the air region surrounding the waveguide: the optical path given by Eq. 3.1 corresponds to a geometrical approximation where light bounces exactly at the interfaces – in other words, we neglected the so-called Goos-Hänchen effect.[1] In order to go further, we need to solve Maxwell's equations. Fortunately in the present case where the structure is invariant in the y and z directions, Maxwell's equations are greatly simplified. As the structure is invariant in the y direction, solutions to this equation can be classified in TE and TM modes. These stand for 'transverse electric' and 'transverse magnetic', and indicate that field E (respectively H) is in the transverse y direction:

$$\begin{array}{ll} \text{TE} \quad \rightarrow \quad \mathbf{E} = \left| \begin{array}{c} 0 \\ E_y \\ 0 \end{array} \right. , \mathbf{H} = \left| \begin{array}{c} H_x \\ 0 \\ H_z \end{array} \right. \\ \text{TM} \quad \rightarrow \quad \mathbf{E} = \left| \begin{array}{c} E_x \\ 0 \\ E_z \end{array} \right. , \mathbf{H} = \left| \begin{array}{c} 0 \\ H_y \\ 0 \end{array} \right. \end{array} \tag{3.3}$$

Maxwell's equations can then be reduced to the scalar Helmholtz equation, acting on the transverse field (E_y or H_y) only:

$$\begin{array}{ll} \text{TE:} & \left(\partial_x^2 + \partial_z^2 + \mu_0\epsilon\omega^2\right) E_y = 0 \\ \text{TM:} & \left(\partial_x^2 + \partial_z^2 + \mu_0\epsilon\omega^2\right) H_y = 0 \end{array} \tag{3.4}$$

With $\omega = 2\pi/\lambda$. The solutions are then of the form:

$$E_y = E_y(z).e^{i\left(k_{//}x - \omega t\right)} \quad , \quad H_y = H_y(z).e^{i\left(k_{//}x - \omega t\right)} \tag{3.5}$$

Where $k_{//}$ is called the *wavevector* of the guided mode. In general, the time dependence is dropped in all equations for convenience. It is worth noting that the TE Helmholtz equation is very similar to the Schrödinger equation for an electron in a 1D quantum well (this is not true for TM polarization because the boundary conditions differ). The equivalence is best seen in this form:

$$\left(-\Delta + \frac{2m}{\hbar^2}V\right)\psi = U\frac{2m}{\hbar^2}\psi \quad \leftrightarrow \quad \left(-\Delta + (1-\epsilon)\mu_0\omega^2\right)E = \mu_0\omega^2 E \tag{3.6}$$

---

[1] Here c=1.

Finding the guided modes amounts to solving the Helmholtz equation. The continuity conditions lead us to a transcendent relation between wavelength and wavevector, for instance in TE polarization:

$$k_{WG}\frac{L}{2}\tan\left(k_{WG}\frac{L}{2}\right) = k_{air}\frac{L}{2} \qquad \text{with:} \qquad \left\{\begin{array}{l} k_{WG} = \sqrt{k_0^2 n^2 - k_{//}^2} \\ k_{air} = \sqrt{k_0^2 - k_{//}^2} \end{array}\right. \tag{3.7}$$

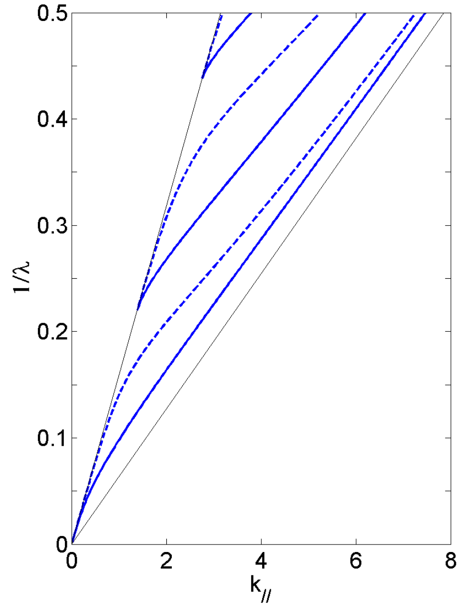

Figure 3.2: Band structure of a dielectric waveguide of index $n = 2.5$ (full: TE modes, dashed: TM modes); λ and $k_{//}$ are in arbitrary units and the thickness of the waveguide is 1 in the same units. The modes are between two lines of equations $\omega = k_{//}c$ ('air line') and $\omega = k_{//}c/2.5$ ('dielectric line'), evidencing that they must be propagative in the dielectric and evanescent in air.

This is a classic problem which can be solved graphically or numerically. As an example, we consider the following structure: a waveguide of thickness 1 (in arbitrary units) and index 2.5 surrounded by air. The relationship between λ and $k_{//}$, called the *dispersion relation* of the guided modes, is plotted for a few modes on Fig. 3.2.

It is now clear that the approximate solution we first derived, $\phi = p\pi$, corresponds to an infinitely confining waveguide ($n_{ext} = 0$, e.g. a quantum well with infinite barriers) where the solutions are simply $k_{//} = p\pi/L$. Indeed, in this case there is no evanescent penetration in the barriers, and the geometric approximation coincides with Maxwell's equations.

We can also introduce a useful variable, called the *effective index*, defined as:

$$n_{eff} = k_{//}/k_0 \tag{3.8}$$

The effective index is convenient because it is always bounded by the extreme values of refractive index of the problem: in our case, $1 < n_{eff} < 2.5$. In addition, n_{eff} gives information on the index 'felt' by a guided mode. For instance, a mode with $n_{eff} \sim 2.5$ is very well confined in the waveguide and only 'sees' the dielectric (its wavevector is nearly that of a plane wave in a medium of index 2.5), whereas a mode of index $n_{eff} \sim 1$ strongly leaks outside of the waveguide and feels the presence of air. This is illustrated on Fig. 3.3 which translates the relation dispersion in terms of effective index and shows the field distribution corresponding to the first guided modes.

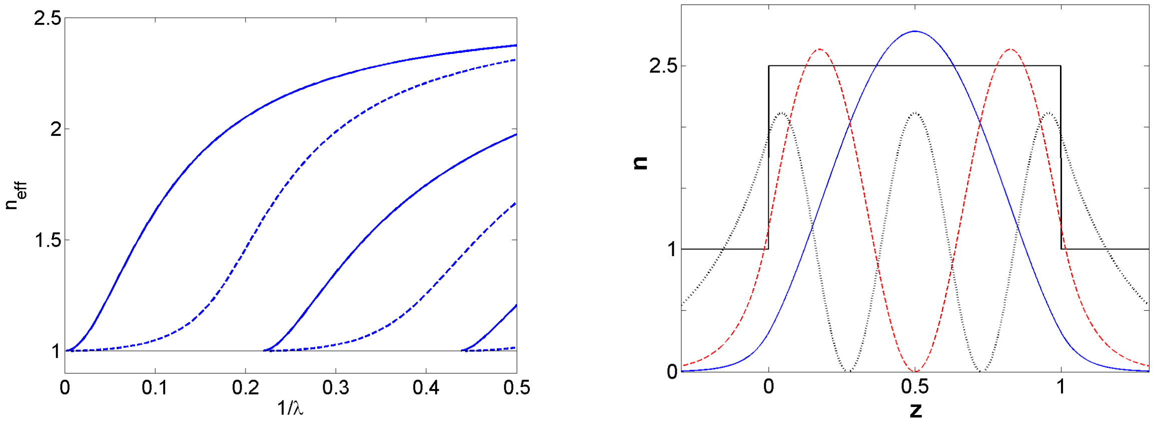

Figure 3.3: (Left) Effective index of guided modes for the same structure as in Fig. 3.2 (full: TE, dashed: TM). Close to cutoff, the effective index of a mode is close to 1 because it leaks strongly in air. With increasing frequency n_{eff} increases toward 2.5 as the modes are more and more confined in the waveguide. (Right) Profile of $|E|^2$ for the TE modes at $1/\lambda = 0.5$ (full: TE_1, dashed: TE_2, dotted: TE_3). As can be seen, modes of higher n_{eff} are more confined in the waveguide.

We have only discussed the simple case of one dielectric layer embedded in air. Generalization to multilayer structures is straightforward in principle. The Helmholtz equation is solved by stating that the solution in each layer is a sum of two counterpropagating waves (either propagative or decaying) and writing the field continuity conditions at the interfaces between layers. These continuity conditions come down to a transcendent relation between λ and $k_{//}$ (as in Eq. 3.7), whose solutions give the guided modes of the structure. In practice, when more than two layers are considered, the equation becomes untractable and has to be established and solved numerically. An elegant way to handle this is the Transfer Matrix formalism, where the continuity conditions are written in the form of 2x2 matrices. One then obtains a transfer matrix $\mathbb{T}$ which describes the whole multilayer system, and finding the modes amounts to finding the poles of $\mathbb{T}$, e.g. the values of $k_{//}$ and λ such that $det(\mathbb{T}) = 0$. A detailed presentation of this formalism can be found in Ref. [2], Chapter 5.

One may wonder about the physical significance of the appearance of delta functions in Eq. 3.2, or equivalently the fact that the solutions of the Helmholtz equation are *discrete*. These should be understood in the same way as the discrete energy levels of an isolated atom (or quantum well) in quantum mechanics. Notably, it is well known that any interaction which enables exchange of energy between an atom and another system, also confers a finite lifetime to the atom. In turn, the energy levels of the atom then lose their discreteness, which can be seen from Heisenberg's relation $\Delta E \Delta t \sim \hbar$.

The same phenomenology applies to guided modes. The easiest way to see this is to add an interaction between guided light and matter in the form of a small absorption in the dielectric material. This can be done by adding a small imaginary part to its refractive index: $n = n' + i.n''$. If the whole space is filled with dielectric, we still have $k_{//} = n.k_0$ and the solutions of Maxwell's equations are decaying plane waves:

$$E = E_0.exp\left(i\left(\frac{\omega n'}{c}x - \omega t\right) - \frac{\omega n''}{c}x\right) \tag{3.9}$$

Likewise, if the dielectric is a slab surrounded by air, the solutions of the dispersion relation have to be found in the complex plane, and $k_{//}$ acquires a small imaginary part: $k_{//} = k' + ik''$. The exponential decay length L_{decay} of the mode (in intensity) is related to k'' by:

$$I = |E|^2 \sim e^{-2k''x} \rightarrow L_{decay} = \frac{1}{2k''} \tag{3.10}$$

To see the impact of this on the guided mode's discreteness, we turn back to the geometric approach of Eq. 3.1. Because of absorption, the light rays lose a small part of their amplitude upon propagation, so that we now get:

$$E(\theta) = E_0 \sum_{p=1}^{\infty} \eta^{2p} e^{i2p\phi} = \frac{E_0}{1 - \eta^2 e^{2i\phi}} \tag{3.11}$$

Where the small amplitude loss per pass is $1 - \eta$. The resulting intensity of the rays, $I = |E_0|^2$, is depicted on Fig. 3.4: the Dirac functions of Eq. 3.2 is replaced by Lorentzians whose parameter is $\sin(\phi) = k_{//}$. Therefore, the discrete guided modes are broadened due to their interaction with matter.

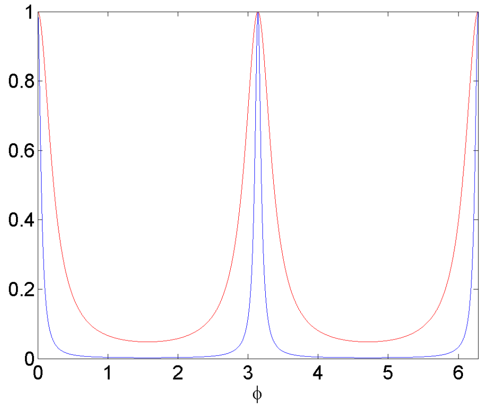

Figure 3.4: Normalized intensity of a ray bouncing in an absorbing waveguide as a function of ϕ, for two values of η.

While the above discussion uses the geometrical approach, the results still hold for the rigorous Maxwell equations. The dispersion relation has to be solved numerically to obtain the imaginary part of the wavevector. In practice, the transfer matrix formalism already evoked can still be used to treat the problem: again, finding the eigenmodes reduces to finding the poles of the transfer matrix $\mathbb{T}$, e.g. the values of $k_{//}$ for which $det(\mathbb{T}) = 0$ (for a fixed ω). However, the poles now have to be found in the complex plane. This can be done by an iterative method such as a gradient method. Fig. 3.5 shows how the solutions depart from the real axis when absorption is introduced.

Finally, let us note that while in this discussion we assumed a real value of ω and obtained an imaginary value of $k_{//}$, another valid choice consists in setting a real value for $k_{//}$ and finding a complex ω. In the first convention, k'' gives the exponential decay length of a mode upon propagation, while in the second convention ω'' gives the time decay of a mode excited uniformly in all space.[2]

---

[2] An even more general choice consist in taking a complex ω and finding the associated complex $k_{//}$: the solutions of the dispersion relation form a hypersurface of $\mathbb{C}^2$. These general solutions correspond, for instance, to the time and space decay of a lossy pulse. They give a rather limited physical insight in our case.

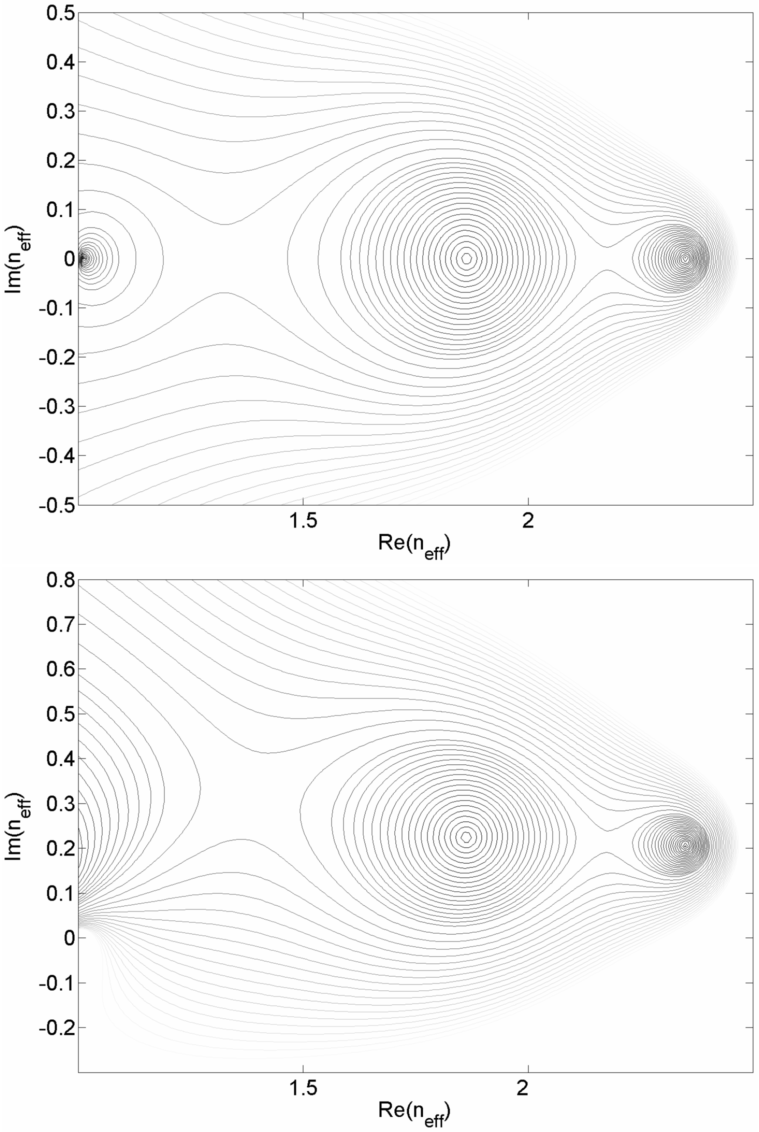

Figure 3.5: $|det(\mathbb{T})|$ as a function of the real and imaginary part of n_{eff}, for the same waveguide as previously. (Top) When the index of the waveguide is real ($n = 2.5$) the poles are on the real axis: guided modes have a real wavevector. Here, we recover the 3 TE modes already described. (Bottom) With absorption ($n = 2.5 + 0.2i$) the poles shift to complex values. In this case, the third mode is cutoff and a complex behavior emerges near the cutoff region.

3.1.2 Periodic corrugation of a waveguide

Bloch modes

Let us now introduce a periodic corrugation (period a) in the waveguide (Fig. 3.6) and look for its propagating modes. As a preliminary, let us decompose the dielectric constant in region (2) $\epsilon = n^2$ in Fourier series:

$$\epsilon = \sum_{p=-\infty}^{\infty} \epsilon_p e^{ipG_0 x} \quad , \quad G_0 = \frac{2\pi}{a} \tag{3.12}$$

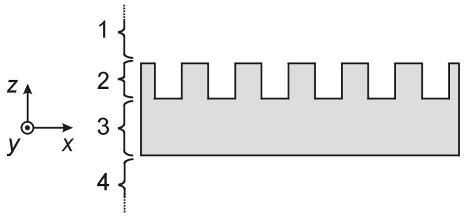

Figure 3.6: Waveguide with a periodic corrugation in region (2). We consider propagation along x, and grooves along y.

As was the case for simple waveguides, the solutions of Maxwell's equations can still be divided in two sets, TE and TM Bloch modes, with the same definition as previously: the electric field of a TE (magnetic field of a TM) mode is along the invariance direction y. Let us for instance look for a TE mode. To hint at the general solution of the Helmholtz equation, let us first try to proceed as for a 'bare' waveguide and look for a solution of the form:

$$E = E_0(z) e^{ik_{//} x} \tag{3.13}$$

Upon inserting such a solution in Maxwell's equation in region (2), we obtain:

$$k_{//}^2 E_0(z) = k_0 \sum_p \epsilon_p e^{ipG_0 x} E_0(z) \tag{3.14}$$

Therefore, a field with a simple $exp(ik_{//}x)$ dependence in the x direction cannot be solution of Maxwell's equations: injecting this form generates an infinity of exponential terms associated with the Fourier harmonics of ϵ. Obviously, the solution has to be of a more general form in all space:

$$E = \sum_p E_p(z) e^{ipG_0 x} e^{ik_{//} x} \tag{3.15}$$

By introducing this form in the Helmholtz equation, it can be checked that this is indeed a suitable solution, provided the coefficients E_p obey a series of linear relations whose coefficients depend on ϵ:

$$(k_{//} + pG_0)^2 E_p = k_0^2 \sum_{p'=-\infty}^{\infty} \epsilon_{p-p'} E_{p'} \tag{3.16}$$

Eq. 3.15 is an expression of the Bloch theorem, well-known in solid-state physics, and also called the Floquet or Floquet-Bloch theorem. Such solutions are called *Bloch modes*. In each region of Fig. 3.6, the field is a solution of Eq. 3.16, and Maxwell's equations are fully solved by satisfying the continuity conditions of the field at the boundaries between different regions, which link $E_p(z^+)$ to $E_p(z^-)$. As for simple waveguides, solving this equation leads to a relationship between k_0 and ω − the dispersion relation of the structure.

In the above, it is apparent that the periodicity of ϵ *mixes* different harmonics in the corrugated region. In regions where n is homogeneous (i.e. outside of the corrugated region), the Fourier transform of the dielectric constant is diagonal and all harmonics are independent. It can then be checked that the z-dependence of each harmonic p is the same as for a plane wave of horizontal wavevector $k_{//}+pG_0$:

$$E_p(z) = A_p e^{ik_z^p z} + B_p e^{-ik_z^p z} \quad , \quad k_z^p = \sqrt{n^2 k_0^2 - (k_{//} + pG_0)^2} \tag{3.17}$$

It is worth noting that, in the expression of a Bloch mode, there is an ambiguity in the definition of $k_{//}$: it is only defined modulo $2\pi/a$. While it is still convenient to refer to the wavevector of a Bloch mode, one should bear in mind that this quantity is ill-defined. Although this fact may seem trivial, it is often disregarded, which sometimes leads to controversial interpretations (see the discussion below).

If the effect of the corrugation is weak, most coefficients of the Bloch mode are small, and a convenient convention is to assign $k_{//}$ to the fundamental harmonic which carries most of the mode's power. This convention has the advantage of offering continuity with the case of a guided mode in the absence of corrugation: a guided mode is simply a Bloch mode with a single non-zero harmonic. Moreover, in this case, the Bloch mode can be understood in a kinematic view: upon its propagation, the fundamental is scattered by each corrugation of the periodic region; because of the periodicity the scattered field is concentrated in diffraction orders corresponding to the other harmonics of the Bloch wave.

On the other hand, when the effect of the corrugation is not weak, several harmonics carry a significant fraction of energy and the Bloch mode can only be considered as a whole. In this case, there is no canonic choice for $k_{//}$. From Eq. 3.16, it is seen that the coupling between different harmonics of a Bloch mode are caused by the Fourier coefficients $\epsilon(pG_0)$ of the dielectric constant. Therefore, this quantity is often called the *photonic strength* of the periodic structure. In a structure with high photonic strength, mixing of harmonics is significant. In general, a high photonic strength is caused by a high contrast in refractive index in the periodic corrugation and a high filling factor (defined in our case as the volume fraction of air holes in the corrugation).

Band gaps

Let us now come to the peculiar situation where $k_{//} = G_0/2$. In this case, the wavevector corresponding to harmonic $p = -1$ is $-k_{//}$, and harmonics (0) and (−1) have a symmetrical role in the Helmholtz equation: if we neglect all other harmonics, the Bloch mode is made of two counter-propagating harmonics with equal amplitude. This classic approximation, called the Coupled wave theory, is justified if the photonic strength is small and all other harmonics are negligible. In this case, it can easily be shown analytically that $k_{//}$ acquires an imaginary component (even in the absence of absorption).[3, 4] Moreover, from our symmetry argument it is clear that the flow of the Poynting vector in the x direction is zero. The interpretation of this phenomenon is that, due to coherent scattering from the (0) to the (−1) harmonic, all incoming light is reflected back. The frequency band where reflection occurs and the generated Bloch mode carries no energy is called a *stop band* or a *band gap*, in analogy with the energy gaps of electronic bands in crystals. This phenomenon explains the reflective effect of DBRs and the feedback phenomenon in DFBs.

More generally, harmonics (p) and ($-p-1$) have symmetrical roles in Maxwell's equations.[3] Therefore, the existence of band gaps is general and not linked to a truncation of harmonics of the Bloch

---

[3] At least in the absence of absorption in the medium.

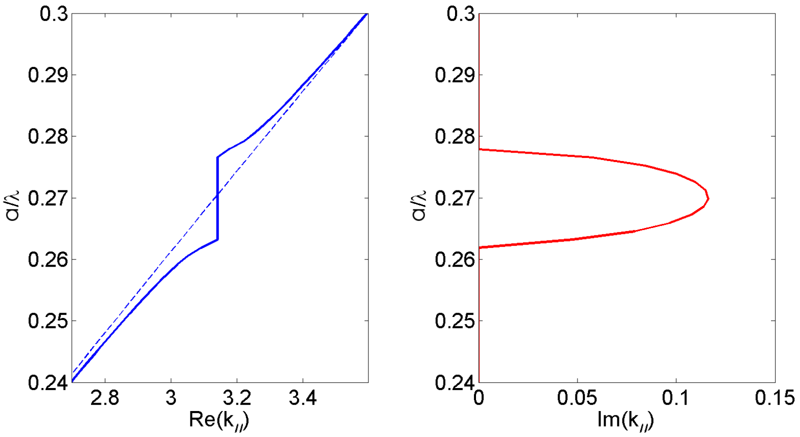

Figure 3.7: (Left) Full line: Dispersion relation of a Bloch mode around a band gap: the gap opens when $k_{//} = \pi/a$. Dashed line: dispersion of a guided mode in a structure with the same average index: there is no gap opening. (Right) Imaginary part of $k_{//}$. Inside the gap, the Bloch mode is evanescent and light is reflected back.

mode. An example of such a stop band is shown on Fig. 3.7. The result is obtained by solving numerically Maxwell's equations, taking a finite number of harmonics into account, by one of the methods described in Chapter 6. The structure considered in this case is a waveguide of index 2.5 and total thickness $0.6a$, surrounded by air and perforated to a depth $0.2a$ by an air grating of period a, with square teeth of filling factor 0.3.

The next case of interest happens when $k_{//} = G_0$. From the same arguments, another band gap then appears due to interaction between harmonics (0) and (−2). More generally, a gap opens whenever $k_{//} = p.G_0/2$.

Leaky modes

As was already stated, outside of the grating, the z-dependence of each harmonic (p) of the Bloch mode is that of a plane wave of horizontal wavevector $k_{//} + pG_0$. Notably, in the substrate of index n_{subs} the vertical wavevector of each harmonic is:

$$k^p_{z,subs} = \sqrt{n^2_{subs} k_0^2 - (k_{//} + pG_0)^2} \tag{3.18}$$

A similar relation holds in the superstrate, with the modification $n_{subs} \rightarrow n_{sup}$. As long as k_z^p is imaginary for all p, all harmonics are evanescent and no power can be radiated in the vertical direction. The Bloch mode is truly guided, in the sense that it propagates in the x direction without losing energy to the substrate and superstrate. However, if k_z becomes real for one harmonic, power is radiated to the substrate or superstrate by that harmonic. Therefore, the Bloch mode loses energy upon propagation and can no longer be seen as strictly guided. Accordingly, its wavevector acquires an imaginary part, which describes the energy loss rate. Such a mode is called a *leaky mode*. The condition for harmonic (p) to diffract to the substrate is:

$$k^p_{z,subs} \in \mathbb{R} \rightarrow n_{subs} k_0 > k_{//} + pG_0 \tag{3.19}$$

In other words, the in-plane wavevector of the harmonic should be smaller than the total wavevector in the substrate (a similar relation holds for the superstrate). This is best seen graphically on the so-called Ewald construction, by representing the in-plane wavevector of each harmonic by a point and seeing which points fall within a circle of radius $n_{subs}k_0$ (Fig. 3.8).

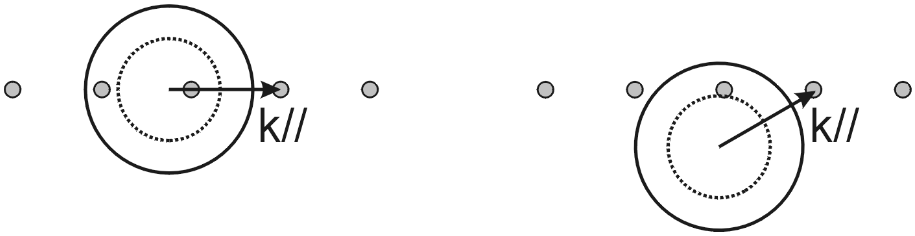

Figure 3.8: Ewald constructions for a one-dimensional grating. The arrow represents the in-plane wavevector $k_{//}$, the points are the reciprocal lattice points (giving the in-plane wavevectors of the Bloch mode's harmonics), and the full and dashed circles have radiuses $n_{subs}k_0$ and $n_{sup}k_0$. (Left) Normal incidence: $k_{//}$ is orthogonal to the grating. Here, two points fall in the substrate circle, causing diffraction to the substrate, and one point in the superstrate circle, causing diffraction to the superstrate. (Right) Same as previously, but with $k_{//}$ in a different direction. Only one point falls in the substrate circle.

Let us exemplify this phenomenon on the same structure as previously. The dispersion relation of the Bloch mode is now plotted for a wider range of frequencies on Fig. 3.9. For a more convenient representation, the band structure is folded back in the region $0 < k_{//} < G_0$, or *first Brillouin zone* (FBZ). This representation is inspired by the electronic band structure of solids. It takes advantage of the fact that, whenever a harmonic $k_{//} + pG_0$ leaves the FBZ, another harmonic enters it, so that the dispersion can always be brought back to the FBZ 'modulo G_0'.

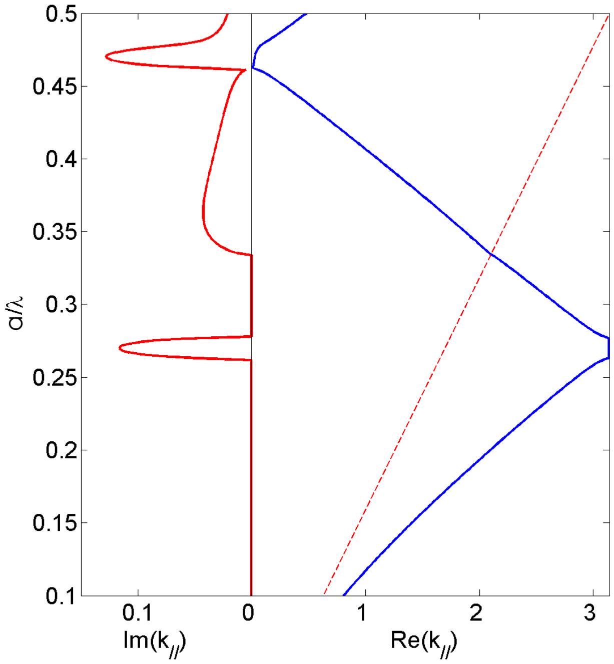

Figure 3.9: (Right side) Dispersion relation of the Bloch mode for the same structure as previously, on a wider range. When the dispersion crosses the air line (dotted line), the diffraction condition is fulfilled and the mode becomes leaky. Gaps open when the dispersion reaches either edge of the first Brillouin zone. All these phenomena are manifested by the evolution of k'', the imaginary part of $k_{//}$ (Left side). Notice the difference in horizontal scale between both plots.

In addition, the line corresponding to $\omega = k_{//}c$ is plotted on the band structure. This line simply represents the diffraction condition of Eq. 3.19, and is called the *air line*, *air cone* or *air lightline*. When the relation dispersion of the Bloch mode crosses this line, the diffraction condition is fulfilled and the Bloch mode becomes leaky. As can be seen on Fig. 3.8, this corresponds to harmonic $p = -1$ becoming radiative to air. Accordingly, $k_{//}$ acquires an imaginary part $k'' = Im(k_{//})$. Whereas in the first bandgap this was associated to reflection of energy, this imaginary part represents loss to air.

Finally, when the frequency of the Bloch mode increases further, it reaches another Brillouin zone boundary (corresponding to $k_{//} = G_0$) and another gap opens, as already predicted. However, several features differ from the first band gap. First, the second band gap is not vertical, e.g. the dispersion relation does not stick to the axis $k_{//} = 0$. This is simply due to the fact that the field symmetry between x and $-x$ which guaranteed the verticality of the first gap, no longer holds in the presence of diffraction losses. Moreover, whereas the imaginary part of $k_{//}$ in the first gap could unambiguously be attributed to a phenomenon of reflection, this is no longer true in the second gap because reflection (due to the $p = -2$ harmonic) has to compete with diffraction to air (due to $p = -1$).

In order to distinguish the contribution of both phenomena, we have to compute the energy flows (flows of the Poynting vector) of the Bloch mode in various directions. This can be done easily because crossed terms corresponding to two different harmonics interfere destructively, so that the balance of power of the Bloch mode can be performed separately for each harmonic. The details of the derivation are given in Annex A. We can thus compute the diffraction and reflection rates of the Bloch mode. We define $\mathcal{P}_{in}$, $\mathcal{P}_{ref}$, $\mathcal{P}_{up}$ and $\mathcal{P}_{down}$ as the total power flow forward, backward, upward and downward respectively (per unit length). We then have:

$$\begin{aligned} R &= \mathcal{P}_{ref}/\mathcal{P}_{in} \\ U &= \mathcal{P}_{up}/\mathcal{P}_{in} \\ D &= \mathcal{P}_{down}/\mathcal{P}_{in} \end{aligned} \tag{3.20}$$

Where R is the reflection coefficient of the Bloch mode, and U (respectively D) is the fraction of the Bloch mode's power radiated upwards (downwards). Due to energy conservation, we have $R + U + D = 1$.[4] Fig. 3.10 presents the respective contribution of R, U and D to the Bloch mode's loss.

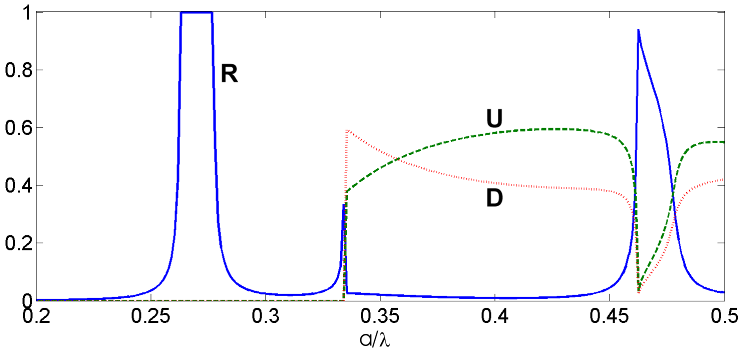

Figure 3.10: Balance of power for the Bloch mode of Fig. 3.8. For $a/\lambda > 0.25$, the reflection coefficient increases and reaches 1 in the band gap. For $a/\lambda \sim 0.33$, the Bloch mode crosses the light line and becomes leaky. U and D are different because the structure is not symmetric vertically. The second band gap is reached for $a/\lambda \sim 0.46$: R increases sharply, but part of the mode's power is still lost by diffraction. Notice the large asymmetry of the second band gap.

---

[4] For a leaky mode, there is no energy transmitted at $x \to \infty$

As can be seen, diffractive loss still plays a non-negligible role in the second band gap. This result depends on the structure and should not be considered general. It is also interesting to note the non-symmetric shape of the second stop band: the reflective effect is much more efficient at the beginning of the band and then degrades as radiation losses become stronger. This is actually a well known property of band gaps: in the presence of losses (be they diffractive or due to absorption) reflexion is highest at the low-frequency edge of the stop band.[5]

For the sake of completeness, we also represent on Fig. 3.11 the profile of the electric field E_y in the structure for $a/\lambda = 0.4$. The main harmonic $p = 0$ looks like a guided mode. Harmonic $p = -1$ is propagative in air where it diffracts the Bloch mode's energy. All other harmonics have small amplitude, as can be seen on the next largest harmonic is $p = -2$. It is also interesting to note that this harmonic is largest in the grating region, where it is 'generated' by scattering of the fundamental harmonic; outside of the grating it is strongly evanescent and decays rapidly.

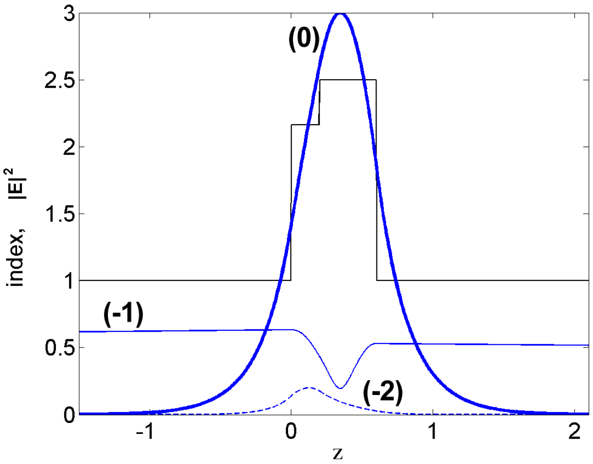

Figure 3.11: Amplitude (along the z direction) of a few harmonics of the Bloch mode for $a/\lambda = 0.44$. Thick line: main harmonic $p = 0$. Thin line: radiative harmonic $p = -1$. Dashed line: $p = -2$. The average index profile of the structure ($n(z) =< n(x, z) >$) is superimposed. Note that harmonic (-1) slowly decays away from the structure, as discussed in Annex A.

Finally, it is important to note that, while the *existence* of a leaky mode can be obtained simply from a graphic construction (Ewald construction, or intersection of the band structure with the air line), this gives us no information about the *strength* of the diffraction phenomenon. This can only be obtained by solving Maxwell's equations and determining all the properties of the Bloch mode.

2-dimensional photonic crystals

We now consider a structure which includes a corrugation periodic in two dimensions , usually called a photonic crystal (PhC), and generalize the above results. We first discuss the textbook problem of a strictly 2-dimensional crystal with no third dimension, before embedding this crystal in a 3D structure.

Strictly 2-dimensional structure To any 2-dimensional periodic crystal (rectangular, square, triangular, hexagonal) corresponds a *reciprocal lattice* (RL). We denote as $\{\mathbf{G}_1, \mathbf{G}_2\}$ the basis of the RL:

$$\mathbf{G} \in RL = u\mathbf{G}_1 + v\mathbf{G}_2 \tag{3.21}$$

For a square or triangular lattice, we call a the period of the crystal. This definition calls for a few comments. In the case of a square lattice, it is unambiguous. However, in the case of a triangular lattice, one can define it as the distance between holes, but it is also possible to see a triangular lattice as generated by three 1D gratings tilted by 60^o, in which case a can be taken as the period of the gratings (Fig. 3.12). In this thesis, following a general convention, the first choice is made, but it should be noted that this modifies the length of the reciprocal space basis vectors from $G_0 = 2\pi/a$ to $G_0 = 4\pi/a\sqrt{3}$, and makes comparison with square lattices less straightforward. In addition, we adopt the convention of expressing all lengths in units of a.

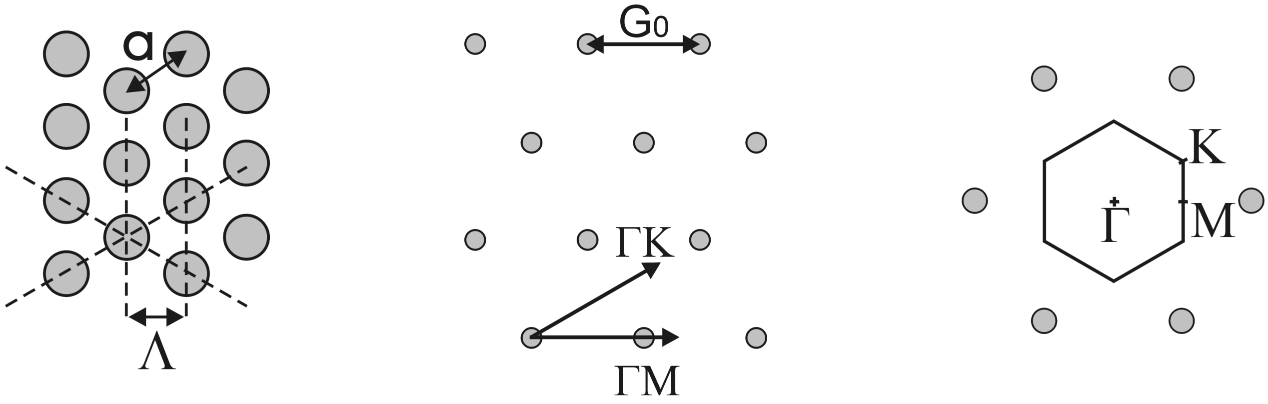

Figure 3.12: (Left) Possible choices for the lattice constant of a triangular lattice: conventionally, the distance between holes a is chosen, but the distance between hole columns Λ could also be considered. (Middle) Reciprocal lattice of a triangular lattice. The high symmetry directions and length of the basic RL vector are indicated. (Right) Detail of the first Brillouin zone of a triangular lattice, with high symmetry points Γ, K and M.

We also introduce the *filling factor* f of the PhC as the fraction of the PhC surface occupied by holes. For circular holes in a square and triangular lattice respectively, the filling factor is related to the holes radius R by:

$$\text{Square}: \; f = \frac{\pi R^2}{a^2} \qquad \text{Triangular}: \; f = \frac{2\pi R^2}{\sqrt{3}a^2} \tag{3.22}$$

The first Brillouin zone (FBZ) is defined as the points of the reciprocal space closest to the origin. The FBZ is convenient because, as in the 1D case, all band structures can be folded back inside of it modulo translations by $\mathbf{G}_1$ and $\mathbf{G}_2$. Therefore, in general, band structures are plotted in the FBZ. Usually, as for semi-conductors, only the high-symmetry directions ΓM and ΓK are investigated, and the band structures are expected to behave smoothly between these directions.

Due to the 2D nature of the problem, the solutions of Maxwell's equations (Bloch modes) can be classified in two families, as was the case above for waveguides (and waveguides with a 1D corrugation): TE (also called H) and TM (or E) modes.

$$\begin{array}{lcl} \text{TE (H)} & \rightarrow & \mathbf{E} = \left| \begin{array}{l} E_x \\ E_y \\ 0 \end{array} \right. , \mathbf{H} = \left| \begin{array}{c} 0 \\ 0 \\ H_z \end{array} \right. \\ \text{TM (E)} & \rightarrow & \mathbf{E} = \left| \begin{array}{l} 0 \\ 0 \\ E_z \end{array} \right. , \mathbf{H} = \left| \begin{array}{c} H_x \\ H_y \\ 0 \end{array} \right. \end{array} \tag{3.23}$$

Here the transverse direction is z, so that a 'transverse electric' mode has an electric field along z (against y for a waveguide). As will be seen later, both conventions collide in the case of a 3D structure. The Bloch modes of a 2D PhC are of the form:

$$\begin{aligned} \text{TE (H)} \quad &\rightarrow \quad H_z(\mathbf{r}) = \sum_{\mathbf{G}\in RL} H_{z,\mathbf{G}} exp\left(i\left(\mathbf{k}_{//}+\mathbf{G}\right)\cdot\mathbf{r}\right) \\ \text{TM (E)} \quad &\rightarrow \quad E_z(\mathbf{r}) = \sum_{\mathbf{G}\in RL} E_{z,\mathbf{G}} exp\left(i\left(\mathbf{k}_{//}+\mathbf{G}\right)\cdot\mathbf{r}\right) \end{aligned} \tag{3.24}$$

Typical examples of the band structures of 2D PhCs are given in Fig. 3.13.

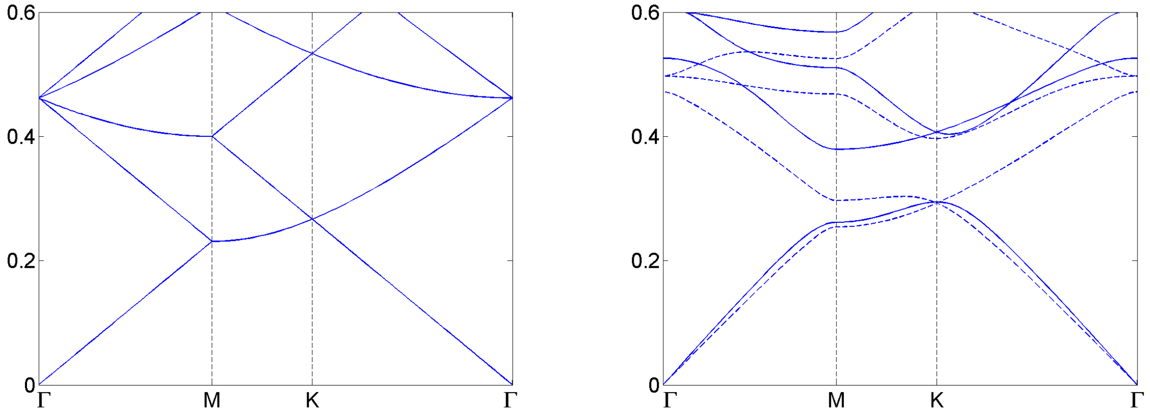

Figure 3.13: Band structures of triangular lattice PhCs made of circular air holes in a GaN ($n = 2.5$) matrix. (Left) $f = 0$, e.g. no holes. The dispersion is that of free photons ($\omega = k.c/2.5$), folded in the FBZ. Note that the folding in 2D introduces curved and locally flat bands. (Right) $f = 0.4$, the degeneracy between H (full line) and E (dashed line) modes is lifted. An omnidirectional gap opens in H polarization.

Let us quickly comment on these. When $f = 0$, there is no photonic crystal and we should recover the dispersion of plane waves in the matrix material. However, as can be seen, multiple photonic bands actually appear. These are produced by folding of the free photon dispersion in the FBZ. Their physical meaning seems unclear since the folding is completely artificial in the absence of a periodic structure. The key to this apparent paradox has already been pointed out: $k_{//}$ is ill-defined for a Bloch mode. Therefore, the photonic bands whose dispersion differs from a free photon simply correspond to Bloch modes where $k//$ has been assigned to a harmonic with zero amplitude, while the only non-zero harmonic (the actual guided mode) corresponds to some other wavevector $\mathbf{k}_{//} + \mathbf{G}$. For more clarity, one of these Bloch modes is represented in Fig. 3.14. Clearly, when $k_{//}$ scans the ΓM direction, the wavevector of the actual guided mode has a complex locus (with varying angle with respect to ΓM), which produces the curved dispersion in the band structure.

When the filling factor increases ($f = 0.4$) photonic effects appear and band gaps open in some directions. In our case, there is an omnidirectional band gap (a frequency region without photonic band) in H polarization but not in E polarization. This classic result can be justified qualitatively by arguing that, because it is discontinuous at dielectric boundaries, the in-plane electric field strongly 'feels' them (and hence the effect of the PhC). The 'artificial' photonic bands of the $f = 0$ case now make sense because they are assigned to an harmonic with non-zero magnitude. However, as can be easily guessed by continuity with the $f = 0$ situation, a large part of the power is still concentrated in the former guided harmonic. It is interesting to note that sometimes, surprising effects (negative refraction, flat dispersion...) of PhCs are only described by considering the band structure in the FBZ.

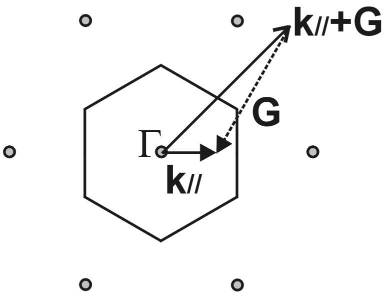

Figure 3.14: Artificial folding of a guided mode as a Bloch mode. The actual wavevector of the guided mode $\mathbf{k}_{//}+\mathbf{G}$ (which does not propagate in a special symmetry direction), is folded by a reciprocal lattice vector $\mathbf{G}$ to obtain the Bloch mode's wavevector $\mathbf{k}_{//}$ in the ΓM direction.

From our argument, it appears that seemingly interesting features of the band structure may actually correspond to a harmonic which carries very little power, and hence correspond to limited physical effects. Sometimes, a full discussion of a PhC's properties requires a detailed study of the Bloch mode's structure.

2D PhC in a 3D structures The structures we wish to study are 3D structures incorporating a 2D photonic crystal (such as a waveguide partly etched by a PhC, as in Fig. 3.15). In this case, most notations still hold. The structure can be considered as strictly periodic in the x, y directions although the index is only periodic in the PhC region, and constant otherwise. Therefore, the reciprocal lattice can be defined as before.

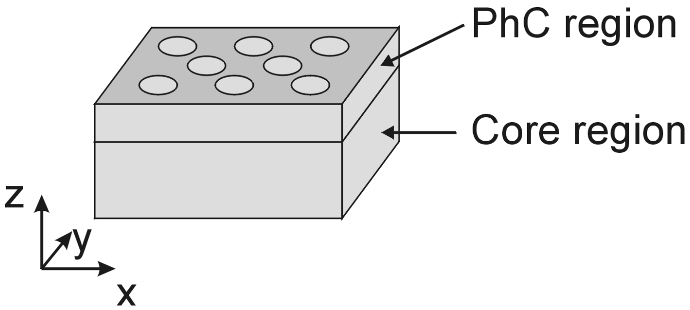

Figure 3.15: Typical structure made of a waveguide partially etched by a 2-dimensional photonic crystal. The core region corresponds to the unetched part of the waveguide.

Since the periodic structure is embedded between homogeneous media (in the z direction), leaky modes can once again be defined when one Bloch mode harmonic falls in the air or substrate cone. As before, leaky modes can be characterized with an Ewald construction (Fig. 3.16), where the reciprocal lattice is now 2-dimensional. As can be seen, 2D PhCs offer more directions for light diffraction than 1D gratings.

As there is no invariance direction, the classification of Bloch modes in two families is no longer valid. The Bloch theorem takes the following form for a 2D PhC in a 3D structure:

$$\mathbf{E}(z,\mathbf{r}) = \sum_{\mathbf{G}\in RL} \mathbf{E}_{\mathbf{G}}(z) exp\left(i\left(\mathbf{k}_{//}+\mathbf{G}\right)\cdot\mathbf{r}\right) \tag{3.25}$$

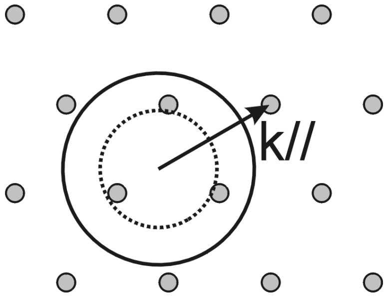

Figure 3.16: Ewald construction for a triangular lattice PhC, with a wavevector along ΓK. The dashed and full circles represent the diffraction conditions to air and the substrate, respectively. Here, one harmonic diffracts to air and three to the substrate (as compared to Fig. 3.8 where only one harmonic diffracts to the substrate).

The coefficients $\mathbf{E_G}$ of the harmonics are now vectors with x, y and z components.[5] Although TE and TM polarizations no longer hold, it is tempting to assign an approximate polarization, at least in the case of weak photonic strength (shallow PhC for instance), where the former definitions should still nearly be valid. Unfortunately, the conventions of the 'waveguide approach' and '2D PhC' approach are not compatible: a field with a strong guided-like E_x component would be seen as TM from a waveguide point of view, and TE from a PhC point of view.

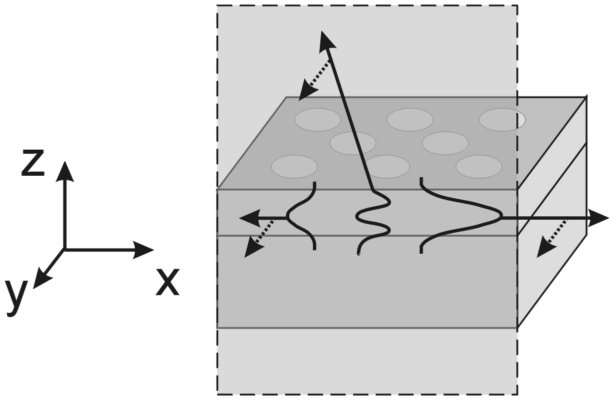

Figure 3.17: Sketch of a pseudo-TE Bloch mode in a 3D structure. All harmonics whose wavevectors are in the high-symmetry xz plane (e.g. those whose $\mathbf{k}_{//} + \mathbf{G}$ is along x) are polarized along y. Therefore, if one of these is leaky and is collected along the xz plane, the spectrum is polarized. On the other hand, harmonics with $G_y \neq 0$ (not represented) have no special polarization. Conversely, for pseudo-TM modes the polarized harmonics are TM.

An interesting symmetry property still holds: along the directions of high symmetry of the PhC (ΓM, ΓK), the harmonics collinear to $k_{//}$ (e.g. those for which the y component of $\mathbf{G}$ is zero) are either TE or TM, in the waveguide sense. Although this property is limited, it turns out to be useful from an experimental point of view when we collect from outside the field diffracted by a leaky harmonic, as we will soon do. In this case, if the PhC is aligned along a symmetry direction, the diffracted

---

[5] However, due to the transversality condition of Maxwell's equations, $\mathbf{E_G}$ is always orthogonal to $\mathbf{k}_{//} + \mathbf{G}$: all harmonics correspond to transverse fields.

harmonic is either TE or TM polarized depending on the Bloch mode (Fig. 3.17). This enables us to experimentally divide the modes in two families by using a simple polarizer. In the following of the thesis, the Bloch modes are referred to as pseudo-TE or pseudo-TM.

3.1.3 Conclusion

Periodic structures sustain Bloch modes, which are a generalization of the guided modes of a planar waveguide. Some of these can be leaky modes, which radiate power to air upon their propagation. Our strategy is to use these leaky modes in order to extract guided light of an LED. The existence of a leaky mode can simply be determined graphically from the band structure of the system, but information about the *efficiency* of light extraction requires a full calculation.

3.2 A few theoretical trends

We have seen how photonic crystals could sustain leaky modes and hence extract guided light. To gain more insight on the efficiency of this phenomenon, we now present a few theoretical results which quantify the extraction efficiency. We do not wish to discuss the effect of all parameters here, but only to give a few orders of magnitude. Therefore, some parameters are kept constant: we always consider a triangular lattice PhC (which offers more extraction directions than a 1D grating, as seen on Fig. 3.16) of filling factor $f \sim 0.3-0.4$, a reasonable value from the point of view of fabrication. We only consider diffraction around the *second Bragg order*, e.g. using a lattice constant a such that the reduced frequency is in the range $a/\lambda \sim 0.4-0.5$. These choices will be justified in the next chapter.

Let us recall that for a Bloch mode with wavevector $k_{//} = k' + ik''$, the exponential decay length is $L_{decay} = 1/2k''$. Therefore k'' is a good quantity to describe the extraction efficiency of a PhC.

3.2.1 Band structure of a 3D PhC

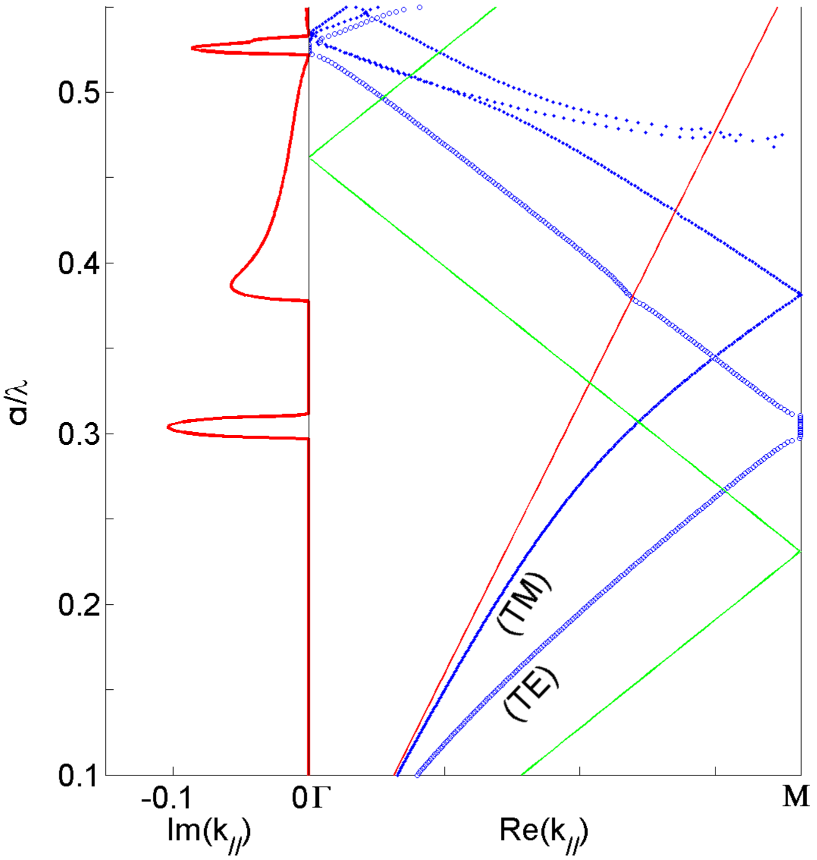

Figure 3.18: (Right half) Band structure of a 2D PhC in a 3D structure, in the ΓM direction. The band structure is now more intricate, with several bands stemming from one guided mode due to multiple foldings (manifesting that the PhC is 2D) and anticrossings which mix TE guided modes and TM guided modes. (Left half) Imaginary part of k" for the Bloch mode whose dispersion is plotted as hollow circles. Notice the difference in horizontal scale between both plots.

First, let us come back to the model 1D grating studied in Fig. 3.9 and see what happens when the 1D grating is replaced by a triangular lattice PhC. Our new structure is therefore a waveguide of index 2.5 and total thickness $0.6a$, surrounded by air and etched to a depth $0.2a$ by a triangular lattice PhC of period a, with circular air holes of filling factor 0.3. Fig. 3.18 presents the band structure in the ΓM direction.

Many features are reminiscent of the 1D case, but the band structure is more intricate. At low frequency, $\lambda >> a$ and the effect of the PhC is simply that of an homogeneous layer, the index modulation being averaged: in this region one recognizes the dispersion of a TE and a TM guided mode. We label these modes, whose dispersion is close to that of guided modes, as *A-type* modes. In the region where $\lambda \sim a$, the effect of the PhC appears. Again, we observe band gaps at the FBZ edges, with a larger gap for the former TE guided mode than for the former TM guided mode. Since the FBZ is larger than for a 1D grating (the limit being at $k_{//} = 2\pi/a\sqrt{3}$ rather than $k_{//} = \pi/a$), gaps and the crossing of the light line occur at higher frequency.

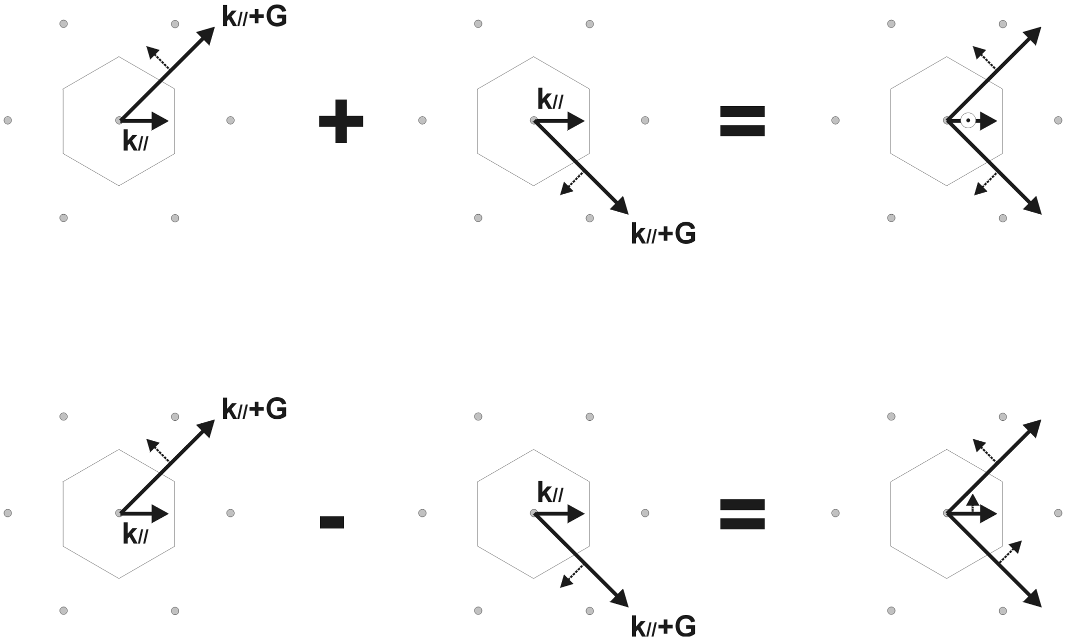

Figure 3.19: Construction of B-type modes. We start from two guided modes, which are TE-polarized in the waveguide sense, e.g. their polarization (dotted arrows) is in-plane. Hybridization of these modes yields two Bloch-modes which are respectively pseudo-TE and pseudo-TM in the PhC sense, e.g. considering the polarization of the (small) harmonic along ΓM. This harmonic is responsible for radiation to air, so that its polarization can indeed be measured in experiments.

Around $a/\lambda = 0.48$, two more modes appear from the M point, with a flatter slope than the two previous modes. We label these as *B-type* modes. They originate from 'non-collinear' foldings in the FBZ, i.e. foldings where the harmonic with most of the Bloch mode's power is not in the ΓM direction, as depicted on Fig. 3.19. One of these B-type modes is pseudo-TM, and the other pseudo-TE.

At $a/\lambda \sim 0.5$, the pseudo-TM B-type mode anticrosses with the pseudo-TM A-type mode. This shows how one should be careful when understanding the meaning of polarization in a 3D structure. The pseudo-TM A-type mode is indeed close to a TM guided mode of a waveguide, with some smaller harmonics. On the other hand, the pseudo-TM B-type mode is mainly made of two TE-like guided modes (but which do not propagate along x) and has a small radiative harmonic, which is TM-polarized. Due to their similar symmetry, both modes can couple, and in the anticrossing region there is no simple description of their structure.

This mode mixing has an additional implication. In general, when considering light emission from quantum wells in a planar structure, it is safe to ignore TM guided modes (at least in first approximation), because transitions corresponding to electrons-heavy holes recombinations produce strongly TE-polarized light at glancing angles: most of the guided light is TE (see Appendix B). However, we now see that some pseudo-TM Bloch modes are mainly made of TE-polarized guided modes and certainly couple to electron-heavy holes recombinations. Moreover, due to the anticrossings just described, the nature of a band can change from being (nearly) a true TM guided mode to a 'fake' pseudo-TM Bloch mode. Therefore, we have to conclude that all photonic bands can be of importance, no matter what their polarization is.

Finally, it is worth noting that one should be careful in interpreting the value of k'' for B-type modes as obtained from calculations. It is typically larger than for A-type modes, but this is an artifact due to the fact that the mode's energy is carried by harmonics which propagate at an angle φ with respect to ΓM. Therefore, when the Bloch mode propagates for a distance L in the ΓM direction, the strong harmonics actually propagate for a longer distance $L/\cos(\varphi)$, and hence lose more energy. In conclusion, the value of k'' for such modes should be normalized by a factor $\cos(\varphi)$ – at least in the case where a strong harmonic can be defined. In structures with stronger photonic effects, many harmonics can be strong and this simple normalization is no longer possible. Nevertheless, one should keep in mind that the interpretation of energy flows for a Bloch mode is non-trivial, and that folding in the FBZ is a source for possible misinterpretation.

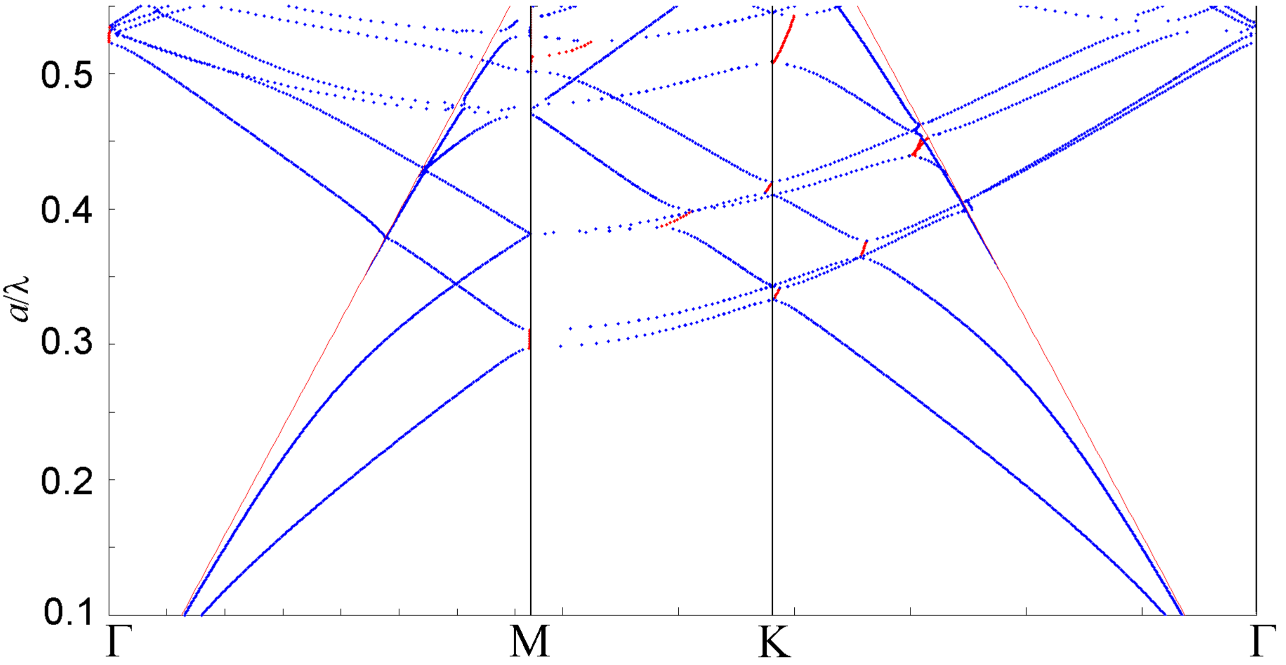

Figure 3.20: Complete band structure along the high-symmetry directions. The left side (ΓM direction) is the same as Fig. 3.18. In other directions (ΓK and KM), the edge of the FBZ is further and modes become leaky at higher frequency.

For completeness, let us extend the previous calculation to other high-symmetry directions of the FBZ (Fig. 3.20). Most features of this band structure are reminiscent of the 2D band structure of Fig. 3.13.[6]

The main information of this complete band structure is that, along ΓK, the air cone is reached at higher frequency than along ΓM ($a/\lambda \sim 0.4$) because the RL points in this direction are further away

---

[6] It is worth noting that directions ΓK and KM both correspond to the same physical propagation direction in the PhC, tilted 30^o with respect to ΓM. Their different names just refer to aligned points in the reciprocal space.

from the center of the reciprocal space. One should not be deceived by the B-type modes which appear at $a/\lambda = 0.3$ and cross the light line at $a/\lambda \sim 0.36$. Their structure is similar to that depicted in Fig. 3.19. They are mostly made of 2 harmonics which *do not* propagate along ΓK inside the dielectric layer. On the other hand, the A-type modes along ΓK do correspond to light propagating along ΓK; as can be seen, they reach point M at $a/\lambda \sim 0.45$, where they fold back. Thus, they remain under the light cone everywhere in this figure. They would only become leaky around $a/\lambda \sim 0.65$. Therefore, the present PhC is unable to extract guided light in some propagation directions, at least at frequencies around 0.5.

The band structure of a 3D object is rich with information about its optical properties. It combines characteristics of 2D PhCs and of dielectric waveguides, and allows a description of the light extraction phenomenon when photonic bands cross the light line. However, one should be careful when drawing conclusions from a band structure: band foldings in the first Brillouin zone lead to delicate interpretation.

3.2.2 Etch depth and light extraction

Let us now come to the impact of the PhC depth d on the extraction efficiency. Before turning to calculations, we can hint at a few trends. First, the extraction efficiency should obviously vanish in the limit $d \rightarrow 0$. In the limit $d << \lambda$, the trend of extraction efficiency is well-known. It is that of scattering by small particles, with a radiating perturbation:

$$k'' \sim \int\int (\Delta\epsilon E)^2 \tag{3.26}$$

The unperturbed field E (e.g. in the absence of PhC) can be taken in this integral because of the weakness of the perturbation, which results in losses:

$$k'' \sim d^2 \tag{3.27}$$

On the other hand, it is also well-known from the literature that if one wants to suppress (or strongly reduce) the losses of a leaky mode, it is also possible to etch the PhC very deep (e.g. far into the substrate where the Bloch mode is evanescent). Indeed, in this case, the Bloch mode 'feels' a dielectric environment which is 'separable' in space (roughly speaking, $\epsilon \sim f(x,y)g(z)$) which in turn leads to reduced loss: this is the so-called *intrinsic regime.*[6] This approach is routinely used for PhCs in foreseen telecommunication applications, where one wants to guide the light with as little loss as possible. Due to this effect, the extraction efficiency of a Bloch mode can be expected to be small when $d \rightarrow \infty$ (PhC etched into the substrate).

Besides, it is also possible to give an analytical trend for the extraction efficiency as a function of etch depth, in the intermediate regime where both d and the thickness t of the core (the *unetched* part of the waveguide) are of the same order of magnitude as λ (Fig. 3.21). More precisely, for a given Bloch mode, there exists a cutoff thickness t_c: intuitively, for $t > t_c$ the mode is well localized in the core, below the PhC, and the effect of the PhC is limited. When $t < t_c$ the mode leaks significantly in the PhC region and photonic effects become stronger.

Let us consider the case $t > t_c$, and also assume that the PhC is reasonably deep (not small compared to λ). We now assume that the Bloch mode consists of a fundamental $\mathcal{E}_0$, akin to a guided mode, which generates small harmonics $\mathcal{E}_m$ through interaction with the photonic crystal region. Let us take the simple case where only one of these harmonics, $\mathcal{E}_{-1}$, is propagative in the substrate or superstrate, and therefore gives an imaginary component k'' to the wavevector because of losses. In

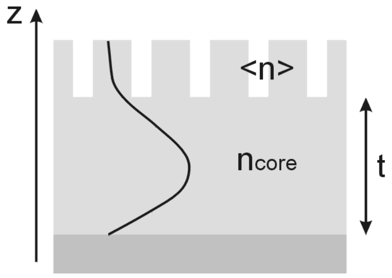

Figure 3.21: Approximation of a Bloch mode when the core thickness t is sufficient for the fundamental harmonic of the mode $\mathcal{E}_0$ to be strongly localized in the core region. The refractive index felt by $\mathcal{E}_0$ in each region is indicated.

this case, it can easily be shown that the power radiated by this harmonic is proportional to its vertical Poynting flow, normalized by the incoming power of the Bloch mode, so that:

$$k'' \sim \frac{k_z^{up}(\mathcal{E}_{-1}^{up})^2 + k_z^{down}(\mathcal{E}_{-1}^{down})^2}{k_{//}\int_{-\infty}^{\infty}|\mathcal{E}_0|^2\,dz} \tag{3.28}$$

Where *up* (resp. *down*) refers to quantities in the air (substrate) and k_z is the vertical wavevector. In this expression, the numerator is mostly an oscillating function of the unetched thickness t, with small variations in average value (for a precise form, the reader can refer to Ref. [7] where this perturbative approach is treated in great details). On the other hand, the denominator can be easily estimated using a simple model of 'infinite quantum well' (Fig. 3.21), where $\mathcal{E}_0$ is assumed not to penetrate the regions of PhC and substrate. The effective index n_{eff} of the Bloch mode, defined as $n_{eff} = k_{//}/k_0$, is then approximately given by:

$$n_{eff}^2 = n_{core}^2 - \left(\frac{\pi}{k_0 t}\right)^2 \tag{3.29}$$

We now define

$$\begin{aligned} < n >^2 &= f n_{air}^2 + (1-f) n_{core}^2 & (3.30) \\ K &= \frac{< n >^2 - n_{eff}^2}{n_{core}^2 - n_{eff}^2} & (3.31) \end{aligned}$$

It can then be shown after some simple algebra that

$$\int_{-\infty}^{\infty}|\mathcal{E}_0|^2\,dz = \frac{(1+K^2)t}{2} + o(t^3) \tag{3.32}$$

Which finally yields

$$k'' \sim \frac{2}{(1+K^2)t} \sim t^{-3} \tag{3.33}$$

We now have a fairly accurate idea of the evolution of k'' with etch depth of the PhC: starting from zero, it quickly reaches a perturbative regime where it increases like t^{-3}. The Bloch mode then enters a regime of strong photonic interaction where k'' reaches a maximum before decreasing again in the intrinsic regime.[7]

---

[7] Of course, all this assumes that the Bloch mode can be sustained for all values of d.

Let us test this qualitative discussion against electromagnetic simulations. To this effect, we consider the following model case: a GaN ($n = 2.5$) waveguide of total thickness $8a$ with an air superstrate and a sapphire ($n = 1.7$) substrate, etched by a triangular lattice PhC of filling factor $f = 0.35$. This waveguide is rather thick, which gives us room to observe the various regimes of light extraction.

Although such a waveguide supports several guided modes, we only consider the fundamental TE_1 mode, propagating along the ΓM direction of the crystal, at a reduced frequency $u = a/\lambda = 0.44$ (close to the second Bragg order). The more complex question of multimode light extraction will be addressed in the next chapter. The effective index and radiative losses of this Bloch mode are plotted on Fig. 3.22 as a function of PhC depth.

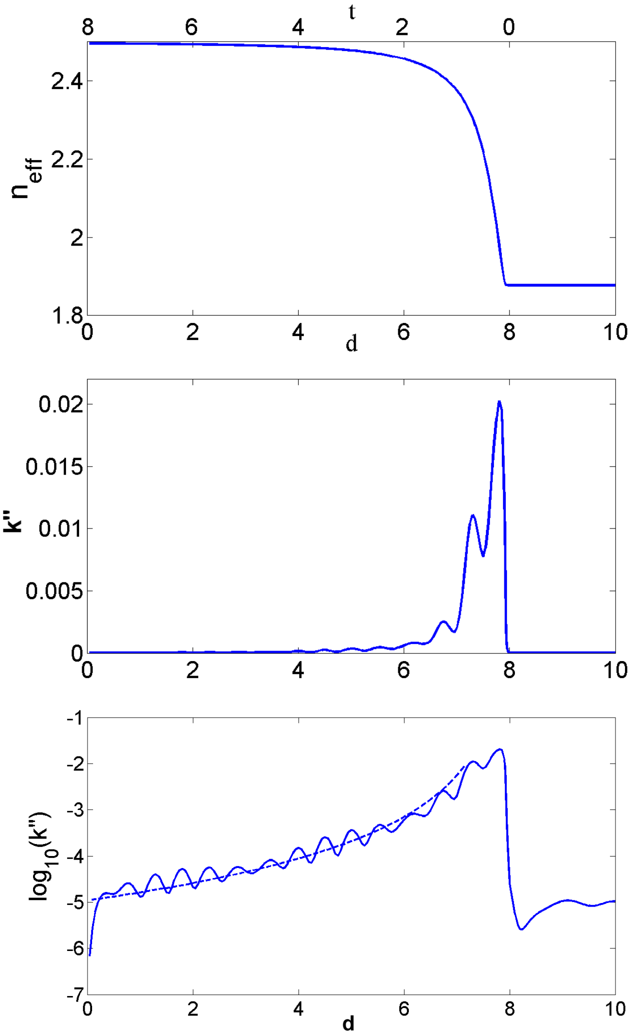

Figure 3.22: Extraction efficiency of the TE_1 Bloch mode as a function of PhC etch depth, at $a/\lambda = 0.44$. (Top) Effective index of the Bloch mode. n_{eff} remains constant after $d = 8$, when the etch goes through the substrate. (Center) Imaginary part of the wavevector. (Bottom) Same as (Center) in log scale. Dashed lines: fit by a t^{-3} function.

As expected, losses increase approximately like t^{-3} (apart from some interference modulations) as long as the Bloch mode is mainly located in the core of the unetched waveguide – as can be seen by the value of its effective index, close to 2.5. When the thickness of the unetched WG becomes smaller than $\sim \lambda/2n$, the mode can not be localized in the core and starts leaking in the etched region. Its effective index decreases, while the radiative loss reaches a maximum. Finally, when the PhC is etched through the GaN and into the sapphire substrate, radiative losses decrease rapidly, and reach the intrinsic regime.[8] In summary, the expected extraction regimes correspond well with the simulation.

It should be noted that a Bloch mode always exist in the present example, even when holes are etched completely through the GaN but not into the sapphire, because the average index of etched GaN (~ 2.2) is still higher than that of sapphire (1.7). This is not the case in most optoelectronic or silica-based materials systems, for instance in a GaAs waveguide ($n = 3.6$) confined by an AlGaAs ($n = 3$) cladding, where Bloch modes are cutoff for excessive values of d.

3.2.3 Loss to air and substrate

Let us now come back to the oscillatory behavior of k'' which can be observed on Fig. 3.22. Our simple trend $k'' \sim t^{-3}$ does not account for it, because we have considered the numerator of Eq. 3.28 as constant. It can be checked numerically that the oscillations of k'' are mainly caused by the variation of this numerator, which is clearly composed of two terms corresponding respectively to loss toward air and substrate.

Therefore, we are led to distinguish these two contributions to the total loss k''. Let us define $\mathcal{P}_{in}$ as the incident power of the Bloch mode, and $d\mathcal{P}_{up}$ and $d\mathcal{P}_{down}$ as the power radiated per unit length (e.g. per lattice constant) by the leaky harmonic, to air and substrate respectively. We simply have, with the same notations as above:[9]

$$\begin{aligned} d\mathcal{P}_{up} &= k_z^{up}(\mathcal{E}_{-1}^{up})^2/\mathcal{P}_{in} \\ d\mathcal{P}_{down} &= k_z^{down}(\mathcal{E}_{-1}^{down})^2/\mathcal{P}_{in} \end{aligned} \tag{3.34}$$

We can now compare $d\mathcal{P}_{up}$ and $d\mathcal{P}_{down}$, as is done on Fig. 3.23. Both quantities undergo strong oscillations when d varies. This is simply due to Fabry-Pérot type oscillations of the power emitted upwards and downwards, produced by partial reflections of the (-1) harmonic at the interfaces with air and substrate.

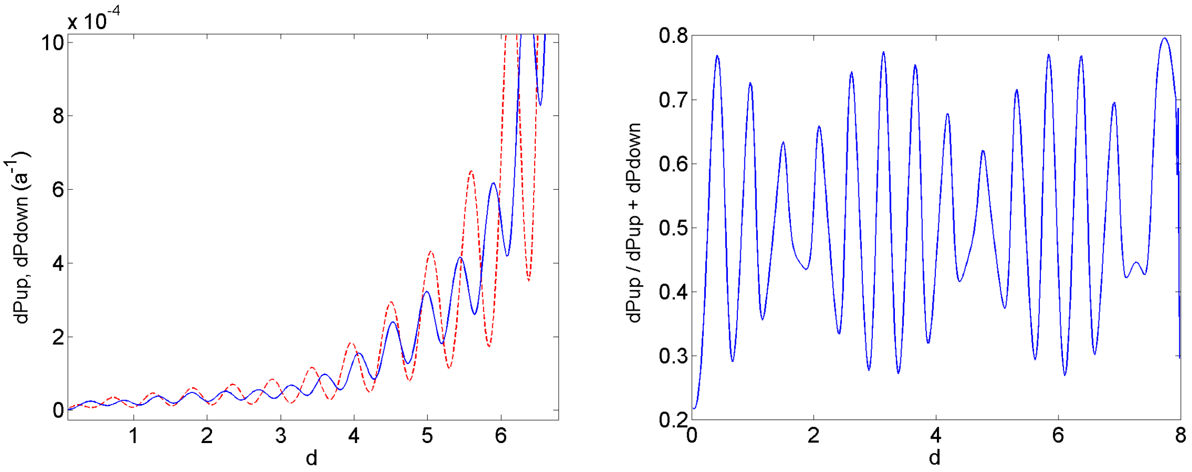

Figure 3.23: (Left) Fraction of the Bloch mode's energy radiated per unit length to air (full line) and substrate (dashed line). For clarity the plot stops at $d \sim 7$. Both loss channels oscillate with a chirped phase. (Right) Fraction of the diffracted light which is radiated to air. The chirp in phases between $d\mathcal{P}_{top}$ and $d\mathcal{P}_{bot}$ leads to beatings.

---

[8] The intrinsic regime is reached rapidly here (e.g. even for shallow holes in the substrate) because the mode is strongly evanescent in the substrate, $n_{eff} - n_{subs}$ being large.

[9] More details about the calculation of energy flows of a Bloch mode can be found in Annex A.

As a result, the fraction of the Bloch mode which is diffracted to air is given by $d\mathcal{P}_{up}/(d\mathcal{P}_{up} + d\mathcal{P}_{down})$. This quantity, also plotted on Fig. 3.23, shows the Fabry-Pérot-like oscillations which can be expected when collecting light diffracted to air in an experiment. It can be checked that the average value of this quantity is 1/2.

The origin of the oscillations can be checked by looking at the vertical profile of the Bloch mode's harmonics (Fig. 3.24). The radiative harmonic (-1) is seen to oscillate inside the structure due to reflexions at the interfaces.

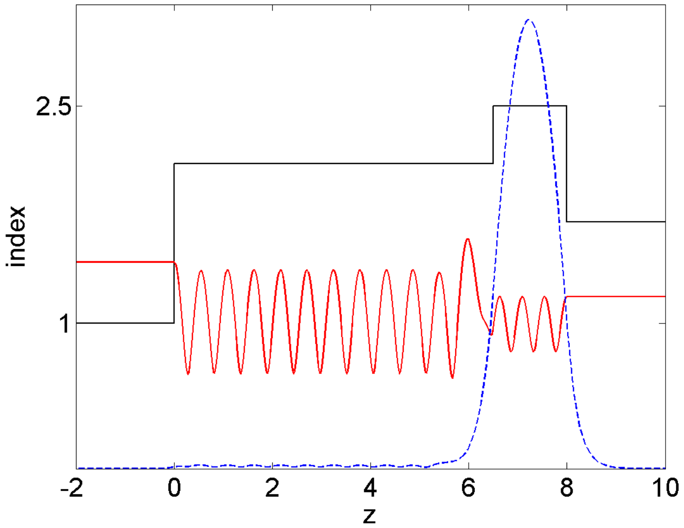

Figure 3.24: Profile of the fundamental (dashed line) and (-1) harmonic (full line) of the Bloch mode in the z direction, for an etch depth $d = 6.5$. The amplitude of the (-1) harmonic has been multiplied by 10 for clarity. The average index in the structure is also indicated.

This field profile also reveals why, in Fig. 3.23, oscillations to air and to the substrate have a chirped phase relation. Indeed, the radiative harmonic feels two sub-cavities of thicknesses d and t (with $<n>= 2.2$ and 2.5, respectively). The radiative harmonic therefore oscillates with a different phase in each cavity, yielding the beating of Fig. 3.23.

As a consequence of this effect, the extracted light can be directed preferentially to air or to the substrate. One may consider making the most of this effect by using a 'hot spot' where most of the diffraction occurs upwards. Unfortunately, the tolerance around such spots is quite narrow. From a fabrication point of view, it would require control of the PhC depth within a few dozen nanometers. Besides, the optimal d varies with wavelength so that an optimum is not necessarily possible for a polychromatic source. Finally, as will soon be seen, the multimode nature of GaN waveguides completely averages out this effect anyway.

On the other hand, it must be reminded that sapphire substrates are transparent (with virtually no loss) in the visible. Therefore, a much simpler solution consists in placing a far-field mirror (such as an Ag or Al layer) beneath the sapphire substrate in order to redirect light emitted downward. The only drawback of this method is that the apparent emitting surface is enlarged due to the round-trip of light in sapphire, which is somehow detrimental to brightness but still acceptable.[10]

---

[10] The thickness of the sapphire substrate is $\sim 500\mu$m: light propagating in sapphire with an angle $\sim 45^o$ travels 1 mm laterally before escaping to air: this is still reasonable, especially for high power LEDs whose emitting region is ~ 1 mm wide anyway.

3.3 Photonic crystals in GaN: photoluminescence experiments

We now come to the first experimental results on GaN photonic crystals obtained at UCSB. We present the photoluminescence experiments, their interpretations in terms of photonic band structure, and the implications for efficient light extraction.

3.3.1 Photonic crystals fabrication

Photonic crystals regions were formed in PL samples to characterize their optical properties. The fabrication process is as follows:

Pattern definition	Hard mask deposition	PECVD SiO_2 evaporation
	E-beam resist deposition	ZEP 512 2:1 (4000 RPM,1')
	Bake	180^oC, 1'
	Au layer deposition	Thermal evaporator, 10 nm Au
	Pattern definition	E-beam lithography
	Gold removal	Au etchant, 5s dip
	Resist lift-off	Amylacetate 60s dip
		MIBK 15s dip
		Isopropanol 10s dip
PhC etch	SiO_2 hard mask etch	RIE 3 CHF_3 etch, 6 nm/min
	GaN etch	RIE 5 Cl_2 etch, 100 nm/min

The SiO_2 hard mask is useful to obtain etch depths larger than 100 nm, because of its good resistance to the GaN etch. While the maximum depth I used for this thesis was under 300 nm, deeper-etched structures may be of interest for some applications such as DFB lasers; it has been checked that a SiO_2 hard mask can sustain GaN RIE etchings down to 700 nm. The GaN etch used above is the regular etch used for most LED processes; it turns out to produce fairly vertical sidewalls, at least for the small aspect ratios involved, close to 1.

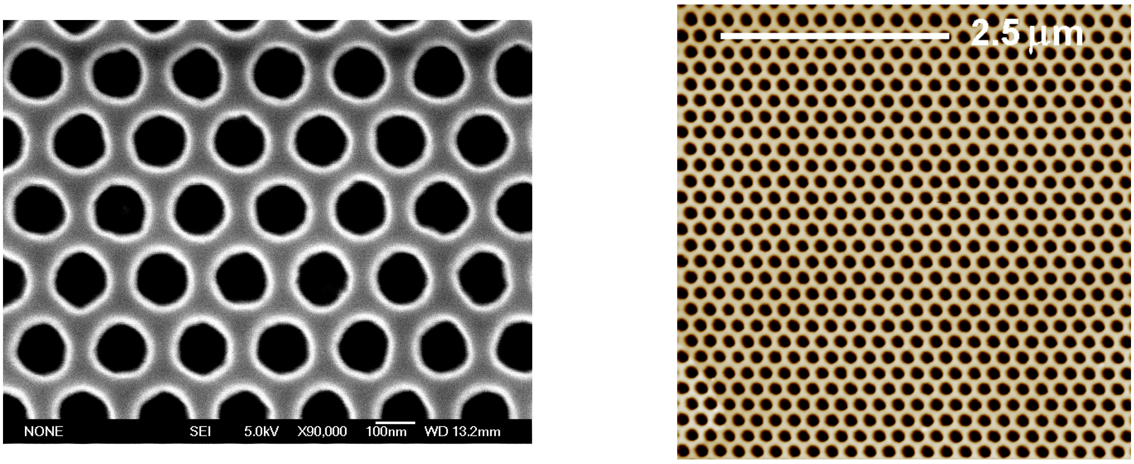

Figure 3.25: Scanning electron microscope (left) and atomic force microscope (right) images of a photonic crystal on a PL sample, with lattice constant $a = 200$ nm and filling factor $f = 0.3$.

For the PL experiments, I used epitaxial layers grown by Rajat Sharma, with a total thickness of 2.9μm and a region of InGaN multi-quantum wells, buried $\sim 100nm$ below the surface. The QWs emit around 425-450 nm. On these layers, triangular lattice patterns with a lattice constant $a = 200$ nm and filling factors ranging from 0.2 to 0.37 were formed. By calibration of the GaN etch, their depth is estimated to ~ 180 nm (atomic force microscope measurements also confirm that the depth is at least 170 nm). The PhC regions are $\sim 160\mu$m x 320μm large. Fig. 3.25 shows several images of the PhC regions.

3.3.2 Angle-resolved photoluminescence experiments

The excitation source for PL experiments is a HeCd laser with emission at 325 nm, and a focused spot of diameter 100 μm. The sample can be measured under two excitation conditions: (1) with the exciting laser impinging on a bare GaN surface and (2) on the PhC region (Fig. 3.26). In the first case, the excitation spot is focused a few hundred μm away from the PhC, so that its size can be neglected to the first order. In all cases, the total area of the light-emitting region is less than 1 mm^2, which is small compared to the rotating arm of the angular sample (10 to 15 cm). Therefore, the source can be considered point-like in all measurements.

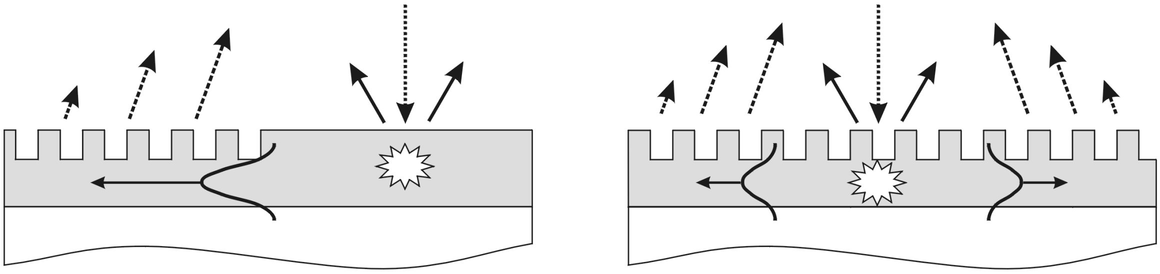

Figure 3.26: Excitation schemes in PL experiments. (Dotted arrows) UV laser excitation (Full arrows) Direct emission from the quantum wells (Dashed arrows) Diffraction of guided light by the photonic crystal. (Left) Scheme (1), the laser excites the bare GaN surface close to the PhC. (Right) Scheme (2), the laser excites the PhC region directly. Light extraction by the PhC is schematically shown as occurring backward, because the PhC operates below the second Bragg order.

Let us first consider excitation scheme (1). We collect the spectra with a polarizer placed at the extremity of the collecting arm, in order to discriminate the two families of Bloch modes described earlier (pseudo-TE and pseudo-TM). Spectra collected at various angles with the angle-resolved setup are shown on Fig. 3.27. Some features of the spectra are familiar. For instance, the spectrum corresponding to $\lambda = 418nm$ looks like a regular PL spectrum, with Fabry-Pérot interferences modulating the light emission to air. However, at other wavelengths, sharp luminescence peaks are collected for $\theta > 0$. These correspond to light extraction by the PhC. The angular range where diffraction occurs is as expected: the lattice constant $a = 200$ nm corresponds to Bloch modes slightly below the second Bragg order, where the light is diffracted 'backwards' (in other words, the in-plane wavevector of the (-1) harmonic is in the direction opposite to $k_{//}$, as in Fig. 3.26).

To characterize the dispersion of these extraction peaks, angle-resolved spectra collected for all values of θ are merged into a 2D plot on Fig. 3.28. The left part of this 2D plot is very similar to the measurements on regular GaN LEDs already seen in the previous chapter. Diffraction by the PhC clearly appears as a series of lines superimposed on this spectrum. As already said, it occurs in directions $\theta > 0$. The diffraction peaks are dispersive with respect to wavelength.

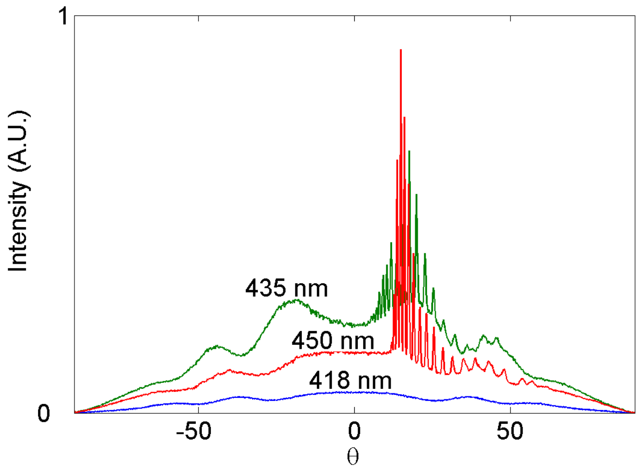

Figure 3.27: Monochromatic angle-resolved spectra with excitation scheme 1, for 3 different collection wavelengths. Sharp peaks due to light diffraction by the PhC appear at some angles and wavelengths.

3.3.3 Photonic band structure

In order to isolate these peaks in excitation scheme 1, we now take the left half of the angular spectrum (direct emission from the quantum wells) and subtract it from the right half of the spectrum: therefore, only the additional signal from the PhC is kept. Moreover, to study the dispersion of the PhC signal, we change the axes of the plot from $(\theta,\ \lambda)$ to $(k_{//},\ a/\lambda)$, where $k_{//} = 2\pi\sin(\theta)/\lambda$. Finally, the spectrum needs to be normalized by the emission lineshape of the quantum well in order to observe the PhC's intrinsic extraction efficiency at all frequencies. To do so, the lineshape of the QW is obtained by integrating the left half of the plot over all angles, thus averaging the effect of Fabry-Pérot modulations and restoring the intrinsic QW emission. The whole spectrum is then normalized by this lineshape.

We then obtain Fig. 3.29, which is actually a part of the band structure of the PhC. As a guide for the eye the light line of air, and the folded light lines of sapphire and GaN are also indicated. Their respective equations are:

$$\omega = k_{//}c, \quad \omega = G_0 - k_{//}c/1.7, \quad \omega = G_0 - k_{//}c/n_{GaN} \tag{3.35}$$

Obviously, this experimental band structure is much more complex than those we encountered so far in calculations. The main reason for this is that for simplicity, these calculations were performed on thin film layers supporting only one Bloch mode.[11] Here, multiple photonic bands are measured above the light line of air and correspond to the multiple Bloch modes supported by the thick GaN structure – of course, no signal is collected below the light line of air, which corresponds to $\theta = 90^o$. The photonic bands are also located above the folded GaN line, which confirms that they correspond to modes guided (propagative) in the GaN layer.

Most of these bands look like a series of parallel lines whose spacing increases with $k_{//}$. Notably, these lines also seem nearly parallel to the light line of GaN, a feature reminiscent of guided modes strongly localized in a waveguide. A closer look reveals a more complex band structure for $k_{//} \sim 2$ and $a/\lambda \sim 0.44 - 0.46$. Finally, it is interesting to note that there is a cutoff in photonic bands above the sapphire folded line. This is simply due to the fact that light above the sapphire line is propagative in the sapphire and therefore no longer guided in the GaN layer (this is the so-called substrate light). In a geometrical view, this light travels large distances in the sapphire substrate between two bounces

---

[11] Actually, another mode was sometimes present but neglected for clarity

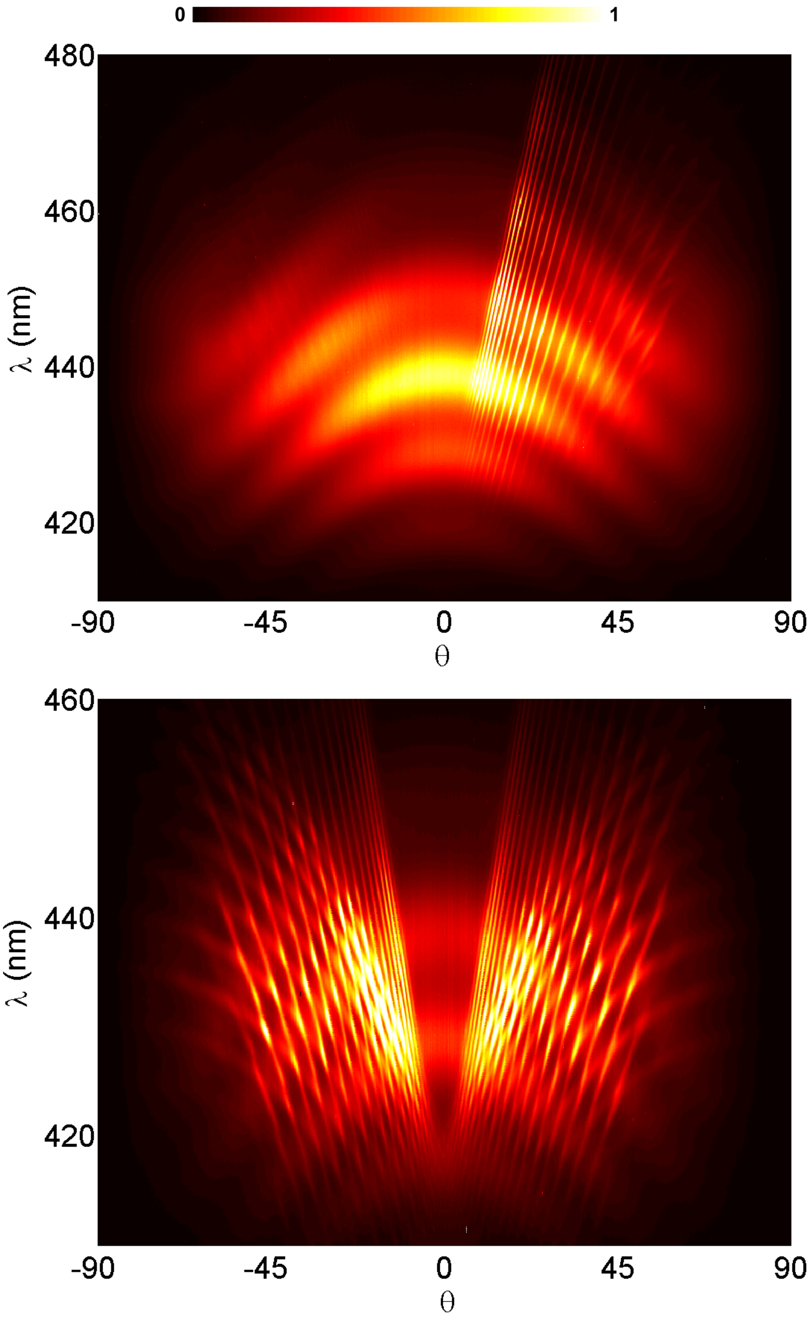

Figure 3.28: Angle-resolved photoluminescence measurements on photonic crystals (ΓM direction, TE polarization). (Top) Excitation scheme 1, the PhC only diffracts in one direction. (Bottom) Excitation scheme 2: more PhC bands are excited, and the spectrum is symmetric.

on the PhC, and therefore has a vanishing extraction efficiency: hence the absence of signal above the sapphire line.

Let us now give a qualitative justification of this complex band structure. As the GaN waveguide is thick (several μm) it supports several dozen guided modes. When a PhC pattern is formed on this structure, each of these modes gives rise to a set of photonic bands, which can be understood by folding the dispersion of each guided mode in the first Brillouin zone. Fig. 3.31 illustrates this construction.

From this, the set of lines parallel to the GaN light line can be interpreted as the A-type modes

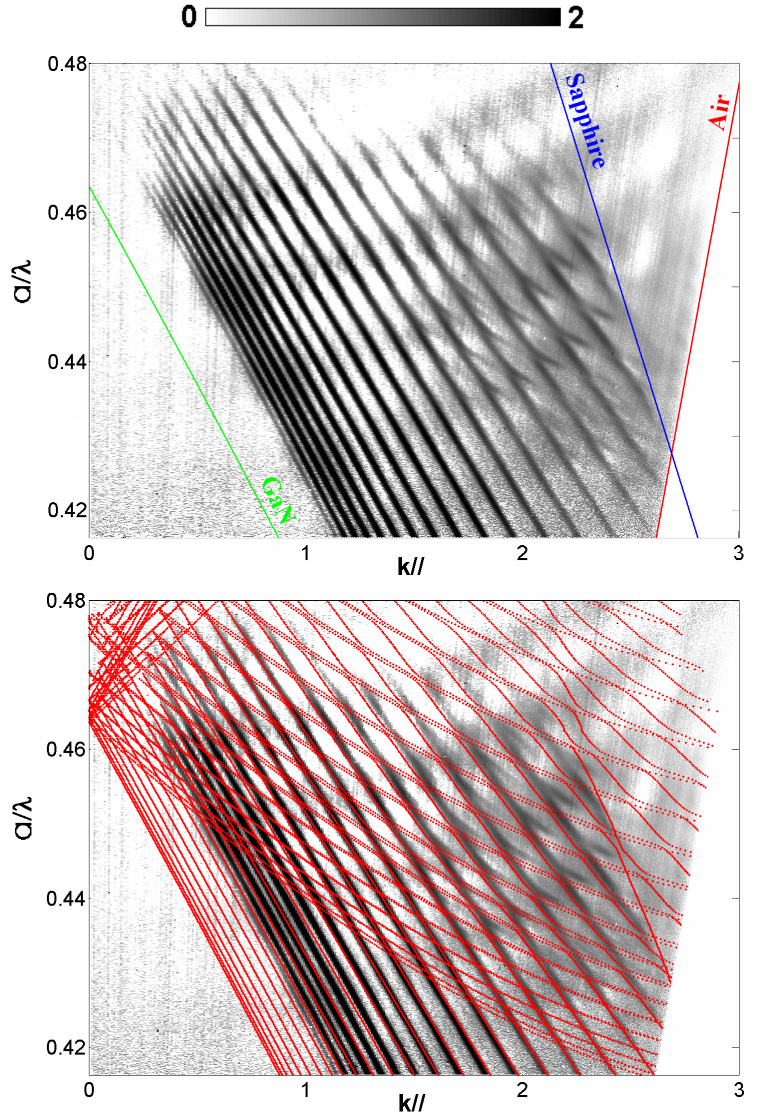

Figure 3.29: Experimental band structure of the photonic crystal. The signal is plotted as grey levels on a log_{10} scale (black corresponding to signal, white to background). $k_{//}$ is in a^{-1} units. (Top) Experimental band structure as measured. The red, blue and green lines correspond to the light lines of air, sapphire and GaN respectively. (Bottom) Same with the result of a 3D calculation superimposed as red dots.

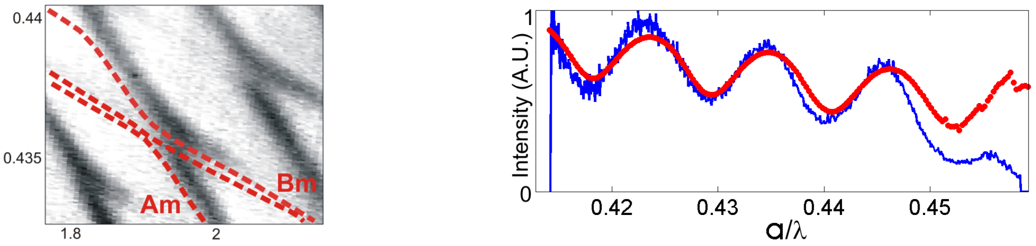

Figure 3.30: (Left) Anticrossing between an A-type and a B-type mode. (Right) Experimental (blue) and calculated (red) intensity of an A-type mode (specifically, the mode corresponding to $n_{eff} = 2.3$), showing Fabry-Pérot-like oscillations.

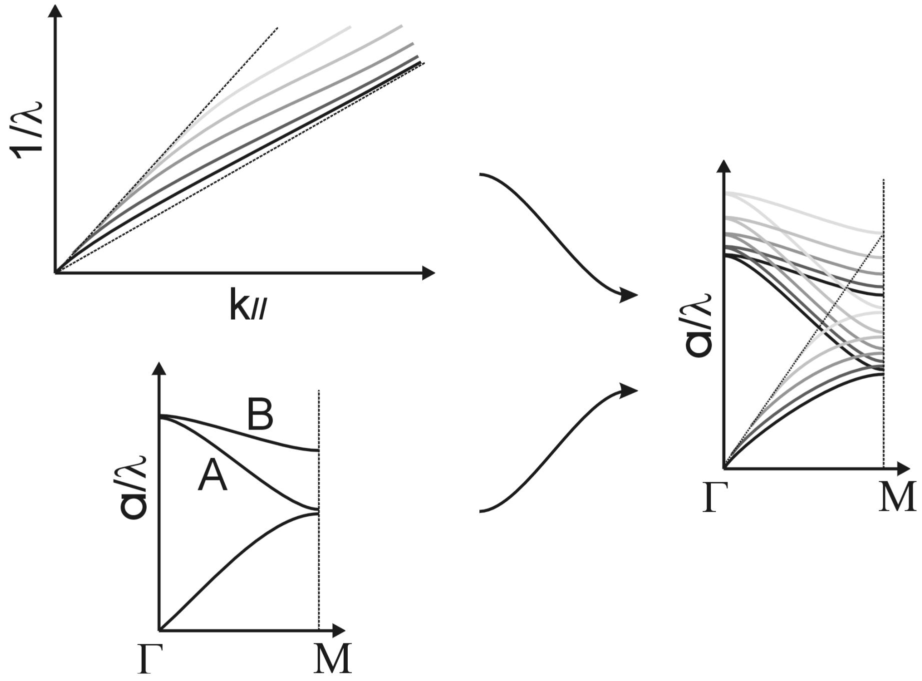

Figure 3.31: Origin of the band structure of a multimode 2D PhC. (Top left) The original GaN waveguide supports numerous guided modes. (Bottom left) Typical band structure of a 2D PhC, with bands folded in the FBZ. Notice that the multiple foldings produce 2 bands close to the second Bragg order; (A) is produced by a simple folding collinear to ΓM, while the nearly degenerate doublet (B) is due to a non-collinear folding such as in Fig. 3.14. (Right) Folding of the multiple guided modes' dispersions yields the intricate band structure of the multimode system. Once the photonic bands cross the light line (dotted line) they become leaky and can be collected experimentally.

of Fig. 3.31: they have a dispersion close to that of a free photon in GaN, due to the weak photonic strength of the shallow PhC. The spacing between these A-type mode increases with mode number, as is the case in a waveguide (where the wavevector of the p^{th} mode is typically shifted from the core index with a $\sim p^2$ scaling).

In addition, B-type modes appear (although faintly) in the region $k_{//} \sim 2$, $a/\lambda \sim 0.44 - 0.46$. This calls for a quick comment: the structure of such modes corresponds to the sketch of Fig. 3.14. Hence their *fundamental* component does not propagate in the ΓM direction of excitation, so that they should not be excited by the UV laser spot. They observation can be partly justified by the spread of the laser spot, which makes excitation not strictly directional. In addition, it is worth noting that A-type and B-type modes undergo multiple anticrossings, as seen on Fig. 3.30. These anticrossing manifest hybridization of both types of modes, which also indicates a second channel for exciting B-type modes: at the anticrossings, the simple picture of Fig. 3.14 no longer holds. It is interesting that these anticrossing occur in spite of the weak photonic strength of the PhC. It may naively be thought that such a PhC only acts as a sum of three 1D gratings tilted by 60^o, because only first-order diffractions matter. However, hybridization of the modes manifests the 2D nature of the PhC.

After this qualitative analysis, we can resort to electromagnetic calculations to confirm our understanding of the band structure. Fig. 3.29 shows the result of a 3D calculation, taking the exact structure into account. As can be seen, there is an excellent fit between the measured and calculated band structures (at least in the regions where experimental signal is collected). It is worth mentioning that this was obtained without any fitting parameter, only using the nominal values of the structure.

Taking into account the index dispersion of GaN (taken from Ref. [8]) is essential to obtain the correct band structure (for instance, at $\lambda = 425$ nm, the refractive index is $n = 2.5$ but the group index is $n_g \sim 3$.)

Looking at the calculation into more details, it can be seen that the effect of cutoff above the sapphire line is also observed as a disruption in the numerical band structure.[12] Besides, finer details of the band structure are well reproduced by the calculation (Fig. 3.30). For instance, the bands anticrossings have a similar strength. The intensity of a given photonic band as a function of frequency also meets well the experimental value: the Fabry-Pérot type oscillations discussed in section 3.2.3 are well fitted.

As a side note, the efficiency of the 'hybrid' calculation method (described in Chapter 6) is highlighted here: the strongly multimode band structure is obtained without having to follow each Bloch mode individually, which would be very tedious in view of the multiple anticrossings displayed.

3.3.4 Efficient light extraction

Let us now comment on some discrepancies between the measurement and the calculation. First, the experimental signal decreases at high frequency, and no photonic bands are measured for frequencies higher than 0.48, although Bloch modes exist in theory. Initially, I suggested that bad coupling between incoming guided modes and these high-frequency Bloch modes could account for the lack of signal. However, as will be confirmed in the following section, reabsorption of guided modes by the material accounts well for the 'darkness' of these bands. Indeed, $a/\lambda \sim 0.48$ corresponds to the high-energy tail of the QW emission. Although some light is emitted at such wavelengths, guided modes experience much higher reabsorption in the quantum wells and therefore disappear before reaching the PhC region, located hundreds of μm away from the excitation region. This absorption effect also accounts for the discrepancy between the measured and calculated intensity at high energy in Fig. 3.30.

More interesting is the non-observation of Bloch modes of high effective index, i.e. the Bloch modes closest to the GaN line, which we call *low-order modes*. At least seven such modes are calculated but not measured: the first observed Bloch mode has an effective index $n_{eff} \sim n_{GaN} - 0.1$. This can be understood by considering the extraction efficiency of each mode. The lowest-order mode ($n_{eff} \sim n_{GaN} \sim 2.5$) is strongly localized in the unetched GaN core, and barely leaks in the PhC region whose average index is 2.15. Therefore, its extraction efficiency per unit length is very low, and a very long PhC would be necessary to efficiently extract it. Modes of lower n_{eff} have higher penetration in the PhC region, and hence higher extraction efficiencies. When the extraction efficiency is sufficient (e.g. when $1/k''$ is on the order of the PhC's length), the modes can be collected experimentally. The numerical calculation confirms that for the modes observed experimentally, or *high-order modes*, the imaginary part of the wavevector k'' is on the order of a few 10^{-4} to 10^{-3} (in a^{-1} units). This translates into extraction lengths of one hundred to a few hundred μm, comparable to the length of the fabricated PhC. On the other hand, for low-order modes k'' collapses: the extraction length would be of several centimeters for the lowest-order mode. The transition between low and high order modes seems quite abrupt on Fig. 3.29: only the two first A-modes seem fainter than the following. This is simply a visual effect due to the log scale and to the choice of the color scale, which saturate all well-extracted modes.

---

[12] One may actually wonder how modes *can* be calculated over this line, where they are no longer guided. This is a virtue of the 'hybrid' numerical method used here: to obtain this figure, only a few Bloch modes were actually calculated, but other eigenvalues of the numerical problems also correspond to other solutions (albeit with a larger numerical imprecision). Therefore, the whole band structure is obtained with only a few calculations. In addition, the method also naturally finds 'resonances' above the sapphire line: although these are no longer guided modes, they correspond to constructive interferences in the GaN layer. These resonances are the theoretical points plotted above the sapphire line; their extension under the sapphire line corresponds to true Bloch modes.

This implies that *not all* of the guided light can be extracted efficiently using a shallow-etched PhC, because the PhC does not interact well with all the guided modes of the thick GaN waveguide. Using larger PhC surfaces would hardly solve the problem because of the very low value of k'' for low-order modes. Unfortunately, the low-order modes also carry a very large fraction of the total emitted light: typically 30% to 40%. This is due to the fact that these modes correpond to the largest solid angle for light emission. Obviously, this is not acceptable for efficient guided modes extraction. Several strategies to deal with this issue will be presented in the next chapter.

3.3.5 Full characterization of the PhC's band structure

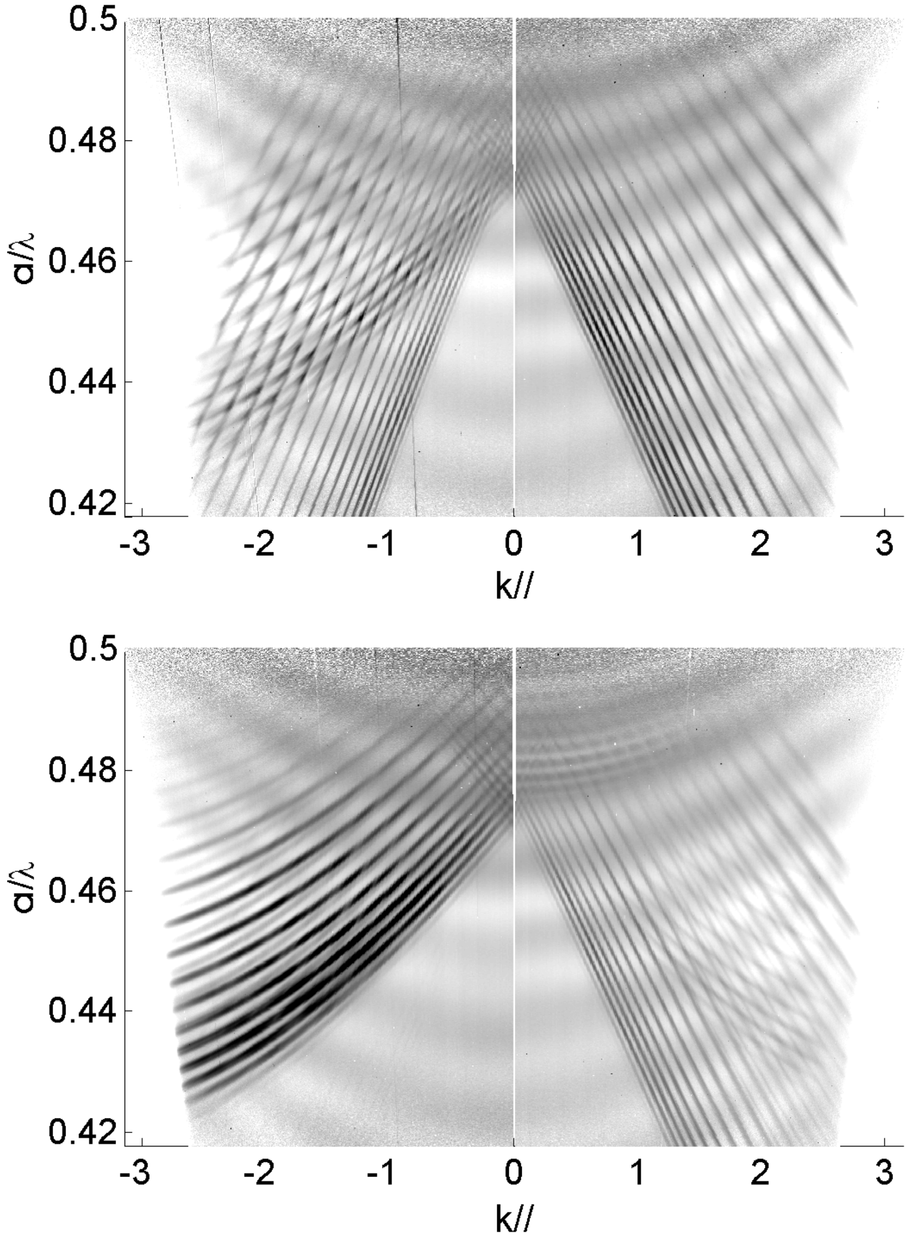

Figure 3.32: band structure of the PhC with internal excitation. Top: TE polarization, bottom: TM polarization. Left: ΓM direction, right: ΓK direction.

So far, we have only considered PhCs excited following scheme (1), e.g. with excitation outside of the PhC region. Let us now come to the second excitation scheme, where the UV laser impinges directly on the PhC. An angle-resolved measurement is presented on Fig. 3.28. Several differences appear with respect to the former excitation scheme. First, the spectrum is now symmetric around $\theta = 0$. Indeed, as light is generated inside the PhC, Bloch modes propagating both in the $+x$ and $-x$ direction are excited, as sketched on Fig. 3.26.

Besides, more photonic bands appear than formerly. Again, this is due to the fact that Bloch modes now propagate in all azimuthal directions. Therefore, B-type modes (whose main component have an azimuthal angle with respect to the x axis of the setup, see Fig. 3.19) are excited. This is best seen by considering the band structure corresponding to the angular measurement. We can obtain it by the same procedure as before. However, we no longer have access to the direct emission of the quantum well (because the PhC now diffracts in both directions) so that the band structure also displays the direct emission. Fig. 3.32 displays the experimental band structure in both directions ΓM and ΓK, and in TE and TM polarization. Thus, the band structure of the PhC's leaky modes is fully characterized.

All the bands which can be expected from the band structure of a 2D PhC are indeed observed, with proper polarization properties. For instance along ΓM, there are two kinds of B-type modes, respectively pseudo-TE and pseudo-TM polarized, whereas there is only one kind of A-type mode, which is pseudo-TE.

Bands are now observed at high frequency, which was not the case with scheme 1. This confirms that the guided light propagating at high frequency is reabsorbed by the material on a short scale (less than the $\sim 400\mu$m separating the excitation from the PhC in excitation scheme 1). Here on the other hand, as light is generated directly in the PhC, part of it can be extracted even at high frequency. This indicates that, for efficient extraction of all the emitted light, one should avoid as much as possible propagation of guided modes, and ideally generate light directly in the PhC.

In addition, photonic bands are observed in the ΓK direction. This fact has already been discussed above (section 3.2.1): this signal originates from Bloch modes whose main harmonics do not propagate along ΓK inside the GaN layer, but whose radiative harmonic is folded along ΓK. On the other hand, Bloch modes whose main harmonic does propagate along ΓK are under the light cone and are not measured.

3.3.6 Conclusion

Leaky modes of photonic crystals can be used in order to extract guided light from a GaN layer. Experimental observation of the photonic band structure of a PhC confirms that these leaky modes behave as expected from theory. By varying the experimental conditions, the structure can be fully characterized above the light line: angular-resolved luminescence is thus a powerful and accurate analysis tool. The measurements notably point out the existence of low-order modes, whose interaction with the PhC is insufficient to provide extraction within a reasonable scale. These modes carry a large fraction ($\sim 30\%$) of the total emitted light and any efficient light extraction scheme needs to address them.

Bibliography

[1] H. K. V. Lotsch. Beam displacement at total reflection - Goos-Hanchen effect. *Optik*, 32(3):189, 1970.

[2] H. Benisty, J.-M. Gerard, R. Houdre, J. Rarity, and C. Weisbuch (Eds). *Confined Photons and Systems (Lectures of the summer school of Cargese, Corsica, 1998).* Lecture Notes in Physics. Springer, Berlin, 1998.

[3] T. Tamir. *Guided wave optoelectronics*, volume 26 of *Springer series in electronics and photonics.* Springer Verlag, Berlin, 1990.

[4] H. Kogelnik and C. V. Shank. Coupled-wave theory of distributed feedback lasers. *Journal of Applied Physics*, 43(5):2327, 1972.

[5] R. F. Kazarinov and C. H. Henry. 2nd-order distributed feedback lasers with mode selection provided by 1st-order radiation losses. *IEEE Journal of Quantum Electronics*, 21(2):144–150, 1985.

[6] H. Benisty, P. Lalanne, S. Olivier, M. Rattier, C. Weisbuch, C. J. M. Smith, T. F. Krauss, C. Jouanin, and D. Cassagne. Finite-depth and intrinsic losses in vertically etched two-dimensional photonic crystals. *Optical and Quantum Electronics*, 34(1-3):205–215, 2002.

[7] W. Streifer, D. R. Scifres, and R. D. Burnham. Analysis of grating-coupled radiation in GaAs-GaAlAs lasers and waveguides. *IEEE Journal of Quantum Electronics*, 12(7):422–428, 1976.

[8] H. Y. Zhang, X. H. He, Y. H. Shih, M. Schurman, Z. C. Feng, and R. A. Stall. Waveguide study and refractive indices of GaN:Mg epitaxial film. *Optics Letters*, 21(19):1529–1531, 1996.

Chapter 4

Photonic crystal LEDs

The theoretical approach and PL measurements performed in the previous chapter hinted at some key points for optimization of photonic crystal LEDs. Although the problem of light extraction is intrinsically 3-dimensional, they indicate that the vertical and horizontal directions can to some extent be decoupled, at least in first approximation. In the horizontal direction, the main parameters of interest are the choice of the crystal lattice and filling factor. In the vertical direction, the multimode nature of GaN LEDs is problematic because the lowest-order guided modes do not interact with the photonic crystal.

In this chapter, several implementations of PhC-LEDs are introduced. Each of these addresses one or several issues which limit efficient light extraction. The three first implementations are mostly the fruit of personal work, and were brought to the level of operating LEDs. The others are larger-scale projects pursued at UCSB, where I contributed to the theoretical design and modeling, and optical characterization.

4.1 Tailoring of guided modes distribution

This first generation of PhC-LEDs addresses the problem of unextracted low-order modes. As argued in the previous chapter, modes of low effective index (say $n_{eff} > 2.3$) carry a lot of emitted light ($\sim 30\%$ of the total light emission) but are not well diffracted by shallow photonic crystal due to their poor overlap with the etched region.

4.1.1 Is deep etching a solution ?

The first way one may consider to enhance the interaction between low-order modes and the photonic crystal is to etch the PhC deeper: at some point, even the modes strongly localized in the GaN layer should leak into the PhC. However, one may readily hint that this will only happen if the un-etched GaN thickness is small enough that low-order modes are poorly confined. Therefore, if one wants the fundamental mode to interact with the PhC, the un-etched GaN depth should be close to a monomode waveguide.

A model calculation on a simple system confirms this intuitive view. Starting from a relatively thick GaN waveguide of thickness $4a$, we compute the extraction efficiency of each mode when a 1D grating (filling factor $f = 0.5$) is etched into the waveguide (the choice of a 1D grating makes the result easier to read because possible anticrossing between different in-plane modes are avoided; however the result also holds for a 2D PhC). The unetched waveguide supports 6 TE modes and 6 TM modes, at a normalized frequency $u = 0.39$ (this frequency is just below the second Bragg order for the first guided mode). Fig. 4.1 displays the effective index and imaginary part of the wavevector of each mode, as

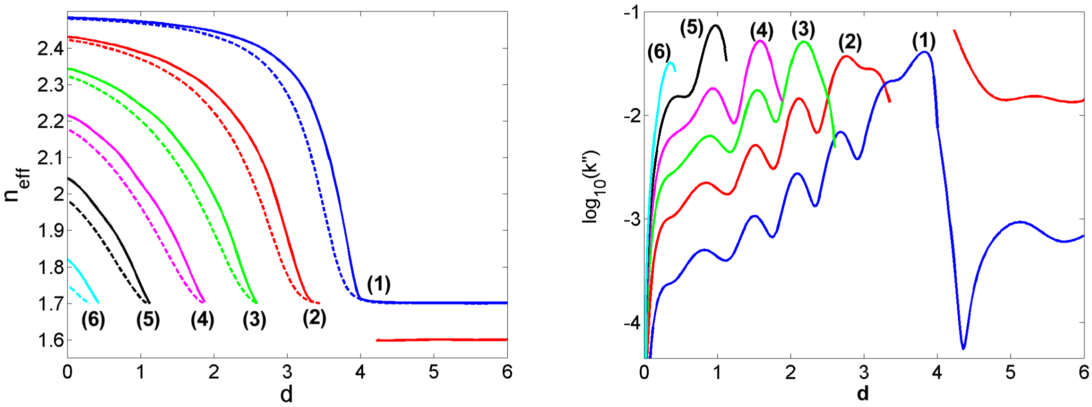

Figure 4.1: (a) Effective index of the TE (solid) and TM (dashed) modes supported by a thick GaN waveguide with varying PhC depth (b) Corresponding diffraction efficiencies (TE modes only for clarity)

a function of the grating depth. The modes are progressively cutoff as the grating is etched into the waveguide. Only the fundamental TE_1 and TM_1 modes remain guided for all values of t.[1] However, when the sapphire substrate is etched deep enough, mode TE_2 reappears as a pseudo-guided mode, with an effective index between that of bulk sapphire and etched sapphire.

As can be seen, for small depths the extraction efficiency increases with the mode number. If we set a minimal threshold for sufficient extraction at $k'' = 10^{-2}$, only 2 out of 5 modes are extracted for a grating of depth a (or a depth of $\sim$ 200nm in real units). As the grating is etched deeper, the extraction efficiency of low-order modes increases while the highest-order modes are cutoff because the effective thickness of the GaN waveguide decreases. As seen in Chapter 3, the extraction efficiency can be simply linked to the thickness of the un-etched GaN layer, $t = 4a - d$, by:

$$k'' \sim t^{-3} \tag{4.1}$$

This is true apart from some oscillatory behavior, and as long as the waveguide is multimode. This tells us that the relevant parameter to estimate extraction efficiency is not the grating depth d but rather the un-etched GaN core thickness t. This relation also proves that, no matter what etch depth we use, the number of modes above a given extraction threshold is roughly constant, while the total number of supported modes decreases.

This is clearly apparent on Fig. 4.1: for the fundamental mode to be above the cutoff chosen earlier, one has to etch to a depth $d = 3a$, leaving an un-etched thickness $t = a$. At such a depth, only 2 modes are supported in the structure: thus, we recover the anticipated result that the un-etched GaN region should be nearly monomode for efficient extraction of the fundamental guided mode.

Unfortunately, this strategy also presents serious drawbacks. First, actual deep-etching of GaN is quite challenging. While the above calculation is simplified, it can be generalized to a realistic structure of thickness $15a$ ($\sim 3\mu$m) with a 2D PhC of filling factor $f = 0.35$. The extraction efficiency for the TE_1 mode in this structure is shown on Fig. 4.2: even if a modest extraction cutoff of $k'' = 10^{-3}$ is chosen (corresponding to an extraction length of $\sim 100\mu$m), the necessary etch depth is $13.5a$ or 2.7μm. This is by far impossible with the present state of the art in etching techniques. The deepest GaN PhCs reported so far in literature are 450 nm deep, using a multilayer hard mask (Ref. [1]).

Moreover, if one considers a structure where light is generated outside the etched region and transferred to the PhC region, one has to wonder about the coupling efficiency of the incoming guided

---

[1] This is simply due to the fact that the average index in the etched GaN layer is ~ 1.9, *higher* than the index of the sapphire substrate, 1.7. Therefore, the etched layer still acts as a waveguide for the fundamental modes.

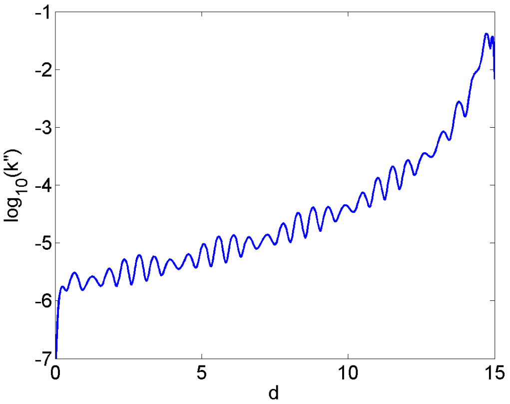

Figure 4.2: Extraction efficiency of the TE_0 mode of a realistic GaN waveguide of thickness $15a$ etched by a 2D PhC of filling factor 0.35 with varying PhC depth. The extraction efficiency starts at a lower value than previously because the waveguide is thicker. It reaches the same peak value close to $t = 0$.

modes to Bloch modes as their profiles can differ significantly. This can lead to insertion loss at the interface between the bare and etched region, where the guided mode can be strongly scattered.

An approximate treatment of this interface loss was proposed in Ref. [2] in which the overlap integral of the guided and Bloch modes intervenes. Let us introduce the set of guided modes of the unetched waveguide $\mathbf{E}_g^p$, $p = 1, 2...$ Moreover, to each actual Bloch mode $\mathbf{E}_B^p$ $(p = 1, 2...)$ of the PhC, we associate the *Forward-propagating half Bloch mode* $\mathbf{E}_F^p$ which is the sum of the Fourier harmonics of $\mathbf{E}_B^p$ propagating in the forward direction:

$$\mathbf{E}_B^p = \sum_G \mathbf{E}_G e^{i(k_{//}+G)x} \quad \rightarrow \quad \mathbf{E}_F^p = \sum_{G,k_{//}+G>0} \mathbf{E}_G e^{i(k_{//}+G)x} \tag{4.2}$$

Following Ref. [2], we now describe the transmission from a guided mode $\mathbf{E}_g^p$ to a Bloch mode $\mathbf{E}_B^{p'}$ as resulting from a double scattering process:[2] first, $\mathbf{E}_g^p$ excites the forward-propagating component $\mathbf{E}_F^{p'}$ of the Bloch mode with an efficiency $\eta_{p,p'}$, which in turns generates the backwards-propagating harmonics of the total Bloch mode along its propagation, with efficiency 1. Therefore, the coupling efficiency we are looking for is simply $\eta_{p,p'}$, which is given by the projection[3] of $\mathbf{E}_F^{p'}$ on $\mathbf{E}_g^p$:

$$\eta_{p,p'} = \frac{Re\left\{\left(\iint dydz(\mathbf{E}_g^p \times \mathbf{H}_F^{p'*}) \cdot \mathbf{u}_x \iint dydz(\mathbf{E}_F^p \times \mathbf{H}_g^{p'*}) \cdot \mathbf{u}_x\right) / \left(\iint dydz(\mathbf{E}_F^p \times \mathbf{H}_F^{p'*}) \cdot \mathbf{u}_x\right)\right\}}{Re\left\{\iint dydz(\mathbf{E}_g^p \times \mathbf{H}_g^{p'*}) \cdot \mathbf{u}_x\right\}} \tag{4.3}$$

In this formula, integrations are performed over the whole yz plane, $\mathbf{u}_x$ is the unitary vector along the propagation direction x, and Re indicates the real part.

To my knowledge, the domain of validity of this formula, which comes from the classic theory of waveguides,[3] is currently not fully assessed. Lalanne checked that its results are consistent with an exact electromagnetic calculation for reflexion of guided modes in the gap of a 1D grating. More

---

[2] In Ref. [2], a series of three successive scatterings is considered because the Bloch mode is in a gap and the authors look for the efficiency of the reflection process. We are only interested in the forward coupling.

[3] The set of guided modes is complete if the evanescent modes are included. Therefore, any half-Bloch mode mode can be projected on their basis. Here, we only conserve projection on guided mode p.

generally, it has been argued recently (Refs. [4, 5]) that it was valid for 1D gratings at normal incidence, while interface coupling with 2D PhCs needs a more complicated treatment. Therefore, we shall apply it to the 1D grating of thickness $4a$ studied above (Fig. 4.1).

Fig. 4.3 depicts the coupling efficiency of the TE guided modes of the unetched waveguide into the etched region. For each guided mode, we use the expression of Eq. 4.3, but here we take into account coupling to all the Bloch modes supported in the etched region. Therefore, Eq. 4.3 is computed for all the Bloch modes ($p' = 1, 2...$) and then summed over p' to yield the total coupling efficiency of a guided mode in the etched region.

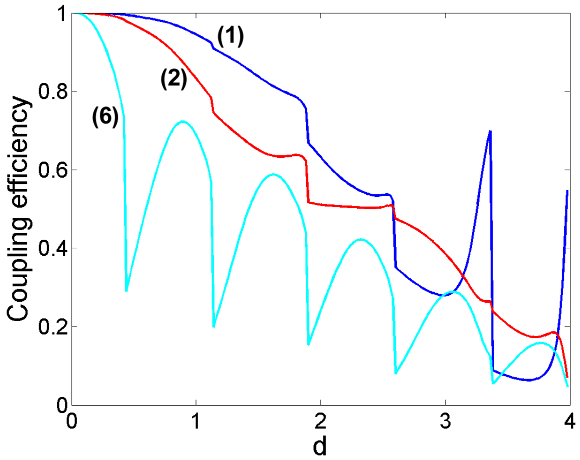

Figure 4.3: Coupling efficiency of the guided modes in the etched region for varying PhC depth and $f = 0.5$. For clarity, only modes 1, 2 and 6 are depicted here (all other modes follow the same behavior).

As expected, the coupling efficiency collapses when the etch depth increases. For higher-order modes (such as mode TE_6) shallower etches are sufficient to prevent good coupling. The discontinuities in the coupling efficiency are due to the cutoff of Bloch modes.

Somehow unexpectedly, the coupling does not decrease monotonously – see for instance the sharp increase for coupling of the fundamental guided mode when $d \rightarrow 4$. Indeed, as shown on Fig. 4.4, when $d = 3.5$ the PhC region only supports one Bloch mode which is still mostly localized in the unetched GaN region: its profile is very different from that of the incoming fundamental mode, leading to strong coupling losses. For $d = 4$, the Bloch mode can no longer be localized in the unetched region, and has to leak in the PhC region. Its profile returns to that of the fundamental guided mode, and coupling is enhanced. The same phenomenon accounts for the sawtooth-shaped coupling efficiency of the 6^{th} guided mode: the efficiency rises each time a Bloch mode leaks in the PhC region, and then suddenly collapses when this same Bloch mode is cutoff.

This difficulty in coupling light in the PhC reflects the fact that, as the etch depth increases, the PhC carries fewer Bloch modes. In mathematical terms, the set of Bloch mode then constitutes a poor basis for projection of the guided modes.[4] Of course, what happens exactly to the uncoupled fraction of each mode is unclear: it may be diffracted out-of-plane, either in the substrate or in the air. However, the lack of insight on this diffraction phenomenon is not encouraging for a deterministic approach of light extraction. Moreover, Finite Difference Time Domain calculations found in literature indicate that the loss is preferentially directed toward the substrate.[6]

---

[4] In other words, it is not possible to build a bijection between two bases of different sizes. In our case, the basis of guided modes is always larger than the basis of Bloch modes, whose cardinal decreases with etch depth. Of course, this is due to the fact that all evanescent and non-guided modes have been removed from the basis.

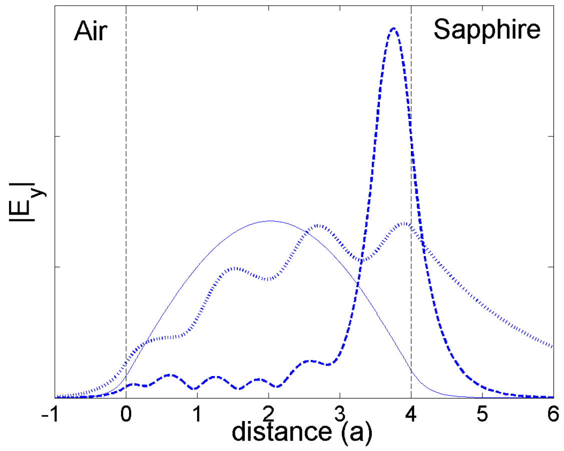

Figure 4.4: Profile of the fundamental harmonic ($\mathbf{G} = 0$) of the y component of the electric field E_y across the structure. The vertical lines are the boundary of the air and substrate regions. (Full) guided mode in the unetched waveguide. (Dashed) Bloch mode for an etch depth of $3.5a$ (Dotted) Bloch mode for an etch depth of $4a$

Let us note that FDTD calculations carried out in Ref. [1] on a deep-etched GaN structure lead to similar conclusions regarding coupling efficiency: Chen *et al.* observe that light transmission through a few rows of a deep PhC is very poor (in the absence of a band gap). While they do not discuss in detail the origins for this poor transmission (light extraction versus bad coupling for instance), their results are compatible with the present ones.

Finally, it can be argued that the high filling factor chosen here ($f = 0.5$) is especially detrimental to coupling since the deep-etched grating only carries one Bloch mode. To check this, we now consider the same grating but with a filling factor of 0.3 only. In this case, the fully etched structure still supports 4 Bloch modes. Indeed, the coupling loss (Fig. 4.5) is clearly reduced. The fundamental mode has good coupling regardless of the etch depth. Modes 2, 3 and 4 (not shown) have similar behavior and a coupling efficiency above 80% at all depths. On the other hand, modes 5 and 6 are still poorly coupled in the case of deep etching.

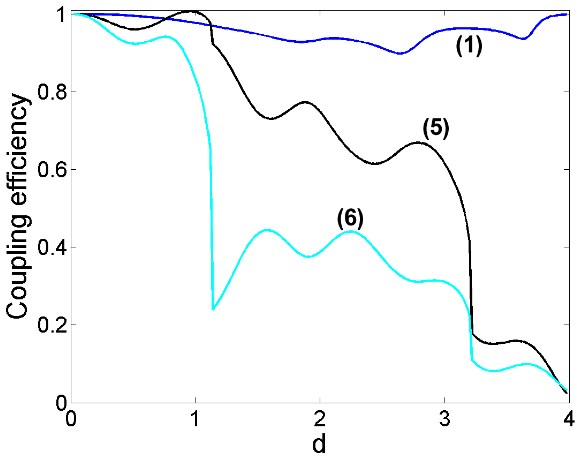

Figure 4.5: Coupling efficiency of the guided modes in the etched region for varying PhC depth and $f = 0.3$. Modes 1, 5 and 6 are depicted here.

This result is inevitable, as the etched region necessarily supports less modes than the original waveguide. From basic mode-counting arguments, we can argue that the coupling efficiency averaged over all modes is roughly the ratio of the number of Bloch modes to the number of guided modes.

Incidentally, Fig. 4.1 gives us another important indication: even if we retain a reasonable depth ($d \sim a$) and accept to extract only some of the modes (the excited modes), it is always preferable to reduce the core thickness t to enhance the extraction efficiency of these modes. Unfortunately, t can not be made arbitrarily low in practice, because of dislocations in GaN close to the sapphire interface. A value $t \sim 1.5 - 2\mu$m seems an acceptable tradeoff between growth requirements and optical properties.

From this discussion, we conclude that deep-etching of GaN is at best a challenging option. Feasibility of deep-etched (several μm) PhCs is currently unclear. Insertion losses prevent light from coupling into the PhC. Therefore, we are led to retain shallow PhCs where only excited modes are well extracted. Even for these, the core thickness t should be kept as small as possible. In the following, we consider alternative strategies to efficiently extract all of the guided modes.

We should note however that the previous discussion leaves aside the case where light is generated *inside* the patterned region. Conventional wisdom of semiconductors suggests that luminescence properties should be strongly degraded in this case, due to the numerous non-radiative recombinations which can take place at the surface of the PhC holes. We postpone this discussion to section 4.5.

4.1.2 Modification of the epitaxial layers: the Cap Layer Mode

Rather than questioning the geometry of the PhC extractor itself as above, a possible approach consists in modifying the way light is emitted in order to get rid of low-order modes. In general, modification of the spontaneous emission of the QWs can be obtained by modifying their optical environment. The simplest way to do this is to modify the epitaxial layers in order to provide refractive index contrast. Indium or aluminum can be incorporated to GaN in order, respectively, to increase or decrease the refractive index. Since InGaN possesses a smaller band gap than GaN, it absorbs more in the visible region and should ideally be avoided (especially since light tends to be localized in high index materials). AlGaN, on the other hand, is transparent in the visible and possesses a lower index than GaN. It can thus be used as an optical barrier. Therefore, we introduce a structure where an AlGaN layer is grown between the GaN buffer and the pn junction:

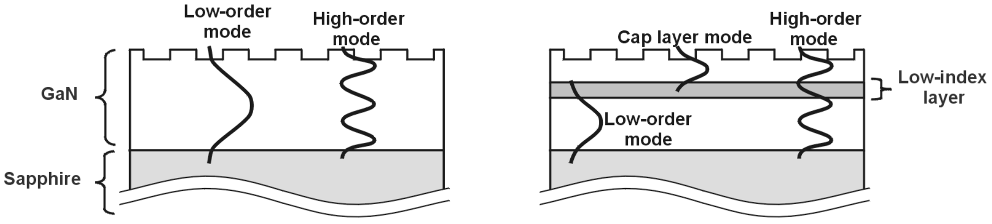

Figure 4.6: Guided modes distribution in a conventional GaN LED (left) and in an LED with a low-index layer (right). In the conventional LED, only low-order and high-order modes are present. In the modified structure, the optical barrier repels the low-order modes in the GaN buffer, and enables a mode to be guided in the thin cap layer.

The distribution of guided modes in the new structure, shown on Fig. 4.6, can be inferred from an analogy with a system of coupled quantum wells (Fig. 4.7). The shallow AlGaN barrier only acts on low-order modes with $n_{eff} < n_{AlGaN}$. It repels these modes below the AlGaN layer. On the other hand, high-order modes barely feel this barrier and are not affected by its presence. Finally, if the thickness of the *pn* junction on top of the AlGaN barrier (or "cap layer") is sufficient, a guided mode can be localized in this thin effective waveguide. For good localization, the AlGaN barrier should be thick enough for this "cap layer mode" (CLM) to be isolated from the GaN buffer.

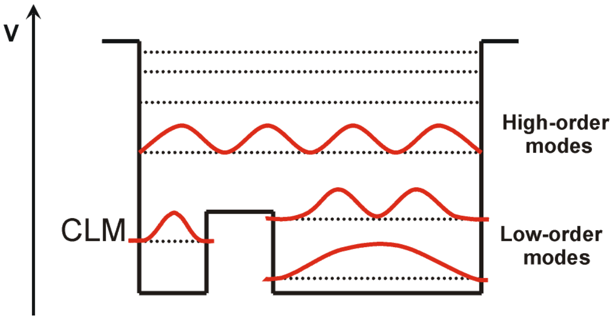

Figure 4.7: Analogy between the modified epitaxial structure and a system of coupled quantum wells. The AlGaN layer acts as a shallow potential barrier which decouples the GaN buffer and the cap layer. The excited modes, on the other hand, are unaffected.

The expected effect of this CLM is twofold. First, because it is maximal at the QWs location, it should receive a large fraction of the emitted light – whereas low-order modes, localized on the other side of the AlGaN barrier, have little overlap with the QWs. Second, since this mode is pinched close to the surface, its penetration into the PhC should be higher and its extraction efficiency better.

As will now be shown, these two qualitative arguments are well substantiated by modeling.

Light emission in the CLM

Here, we consider the case where current injection is separated from the PhC region. In order to estimate quantitatively light emission into the CLM, we once again resort to calculations of dipole emission in a planar structure, based on the transfer matrix approach.[7] Fig. 4.8 presents the fraction of total dipole emission which goes to the cap layer mode, when the thickness of the cap layer and the position of the quantum well is varied. This calculation assumes a 1μm thick low-index layer of index 2.4 (versus 2.5 for GaN), which is rather optimistic. In large areas of the plot, the emission in the CLM is above 25 %. These zones are rather broad, which means that several quantum wells can be used around a given position – this is of importance since multi-quantum well structures usually give much better internal quantum efficiency than single quantum wells. Note that, when the GaN is thinner than 120 nm, no mode is supported in the cap layer: the emission into the CLM then drops to zero. Likewise, above 420 nm, two CLMs are supported, yielding two maxima of the plot.

We now consider a specific spot of Fig. 4.8, with a 300 nm thick cap layer and a quantum well placed in its middle. This cap layer thickness is sufficient to grow a good quality *pn* junction (this is mainly limited by the growth of *p*-GaN, which must usually be at least 100 nm thick to obtain acceptable Si doping). Fig. 4.9 compares the emission diagrams of this structure with that of a simple 3μm thick GaN structure, in TE polarization.[5]

In the presence of the AlGaN layer, nearly *all the light* emitted at $n_{eff} < n_{AlGaN}$ is channeled in the CLM, as evidenced by the presence of only one emission peak for this range of angles. This is not surprising, since the coupling between a dipole and a mode is of the form $\mathbf{d} \cdot \mathbf{E}$, where $\mathbf{d}$ is the dipole moment and $\mathbf{E}$ the electric field of the mode at the dipole location. The low-order modes are

---

[5] We only present the case of TE polarization because most of the guided light is TE-polarized. The TM emission, corresponding to dipoles oriented perpendicular to the emission plane, has a $cos(\theta)^2$ dependence and vanishes at angles corresponding to low-order modes.

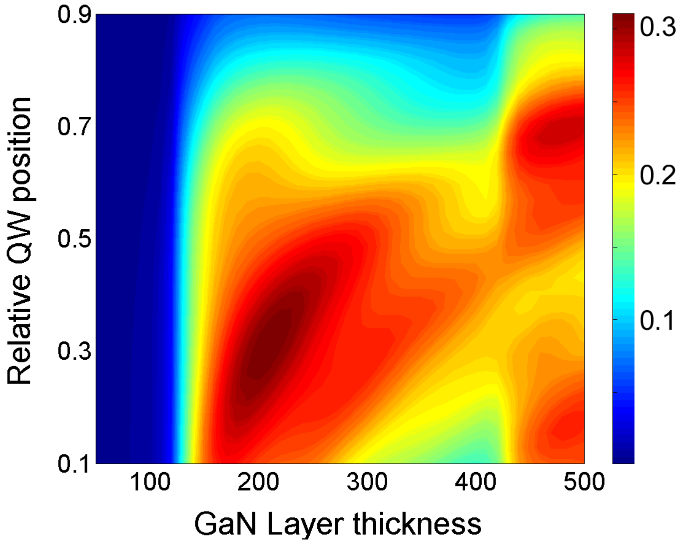

Figure 4.8: Fraction of the total emission channeled in the cap layer mode, for an epitaxial structure with a 1μm thick layer of index 2.4. The 'relative QW position' refers to the position of the quantum well inside the cap layer (0 corresponding to the low-index layer and 1 to air).

evanescent in the AlGaN layer, and therefore very weak at the QW. On the other hand, the CLM is maximal in the region of the QW. Finally, high-order modes are unaffected by the AlGaN layer and they receive as much light as in the original GaN structure.

Obviously, the refractive index of the AlGaN layer sets the maximum n_{eff} which can be guided in the cap layer. Here, we only considered $n_{AlGaN} = 2.4$ (or more generally $n_{AlGaN} = n_{GaN} - 0.1$) which is a reasonable value (see below). Ideally, an index contrast of 0.2 or 0.3 would even further quench light emission in low-order modes.

Extraction efficiency of the CLM

We now turn to the interaction between the CLM and the PhC. First, we consider an epitaxial structure with a 1μm thick GaN buffer, a 1μm thick layer of index 2.4 with a 300 nm thick cap layer, with varying PhC depth d. This structure is somehow optimistic (especially, the GaN buffer layer is rather thin) but still reasonable. Fig. 4.10 displays the extraction efficiency of the CLM and two excited modes in the ΓM direction, as a function of the depth d of the PhC of filling factor 0.3 and lattice constant $a = 200$ nm.

As can be seen, for values of $d \sim 0.7a$ the CLM has an imaginary wavevector of more than 10^{-3}, which translates into an extraction length smaller than 100 μm. This length is acceptable for an LED. When the PhC is etched deeper, the extraction length of the CLM collapses because it leaks outside of the cap layer – this is also visible on the effective index of the CLM, which decreases below the value of the AlGaN barrier. As regards excited modes, the extraction efficiency depends on the mode considered: modes of lower n_{eff} penetrate more in the PhC and their extraction is better. The two excited modes presented on Fig. 4.10 respectively correspond to $n_{eff} = 2.25$ and $n_{eff} = 2$ (when no PhC is etched). The former has a modest extraction rate (10^{-3} at best), but overall the extraction length of excited modes is acceptable. Low-order modes (not shown on the figure) now have a vanishing extraction efficiency, as could be expected.

We now consider a slightly more optimistic structure with a 1.4μm thick GaN buffer, a 600 nm thick layer of index 2.3 with a 400 nm thick cap layer. The total thickness is equivalent to that of the

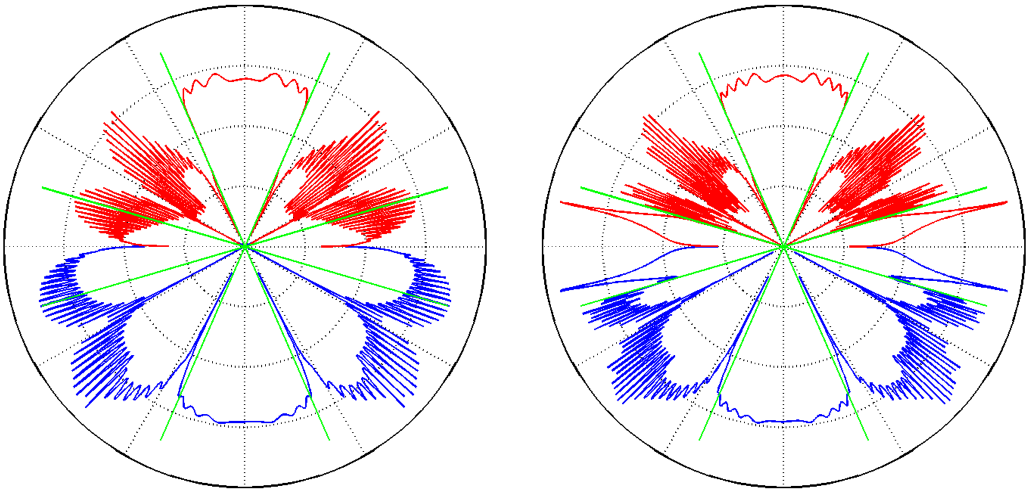

Figure 4.9: Emission diagram of a quantum well without (left) and with (right) a low-index layer (TE polarization, log scale). The (green) radial lines indicate the angles corresponding to $n_{eff} = 1$ and $n_{eff} = 2.4$, respectively. In the presence of the low-index layer, the multiple peaks corresponding to the low-order modes are replaced by only one strong peak which corresponds to emission in the CLM.

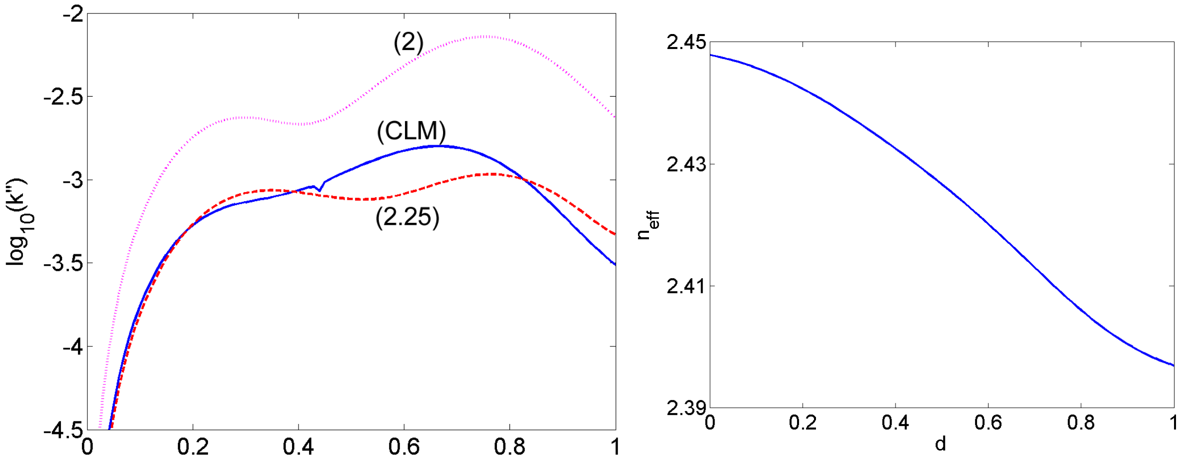

Figure 4.10: (Left) Extraction efficiency (in the ΓM direction) of the CLM (full line), an excited mode of $n_{eff} = 2.25$ (dashed line) and an excited mode of $n_{eff} = 2$ (dotted line) with an AlGaN layer of thickness 1μm and index 2.4. The small dip in the CLM's curve at $d \sim 0.4$ is due to resonant coupling with a low-order mode. (Right) Effective index of the CLM. When $n_{CLM} < 2.4$ the CLM is no longer guided in the cap layer.

previous structure, but the index of the AlGaN layer is lower. Its thickness is also decreased in order to account for the difficulty to grow AlGaN layers with high Al content. The extraction efficiency for the same modes as above is shown on Fig. 4.11.

The conclusions are only slightly different. The CLM is more efficiently confined by the AlGaN barrier and therefore reaches higher extraction efficiencies before being cutoff. As could be expected, the effect on the excited modes with $n_{eff} = 2$ is small. The other excited mode is more affected because its effective index is close to that of the AlGaN layer. Even lower AlGaN indices would further enhance the CLM's extraction and would prevent some excited modes from receiving emitted light.

It should be noted that this whole discussion concerns the ΓM direction. Similar conclusions hold

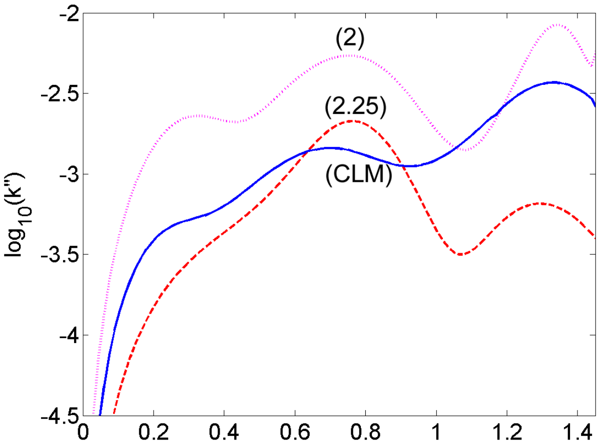

Figure 4.11: Same as Fig. 4.10 but with an AlGaN layer of thickness 600 nm and index 2.3.

in other directions, *as long as extraction to air is possible.* For instance, this is not the case in the ΓK direction at the second Bragg order, where there is no diffraction to air. The choice of the crystal lattice will be addressed in section 4.2. The current study only concerns *vertical* design of the structure.

We conclude that in an optimized structure, the CLM can receive all the light otherwise emitted in the low-order modes. In such a structure, the extraction efficiency of all excited modes is sufficient ($\sim 10^{-3}a^{-1}$), so that all of the guided light can be efficiently extracted over a reasonable length – at least in crystal directions where there is a diffraction channel to air.

4.1.3 Tailoring of guided modes distribution: implementation in LEDs

A sketch of the target LED structure is depicted on Fig. 4.12

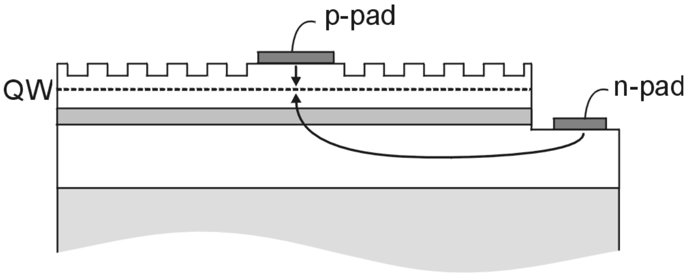

Figure 4.12: GaN-on-sapphire PhC LEDs incorporating a low-index layer. Here, the light generation region is distinct from the PhC extractor. The arrows indicate carriers flow, with current spreading in n-GaN.

The main difficulty for practical implementation of such LEDs lies in the growth of the desired structure. Due to the lattice mismatch between GaN and $\mathrm{Al}_x\mathrm{Ga}_{1-x}\mathrm{N}$, GaN grown on top of $\mathrm{Al}_x\mathrm{Ga}_{1-x}\mathrm{N}$ can be heavily cracked. The dislocations increase for higher Al content and thicker $\mathrm{Al}_x\mathrm{Ga}_{1-x}\mathrm{N}$ layers, thus limiting the strength of the optical barrier. In practice, x certainly has to be smaller than 25%, and even at that content, cracking is usually heavy. Fig. 4.13 displays the surface of a regular LED processed on a structure with a 500-nm thick $\mathrm{Al}_{20}\mathrm{Ga}_{80}\mathrm{N}$ layer. The numerous cracks prevent uniform current injection by damaging the contacts, decrease the internal quantum efficiency by introducing non-radiative recombination surfaces, and diffract the light guided in the CLM.

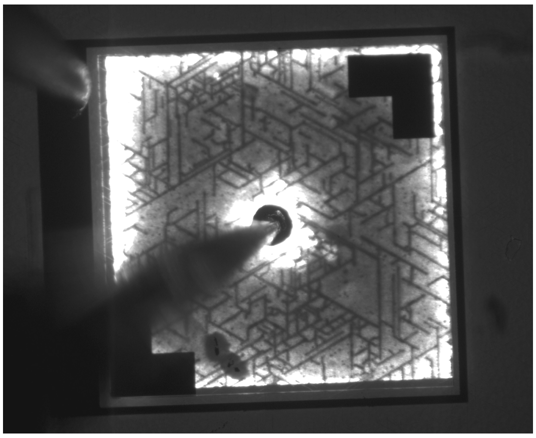

Figure 4.13: Optical microscope picture of a regular LED on a cracked epitaxial layer, with slight current injection. All the surface of the LED mesa is covered by a semi-transparent Ni/Au contact, but the cracks prevent uniform current spreading.

So far, optimization of the growth parameters in order to obtain the best optical barrier while avoiding cracking have not been established, despite efforts by Rajat Sharma and Mike Iza. It should be noted that the AlGaN layer used in these PhC-LEDs is very close to the cladding layers used for mode confinement in GaN lasers. These layers are well-known for being difficult to grow but good claddings have already been demonstrated, at least in an industrial environment.

Estimating the refractive index as a function of the Al content is not easy since literature on the subject is scarce. A simple model is proposed in [8]. In this model, valid for low Al contents, it is assumed that the dispersion of AlGaN follows that of GaN with a rigid shift given by the band gap difference between GaN and AlGaN. The index shift as a function of Al content is shown on Fig. 4.14.

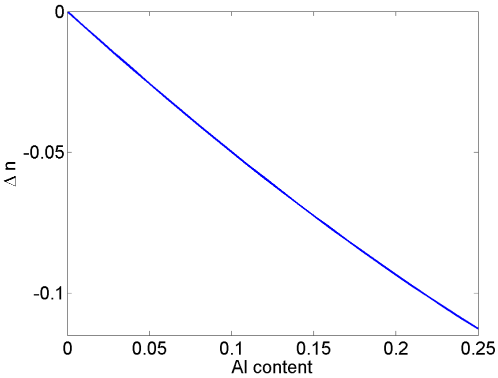

Figure 4.14: Refractive index contrast with respect to GaN as a function of Al content.

This yields an index contrast of only 0.1 for 20% Al. This value is conservative, as other sources in the literature suggest an index contrast of 0.15 for the same Al content. Anyway, this curve can be taken as an estimate of the index contrast and shows that it can only be modest.

The LEDs presented in the following correspond to a structure grown by Rajat Sharma. After a 3 μm thick GaN buffer layer, a 800 nm thick AlGaN layer was grown with an Al fraction of $\sim 12\%$, followed by a 600 nm thick *pn* junction with a multi-quantum well region at its center. From the above, the index contrast for this Al content is at least 0.07 (i.e. $n_{AlGaN} = n_{GaN} - 0.07$), but the experimental results shown below are compatible with a slightly higher index contrast. In any case, considering the thickness of the layer, this is sufficient to confine efficiently a cap layer mode. The wafers displayed limited cracking, but were very inhomogeneous in terms of emission wavelength and internal quantum efficiency.

Regular LEDs were processed from this wafer. Integration of PhCs to the process of regular LEDs causes no difficulty. One simply has to align the optical lithography mask to the PhC region. The main steps of the process are depicted in table 4.1.3.

Photonic crystal formation		
p-contact evaporation	Transparent electrode deposition	Ebeam 3
Mesa formation	Resist coating	Bake
		AZ 4210 spin
		Pre bake
	Exposure	
	Develop	AZ400K : DI 1:4
		Hard bake
	Transparent electrode etching	Gold etchant
	Dry etch	RIE5
	PR removal	Acetone+Iso
n-contact	Resist coating	Bake
		HMDS spin
		AZ 5214 spin
		Pre bake
	Exposure	
	PR reversing	Bake
		Flood expose
	Develop	MF701
	n contact deposition	Ebeam 3
	Liftoff	Acetone+Iso
p-pad	Resist coating	Bake
		HMDS spin
		AZ 5214 spin
		Pre bake
	Exposure	
	PR reversing	Bake
		Flood expose
	Develop	MF701
	Descum	Asher
	n contact deposition	Ebeam 3
	Liftoff	Acetone+Iso

LEDs with lattice constants $a = 190$, 200 and 215 nm were fabricated. Fig. 4.15 shows images of the fabricated LEDs.

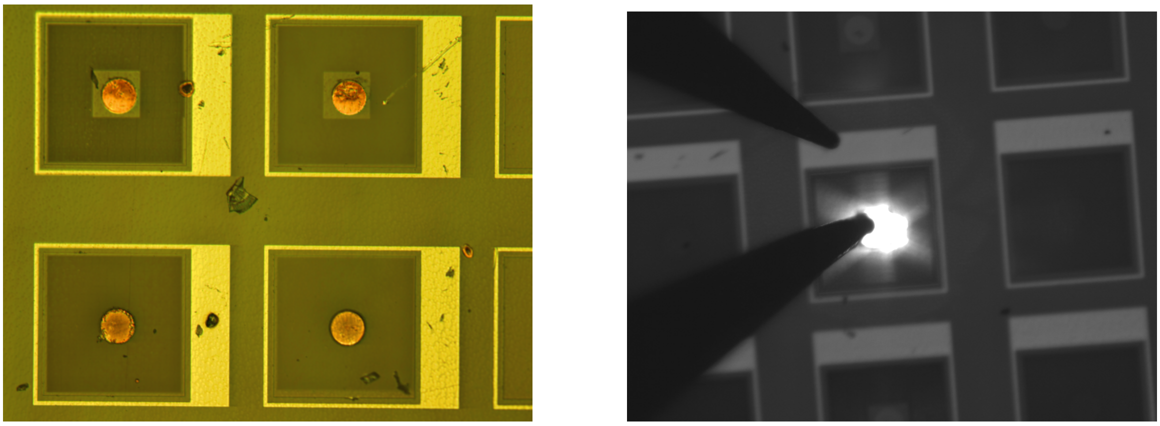

Figure 4.15: Microscope pictures of PhC-LEDs. The area of the mesas is 300 μm x 300 μm , and the p-contact is circular with diameter 100 μm. (Left) Under exterior illumination. The dark regions correspond to the PhCs. (Right) Under current injection. Light is only generated under to opaque p-contact. Light extraction is clearly visible along the six ΓM directions.

The fabricated LEDs were characterized by angle-resolved electroluminescence. Fig. 4.16 shows angular spectra of LEDs in various polarizations and along various directions.

Fig. 4.17 shows the corresponding band structures – in this case however, the direct emission from the quantum well is superimposed on the photonic bands because it can not be easily isolated. As has already been pointed out in photoluminescence spectra (Chapter 3, section 3.3), although guided modes propagating along ΓK are not extracted, part of the diffracted light is collected along ΓK. Actually, this corresponds to a significant part of the light extraction on these spectra (notice the very strong lines in TM polarization).

When these band structures are compared with those of photoluminescence samples, one recognizes the numerous bands corresponding to high-order modes. As the current wafer is overall thicker (4 μm) than the PL samples, it supports more high-order modes which are now close to a continuum. In addition to these modes, a new, intense set of lines appears. This set stems from the CLM. Its intensity manifests the macroscopic fraction of the total emission it carries.

In order to check that this set of lines is indeed associated with the CLM, and to further analyze the spectra, we now superimpose several theoretical dispersion lines on one of these band structures (Fig. 4.18). For the AlGaN layer, we assume an approximate index contrast of 0.1 with GaN. The CLM can very well be fitted using an effective index $n_{eff} = n_{GaN} - 0.045$, between the indexes of GaN and AlGaN,[6] whereas all the high-order modes are on the other side of the AlGaN line. Moreover, the bands corresponding to the CLM vanish for frequencies above $u = 0.52$, whereas excited modes can still be seen –although faintly– until $u = 0.53$. This suggests that absorption is stronger for the CLM than for other modes, which is consistent with the fact that it has a much larger modal overlap with the multi-quantum well region. Finally, a cutoff of the guided modes is clearly observed above the sapphire line $n = 1.7$.[7] This confirms that, when light can propagate in the sapphire substrate, its extraction efficiency by the grating is very poor: since the PhC is only ~100 μm wide around the light generation region, the substrate light is not extracted. In contrast, samples with a PhC area of 1cm^2

---

[6] As for photoluminescence spectra, the dispersion of the GaN index has to be taken into account for a proper fit.

[7] Some photonic bands are still present beyond the sapphire line. However, these are of type 'B' in the nomenclature of Chapter 3. In other words, they correspond to a folding in the first Brillouin zone which is not collinear with $k_{//}$: their main harmonic is actually below the sapphire line.

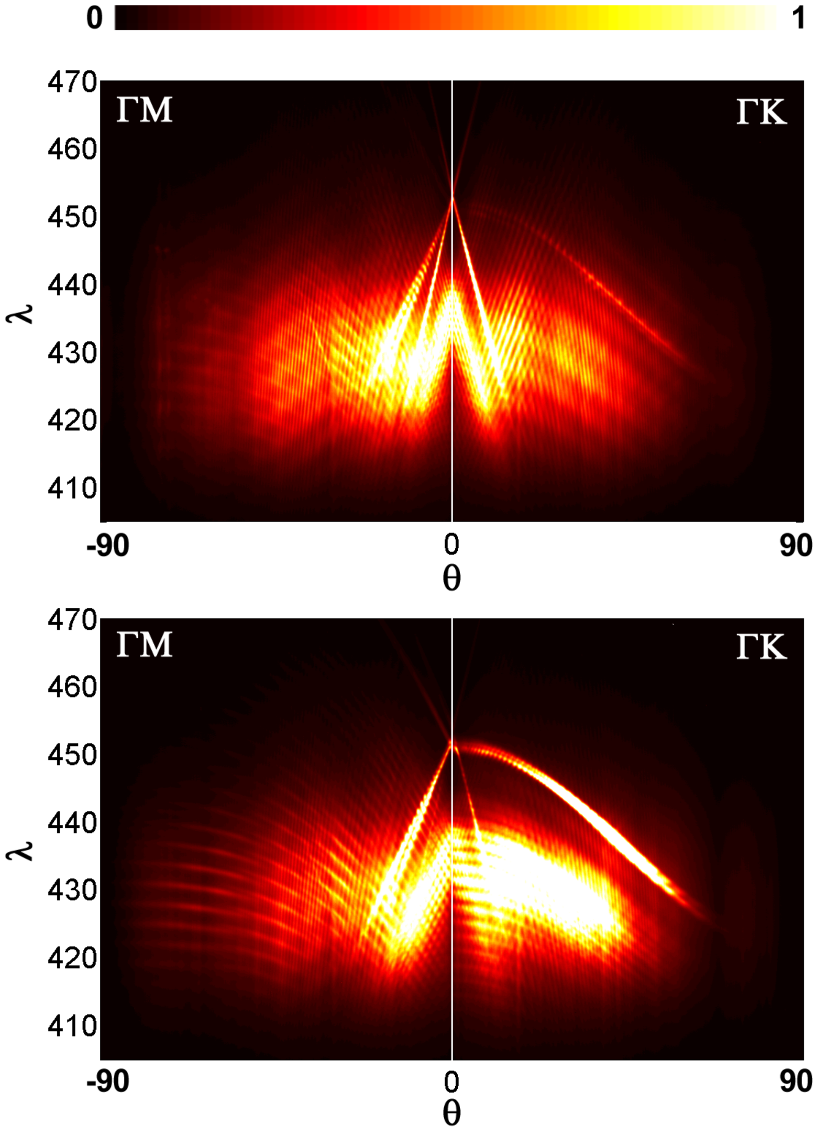

Figure 4.16: Angular spectra collected on PhC-LEDs incorporating an AlGaN layer, with $a = 215nm$ (top: TE polarization, bottom: TM polarization). The effect of the AlGaN layer can already be seen on the raw angular spectra, where new intense lines appear.

have recently been fabricated by nano-imprint at UCSB by Frederic Diana. When photoluminescence is performed on such samples, the sapphire cutoff is not observed because the PhC is large enough to extract substrate light.

We now come to the light extraction enhancement brought by the PhC. This can be measured by two methods. The first is a direct measurement of the total output power of the LED: for identical injection, the light extraction enhancement is just the ratio of the power of a PhC-LED by that of a regular LED. The strength of this measurement is that it is direct and in principle accurate. On the other hand, light is only collected within a given numerical aperture (NA $\sim$ 0.5 in the case of the Nakamura power measurement setup), so that the enhancement does not correspond to all directions.

The power measurements were performed on the LEDs with a semi-transparent p-contact (before the opaque p-contact shown on Fig. 4.15 was deposited). However, even with a semi-transparent p-

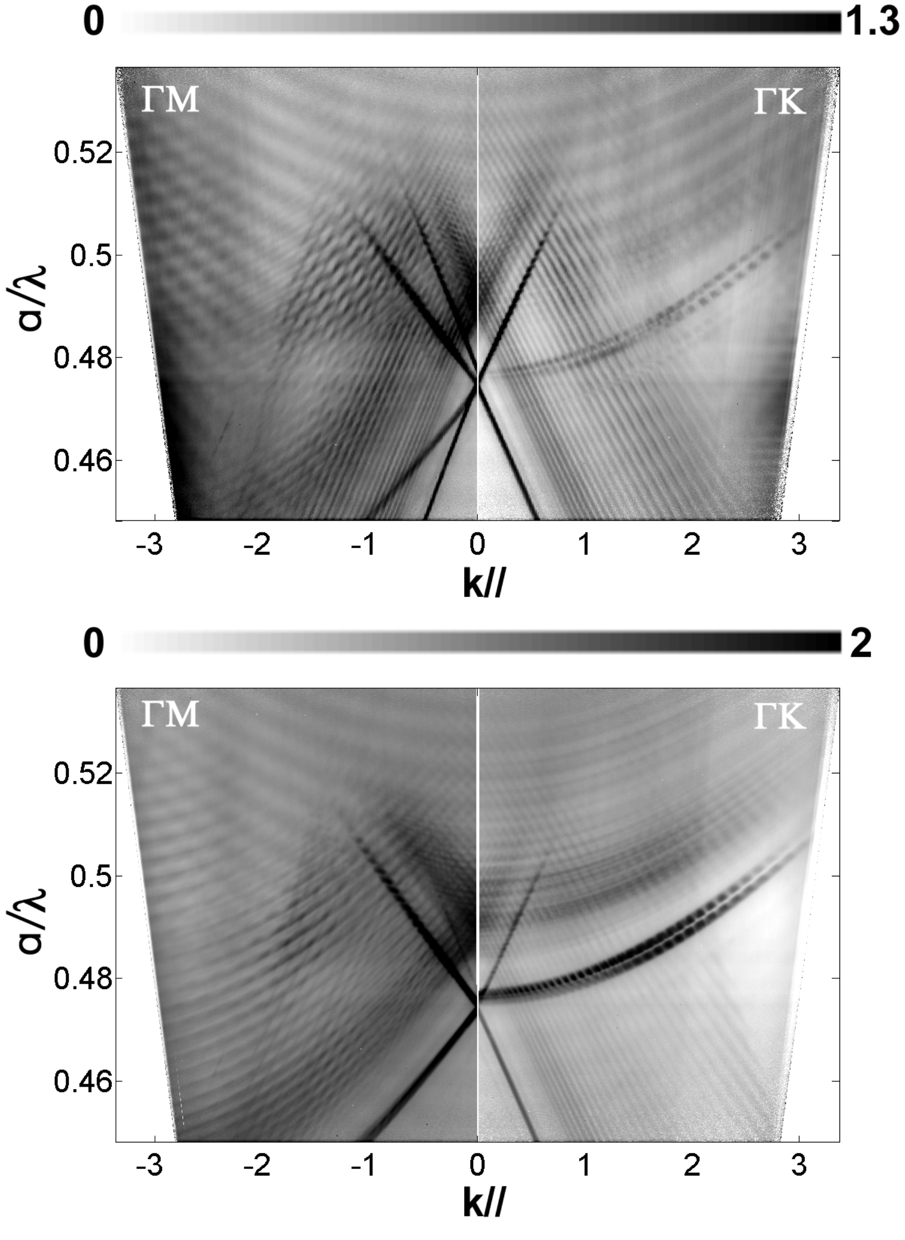

Figure 4.17: Band structures corresponding to the spectra of Fig. 4.16.

contact, the direct upwards emission from classic LEDs is limited by contact absorption. Therefore, in order to get a fair comparison, an Al mirror was also placed below the sample to redirect the light emitted downward. The comparison between a classic LED and a PhC LED with $a = 215$ nm is shown on Fig. 4.19. The inhomogeneity of the material limits the accuracy of this comparison: in some cases, the output power of two adjacent classic LEDs varies by as much as 10%.

The light extraction enhancement is rather modest: 70% at an injection current of 10 mA DC. This is clearly small compared to the amount of guided light available. However, several facors limit the efficiency of these LEDs. First, the epitaxial layers are not optimized (the index contrast is still rather low, and the quantum wells are not located at an optimal position for emission into the CLM). Moreover, the PhC region only extends over 100 μm around the p-contact. Since the extraction length

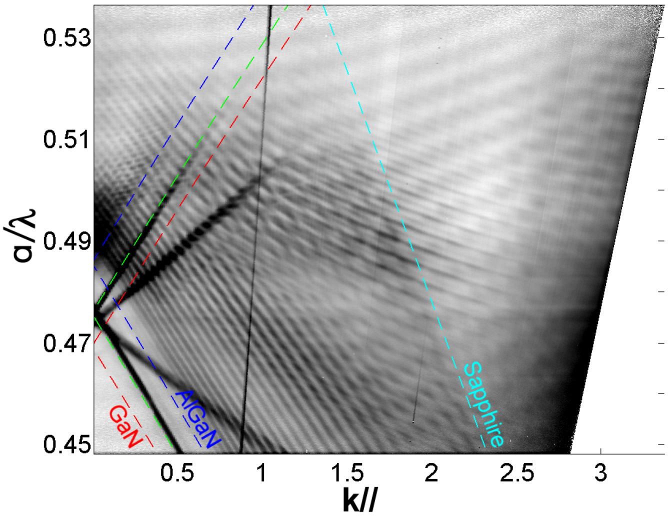

Figure 4.18: Band structure along ΓM in TE polarization with several dispersions superimposed as dashed lines. Red: GaN line (e.g. $\omega = k_{//}c/n_{GaN}$). Green: fit of the CLM with an effective index $n_{GaN} - 0.045$. Blue: approximate AlGaN line with index $n_{GaN} - 0.1$. Cyan: sapphire line, $n_{sapphire} = 1.7$.

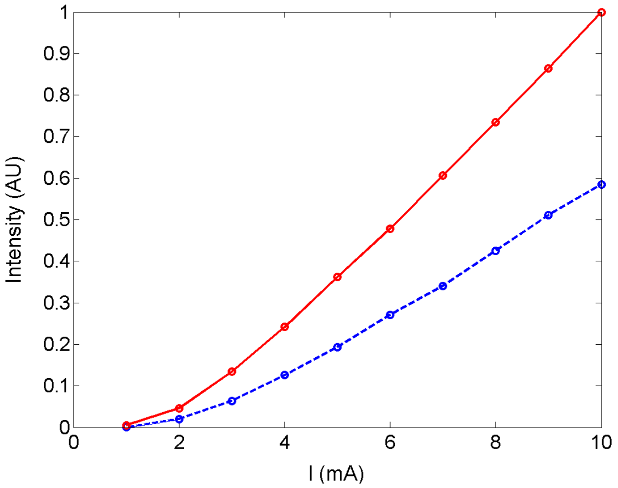

Figure 4.19: Power collected from two LEDs under electrical injection. Full: PhC LED. Dashed: conventional LED. Both LEDs are measured under the same conditions, whit a mirror under the sapphire substrate.

of most guided modes is 100 μm at best, they can not be fully extracted.

The second comparison method is an extrapolation using the angular spectra. We take advantage of the existence of a region of low frequency where the PhC does not emit light, and the collected signal is only due to direct emission (specifically, the triangle with $k_{//} \in [0; 0.5]$ and $a/\lambda \in [0.45; 0.47]$ in Fig. 4.18). The original angular spectra of a regular LED and a PhC LED can thus be normalized by a multiplying factor so that their emission is equal in this region.[8] The underlying assumption is that direct emission is not affected by the PhC's presence, which is reasonable for such perturbative PhCs – especially since light is emitted in an unpatterned region.

---

[8] This is somehow complicated by slight variations of thickness and emitting wavelength between LEDs. Besides, the presence of the PhC modifies the average reflectivity of the top surface and hence the contrast of the Fabry-Pérot fringes. However, this normalization can still fairly well be performed.

The extraction enhancement can then be estimated by integrating the normalized angular spectra (taking into account the proper solid angle factors). The advantage of this method is that one is not limited by a numerical aperture: all values of the polar angle θ are collected. On the other hand, only a few azimuthal angles φ are scanned and averaged (the ΓM and ΓK directions in our case) so that its accuracy is limited.

This procedure yields an extraction efficiency enhancement of 100 % for the same LED as above (and putting a mirror under the sapphire substrate, as previously). Both enhancements are of the same order of magnitude, and the discrepancy is acceptable considering the various error factors of each method.

4.1.4 Fine tuning of a and directionality

From Fig. 4.17, it is clear that the directionality of emission depends strongly of the reduced frequency $u = a/\lambda$. For instance, if $u = 0.45$ most photonic bands are around the middle of the Brillouin zone, so that diffraction occurs around 45^o in air, whereas if $u = 0.5$ the photonic bands are distributed around the Γ point and diffraction occurs closer to the vertical. Fig. 4.20 illustrates this ability at tuning the LED's directionality by slightly modifying the lattice constant.

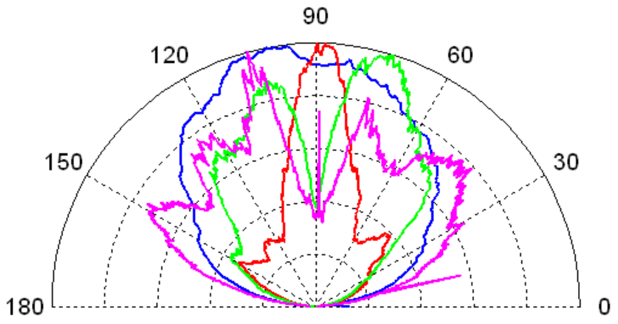

Figure 4.20: Normalized wavelength-integrated far-field patterns of PhCLEDs (summed over polarizations, and over the ΓM and ΓK directions). (Blue) regular LED without PhC: the pattern is nearly isotropic. (Magenta) $a = 190, u \sim 0.44$ (Green) $a = 200, u \sim 0.46$ (Red) $a = 215, u \sim 0.5$. This last LED emits mostly vertically.

4.1.5 Further exploration of the concept

Since this first proof of concept, several LED samples have been processed using the same principle, in order to observe higher extraction efficiencies. Unfortunately, no better result was observed. On most of the initial wafer, the internal quantum efficiency was very inhomogeneous, so that comparison between adjacent LEDs was impossible (in some cases, variations of output power by a factor of 10 was observed between similar, adjacent LEDs).

So far, the other processed wafers had either too little Al or too much cracking. It should be stressed that, since internal quantum efficiency strongly depends on injection current, LEDs can only safely be compared if their $p-$electrodes have the same area and similar properties. This is not the case for cracked wafers, where cracks affect the electrode quality.

In addition, I investigated the effect of p-injection. In the first LEDs, only the center region emits, and the external region extracts light. This makes processing easy but part of the guided light can be absorbed before reaching the PhC region, as observed in photoluminescence experiments (Chapter 3). Therefore, it is desirable to limit the distance between electrode and PhC. This is all the more the case with metallic electrodes: even the best reflective electrodes (Ag, Al) have reflectivities of 90% at best. This is acceptable for directly extracted light, which bounces on the mirror once at most before escaping the LED. Guided light, on the other hand, bounces on the waveguide walls several times before reaching the PhC region.

I first explored the possibility of forming a semi-transparent electrode on top of the patterned PhC region, in order to obtain uniform current injection in the PhC. Metal evaporation should be avoided once the PhC is formed because metal deposited at the bottom of the holes is likely to increase absorption. Another option consists in first depositing a large area semi-transparent *p*-contact, and forming the PhC on top of this contact. In practice, the usual 2-step dry etch process was used to form the PhC. The Cl_2 etch is likely to etch the thin metal layer (a few nm) without difficulty. However, the etch was actually found to etch the metal layer too well: in most cases, the semi-transparent electrode was completely etched away, even under the SiO_2 hard mask. The only exception was observed in the case of PhCs with a larger lattice constant of 215 nm, probably because a larger area was protected by SiO_2 in this case, limiting the effect of underetch. This result was only obtained once, and no conclusion could be drawn as concerns the beneficial role of injection in the PhC region.

As an alternative to this approach, I also designed a new LED mask where light absorption by the metallic $p-$contact is minimized. To this effect, the contact area should be limited to avoid complete absorption of the guided modes before it reaches the PhC. The mask shown on Fig. 4.21 uses a 20 μm wide grid electrode, where most of the guided light impinges only one or two times on the electrode.

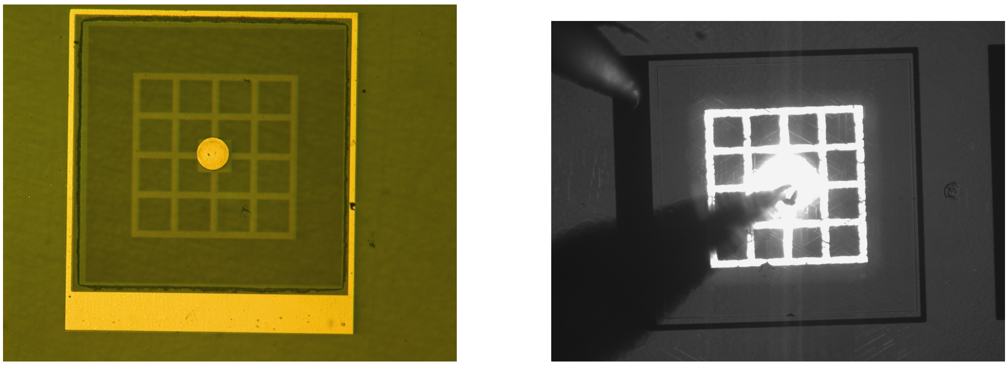

Figure 4.21: Microscope pictures of PhC-LEDs with a semitransparent grid *p*-electrode and an opaque central *p*-pad. The area of the mesas is 800 μm x 800 μm (Left) Under exterior illumination. The PhCs are formed everywhere around the grid electrode. (Right) Under current injection. Cracks are visible in the material.

Clearly, the question of efficient schemes for current injection in these LEDs remains open. The semi-transparent contact used in this work is far from optimal because light absorption is still quite strong. Possible alternatives would include the use of a tunnel junction, as demonstrated in Refs. [9, 10, 11], or use of a transparent contact such as ITO or ZnO.

4.1.6 Conclusion

By introducing layers of lower refractive index in the epitaxial structure, the distribution of guided modes can be modified. Light is only emitted in modes which interact well with the PhC in the vertical direction and can thus be extracted when diffraction to air is possible. This approach, well supported by modeling, is also confirmed experimentally by observation of the cap layer mode in band structures. The current extraction enhancement is limited to +70% – +100% in un-optimized structures. Fully exploiting this approach requires optimization of the epi layers and good current injection, which has proved challenging so far.

4.2 Crystal lattice, Archimedean tilings

In this part, we consider the question of the choice of the crystal lattice. As has already been mentioned, a 2D lattice is usually preferred over a 1D grating because it offers more directions for light extraction (Fig. 4.22). In general, the figures of merit for a crystal lattice are :

- Omnidirectionality (in inner space)
- Extraction length
- Directionality (in outer space)

Ideally, a good PhC extractor should be omnidirectional, e.g. it should extract guided light incoming from any azimuthal angle in the GaN layer. Intuitively, one may think that the lattice with most diffraction directions is the best: for instance, a triangular lattice should extract more light than a square lattice. However, as will now be seen, a reasonable choice of the crystal lattice can only be made by considering diffraction losses in the substrate, which sometimes leads to counter-intuitive results.

Moreover, the extractor should be able to extract light over a reasonable distance. This is both determined by the vertical interaction between modes and the PhC, as seen previously, and by the reciprocal lattice points responsible for light extraction.

Finally, preferential emission around a given outer direction can be desirable in some applications such as display.

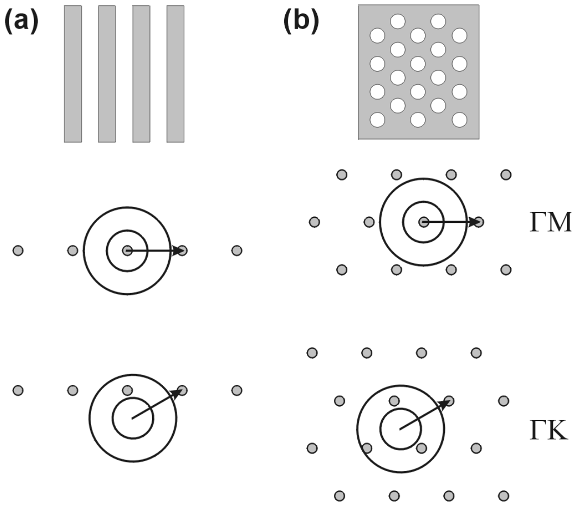

Figure 4.22: Typical Ewald construction for second-order lattices. The smaller circle corresponds to extraction to air, the larger circle to the substrate. (a) 1D grating: light incoming at too large an angle is not diffracted to air (b) Triangular lattice: Diffraction is possible at more angles, but some directions (ΓK here) are still not extracted to air.

In the following, we first discuss which lattice constant (or which *diffraction order*) should be used for efficient diffraction. Then, we explore basics of crystal lattices and discuss the impact of substrate loss. Finally, we focus on a complex crystal lattice, the so-called A7 Archimedean tiling, which displays efficient, omnidirecional light extraction.

4.2.1 Choice of the diffraction order

As seen on Fig. 4.22, even a triangular lattice is not necessarily omnidirectional: when light propagates along the ΓK direction, no point falls in the air cone. This is due to the fact that the lattice constant is *too small* in the case of Fig. 4.22.b. Specifically, this figure corresponds to the *second Bragg order* in the ΓM direction, defined by $k_{//} = 2G_0$ (G_0 being the length of the basic RL vector). In this configuration, the first RL points[9] fall at the center of the air circle in the ΓM directions but are in the substrate circle in the ΓK directions.

An easy way to solve this problem is to increase the lattice constant, or operate at a *high diffraction order*. This makes fabrication of the PhC easier, and ensures that several RL points will fall in the air cone for any propagation direction, as seen on Fig. 4.23.

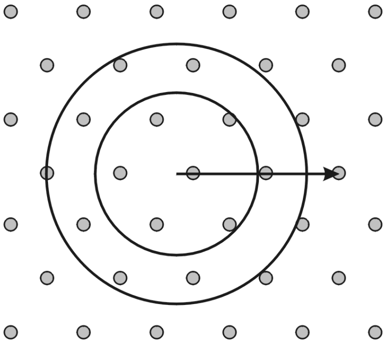

Figure 4.23: High-order diffraction: many RL points are in the air circle, regardless of the mode's direction.

Unfortunately, this also naturally increases the number of points which fall outside the air circle and in the substrate circle. These points cause scattering of guided modes to angles where light can propagate inside the substrate, but not to air. In other words, they cause part of the guided light to be lost to the sapphire substrate. While this light can partially be recovered by a geometric approach (such as shaping the sapphire substrate), this phenomenon clearly limits the interest of the PhC. We call such diffraction *substrate losses*. On average, the ratio of 'substrate points' to 'air points' is the average of the circles' areas, or n_{subs}^2/n_{air}^2. This simple fact pleads against use of high order diffraction.

Things are even worse when one considers the *photonic strength* of the various RL points, e.g. their ability at diffracting light. From Maxwell's equations, it can be seen that the coupling between two Fourier harmonics separated by a RL vector $\mathbf{G}$ is proportional to $\epsilon(\mathbf{G})$, the Fourier transform of the dielectric map. Therefore, in a perturbative approach where most of the Bloch mode's energy is carried by the fundamental harmonic ($\mathbf{G}$=0) and all other harmonics are small, the magnitude of the field of a harmonic is $E_{\mathbf{G}} \sim \epsilon(\mathbf{G})E_0$. In turn, when this harmonic is radiative (either in air or in the substrate), its radiative rate $\mathcal{P}_{rad}$ is given by the flow of the Poynting vector:

$$\mathcal{P}_{rad}(\mathbf{G}) \sim E_{\mathbf{G}}^2 \sim \epsilon(\mathbf{G})^2 \tag{4.4}$$

We define the *photonic strength* of a harmonic as $\epsilon(\mathbf{G})^2$. It indicates the ability of harmonics to diffract light, and can simply be obtained by computing the Fourier transform of the dielectric map. Fig. 4.24 gives the photonic strength in the case of a triangular lattice of filling factor $f = 0.35$.

Obviously, the 6 points closest to the origin of the RL (or *closest neighbors*) have a much higher photonic strength than any other point. This shows that light extraction will occur over a much shorter scale at the second Bragg order than at a high order. More precisely, the closest neighbors have at least 25 times more photonic strength than all other RL points, which means that high-order diffraction occurs over a scale at least 50 times larger than second-Bragg-order based diffraction ![10] As has already

---

[9] E.g. the 6 points closest to the reciprocal space origin.

[10] A factor 25 comes from the photonic strength. In addition, all distances scale with the lattice constant. Therefore, if the lattice constant is doubled in the case of high-order diffraction, the extraction length is multiplied by an additional factor of 2.

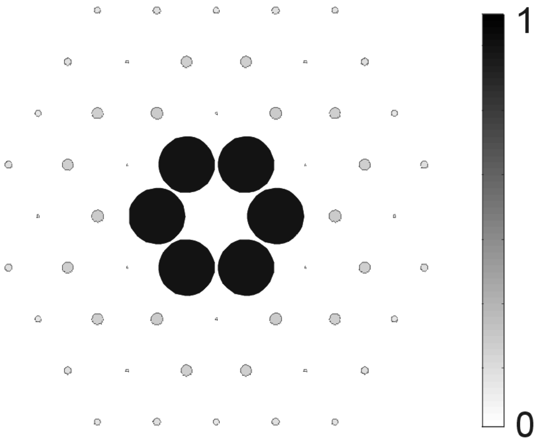

Figure 4.24: Photonic strength for the reciprocal lattice of a triangular lattice photonic crystal with filling factor 0.35. The color scale and the radius of the points are proportional to $\epsilon(\mathbf{G})$, so that the area of the points is proportional to their photonic strength.

been said, extraction lengths are problematic in the case of GaN where even the second order provides modest extraction.

One can wonder how this trend varies with the filling factor of the PhC, which is the only parameter intervening in the above discussion. In general, regardless of the crystal lattice, the Fourier transform for circular holes is $\epsilon(\mathbf{G}) = f.J_1(GR)/GR$, where J_1 is the first Bessel function of the first kind, and R the radius of the holes ($R \sim \sqrt{f}$). The first maximum of J_1 intervenes for $GR \sim 1.84$. This maximum can easily be achieved for the nearest neighbors because $\mathbf{G} = \mathbf{G}_0$: reasonable filling factors (around 0.3) correspond to this first maximum. On the other hand, larger $\mathbf{G}$ vectors would request very small filling factors. Secondary maxima of J_1 are unfortunately damped by the $1/GR$ factor: for large $\mathbf{G}$'s, the photonic strength varies like G^{-3}. Thus, small photonic strength is inherent to high-order RL points – at least in common PhCs with one circular hole per unit cell.

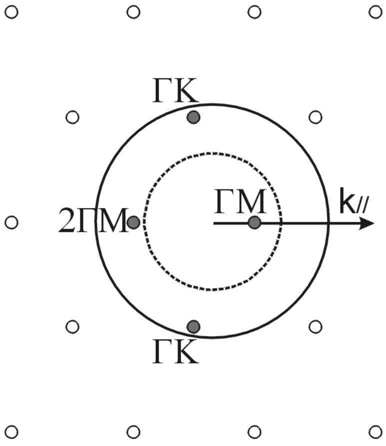

Figure 4.25: Ewald construction for a Bloch mode with $n_{eff} = 2.38$, at a frequency $u = 0.65$ (full line: sapphire cone, dashed line: air cone). One diffraction order (ΓM) falls in the air cone, and three (2ΓM and two ΓK) in the sapphire cone.

Therefore, the second Bragg order seems to be the most reasonable solution for efficient light extraction, in spite of the existence of non-extracted directions. We are still left with the question of substrate losses. Even close to the second Bragg order, some RL points can cause light to be scattered to the substrate. A particularly bad situation is depicted on Fig. 4.25: here, three points cause substrate losses.

Of course, these points have a small photonic strength in general. Yet it is possible to minimize their effect by optimizing the filling factor of the PhC. Fig. 4.26 presents the evolution of the photonic strength with f for the three RL vectors intervening in the case of Fig. 4.25. The photonic strength is simply ϵ^2, but in general the power $\mathcal{P}_{rad}$ diffracted by a harmonic in a realistic case depends on the full 3D geometry of the system. Therefore, we also consider the following 3D structure: a GaN waveguide of thickness $0.8a$ on sapphire etched by a triangular lattice PhC of depth $0.1a$ (a thin structure is considered in order to limit the effect of vertical interferences and simplify the discussion). At a frequency $u = 0.65$, this structure supports the Bloch mode whose Ewald construction is depicted on Fig. 4.25. We compute $\mathcal{P}_{rad}$ for each harmonic and superimpose the result to the photonic strength on Fig. 4.26.

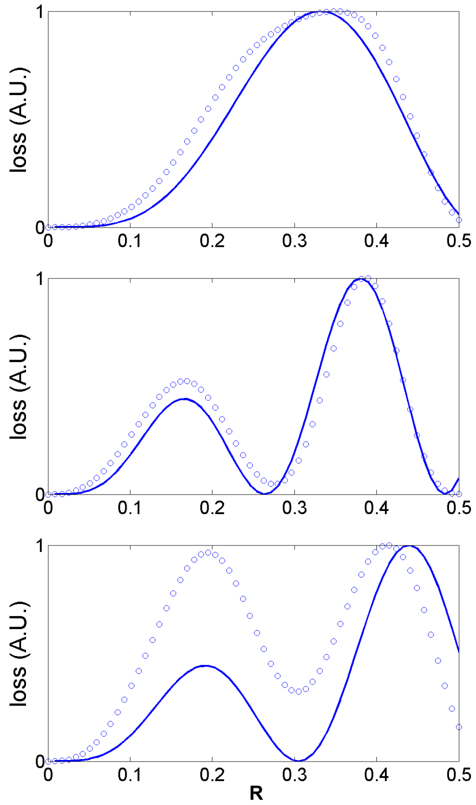

Figure 4.26: Diffraction losses $\mathcal{P}_{rad}$ as a function of holes radius (full: 2D approach, points: 3D calculation). (a) ΓM diffraction (b) ΓK (c) 2ΓM

In general, the behavior of losses in the 3D structure follows well the photonic strength. The discrepancy for the $2\Gamma K$ diffraction comes from second-order interactions between harmonics (the kinematic approach is not fully valid). When the holes radius is close to $R = 0.3$, the useful ΓM diffraction is maximized and the detrimental diffractions are minimized. Fig. 4.26 is presented in arbitrary units for readability, but the 3D calculation gives access to the actual power $\mathcal{P}_{rad}$ emitted in each diffraction order. Fig. 4.27 shows the final balance of losses in each channel in the 3D calculation. For $R = 0.3$ ($f = 0.33$), more than 85% of the loss goes in the useful ΓM diffraction order. Let us add that the case considered here is rather pesssimistic: the second ΓM diffraction is only made possible because we consider a high frequency ($u = 0.65$). Closer to the second Bragg order, this channel is closed.

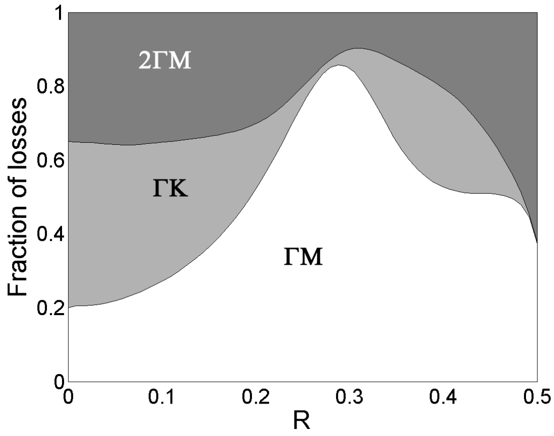

Figure 4.27: Cumulative plot of diffraction losses in the 3 diffraction channels as a function of holes radius, as obtained for the 3D structure in the configuration of Fig. 4.25. The 'useful' loss in the ΓM direction is maximal for $R \sim 0.3$.

The examples given in this section focused on a triangular lattice, but similar conclusions could be drawn for a square lattice.

In summary, diffraction at the second Bragg order provides reasonable extraction efficiency, while high-order diffraction occurs over a prohibitive scale. Close to the second order, extraction can be maximized and substrate losses can be minimized by using an optimal filling factor.

4.2.2 Comparison of crystal lattices

In this section, we consider second-order diffraction and we discuss the choice of a crystal lattice in simplified terms. We restrict ourselves to a 2D problem in order to clarify the discussion. Thus, we temporarily ignore the question of interaction between Bloch modes and the PhC in the vertical direction. This is partly justified by the fact that, as has been seen in the previous part, such a problem can be treated by taking into account the vertical direction only. Therefore, in the following, we merely assume that we need to extract guided modes whose effective index is between that of GaN and that of sapphire:

$$n_{sapphire} < n_{eff} < n_{GaN} \tag{4.5}$$

For a mode to be extracted, we only request that it falls inside the light cone of air. When this is verified, the extraction efficiency is assumed to be sufficient, thanks to suitable design in the vertical direction such as that presented above. Although the distribution of guided modes is discrete, they are usually very dense due to the thickness of the GaN layer. Therefore, we assume a continuum of guided light between n_{GaN} and $n_{sapphire}$.[11] Likewise, we assume uniform distribution of guided light along the azimuthal angle φ.

This approach is kinematic – that is, it only takes into account coupling between the fundamental harmonic of the Bloch mode and other harmonics, but no coupling between the other harmonics. This

---

[11] This assumption is somewhat less valid if a CLM is present, because this mode is in a sense more discrete than other guided modes. However, it only collects the light emitted between n_{GaN} and $n_{GaN} - 0.1$, so that treating this small window of n_{eff} as a continuum is still acceptable.

is a good approximation in the case of 'weak photonic regime' where the PhC is shallow and does not significantly alter the dispersion of guided modes, as is the case for most GaN structures.

Under these assumptions, evaluation of a given lattice just amounts to counting what fraction of the guided light falls under the light cones of air and the substrate: for each value of n_{eff} and φ, we build the Ewald construction of the corresponding mode. The extraction efficiency of the mode to air is then:

$$\eta_{Air} = \frac{\sum\limits_{G \in Air} \epsilon(G)^2}{\sum\limits_{G \in Substrate} \epsilon(G)^2} \tag{4.6}$$

Here, $G \in Air$ means that the wavevector $\mathbf{k}_{//} + \mathbf{G}$ falls in the air cone, and $\epsilon(G)$ is the Fourier transform coefficient of the dielectric map ϵ corresponding to the reciprocal vector $\mathbf{G}$. The above formula simply states that the power carried by the mode is divided among the RL vectors corresponding to radiation either in air or substrate. The weigh of each RL point is taken as its diffraction efficiency, which is proportional to $\epsilon(G)^2$. For instance, if a mode has only one RL point in the air cone (and therefore, also in the substrate cone), η_{Air} is equal to one – one may argue that in this case, half of the power (on average) is radiated downwards to the substrate, but in the case of sapphire this light can easily be redirected upwards by placing a mirror under the sapphire substrate. Likewise, if a mode has one RL point in the air cone and another RL point (of equal photonic strength) only in the substrate cone, its extraction is $\eta_{Air} = 1/2$. Thus, it already appears that having a large density of RL points in the air cone may actually not be a good strategy, because of the competing effect of the substrate. As previously, we speak of *substrate losses* for RL points which are in the substrate cone but not in the air cone.

Using this formula enables a rapid and easy evaluation of various reciprocal lattices. However, the formula is still limited to existing lattices, where $\epsilon(G)$ can be calculated. A further simplification consists in only retaining the strongest RL points in the above sum. As was just seen, diffraction efficiency is usually strongest for the RL points closest to the origin, and the effect of other RL points is negligible to the first order. Therefore, if we only conserve these strongest points of identical photonic strength in the sum, it simplifies to the ratio of points in the air and substrate:

$$\eta_{Air} = \frac{Card(G \in Air)}{Card(G \in Substrate)} \tag{4.7}$$

In this case, the only possible substrate loss is due to the nearest neighbors. Fig. 4.28 depicts a typical case where a nearest neighbor causes substrate loss and limits the extraction efficiency.

The interest of this simplification is that we can now consider generalized reciprocal lattices, with an arbitrary number N of strong RL points. For a 1D grating $N = 2$, for a square lattice $N = 4$ and for a triangular lattice $N = 6$, but one can also conceive hypothetical lattices with other values of N. Although no such crystal lattice exists in general, quasicrystals or complex crystals with a large supercell can efficiently simulate some values of N. Hagelstein *et Al.* give an example of a complex crystal which is close to the case N=8.[12] Likewise, in the case of a short-range order where all PhC holes are separated by a given distance a but where no translational order is present, the Fourier transform of the dielectric constant is a ring of radius $2\pi/a$, which corresponds to the case $N \to \infty$ (Fig. 4.29). Finally, in the next part, other complex crystals close to $N = 12$ will be presented. Therefore, considering generalized lattices with an arbitrary value of N is a problem of interest.

Before coming to numerical results, let us comment on the trends we can expect with varying N. Initially, the efficiency should increase with N as the PhC becomes more omnidirectional. In the limit $N \to \infty$, the optimal efficiency should occur close to the second Bragg order; in this case the efficiency

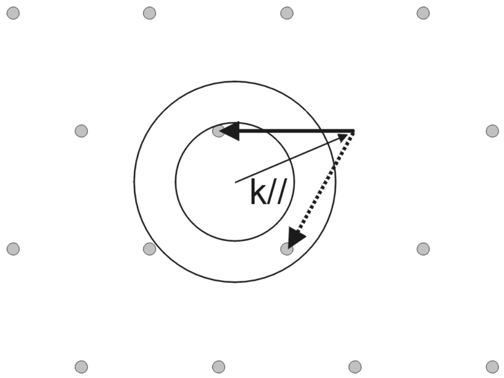

Figure 4.28: Typical 1st-order substrate losses: one first neighbor (full arrow) is in the air circle but another first neighbor of equal photonic strength (dotted arrow) is in the substrate circle, taking away half of the guided mode's energy.

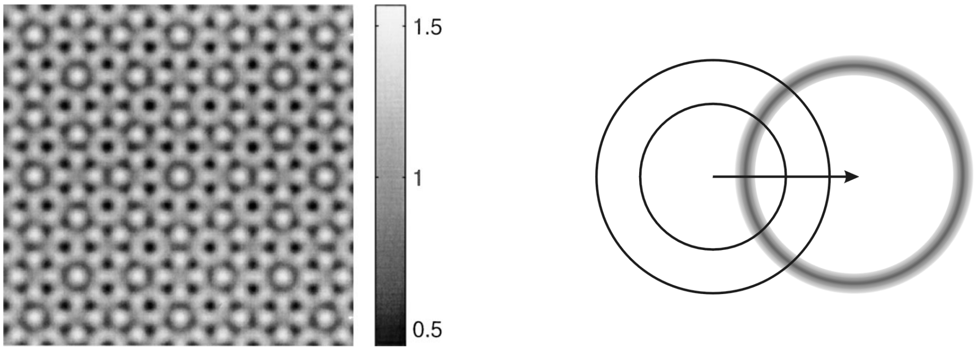

Figure 4.29: (Left) Inverse dielectric map of a supercell producing a pseudo-crystal with $N = 8$ nearest neighbors (after Ref. [12]). (Right) 'Statistical' diffraction by a short-range ordered medium, diffraction points become a ring.

is given by the ratio of the lengths of the air and substrate circle arcs, because the RL is now a circle which scans all azimuthal angles regardless of the mode's direction. Therefore, the optimal efficiency in this case should be $\sim n_{air}/n_{substrate}$. Between these two extreme regimes, the efficiency depends on the precise balance of extraction directions and substrate losses and the optimal value of N is not obvious.

We now compare numerically several lattices with various values of N. In this section only, we use the following convention: the lattice constant a of the crystal is defined such that the spacing between reciprocal lattice points is $G_0 = 2\pi/a$.[12]

First, we consider a given guided mode of effective index 2.5. Fig. 4.30 displays the extraction efficiency η to air and to epoxy as a function of the reduced frequency $u = a/\lambda$, for N=2 (1D grating), 4 (square lattice), 5, 6 (triangular lattice), 7 and $N \to \infty$ (effectively obtained with N=20).

In air, extraction is poor for N=2, because a 1D grating offers few extraction angles. When N increases to 4, 5 and 6, the extraction efficiency increases accordingly, as more extraction directions become available. When N=7, the effect of increased substrate losses starts balancing this beneficial effect, and the extraction efficiency decreases. Finally, the $N \to \infty$ limit corresponds to a non-optimal

---

[12] Conventionally, the relation between a and G_0 depends on the lattice. For instance, in the case of a triangular lattice, $G_0 = 4\pi/a\sqrt{3}$. The definition we choose here offers a unified definition for all lattices which allows for easier comparison, but modifies the scale of the reduced frequency $u = a/\lambda$. For a triangular lattice, u has to be multiplied by $2/\sqrt{3}$ to return to the conventional definition.

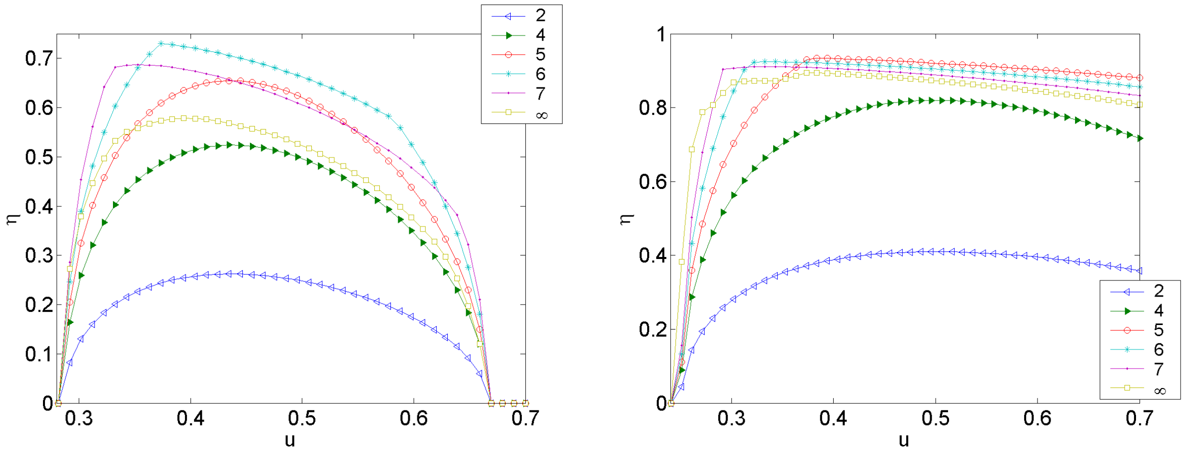

Figure 4.30: Extraction efficiency of a mode with $n_{eff} = 2.5$ to air (left) and to epoxy (right) for N=2, 3, 4, 5, 6, 7 and ∞.

case. The best extraction efficiency in this case is 0.58, very close to the ratio $n_{air}/n_{subsrate}$ predicted above. In epoxy, the situation calls for less comments. Since the index of epoxy is very close to that of sapphire, the question of substrate losses is naturally discarded. Once a sufficient value of N is reached, all lattices are omnidirectional and provide a similar efficiency (however, the directionality of the far-field patterns can be different).

In the case of air, it is worthwhile examining the case $N = 6$ in more details to see how this value beats the limit $N \to \infty$. Fig. 4.31 details the number of diffraction channels to air and to substrate as a function of the mode's azimuthal angle.

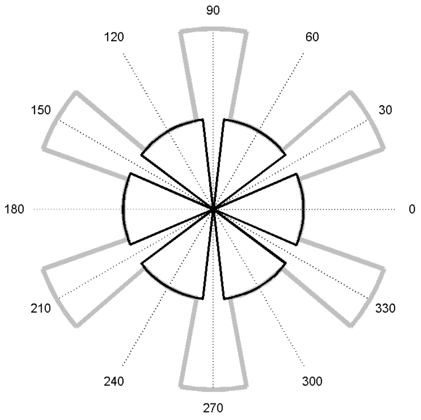

Figure 4.31: Number of diffraction channels to air (black line) and substrate (grey line) as a function of the mode's azimuthal angle, for $n_{eff} = 2.5$ at the second Bragg order ($u = 0.5$). The smaller radius corresponds to 1 diffraction channel, the larger radius to 2 diffraction channels.

As can be seen, the result is quite fortunate. Although in some cases 2 diffraction channels cause substrate losses, this (nearly always) happens at angles where there is no diffraction to air anyway. On the other hand, when a diffraction channel is open to air, there is usually only one diffraction channel to the substrate. Therefore, the detrimental situation where several substrate channels compete with one air channel is nearly always avoided, and η equals one whenever there is a RL point in the air circle. On the other hand, when $N \to \infty$, the ratio of air channels to substrate channels is $\sim n_{air}/n_{substrate}$, and so is η.

So far, our discussion is monomode. To accurately compare lattices, we no need to integrate this calculation over all guided modes ($2.5 > n_{eff} > 1.7$). This requires additional hypotheses on the power carried by each guided mode. Assuming that only TE light is emitted in guided modes (e.g. the emission is due to electron-heavy holes transitions), the intensity emitted by the QW in each mode is just proportional to the corresponding solid angle $d\Omega \sim n_{eff}$. The same calculation as in Fig. 4.30, taking into account all modes, is presented on Fig. 4.32.

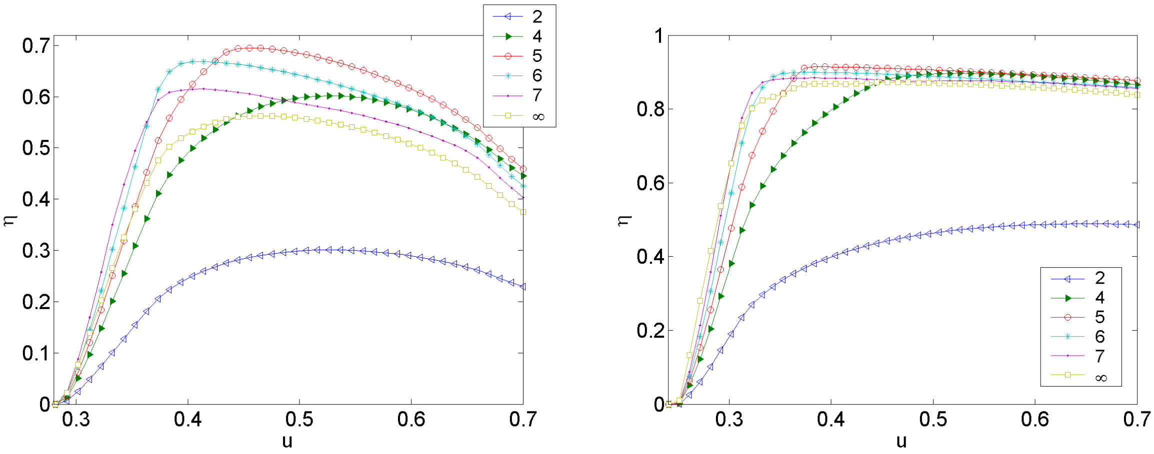

Figure 4.32: Same as Fig. 4.30, integrated over $n_{eff} \in [1.7; 2.5]$ (weighed by the corresponding solid angles).

For extraction to air, the results are slightly modified in the multimode case. The best lattice is now $N = 5$, with an optimal extraction $\eta_{max} \sim 70\%$. The triangular lattice is nearly as good, with $\eta_{max} \sim 67\%$. As the triangular lattice presents the additional advantage of being an existing lattice (with no approximation or complicated construction), it can still be retained as the optimal solution. For extraction to epoxy, we reach the same conclusion as in the monomode case: substrate loss is nearly irrelevant.

Finally, it is interesting to note that these results are rather robust in terms of frequency: the maxima are smooth with respect to u, mainly because of the integration over all directions and effective indexes. This implies that PhC extractors are quite tolerant with respect to fabrication (e.g. the lattice constant does not have to be finely tuned for a given wavelength), and also that extension to a polychromatic source is not problematic – at least for typical GaN linewidths of a few %.

Again, let us stress that these results ignore the question of efficient interaction between the modes and the PhC, which should be addressed by designing the structure in the vertical direction. The figures obtained here simply give the maximal amount of guided light which can be outcoupled by a PhC provided this mode/PhC interaction is sufficient.

As a conclusion, the triangular lattice appears as a reasonable choice for a simple GaN-on-sapphire structure. It is optimal both in the case of air and epoxy, with a maximal guided light extraction efficiency of $\sim 66\%$ and $\sim 90\%$, respectivley. In the case of air however, this result is due to the detrimental losses in the substrate, and the triangular lattice does actually not provide second-order diffraction at all angles.

4.2.3 Archimedean tilings

In this section, we study a complex reciprocal lattice whose behavior is close to a crystal lattice with $N = 12$ nearest RL neighbors. As just mentioned, such a lattice is of little interest in a simple GaN-on-sapphire structure where a triangular lattice is more efficient. On the other hand, one may consider more sophisticate structures where substrate losses are limited or even made impossible, as will be discussed below.

In such structures, increasing the number of nearest neighbors could provide *omnidirectional* extraction, e.g. extraction at all azimuthal angles. If we simply admit that substrate losses are somehow quenched, omnidirectional extraction of a mode of index n_{eff} occurs when $N \geq \pi/n_{eff}$, which corresponds to $N \geq 8$ in the case of GaN.[13] The case $N = 12$ which we will now consider therefore fulfills the omnidirectionality condition.

Quenching substrate losses

First, let us discuss quickly which schemes could limit or ultimately quench substrate losses.

One approach consists in introducing distributed Bragg reflectors (DBRs) in the epitaxial structure. Usually, DBRs are introduced to reflect upwards the fraction of light emitted downwards, and are tuned for maximal reflectivity around normal incidence ($\theta = 0$). However, it is also conceivable to detune the DBR so that it is tuned for maximal reflectivity at polar angles θ which correspond to substrate losses. Let us look back at the typical substrate loss caused by a strong photonic points, shown in Fig. 4.33. We see that (around the second order where $k_{//} = 2G_0$) this configuration occurs when the substrate-diffracting wavevector is in between the air and substrate circles, e.g. for $k_{//} + G \sim k_0(n_{air} + n_{subs})/2$. This corresponds to light propagating in GaN with a polar angle:

$$\theta = asin\left(\frac{n_{air} + n_{subs}}{2n_{eff}}\right) \tag{4.8}$$

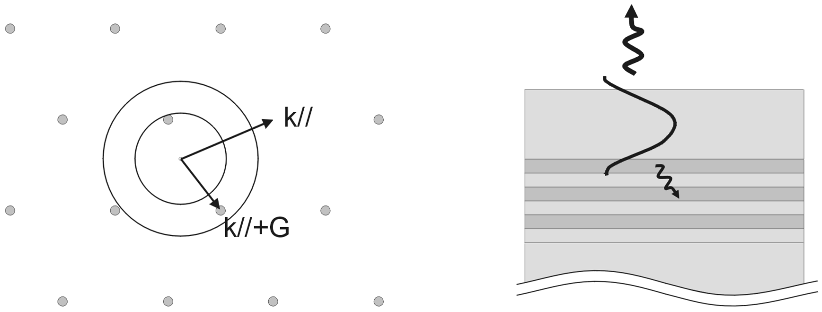

Figure 4.33: (Left) Typical configuration where a strong reciprocal lattice point falls in the substrate cone and causes substrate loss. The lossy harmonic is between the circles of air and substrate. (Right) If a DBR is tuned to polar angles corresponding to this harmonic, substrate loss can be inhibited with respect to extraction to air.

If we now design a DBR to be reflective for such polar angles, the radiation rate to the substrate can be strongly suppressed. As mentioned in Chapter 2, good nitride-based DBRs are very hard to obtain, mainly because the high Al contents needed for good index contrast strain the material and cause cracking. However, very good results have been reported using GaN/AlInN layers, where the indium is used to alleviate the strain while leaving a good index contrast.[13]

Another, more direct approach is simply to get rid of the substrate. Flip-chipped LEDs where the sapphire substrate is removed by laser lift-off have already been presented in Chapter 2 to obtain thin

---

[13] Indeed, each RL point extracts light over an angular range $\sim \pm 1/n_{eff}$.

micro-cavity LEDs. Addition of photonic crystals to these LLO-LEDs will be presented further in this chapter. In this case, the new substrate is metallic and (ideally) reflects light emitted downwards, so that no substrate loss can occur.

As a conclusion, sophisticate yet feasible LED structures should be able to strongly limit or suppress diffraction losses to the sapphire substrate. While such state-of-the-art structures still require significant fabrication efforts, they can eventually be expected to replace simple GaN-on-sapphire LEDs. Therefore, we feel justified in our efforts to characterize an omnidirectional lattice which could be integrated to these structures in the future.

Principle of Archimedean tilings

While only a few 2D crystal lattices exist (namely, with N =2, 4 and 6 closest-neighbors), complex structures can effectively behave as lattices with other values of N. We already quoted several examples: a crystal with a large lattice constant and a complex supercell was proposed as equivalent to the case $N = 8$.[12] A short-range order lattice yields a diffraction ring instead of diffraction points and corresponds to $N \rightarrow \infty$. Several groups have also studied quasiperiodic Penrose lattices.[14, 15]

Yet another class of lattices is the family of Archimedean tilings, first introduced by Sylvain David from IEF in the context of photonic crystals.[16, 17] These lattices are in general made of a regular Bravais lattice (square or triangular) combined with a basis of several atoms which are all separated by a same distance (Fig. 4.34).

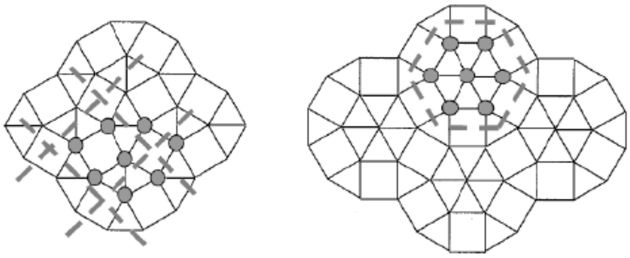

Figure 4.34: (After Ref. [16]) Archimedean lattices based on a square lattice (left) and triangular lattice (right).

Initially, Archimedean tilings were introduced in order to provide isotropic photonic bandgaps: because their ΓM and ΓK directions are more similar than for a simple triangular lattice, the magnitude of the gap is less dependent on the direction.

As was first suggested by Rattier, Archimedean tilings can directly be applied in the context of light extraction where isotropy is also sought. More quantitatively, they provide an interesting alternative when more than 6 nearest neighbors are needed in the reciprocal lattice.[18]

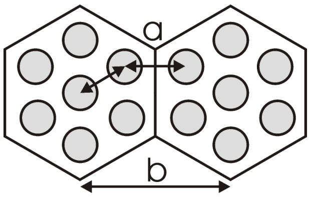

Figure 4.35: A7 Archimedean tiling, made of a triangular lattice (with lattice constant b) and 7 holes per unit cell (with distance a between holes).

Here, we focus on the so-called A7 Archimedean tiling, depicted on Fig. 4.35. The A7 is made of a triangular Bravais lattice with a basis of 7 equi-spaced atoms (or holes, in our case). Here, we chose to call a the distance between two holes, and b the actual crystal lattice, with $b = a(1+\sqrt{3})$. The existence of these two distances in the lattice implies the presence of two characteristic scales in the reciprocal space. b naturally sets the RL, which is a triangular lattice with $G_0 = 4\pi/b\sqrt{3}$. However, the 7 holes should now be considered to get the structure factor of the A7 crystal:

$$S(\mathbf{G}) \sim \sum_{holes} exp(i\mathbf{G}.\mathbf{r}_{hole}) \tag{4.9}$$

The terms of this structure factor can be expected to add coherently for values of $\mathbf{G} \sim 2\pi/a$. Therefore, the strongest RL points should no longer be the points closes to the origin, for which the terms of S are out of phase. Indeed, calculation of the Fourier transform of the A7 dielectric map confirms that the photonic strength is renormalized by the structure factor, and is now carried by 12 points lying further from the reciprocal space origin (Fig. 4.36).

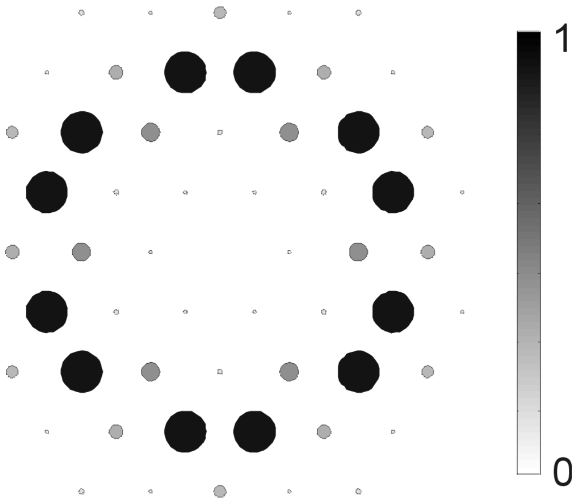

Figure 4.36: Fourier transform of the dielectric map of an A7 lattice with $f = 0.35$ (arbitrary units).

An Ewald construction on the A7 lattice confirms that it is an omnidirectional extractor. However, unlike a 'simple' high-order triangular lattice (with $a >> \lambda$ but only one hole per unit cell), the photonic strength is carried by the points responsible for diffraction to air, with $|\mathbf{G}| \sim 2.5G_0$. Actually, their photonic strength is roughly half that of the 6 nearest neighbors of a classic triangular lattice, but since there are twice as many points diffracting to air, the overall extraction length should be the same for both lattices.

In conclusion, the A7 lattice is expected to provide omnidirectional and efficient (e.g. on a short scale) light extraction.

Archimedean tiling PhC-LEDs: implementation

PhC-LEDs with an A7 lattice were fabricated in the same way as the triangular lattice PhC-LEDs already presented. The same substrate with an AlGaN layer was used. To enable easy comparison between the two lattices, both triangular and A7 PhCs were fabricated on the same sample. Again, the PhC pattern was obtained by e-beam lithography – there is no easy way to obtain A7 patterns with interference lithography (although some convincing demonstrations of complex PhC fabrication by holography have been reported recently [19]).

Fig. 4.37 is an AFM image of a A7 patterns transferred in the GaN layer. Patterns with lattice constants of a =190, 200 and 215 nm were fabricated.

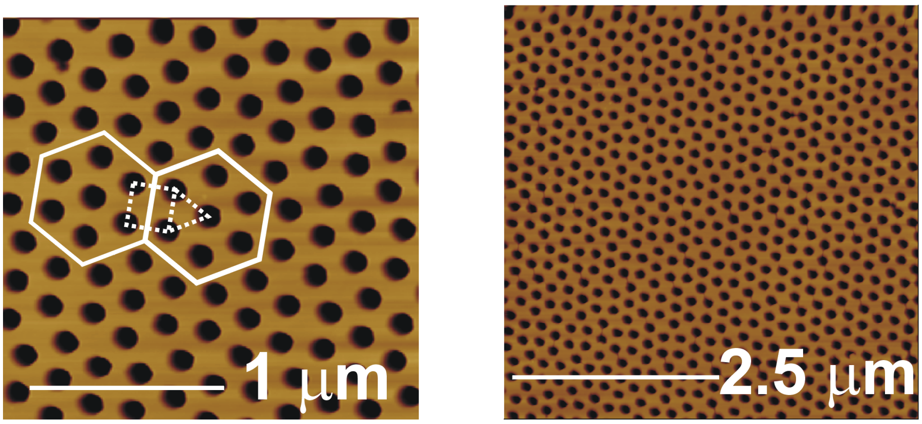

Figure 4.37: Atomic Force Microscope images of A7 patterns in GaN, with a = 215 nm (left) and 200 nm (right).

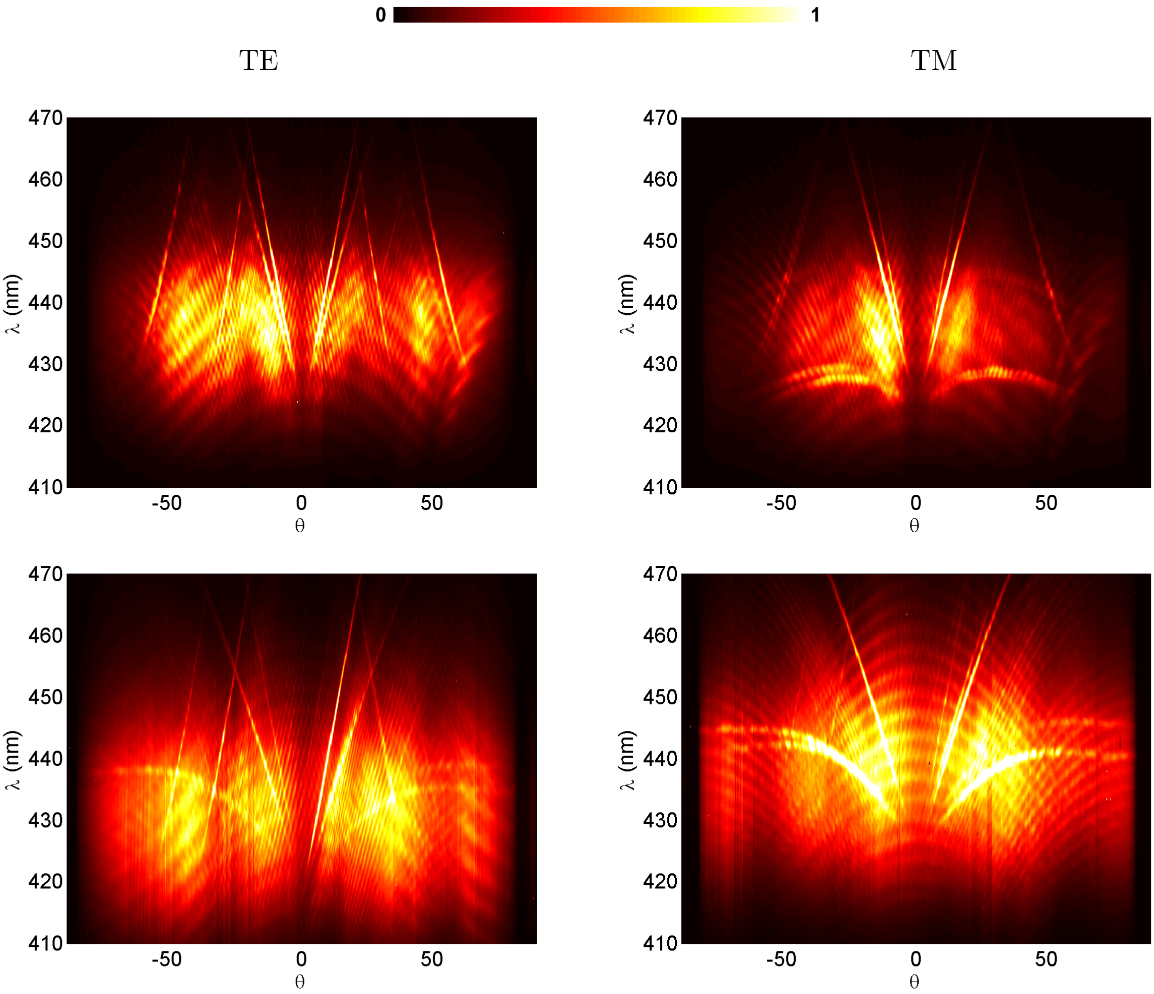

Figure 4.38: Angular spectra of an A7 PhC-LED with a = 190 nm along the ΓM (top) and ΓK (bottom) directions, in TE (left) and TM (right) polarization.

The LEDs were characterized by angle-resolved electroluminescence in order to observe the properties of the A7 lattice. Fig. 4.38 shows raw angular spectra obtained on an LED with $a = 190$ nm in

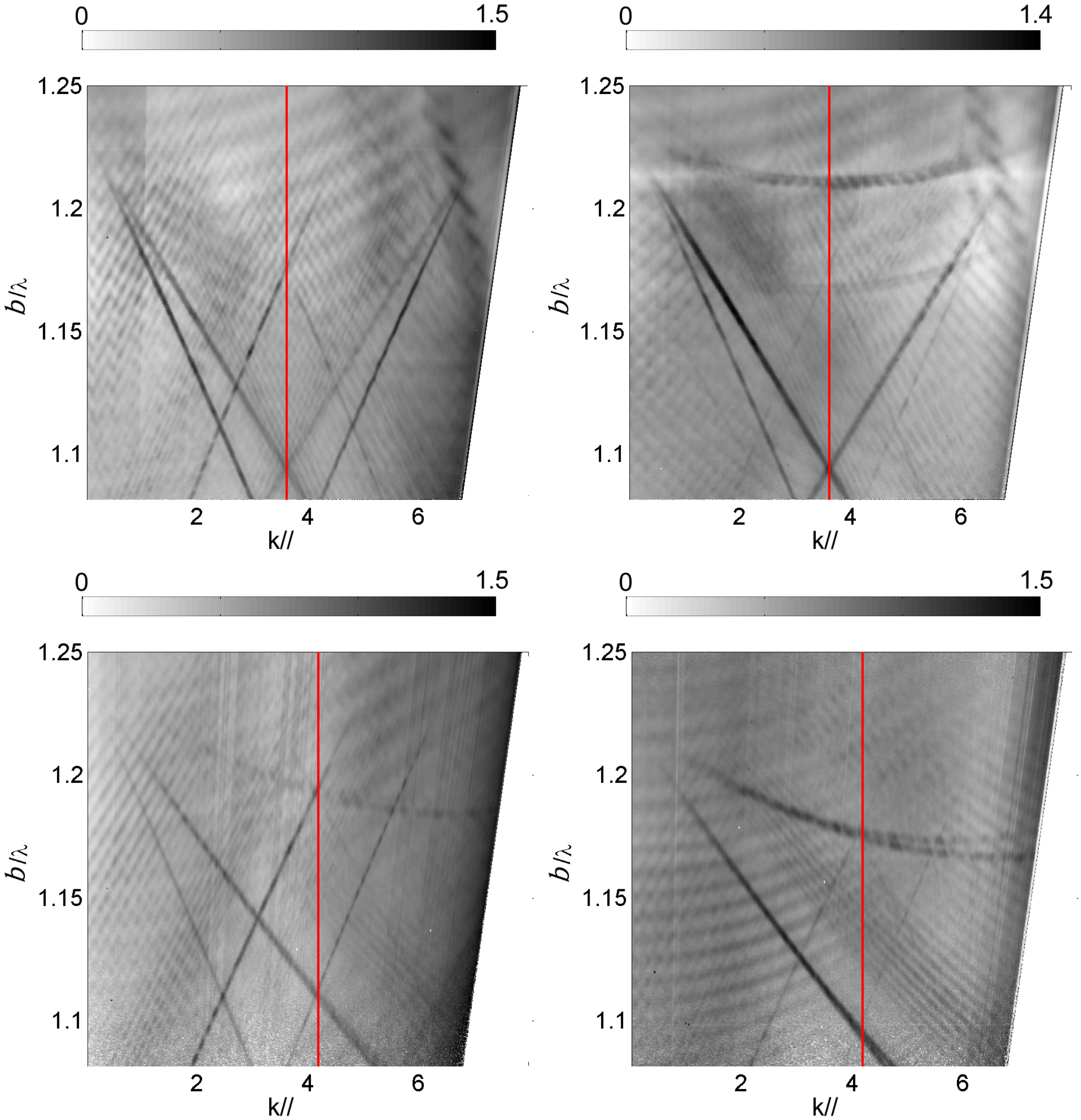

Figure 4.39: Band structures of an A7 PhC-LED with $a = 190$ nm along the ΓM (top) and ΓK (bottom) directions, in TE (left) and TM (right) polarizations. The red line denotes the edge of the first Brillouin zone (e.g. point M or K respectively). The most intense lines correspond to the cap layer mode, as in the case of a triangular lattice PhC.

various directions and polarization conditions. Conversion from angular patterns to band structures is shown on Fig. 4.39.

There are many more photonic bands than in the case of triangular PhCs. This is expected because more RL points diffract to air – in other words, the PhC operates at a larger frequency (b/λ instead of a/λ) so that more photonic bands are folded back in the first Brillouin zone. This is evidenced in Fig. 4.40, where the band structures of a triangular lattice and an A7 are placed in the same dispersion diagram. On this figure, it appears clearly that for the A7 the whole first Brillouin zone is included in the air cone. This is also the case in the ΓK direction, as can be seen on some of the spectra of Fig. 4.39. From this observation, we can conclude that *all photonic bands* have at least one harmonic in the air cone, or in other terms that the A7 is indeed an omnidirectional extractor. On the other hand, substrate losses are not measured, so that we can draw no immediate conclusion on the beneficial effect of the A7.

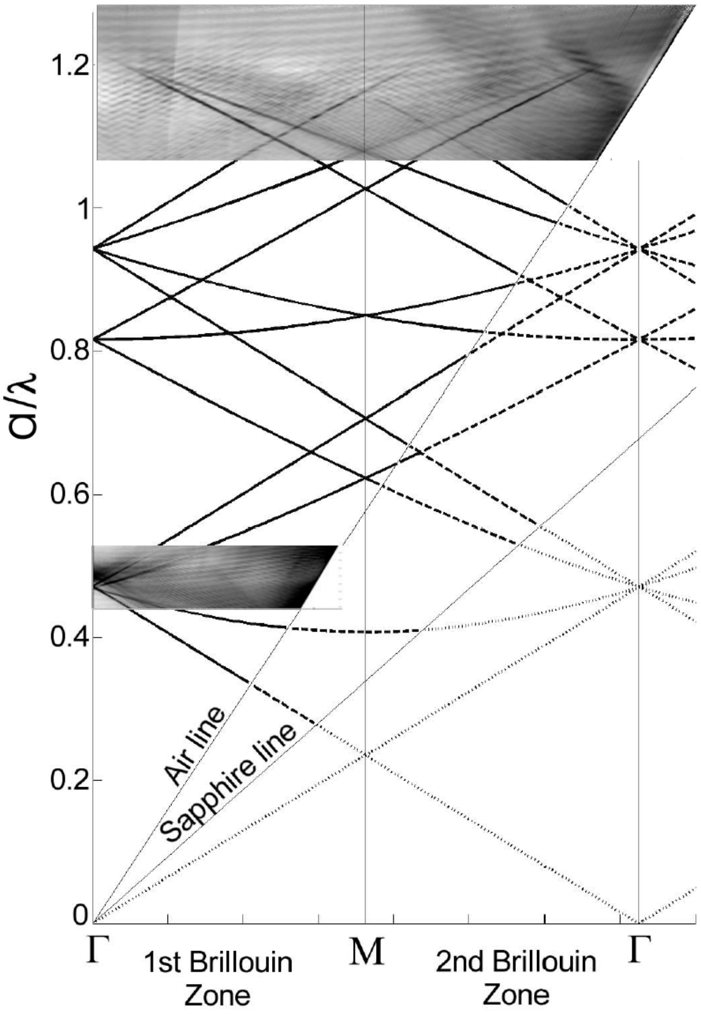

Figure 4.40: Band structures of a triangular lattice and an A7 lattice PhC-LEDs (ΓM direction, TE polarization). The A7 lattice operates at higher frequency than the triangular lattice. The theoretical band structure of a mode with $n_{eff} = 2.45$ is superimposed as black lines above the air cone (extracted modes), dashed lines between the air and sapphire cones (modes diffracted to the substrate), and dotted lines below the sapphire cone (guided modes). This theoretical dispersion coincides well with the experimental lines corresponding to the cap layer mode, for both LEDs. To obtain this good fit without taking index dispersion into account (which is not possible for both lattices at the same time), the vertical scale of both experimental spectra has been slightly stretched.

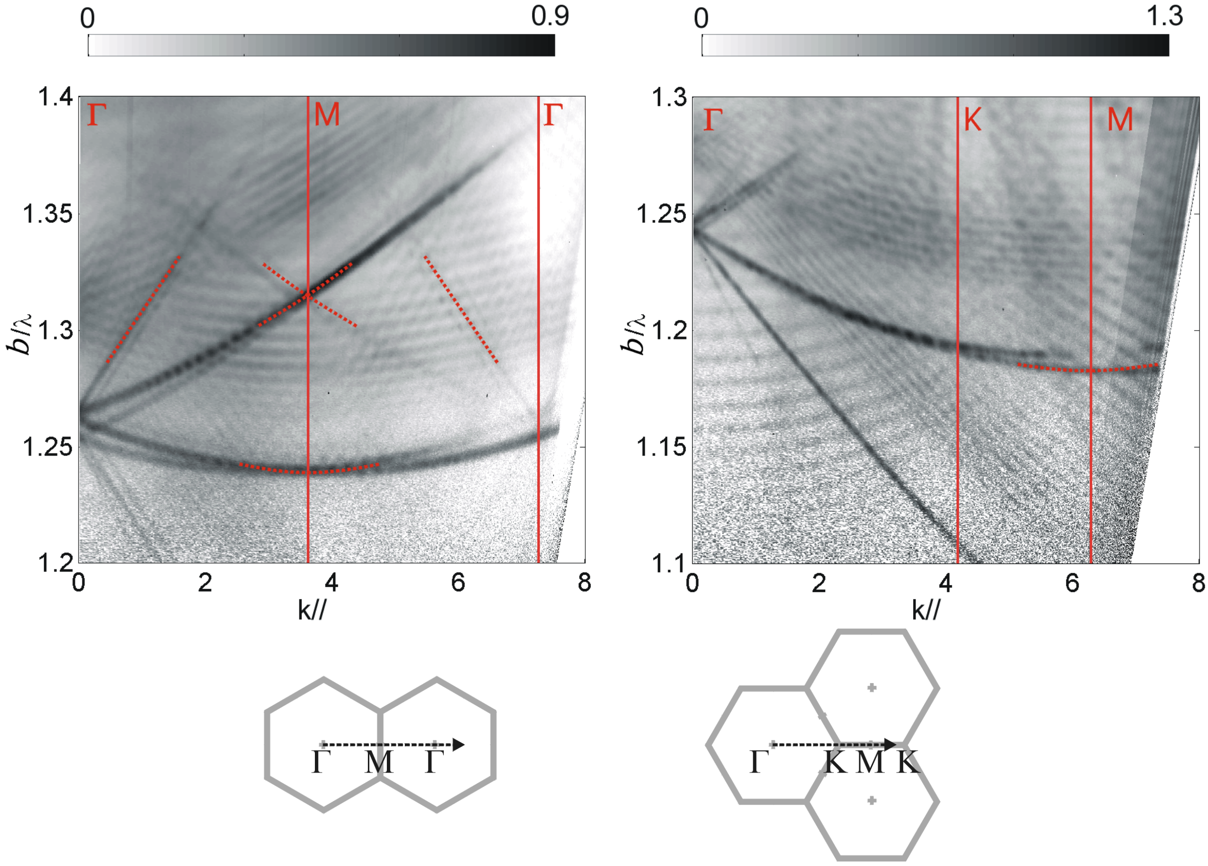

Figure 4.41: (left) Band structures of A7 PhC-LEDs. Left: $a = 215$ nm, ΓM direction, TM polarization. Right: $a = 200$ nm, ΓK direction, TM polarization. The vertical lines denote the high symmetry points of the reciprocal space. The bands display symmetry around point M but not along point K. The dotted lines are a guide to the eye.

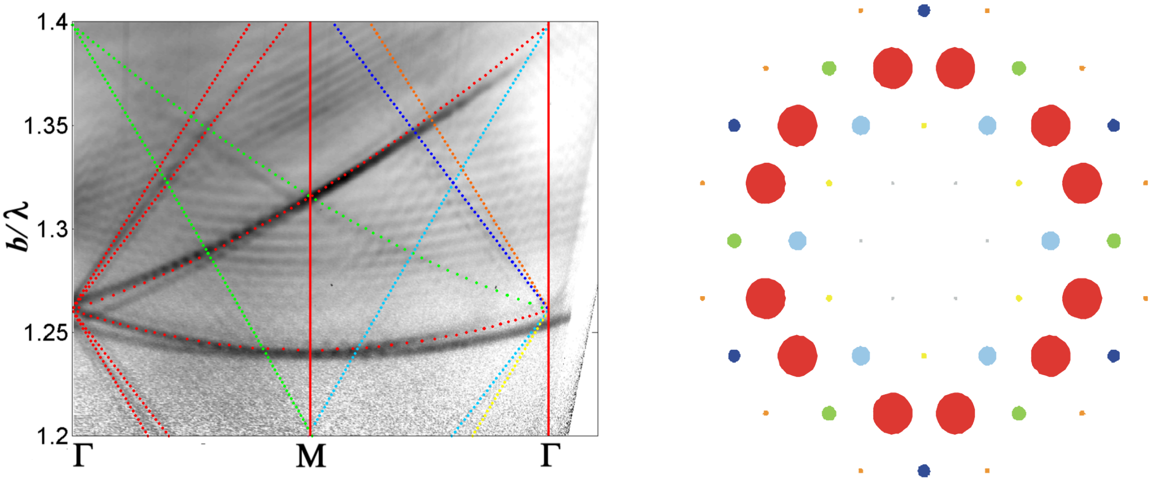

Figure 4.42: Theoretical dispersion of the cap layer mode superimposed on an A7's experimental band structure ($b = 215$ nm, ΓM direction, TM polarization). For the theoretical lines, the color of the dots indicates which RL point is responsible for diffraction to air, as shown to the right. Only the red dots, corresponding to the strongest RL points, are clearly measured experimentally.

Here, the presence of the cap layer mode due to the AlGaN layer proves a precious tool to study the A7's band structure. Because many photonic bands are present, it is very hard to distinguish the individual bands corresponding to the extended modes: they form a quasi-continuum of diffracted light. On the other hand, the cap layer modes retains a discrete nature and is easily distinguished from other bands.

Let us now comment on the symmetry properties of the A7's band structures. As can be seen on the various experimental spectra, the band structures are symmetric around the M point but not around the K point. This is highlighted on Fig. 4.41 for two spectra, along ΓM and ΓK respectively. This can easily be understood when considering the path followed in the reciprocal space during the angular spectra: in the first case, the M point is a point of symmetry, whereas in the second case the K point is not. Therefore, the symmetry properties of the spectra are just a manifestation of the symmetry of the crystal lattice. It is however quite satisfying to observe these symmetry properties in such a direct fashion.

We now come to the main point of interest of the A7 lattice: unlike high-order lattices, they provide *efficient* light extraction over a short scale. As already explained, this is due to the fact that the RL points which carry most of the photonic strength are responsible for diffraction to air. In order to confirm this, we now consider the intensity of the measured photonic bands. Again, we focus on the photonic bands corresponding to the CLM because they are easiest to observe. As we did in the case of a triangular lattice PhC, we fit these lines by the dispersion of a guided mode of effective index $n_{eff} = n_{GaN} - 0.1$, folded back in the first Brillouin zone. The result of this fit is shown on Fig. 4.42. In addition, each of the folded bands is now identified by a color which corresponds to the reciprocal lattice point responsible for extraction to air.

As can clearly be seen, only the bands corresponding to the red dotted lines are well observed experimentally. These lines correspond to the strong points of the reciprocal lattice, while photonic bands corresponding to weaker RL points are not measured experimentally (a more careful study of the experimental data reveals that some other bands faintly appear on the band structure: these correspond to RL points which still carry a small but non-zero photonic strength). This is a direct observation of the photonic strength of the A7's RL points, and the expected behavior is confirmed. It is worth noting that such a direct observation of the photonic behavior of a complex crystal lattice is not usual, most experiments relying on the observation of band gaps through transmission experiments.

This observation implies that light extraction should be roughly as efficient for the A7 LEDs as for the triangular LEDs (although it is not expected to be better for this GaN-on-sapphire structure). This is confirmed by direct power measurements on both LEDs: these reveal similar power output (within 10%) for triangular and A7 PhC-LEDs. In our case, the triangular lattice is slightly more efficient, which is most likely due to substrate losses.

4.2.4 Conclusion

Therefore, we conclude that the use of Archimedean tilings is a sound approach for omnidirectional extraction in GaN. The collective behavior of the 7 holes forming the unit cell was directly confirmed experimentally, confirming that extraction is due to reciprocal lattice points with high photonic strength, and therefore occurs over a reasonably short distance. Its integration in advanced structures where substrate losses are quenched should enable efficient omnidirectional extraction.

4.3 Laser lift-off PhCLEDs

In this section, we present advanced LED structures where a light-extracting photonic crystal is combined with the laser lift-off process already used for the fabrication of microcavity LEDs. We begin with the fabrication and characterization of these LEDs, which we then model to study the effect of metal losses in these structures. Finally, we discuss the onset of strong photonic effects in thin GaN layers, where interaction between light and the photonic crystal significantly alters the modes' dispersion.

4.3.1 Motivation

As has been seen with the previous LED implementations, the simple GaN-on-sapphire approach is limited by several facts. First, the presence of the sapphire substrate causes substrate losses which are difficult to avoid – apart from introducing efficient DBRs, which are still difficult to obtain in GaN compounds.

Second, because thick GaN layers have to be grown, multiple guided modes propagate and some of these (low-order modes) tend to virtually ignore the PhC. Although we have presented a reasonable solution to this problem based on tailoring of the guided modes, this approach still leaves us with a rather modest extraction efficiency: typically, extraction occurs over hundreds of microns, which is still large compared to the scale of an LED (usually 300μm x $300\mu m$). Stronger photonic interaction would be desirable. As has already been discussed, this can only be obtained if the unetched GaN core is thin enough.

Third, the question of efficient p-contacts is still unsolved. One may consider using a semi-transparent metallic contact over the PhC or even using a transparent injector such as ITO, but both of these present drawbacks: absorption is present (especially in the case of thin metallic contacts) and ITO tends to lose its transparency over time.

Finally, other crucial aspects of efficient LEDs have been ignored, such as thermal management and mounting into a package. Sapphire is a poor thermal conductor, which limits the maximum electrical power in GaN-on-sapphire LEDs. Unfortunately, most of the effort in GaN LEDs is directed at obtaining good *high-power* LEDs, which precisely require high current densities.

For all these reasons, the solution usually adopted in the industry to obtain high-power LEDs is to bond the GaN layer to a metal-coated substrate, which then becomes a large-area reflective p-contact. This substrate also provides enhanced thermal dissipation. The sapphire substrate can then be removed ant the GaN layer thinned down, as we have done in Chapter 2 to obtain laser lift-off microcavity LEDs. However, theoretical study of MCLEDs revealed that even the ultimate structures have limited efficiency (40% at best) because a large fraction of the emitted light remains guided, even for very thin, monomode layers. This called for a strategy to extract this remaining light.

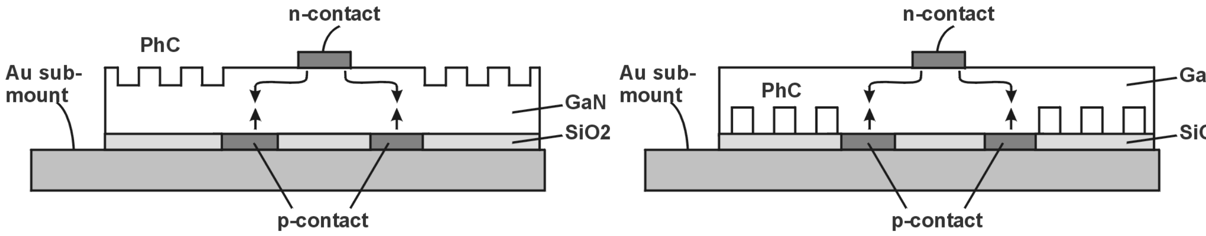

Figure 4.43: Schematic cross-sections of laser lift-off PhC LEDs, with PhCs formed in n-GaN (top) or p-GaN (bottom). Arrows represent current flow in the n and p GaN.

In the following, we study such flip-chipped, laser lift-off LEDs where a photonic crystal is formed to extract the light guided in the thin GaN layer. Fig. 4.43 presents a sketch of possible structures. As in the case of MCLEDs, we can take advantage of the current spreading of electrons in n-GaN to generate light above the p-GaN region. Two configurations are possible: the PhC region can be located at the periphery of the LED as shown on Fig. 4.43, or it can also be formed above the p-contact region, in which case light is generated in the patterned region.

4.3.2 Fabrication

Choice of the PhC location

The fabrication process of MCLEDs has already been presented in Chapter 2. The only difference in the present LEDs is the addition of a PhC at some point in the fabrication process. As for MCLEDs, the wafer bonding and laser lift-off process was performed by Tetsuo Fujii, while I took care of the PhC formation.

The PhC may be formed at several steps of the process, resulting in different structures as in Fig. 4.43. A first option is to etch the PhC in n-GaN in one of the initial steps (for instance, as a first step) and then proceed with the LLO-LED fabrication. In this case, the PhC is embedded close to the metal submount in the final structure. This also presents the advantage of making alignment rather easy: if alignment marks are written during the e-beam lithography, these can be used to align the lithographic masks. On the other hand, if the PhC is formed everywhere on the p-GaN surface, holes have to be injected through the PhC which may hinder good injection (especially since dry etching of the PhC is likely to damage the p-doping).

Another choice consists in performing the bonding, LLO and thinning steps before the PhC fabrication. Then, the PhC is formed on the n-GaN layer, either before or after mesa formation. In this case, alignment problems arise during the e-beam lithography: the e-beam pattern has to be aligned with the p-contacts already formed below the GaN layer. Moreover, if the PhC is formed as a final step (after the mesas and n-contacts), planarization of the e-beam resit can be an issue.

Fabrication

We fabricated several LLO-LEDs samples, using both of the above approaches. In these, the SiO_2 window layer was $\sim$ 200 nm thick. The p-electrode was made of RuO_2/Ni/Ag. The bonding substrate was an AlN ceramic covered with gold.

In the first case (PhCs in p-GaN) all PhC LEDs turned out to be shorted, whereas the classic LLO-LEDs on the same sample worked well. This is almost certainly due to an excessive etch depth of the PhC region, so that the metal deposited on the p-GaN before bonding reached the pn junction. Although the dry etch used was supposed not to exceed the height of the p-GaN layer, fluctuations in the etch rate are sometimes quite important and this scenario is plausible. Fig. 4.44 shows some of these LEDs.

Subsequently, we tried the second implementation: starting from fully processed LLO-LEDs, PhCs were formed on top of some LED mesas. Planarization of the e-beam resist turned out not to be a serious issue, because the mesas were large (800μm x 800μm), limiting the non-uniformity to the edges of the mesas. Likewise, alignment of the e-beam pattern with the mesas was made easy by the difference in electron backscattering between GaN and the metallic substrate, which made the edges of the mesas clearly visible on the e-beam writer.

Unfortunately, some damage occurred to the metallic submount during the PhC formation (probably during a gold etch dip). What happened exactly is unclear, but as a consequence the thermal dissipation of the LEDs became very poor: upon current injection, the submount started boiling on

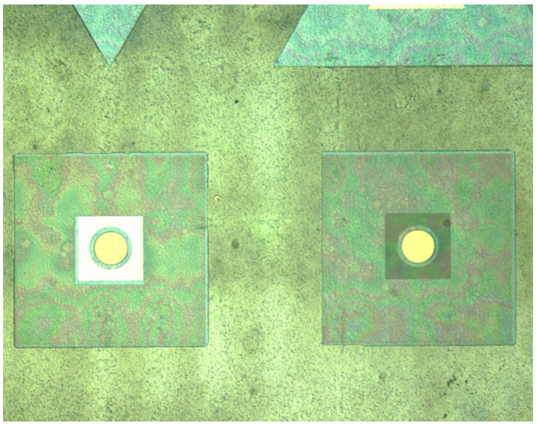

Figure 4.44: Microscope picture of PhC-LLO LEDs with a PhC formed in p-GaN and embedded in the LED. (Left LED) the PhC is formed around the p-contact. (Right LED) the PhC is formed everywhere under the mesa, including the p-contact. Both LEDs are shorted.

the periphery of the LEDs, rapidly destroying them. This may be attributed to an accidental thinning of the Au submount which increased its sheet resistance. Cooling the LEDs while operating them was unsuccessful. In order to increase thermal dissipation, an additional thick Ag/Au layer was deposited around the LED mesas. This layer effectively solved the problem of heating, but on the other hand shorted the LEDs (probably due to a minute misalignment of the lithographic mask with the mesas before this metal deposition). Fig. 4.45 displays several pictures of the fabricated LEDs, and Fig. 4.46 an AFM image of a PhC region.

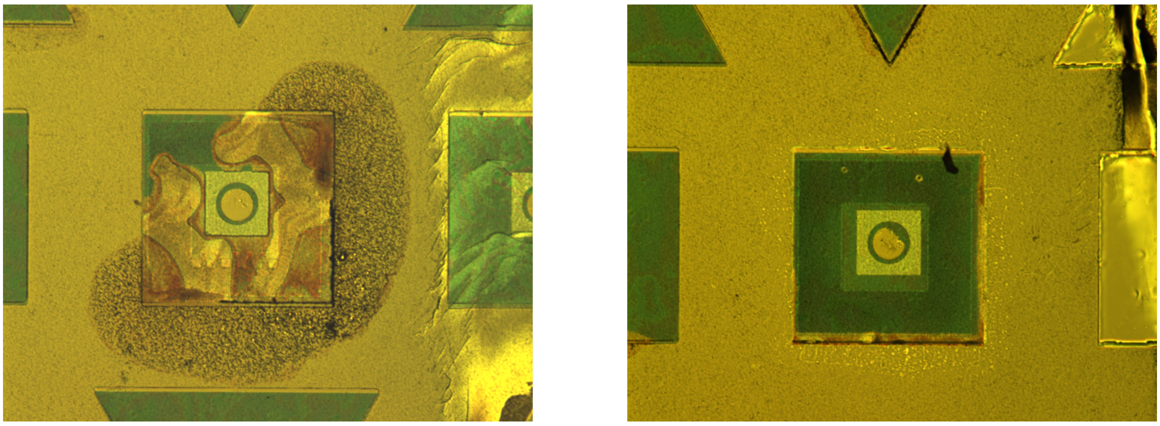

Figure 4.45: Microscope picture of PhC-LLO LEDs with a PhC formed in n-GaN on top of the mesa. (Left) Bad thermal dissipation caused the metallic submount to boil and cover the LEDs. (Right) LED after metal re-deposition: thermal dissipation is increased but the LED is partially shorted.

As a result, these last LEDs could hardly be operated and displayed very poor electrical characteristics. A strong current leakage was present, and high currents (dozens of mA DC) had to be used to generate a measurable light signal. Thus, electrical characterization of these LEDs makes little sense. Fortunately, angle-resolved electroluminescence spectra could still be acquired to observe their photonic properties.

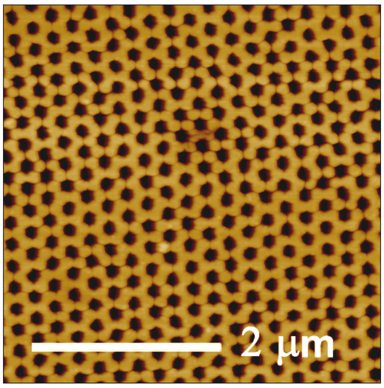

Figure 4.46: AFM image of the PhC pattern on an LLO-LED which could be characterized ($a = 215$ nm).

4.3.3 Photonic characterization

Thanks to the naturally non-uniform chemico-mechanical etching process, several mesas height were obtained on the same sample. These ranged from more than 1μm to a few hundred nm. Therefore, several PhC-LLO LEDs with varying GaN thickness could be characterized by angle-resolved electroluminescence. Fig. 4.47 presents some of these angular measurements.

Photonic bands are visible on all LEDs. Depending on the LED thickness, both the direct emission and the photonic bands are affected. The Fabry-Perot fringe spacing of the direct emission increases for thinner GaN thickness, as in the case of regular MCLEDs. By inspecting the spectra, it can be seen that the first LED of Fig. 4.47 has at least two modes in the air cone (corresponding to a rather thick LED), while the last LED displays so-called 'rabbit's ears' and is clearly in the micro-cavity regime. The thickness t of the GaN layer can be estimated accurately by fitting the fringe spacing, using the same formula as for regular MCLEDs. We obtain respectively for the three LEDs: $t = 1\mu$m, ~ 700 nm and 400 nm. We label these LEDs as 1, 2 and 3. The determination is not as accurate for LED 2 as for the others because the Fabry-Perot fringes are less pronounced in the spectra. This may be due to a local inhomogeneity in the GaN thickness.

In order to observe the PhC's bands more clearly, we once again convert these spectra to band structures. The result, shown on Fig. 4.48, confirms what is already apparent on the angular spectra: the number of photonic bands decreases for thinner GaN layers. This is of course expected since thicker GaN waveguides support more guided modes. The theoretical light line of GaN is also superimposed on these spectra. In addition, the Fabry-Pérot fringes of direct emission are clearly visible on this spectra, especially for LED 1.

The first LED supports numerous guided modes. It is still rather thick and does not differ significantly in nature from the LEDs characterized previously. Among visible modes, those of lowest n_{eff} appear fainter than those of higher n_{eff}. The second LED supports less modes (roughly 5). Finally, the last and thinnest LED only has 2 visible guided modes. Moreover, the blue shift between the GaN line and the first guided mode in this LED is much larger than for the two others, evidencing a thinner waveguide where even the fundamental guided mode has an index significantly smaller than n_{GaN}. The photonic regime of this LED is very different from that of thick, multimode LEDs, and the interaction between the PhC and the modes can be expected to be much stronger.

In addition, modes of low effective index (typically $n_{eff} < 1.7$) do not appear on the band structures. In principle, these modes should now be extracted because no sapphire is present. A possible explanation for their absence is bad coupling between guided modes of the unpatterned region (where light is generated) and these Bloch modes, as already evoked in section 4.1.1. Indeed, these Bloch

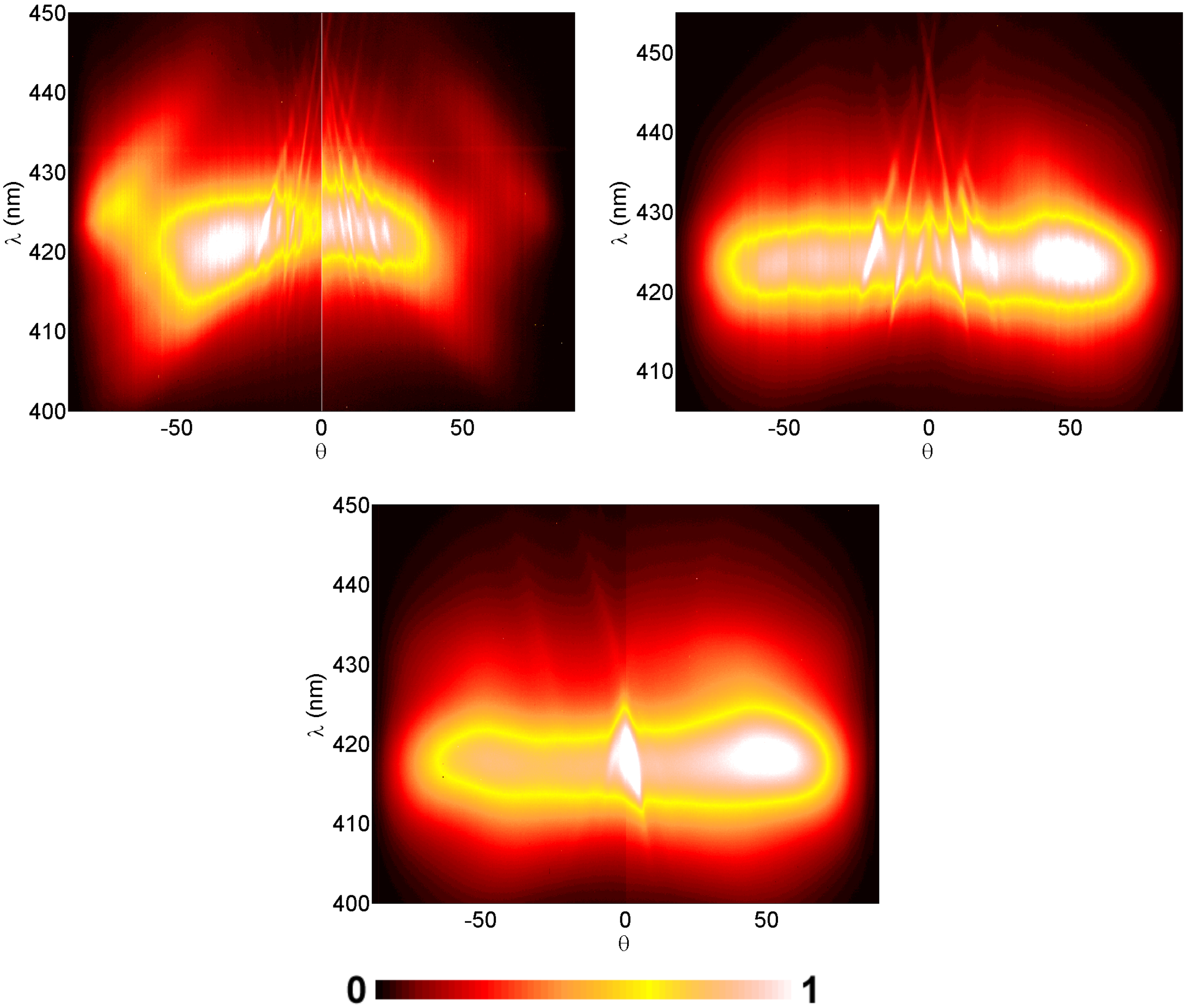

Figure 4.47: Angle-resolved spectra of PhC-LLO LEDs with varying GaN thickness t (ΓM direction, TE polarization). (Top left) $t = 1\mu$m. This LED deteriorated while the spectrum was acquired, so that its intensity decayed from left to right. Therefore, the intensity of the right half of the spectrum is multiplied by a factor x1.5 to observe photonic modes on both sides. (Top right) $t \sim 600$ nm. (Bottom) $t = 400$ nm. This spectrum was acquired in two halves, hence the small stitching mismatch at $\theta = 0$.

modes penetrate in the PhC region and have a vertical profile very different from that of guided modes in the unpatterned region. In addition modes with $n_{eff} < 1.5$ are propagative in the SiO_2 layer and may experience strong loss due to direct absorption in the Au submount. The question of metal absorption will be discussed further.

An unusual feature of all these spectra is the strong variations in intensity along photonic bands. For instance, in the thinnest LED, the fundamental mode is quite intense at low frequencies but then disappears at $u > 0.48$, before reappearing for $u > 0.5$. Likewise, the associated 'B-type' mode[14] is only visible between $u = 0.47$ and $u = 0.5$. Similar oscillations can be seen on other spectra, although they are less apparent.

These oscillations are best viewed on another spectrum, corresponding to LED 2 measured along

---

[14] In the nomenclature of Chapter 3, these are modes whose folding in the first Brillouin zone is not collinear to $k_{//}$, e.g. modes with a 'curved' dispersion.

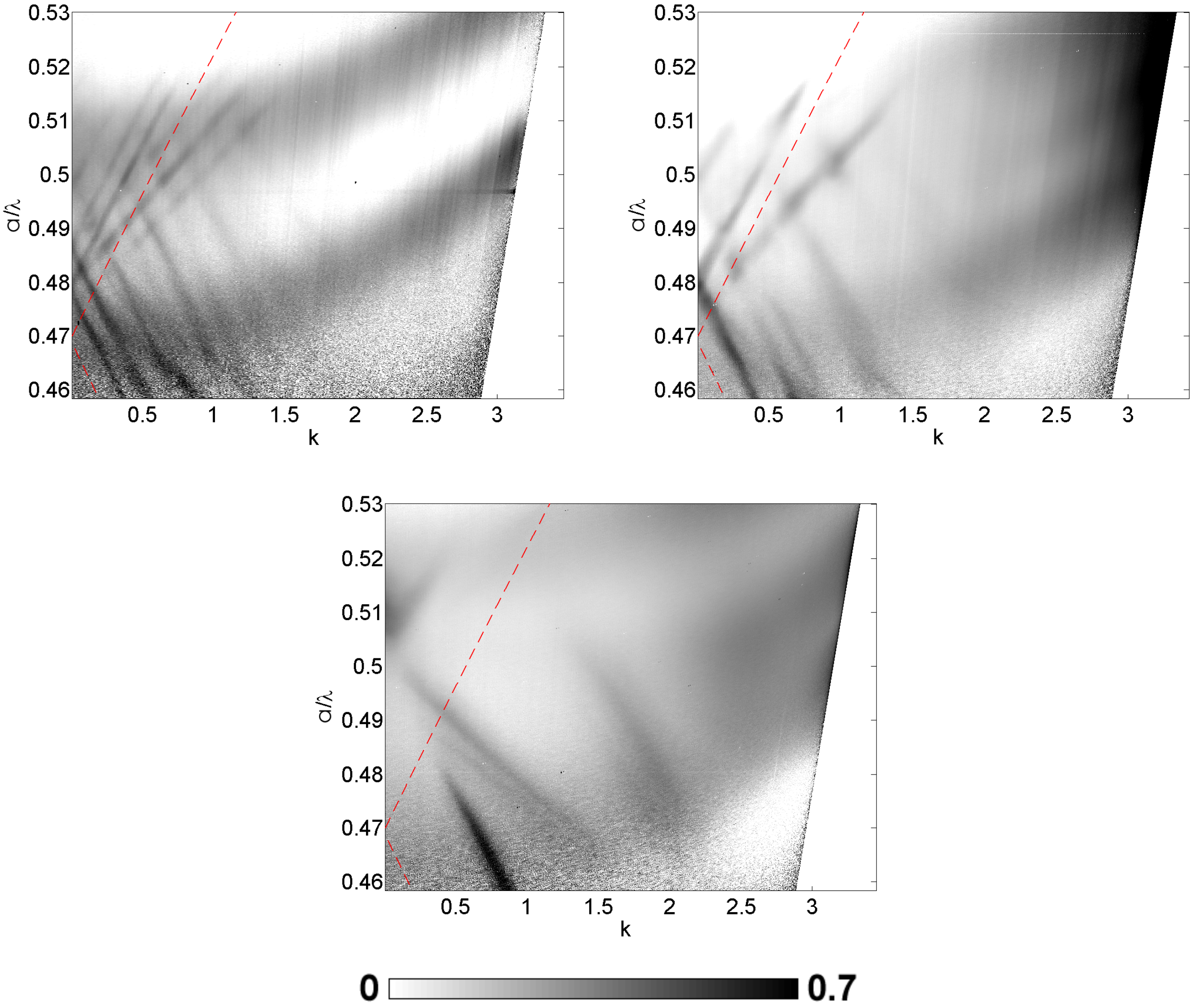

Figure 4.48: Band structure obtained from the angular spectra of Fig. 4.47. The dotted line indicates the light line of GaN ($\omega = k_{//}c/n_{GaN}$). The number of photonic bands decreases for thinner GaN, evidencing that less guided modes are supported.

ΓM in TM polarization. In this spectrum, one photonic band is clearly visible on a wide range of frequencies, and its oscillations are well defined. Therefore, we can follow the band and plot its intensity as a function of frequency. The total band structure and the intensity of this band are plotted on Fig. 4.49. Two features are visible on the band's intensity: first, it decays with frequency because of higher absorption at higher energy, a feature already observed for photonic bands in GaN-on-sapphire LEDs. Second, the oscillations already described modulate the intensity. They have a rather strong contrast of $\sim 60\%$, although a precise evaluation is difficult due to the additional decay with frequency.

These oscillations are reminiscent of the Fabry-Perot-like oscillations already observed in GaN-on-sapphire structures. However, these earlier oscillations corresponded to diffracted light being preferentially emitted upwards (to air) or downwards (to sapphire). Here the oscillations manifest the equivalent phenomenon in the LLO structure: a competition between diffraction to air and absorption in the metallic mirror. Modeling of metal absorption in the next section will confirm this interpretation.

One may also account for the oscillations by suggesting that the extraction efficiency to air oscillates with frequency and that only part of the guided light is extracted when the extraction efficiency is low. However, direct observation of the LEDs under current injection confirms that guided light only propagates for a very short distance in the GaN layer: luminescence of the PhC is only visible within a few dozen microns of the light generation region. Therefore, we have to conclude that the guided modes are completely absorbed/extracted within the LED scale.

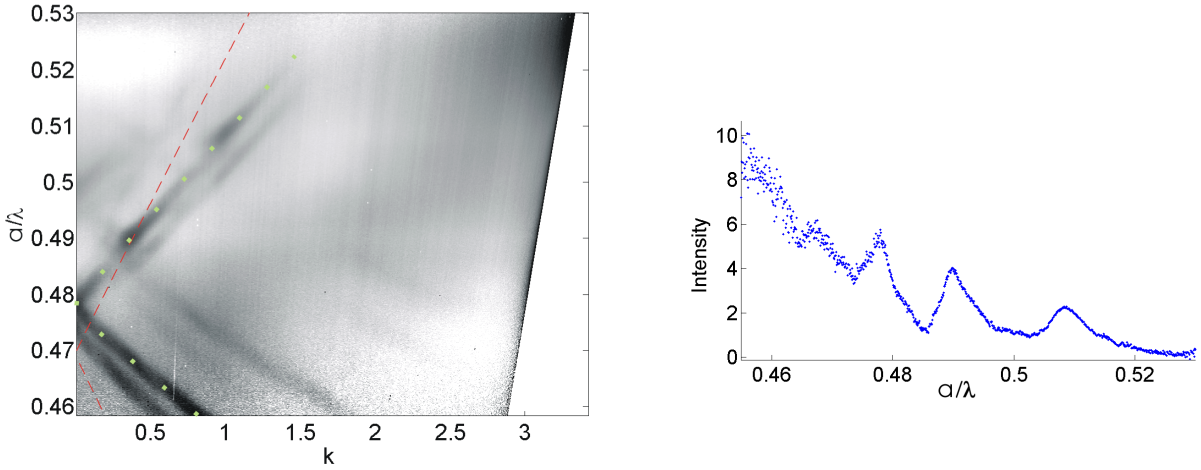

Figure 4.49: (Left) Band structure of LED 2 along ΓM in TM polarization (log scale). One photonic band (with dots superimposed) is well-defined and can be followed. (Right) Intensity of this band as a function of frequency (linear scale). The background signal corresponding to direct emission from the LED has been subtracted to show only the photonic band's signal. The intensity decays with frequency, evidencing overall higher absorption at higher energy. In addition, it displays rather strong oscillations in intensity.

4.3.4 Modelling, metal losses

It appears that loss in the metallic submount is significant, although we expected this layer to act as a mirror and guided light to be diffracted to air. To investigate this effect, we now resort to 3D modeling of the structures, which gives access to the balance of power of Bloch modes. LEDs 1 and 3 were modeled to account for the measured band structures. A good fit is harder to obtain than for GaN-on-sapphire structures, for a number of reasons. First, there is more uncertainty regarding the structure's parameters (depth and sidewall profile of the PhC, exact thickness of the GaN layer for each LED and of the SiO_2 layer between GaN and metal). Second, because photonic interactions are more intense, small variations in these parameters can have a strong effect on the band structure, especially as regards the oscillatory effects we wish to study. This is especially true for LED 3, where the unetched GaN layer is very thin and the fundamental mode's behavior varies rapidly with the structure's details. From AFM measurements, the PhC is at least 220 nm deep (this is a lower bound because the tip's shape prevents us from reaching the bottom of the holes) and has a filling factor $f \sim 0.38$.

LED 1 was well fitted without much difficulty, with the following parameters: 170 nm of SiO_2, a total GaN thickness of 1000 nm, and a PhC of depth 270 nm and filling factor 0.39. LED 3 requested more efforts, and the fit was obtained with: 200 nm of SiO_2, a total GaN thickness of 410 nm, and a PhC of depth 270 nm and filling factor 0.37. It should be noted that these values are in good agreement with the nominal values, and that both LEDs could be fitted using consistent PhC parameters. The following refractive indexes were used: $n_{SiO2} = 1.5$, $n_{Au} = 1.47 + 1.95i$, n_{GaN} as given in Ref. [20]

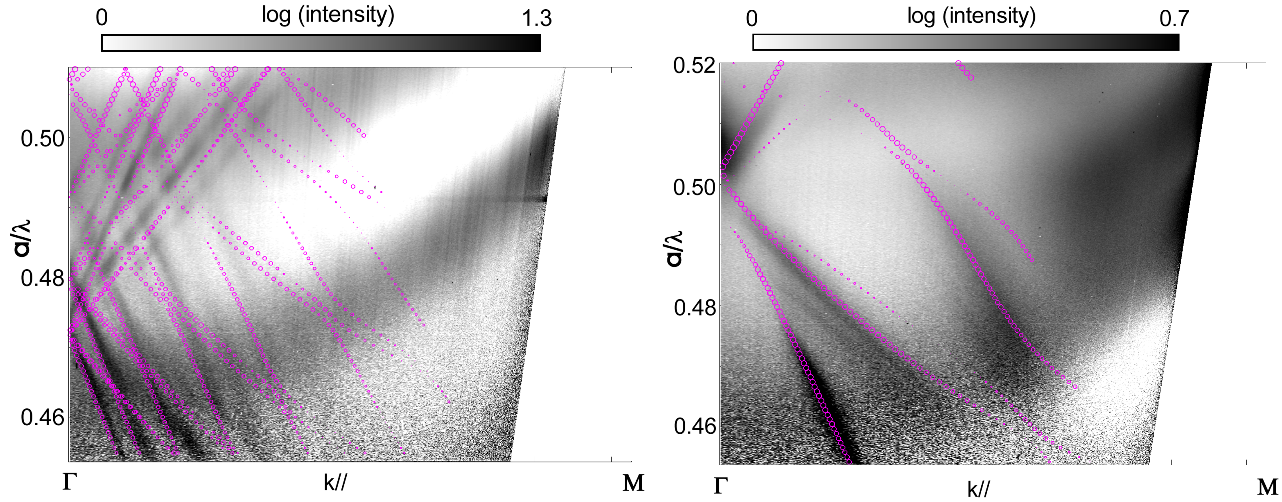

Figure 4.50: Fit of the measured band structures of LEDs 1 and 3 by a 3D calculation. The pink dots represent the calculated bands. The size of the dots is proportional to the intensity of light diffracted to air.

(taking dispersion into account). The result of the calculations, superimposed with the experimental band structures, is shown on Fig. 4.50.

The theoretical band structure follows well the dispersion of the measured bands. As already discussed, bands of low effective index ($n_{eff} < 1.7$) are not measured experimentally. Therefore the corresponding theoretical bands are not displayed. The calculated bands of LED 1 have a nearly free-photon like dispersion, in accordance with the thickness of the waveguide. On the other hand, the dispersion of LED 3 differs more significantly from the free-photon approximation.

The size of the dots in the theoretical band structures is proportional to the intensity diffracted to air. More precisely, the radius of the dots is proportional to $\eta = P_{air}/P_{in}$, where P_{air} is the power flow radiated to air and P_{in} the incoming power flow of a Bloch mode. The oscillatory behavior observed experimentally is rather well reproduced this way. It also appears that some photonic bands are not diffracted to air at all, especially in the case of LED 3.

In order to study further this effect, let us now consider three model structures where metal losses behave differently:

- a) A structure made of an Au mirror, a very thin (20 nm) SiO_2 layer and a 600-nm thick GaN layer etched halfway by a PhC (triangular lattice, filling factor 0.3, lattice constant 200 nm)
- b) Same as (a) but with 200 nm of SiO_2
- c) Same as (b) but with an Ag mirror instead of Au, known to be a poor reflector for blue wavelengths

All of these structures are rather thin and support only a few Bloch modes. For each structure, we compute the ratio η for the lowest-order Bloch mode in the ΓM direction, as a function of frequency (Fig. 4.51). For structure a, the loss in the mirror is very strong at all frequencies, because the thin SiO_2 layer does not isolate the Bloch mode, which penetrates strongly in the Au layer. More precisely, the main harmonic of the Bloch mode leaks through the SiO_2 into the Au layer, leading to strong loss at all frequencies. For structure b, direct loss in the mirror is limited by the thicker SiO2 layer. η oscillates due to vertical interferences of the radiated component of the Bloch mode. More precisely, the radiation rate to the Au submount only slightly varies with frequency, whereas the extraction rate to air undergoes large oscillations. In conclusion, high metal losses happen when extraction to air is not

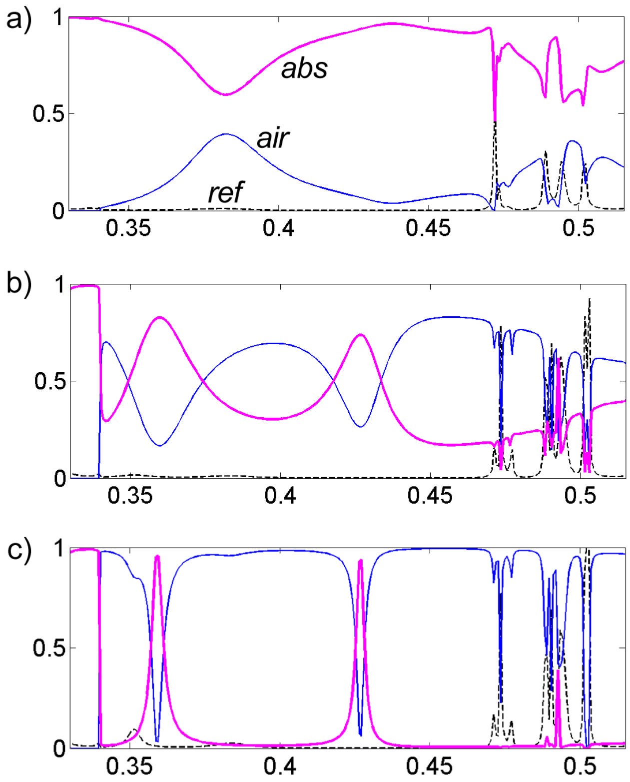

Figure 4.51: Power flows of the fundamental Bloch mode. Thin line: P_{air}/P_{in} Thick line: P_{abs}/P_{in} Dashed line: P_{ref}/P_{in}, (P_{in}: incoming power of the Bloch mode, P_{air}: power radiated to air, P_{abs}: power absorbed in the mirror, P_{ref}: power reflected backwards). (a,b,c) correspond to the structures described in the text. For $u < 0.34$ the mode is under the light cone and $P_{air} = 0$. For $u \sim 0.48 - 0.5$ the mode reaches the edge of the Brillouin zone and undergoes mini-gaps and anticrossing with other modes.

sufficient to compete with metal absorption. As a whole, the loss remains rather high in this structure, on the order or 50%. For structure c, loss is very small thanks to the better reflective properties of silver: apart from some sharp absorption dips, η exceeds 90%.

The fabricated LEDs are in the regime of structure b, where a significant fraction of the guided power is still lost in the metal. The contrast of the oscillations for structure b is 60%, similar to that estimated experimentally from LED 2. On the other hand the interfrange of the oscillations does not match, which comes from various reasons: the thicknesses are not the same, index dispersion is not considered in this calculation, and the modes we considered in Fig. 4.49 are B-type.[15]

In the case of the last structure, where Ag absorbs little light, large windows of good extraction efficiency appear. Therefore, this structure would be a reasonable choice for high-efficiency LLO-PhC LEDs.

4.3.5 Photonic effects in thin PhC-LLO LEDs

Another interesting feature of the thinnest LEDs is revealed by Fig. 4.51: the presence of regions of high reflexion, or stop bands. At these frequencies, the PhC acts as a reflector and a large fraction of the incident Bloch mode is reflected backwards. Although in principle any periodic structure can

---

[15] This means that we are looking at the projection of the mode on an axis which is not colinear to its 'main' k-component, so that the mode effectively propagates for a larger distance, yielding more oscillations in the measurement direction.

open band gaps, this is never observed with shallow PhCs in GaN-on-sapphire because the effect of the photonic crystal is very weak and the gaps are much too small to be seen. On the other hand, thinning the GaN layer brings us to a regime where the few remaining guided modes interact strongly with the PhC.

Such effects are present in LED 3, which is thin enough to produce strong photonic interactions. Therefore, it is instructing to draw again its theoretical band structure, making all bands apparent. However, this structure turns out to be rather complex. Before coming to it, let us first observe in a simpler case the origin and appearance of strongly-modulated photonic structures.

We consider a structure made of an Ag substrate, 100 nm of SiO2, and a 400 nm thick GaN waveguide (with constant index 2.5 for simplicity) etched halfway through by a PhC (triangular lattice, $f = 0.35$, $a = 200\,\mathrm{nm}$) with air as a superstrate. This structure supports a few guided modes, depending on frequency. Moreover Ag acts as a good mirror, so that damping and absorption effects should be limited. We first compute the *unfolded* band structure in a wide range of frequencies ($u = 0.2$ to 0.5). The result is shown on Fig. 4.52.

To some extent, the dispersion of 'simple' guided modes can still be recognized. All modes are located between the lines of GaN and air. Both (pseudo-)TE and TM modes are present, but their ordering no longer follows that of a simple waveguide because the interaction with the PhC depends on polarization. At high enough frequency ($u > 0.42$), 'B-type' modes also appear.

In addition, several band gaps appear. To make them more visible, modes with an imaginary wavevector $k'' > 0.1$ are plotted as red dots. Some gaps are located at the edge of the first Brillouin zone (M point) and correspond to the classic picture of a band gap formed by the interaction of a forward-propagating mode and its backward-propagating counterpart. Other gaps appear *inside* the Brillouin zones and are due to interaction between two different modes (for instance, the forward-propagating fundamental mode TE_1 and the backward-propagating third mode TE_3). Such gaps are sometimes termed *mini-stopbands*, and are reminiscent of the anticrossings between various modes of a 2D PhC waveguide.[21] The 'classic gaps' are almost vertical (e.g. they are localized at $k_{//} = G_0/2$) − they should be exactly vertical in a lossless structure, but the small absorption in Ag breaks this symmetry property. On the other hand the value of $k_{//}$ varies inside the mini-stopbands.

When the modes cross the folded light line, they become leaky and diffraction to air becomes possible. Modes which radiate more than 80% of their power to air are plotted as green dots. As can be seen, this is not the case for all modes. Closer analysis of the modes reveals that the modes which are not well diffracted to air are mostly (pseudo-)TM modes, whose extraction efficiency is always lower than that of (pseudo)-TE modes. This is in principle not a problem for light extraction because guided light emitted by quantum wells is TE-polarized and should not feed these modes.

We can now fold this relation in the first Brillouin zone (Fig. 4.52). The origin of mini-stopbands now becomes clear: they are located at the anticrossings of two counter-propagating modes of different natures. Note that pseudo-TE and TM modes do not interact because of their symmetry (this is only true in the high-symmetry directions of the crystal). However, some mini-stopbands can not be understood in this way: they occur above the (unfolded) air line where no forward-propagating mode exists. To account for their existence, we have to consider Fabry-Pérot modes located above the air light line. Of course, these modes are not well-defined in terms of $k_{//}$ (they are very lossy).

However, the central value of $k_{//}$ is approximately found by the hybrid numerical method (see a discussion of this property in Chapter 6). As can be seen, these modes become confined Bloch modes when they cross the air line. It also appears that some mini-stopbands are due to interaction between a Fabry-Pérot mode and a Bloch mode. From the point of view of grating theory, such events would be associated with Fano resonances in the reflexion spectrum of the structure.

We are now ready to study the theoretical band structure of LED 3, where all the photonic bands are made apparent (Fig. 4.53). Here, the full band structure is revealed. The bands observed on Fig. 4.50

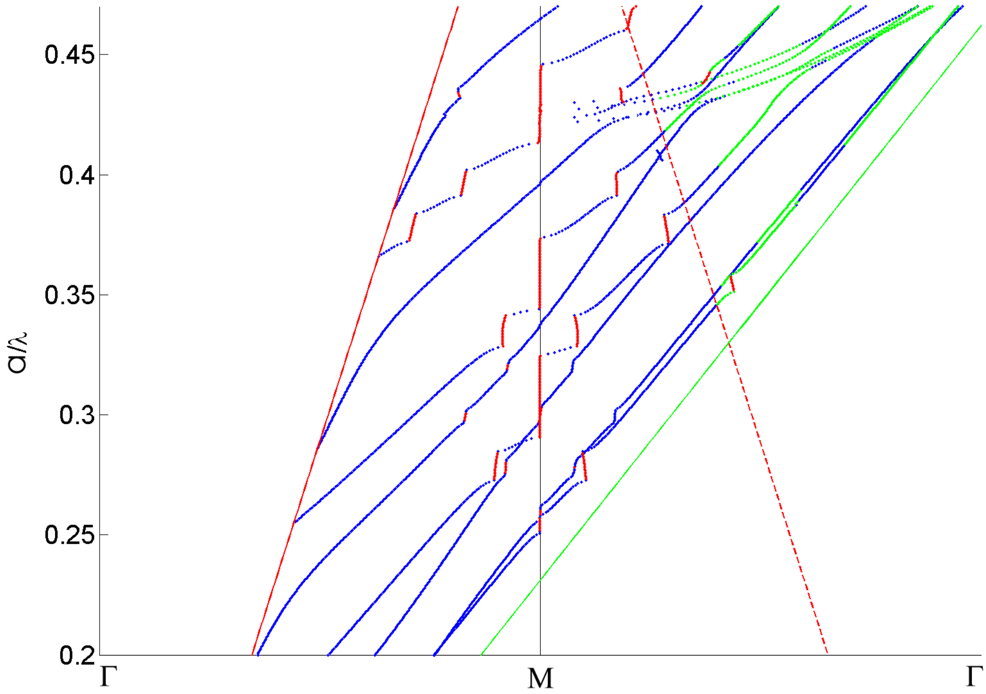

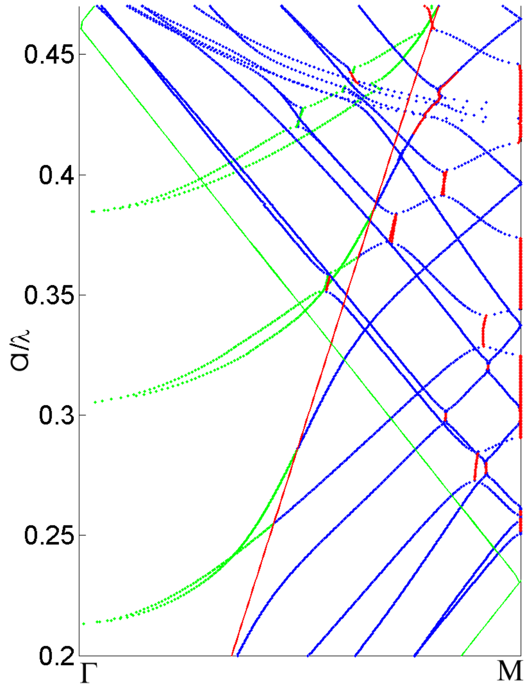

Figure 4.52: Band structure of a thin LLO structure on an Ag submount. (Top) Unfolded band structure. Blue points: propagative Bloch modes. Red points: strongly evanescent Bloch modes ($Im(k'') > 0.1$), corresponding to band gaps. Green dots: Air modes (more than 80% of the mode's power is diffracted to air). The red, green and dashed red lines correspond to the air cone, GaN cone and folded air cone respectively. Air modes only appear above the folded air cone. (Bottom) Same as above, folded in the first Brillouin zone. For clarity, air modes are not distinguished. In addition, Fabry-Pérot modes located above the air cone appear in green: these interact with propagative Bloch modes and cause band gap openings.

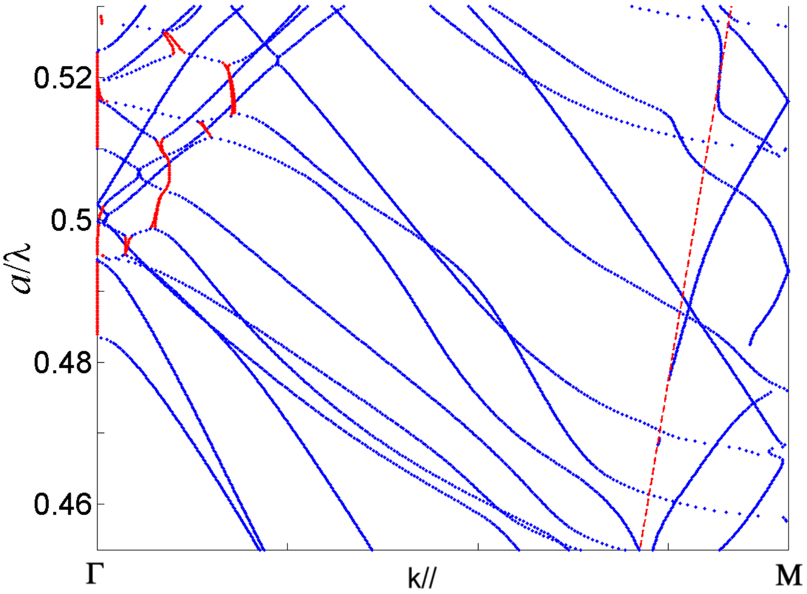

Figure 4.53: Theoretical band structure of LED 3, all bands being apparent. A number of 'dark' bands, which do not appear on the measurement, are revealed. The red dots correspond to mini-stopbands ($Im(k'') > 0.1$).

can be recognized, among many other bands. Some of the bands are not observed experimentally because of their low extraction efficiency to air, others because they are mostly TM-polarized and do not receive much emitted light. Again, a few mini-stopbands can be observed. However, they are not as vertical or properly defined as in the previous calculations: this is caused by the damping in the gold layer, which smooths the gaps and reduces their strength. In general, the dispersion of the bands differs strongly from that of free photons. This is both an effect of the higher photonic strength of the grating, and of the damping in gold.

4.3.6 Conclusion

In summary, PhC-LLO LEDs prove to be promising but very challenging structures. The fabrication process is difficult and the yield is still poor. Moreover, while these LEDs may initially seem like an ideal structure where light can only be extracted to air, losses due to metal absorption can be strong and spoiled the efficiency of the fabricated LEDs. As in the case of other PhC-LEDs, a design effort is necessary in order to circumvent these losses. Calculations indicate that the problem of metal loss can indeed be addressed, and give hope for ultimate high-efficiency LEDs.

4.4 Lateral epitaxial overgrowth PhC-LEDs

Previous implementations have evidenced the key issues for efficient PhC LEDs: designing the PhC so that it interacts well with guided modes, and can easily be integrated in an realistic LED structure, taking into account the question of contacts formation. LLO-PhC LEDs are a viable answer to these concerns, but suffer from difficult fabrication. Among other issues, etching the PhC in the GaN surface is a possible cause for damage because the *pn* junction can be shorted, as happened in some of our LEDs. In addition, the GaN layer must be thinned down significantly for the lowest-order modes to interact with the PhC.

Because of all these limitations, it appears that an ideal structure should avoid surface etching of the GaN layer altogether: ideally, the PhC should be *embedded* in the epitaxial layer. Here, we present a new strategy to obtain such structures.

4.4.1 LEO-PhC LEDs: Principle

If one aims at embedding the PhC in the GaN layer, two options are possible: a PhC made of air holes (obtained for instance by etching) or of another material such as a dielectric. In any case, GaN must then be regrown to bury the PhC. Conventionally, GaN regrowth is mainly used in Lateral Epitaxial Overgrowth (LEO) structures, in order to reduce the density of threading dislocations. This is particularly interesting to obtain high-quality material for laser diodes, where material defects condition the laser's threshold and lifetime. Fig. 4.54 shows how LEO improves material quality. The coalescence of the wings usually poses no problem: they are epitaxially coherent with the underlying crystal.

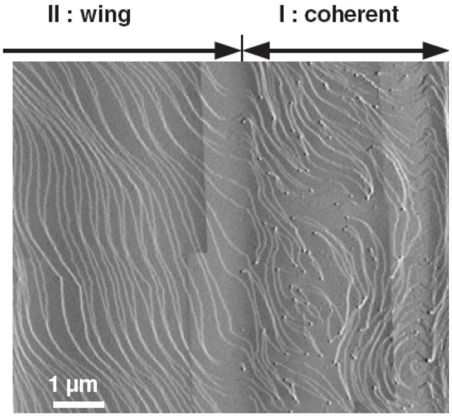

Figure 4.54: (After Ref. [22]) AFM scan of LEO GaN showing the impact on material quality. The right half of the image corresponds to GaN grown vertically ('coherent'). Many threading dislocations, appearing as small black dots in the surface, are present. The left half corresponds to GaN grown laterally from the coherent region over a Si mask. No dislocation is visible in this region.

The typical feature size for conventional LEO is on the order of dozens of microns, and the mask is usually a dielectric such as SiN or SiO_2. It is well known that, depending on the regrowth parameters (temperature, partial pressure, introduction of additional species...) the lateral to vertical ratio of the growth can be control over a wide range. Fig. 4.55 illustrates how variable growth conditions (addition of Mg here) influences the growth morphology. For a more complete discussion, Ref [22] presents a thorough review of LEO in GaN.

Here, our idea is to adapt the LEO process, using a 2D periodic mask with periods $a \sim 200nm$. In this case, in addition to being a mask for overgrowth, the dielectric layer also acts as a PhC extractor. Since the PhC is now inside the GaN matrix, its efficiency should be enhanced. Besides, because the

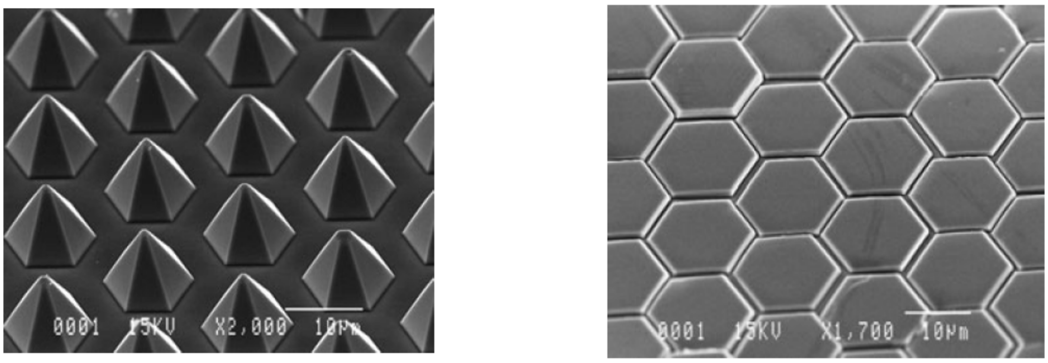

Figure 4.55: (After Refs. [22, 23, 24]) LEO on a 2-dimensional patterned SiN mask. (Left) GaN regrows along the 6 preferential directions of the wurtzite lattice, forming pyramids. (Right) Same growth conditions as previously, except for the addition of Mg compounds in the vapor phase.

average index of the LEO mask layer is lower than that of GaN, it also acts as a lower-index confining layer which can modify the guided modes distribution. Finally, the *p*-GaN surface is planar and a large area electrode can now be formed over the PhC region. Therefore, this structure addresses all the most critical points of GaN PhC-LEDs.

4.4.2 LEO-PhC LEDs: regimes of operation

The most simple case of LEO-PhC LED is depicted on Fig. 4.56. Coalescence is first obtained on an 'usual' scale (more than 1μm) then the *pn* junction is grown. While this makes coalescence easier and ensures good material quality, the interest of the structure from a photonic point of view is not completely obvious. The top GaN region (the region above the LEO mask) is multimode, and supports numerous low-order modes. As has been seen previously, their interaction with the PhC is small. The situation may be slightly better than in the case of a PhC etched in air, because the bottom GaN region tends to attract the guided modes, in contrast to the strongly repelling effect of air. Besides, the average index in the PhC region is a little higher because air is replaced by dielectric, which can increase mode penetration. All this may lead to slightly higher extraction of low-order modes, but probably not to a sufficient value.

The second structure depicted on Fig. 4.56 is more promising. Here, coalescence is achieved within 100 to 200 nm and the *pn* junction is grown as thin as possible. This results in a thin GaN layer on top of the LEO mask. We are now in the configuration already explored by adding a low-index confining layer in the epitaxial structure: if the GaN cap layer is thin enough, it defines one or a few 'cap layer modes' (CLM) which receive a large part of the light emission and are well diffracted by the PhC. However, all parameters are now much more favorable. First, the average index of the LEO layer can be very low (~ 2 for a filling factor of 0.5) so that confinement of the CLM is very efficient: it can channel all light emission between effective indices 2 and 2.5. Moreover, the overlap between the CLM and the PhC may be better because the repelling effect of air 'pushes' the CLM downwards to the LEO region. Finally, in a good configuration, it can be expected that high-order modes as well will feel the effect of the PhC more, because it is now located inside the GaN region.

On the other hand, the challenges raised by this structure are obviously higher. While LEO is well mastered over 1D stripes of μm-large dielectric, going to a 2D pattern with a period of 200 nm is likely to change the behavior of growth. Especially, obtaining good coalescence within a few hundred nm is far from trivial. On the positive side, the wurtzite lattice of GaN is well adapted to the symmetry of

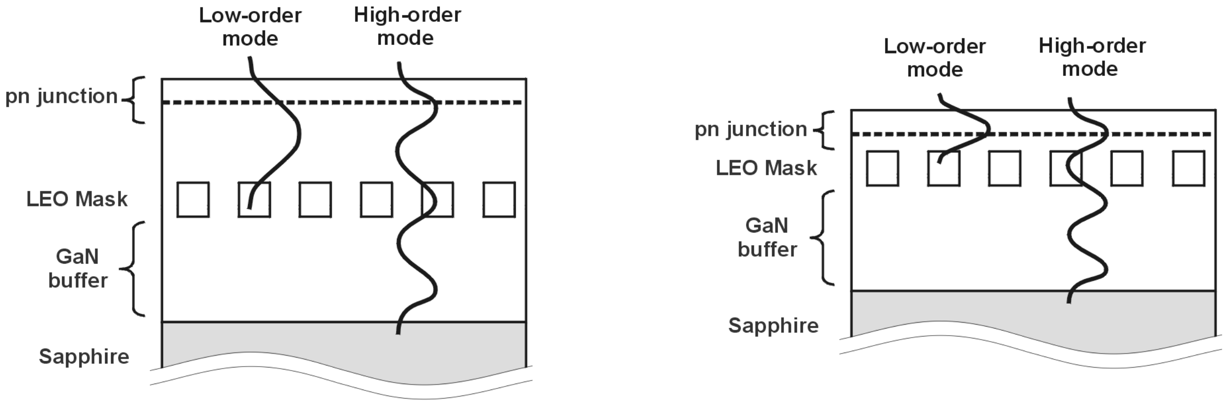

Figure 4.56: (Left) LEO-PhC structure using a large coalescence thickness (one to a few μm) for good coalescence. (Right) same with a very thin coalescence ($\sim$ 100 nm) and a *pn* junction close to the LEO mask

.

triangular PhCs, provided of course both lattices are well-aligned. An additional challenge is raised by the effect of the dielectric on the GaN: the most obvious choice is SiO_2 because of its low index ($n = 1.5$), but outdiffusion of oxygen may contaminate the doping of GaN. In this case, SiN may be preferable in spite of its higher index $n \sim 2$.

4.4.3 Modeling of PhC-LEO LEDs

Modeling of these structures is made difficult by the large space of parameters available. In principle, one can consider varying the mask material, its thickness, the filling factor of the PhC, and the thickness of GaN both in the buffer and cap layer. Of course, fabrication will eventually limit the design: for instance, thin film coalescence over a thick LEO mask is likely to be problematic. Moreover, the *pn* junction itself can not be made arbitrarily thin, be it only because *p*-doping of GaN requires a certain thickness (100 nm at least).

However, these limitations are still unclear. So far, fabrication efforts by Kelly McGroddy at UCSB have been hindered by the difficulty to obtain reproducible large-scale patterning of SiO_2 on a GaN substrate. This is mainly due to the use of holographic lithography to define the PhC pattern, a technique which critically depends on the reflectivity of the sample's surface and hence on the exact thickness of the SiO_2 and resist layers. However, Frederic Diana recently obtained very promising results using nano-imprint lithography on structures with a similar scale. Use of this method can be expected to solve the issue of process control as regards the PhC formation. The real limitation is expected to be found in the coalescence thickness needed for regrowth on small-scale 2D patterns.

Therefore, optimization of the photonic properties an LEO-LED makes little sense at this point, because the result is likely not to be within the bounds of feasible structures. I will only give a simplified discussion of the influence of a few parameters.

One of the most important figures of merit for such LEDs is their ability to confine and extract a CLM: their efficiency relies on this principle. However, studying the behavior of the CLM in a realistic structure is made awkward by multiple anticrossings with the excited modes: it is very difficult to 'follow' the mode properly. This phenomenon is similar to that observed on Fig. 4.10 for the CLM created by an AlGaN layer, but its magnitude is here greatly enhanced by the stronger photonic strength of the grating and its position. To circumvent this difficulty, we replace the actual structure (GaN buffer + sapphire substrate) by an infinite GaN substrate. Thus, high order modes no longer exist and anticrossings are avoided. For the CLM to be well-defined, we deliberately attribute an index of $n = 2.5$ to GaN in the cap layer, and $n = 2.4$ to the GaN substrate. This avoids leakage of the CLM in the GaN substrate, and does not modify excessively the dispersion of the CLM because its index is typically $n_{eff} = 2.45$ (even in the absence of this trick). With these approximations, the CLM can easily be followed when the structure's parameters are varied. Fig. 4.57 shows the variation of the extraction efficiency of the CLM with the thicknesses of the GaN cap layer and of the LEO layer.

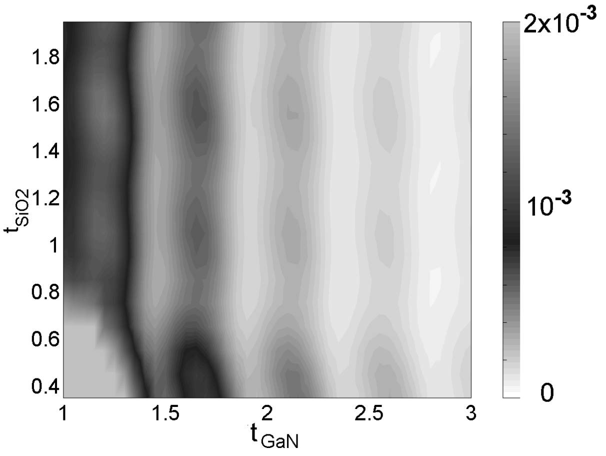

Figure 4.57: Imaginary part of the wavevector (k'') as a function of the GaN cap layer thickness and SiO2 LEO mask thickness (for a PhC with $f = 0.5$ along ΓM and a normalized frequency $u = 0.44$, close to the second Bragg order.). The saturation of the scale for thin GaN and SiO$_2$ is an artifact: it corresponds to a non-localized CLM. k'' is higher than 10^{-3} only for thin GaN cap layer (less than 2). An oscillatory behavior is observed with the SiO$_2$ thickness (see the local maxima with varying t_{SiO2} for $t_{GaN} = 1.7$). It is linked to vertical interferences of the radiative harmonic of the Bloch mode, as in the case of classic GaN-on-sapphire structures.

The conclusion is somewhat lukewarm: efficient extraction of the CLM (say $k'' > 10^{-3}a^{-1}$) is only attained for very thin cap layers: t_{GaN} less than $2a$. This result is actually fully consistent with the discussion of section 4.1.1 where we came to the conclusion that a waveguide needs to be close to cutoff for efficient extraction of the fundamental mode. Here, when $t_{GaN} > 2a$, the CLM is well accommodated in the cap layer and extraction is modest. This highlights the fabrication challenge represented by the LEO approach. In practice, good values are still obtained around $t_{GaN} \sim 1.7a$, corresponding to a total GaN thickness $\sim 350-400$ nm. Although thin, this value still seems reasonable.

As regards the SiO$_2$ thickness, smooth oscillations appear. This is convenient because the SiO$_2$ thickness can be accurately controlled during fabrication, so that an optimal point can be targeted - for instance $t_{SiO2} = 1$ according to Fig. 4.57.

4.4.4 First structures and measurements

The work on PhC-LEO LEDs at UCSB is still at an early stage. The first proof of concept has been demonstrated with 1D gratings of SiO2 embedded in a GaN layer. The grating patterns were prepared by lithographic holography by Kelly McGroddy, and the LEO growth and processing of devices were performed by Brendan Moran.

The fabricated structures consist of a several μm thick GaN buffer, a 90nm thick 1D grating made of SiO2 and GaN (with a filing factor $f \sim 0.5$) and a cap layer integrating the *pn* junction. Several cap layer thicknesses could be obtained. Here, I present angular measurements on the thinnest sample, where the total cap layer thickness could be brought down to $\sim$ 500 nm.[16] This cap layer is already

---

[16] More precisely, GaN coalescence was obtained over 150 nm, followed by a 100 nm thick *n*-GaN region, the multi-

quite thin, even though the growth conditions have not been fully optimized yet. This leaves good prospect to thin it down further by another 100 nm (possibly by thinning the doping regions) to reach the high efficiency region of Fig. 4.57.

Fig. 4.58 presents an angular measurement and the corresponding band structure for one of these samples.

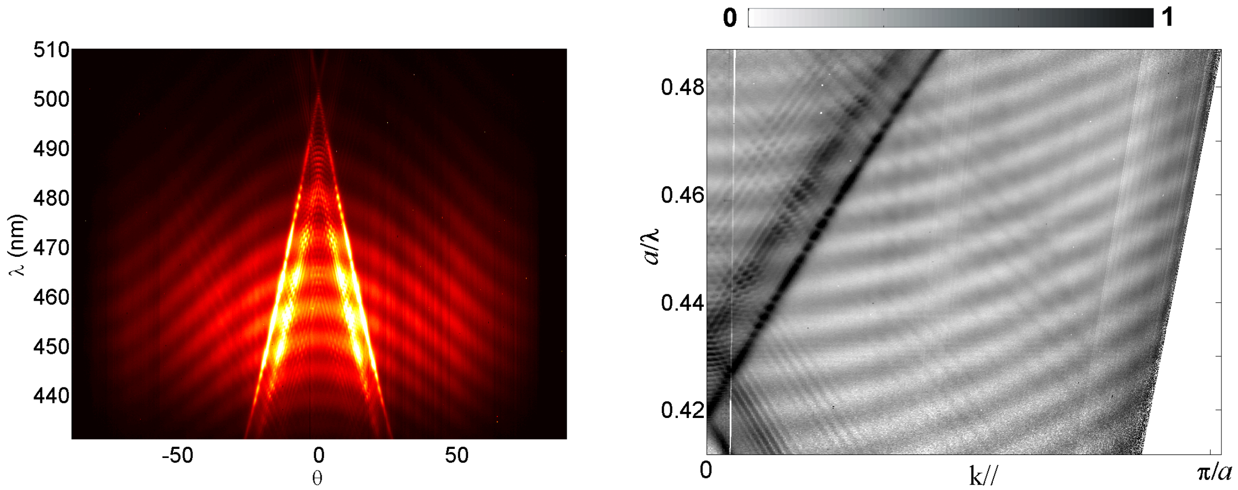

Figure 4.58: (Left) Angular measurement on a LEO-PhC LED with a 1-dimensional grating embedded in the GaN layer. The measurement is performed in a direction perpendicular to the grating groves and in TE polarization. (Right) Corresponding band structure. A well-defined cap layer mode is visible. In addition, a second multiplet resonant feature can be seen at lower n_{eff} (follow by other, much fainter resonances at even lower n_{eff}).

The general features of the band structures are reminiscent of those observed in the case of PhC-LEDs with an AlGaN cap layer. In addition to a quasi-continuum of excited modes, an intense photonic band can be observed. It corresponds to the cap layer mode (CLM) trapped above the grating. This confirms that a well-defined CLM is supported in the structure. However, no direct conclusion can be drawn as regards the extraction efficiency of this mode: in these LEO samples, the grating is present on the whole surface, so that guided modes can be diffracted over very large distances ($\sim$ 1 cm). This is in contrast with the LEDs of previous sections, where the PhC region was of small extent and observation of a mode implied efficient extraction. It is therefore not possible to estimate over which length the CLM has been extracted.

Besides, a second resonant feature appears in the band structure: the few excited modes closest to the CLM are much more intense than other excited modes. If this resonance were fully discrete and corresponded to one photonic band, it would simply be attributed to a second mode localized in the cap layer. Here, although this resonance is not fully discrete, the image of a second CLM still gives us insight: the resonance can be seen as linked to a quasi-mode which is not well localized in the cap layer (its effective index is close to the average index of the LEO mask, so that it is not well confined). In practice, there is a peak in light emission in the direction of this quasi-mode, but which is redistributed over the many excited modes of similar direction. This observation may slightly relax our strict requirement that light be emitted in CLMs to be well extracted: it suggest that a quasi-CLM may play a similar role. However, it is difficult to draw definite conclusions on this point in the absence of extraction length measurements.

---

quantum well region ($\sim$ 100 nm) and a 150 nm thick p-GaN region.

4.4.5 Conclusion

LEO-PhC LEDs are promising structures for light extraction because they combine good photonic properties – definition of a well-extracted cap layer mode – with a geometry which is suitable for practical integration to high efficiency LEDs. The first experimental results on 1D structures are encouraging and compatible with the expectations of these LEDs. However, their fabrication remains a challenge whose constraints are as yet unknown. Their ultimate efficiency will be determined by fabrication limitations, especially as concerns thin-film coalescence of overgrown GaN.

4.5 PhC-LEDs with patterned emitting region

The previous implementations of PhC-LEDs tend to show how, to push extraction efficiency to its limits, one needs to depart from the geometry of a classic GaN structure. Simple surface PhCs suffer from limited efficiency, while the highest theoretical efficiencies are obtained in structures which modify significantly the photonic regime of the LED.

We now discuss an even more peculiar GaN light-emitting structure, where the quantum wells are located in the PhC region itself.

4.5.1 Patterned emitting region: qualitative discussion

The 'Band Gap' approach

Up to now, we have only considered PhCs acting as diffraction grating – and, possibly, modifying the average index in the vertical direction: this consists of a regime of weak to moderate photonic interaction.

It is now worth mentioning another strategy often considered in the literature to enhance light extraction with PhCs. It consists in using the PhC to create a full band gap in all in-plane directions, so that guided modes no longer exist and *all the emitted light* is emitted out-of-plane, in the air cone.[25]

This approach typically suffers from two caveats. First, in the presence of non-radiative losses, the internal quantum efficiency is severely degraded. Indeed, if we denote as τ_{air}, τ_{guided}, and τ_{NR} the lifetimes corresponding to radiation in air, in guided modes and to non-radiative recombinations, the internal quantum efficiency is given by:

$$\begin{array}{lcl} \text{No PhC} & \rightarrow & \eta_{IQE} \sim \dfrac{\tau_{air}^{-1} + \tau_{guided}^{-1}}{\tau_{air}^{-1} + \tau_{guided}^{-1} + \tau_{NR}^{-1}} \\ \text{PhC} & \rightarrow & \eta_{IQE} \sim \dfrac{\tau_{air}^{-1}}{\tau_{air}^{-1} + \tau_{NR}^{-1}} \end{array} \tag{4.10}$$

In a rather good semiconductor, $\eta_{IQE} \sim 80\%$.[17] Besides, if we consider that $\sim 10\%$ of the emitted light is in the air cone, we have $\tau_{guided} \sim \tau_{air}/10$. This leads to a value of $\tau_{NR} \sim \tau_{air}/3$. In this case, when the PhC is etched, η_{IQE} *drops to* 25% ! This effect is simpy due to the reduction of radiative channels, while all loss channels remain constant. This assumption is actually optimistic, because surface-states related non-radiative losses are likely to *increase* in presence of the PhC. Ref. [26] discusses (theoretically and numerically) the effect of non-radiative losses, and concludes that if these losses are too high the 'band gap' approach is not competitive.

Second, in order to obtain a full, omnidirectional band gap, one has to obtain a thin membrane by etching some sacrificial layer (usually with a wet etch) located below the membrane. In such a geometry, it is very hard to place electric contacts to obtain an LED, especially under the membrane.

For all these reasons, this band-gap approach has so far only been successful in photomulinescence demonstrations at cryogenic temperatures, where non-radiative channels are quenched – see Ref. [27] for a clear experimental evidence of the modification of radiative lifetime at low temperature by Noda's team.

Emission of patterned InGaN

However, recent results obtained by Stacia Keller, Chris Schaake *et al.* at UCSB have led to a rather surprising result.[28] Starting from a regular GaN photoluminescence structure with InGaN quantum

---

[17] In GaN/InGaN structures, even $\eta_{IQE} \sim 50\%$ is very good at high current injections.

wells close to the surface, they pattern the sample with a square lattice PhC ($a \sim 200$ nm). The PhC pattern is more than 200 nm deep and the QW region is fully etched. The resulting samples have a poor photoluminescence signal, as could be expected from the above discussion. However, after annealing of the samples under suitable conditions (typically $\sim 1000^o$ C), they observe that the photoluminescence signal is *more than restored.* Fig. 4.59 illustrates this experiment and the corresponding structure.

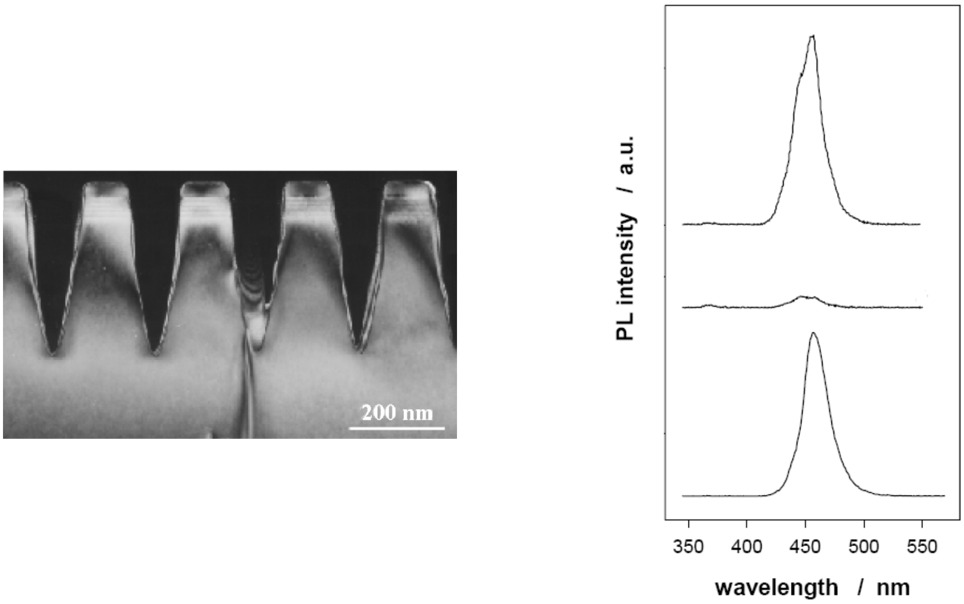

Figure 4.59: [After Ref. [28]] Left: TEM image of a patterned sample. The active region is visible in the patterned layer. Right: Photoluminescence of the sample. (Bottom) Before patterning. (Center) After patterning of a PhC. (Top) After annealing at 900^o C: the PL signal is more intense than on the original sample. Note the small peak-like features of the last spectrum, probably due to diffracted guided modes.

Of course, conclusions of this experiment should be drawn with care. The enhancement in PL signal may be attributed to restoration of the internal quantum efficiency of the material, but also to enhanced light extraction due to the PhC's presence, and possibly to a more efficient absorption of the exciting laser in the presence of the PhC – a common and possibly large effect which is unfortunately often disregarded in literature!

Angular measurements on one of these samples (Fig. 4.60) confirm that light extraction indeed contributes to the PL intensity. However, it is also clear that the PhC's diffraction does not produce the entirety of the signal: from Fig. 4.60, contribution of diffracted modes can roughly be estimated to a few dozen % of the total signal.

Likewise, enhancement of the excitation in the presence of the PhC is possible but is not expected to be a strong effect, because excitation of InGaN PL structures by a HeCd laser is usually efficient.

In conclusion, these results strongly suggest that a proper annealing restores the internal quantum efficiency of an etched surface in GaN structures, although the effect is not fully quantified yet. A more detailed discussion can be found in Ref. [28].

Patterned InGaN: photonic regime

We are thus led to consider these atypical structures, which are at the crossing of the 'grating' and 'band gap' approaches.

On the one hand, it is clear that the PhC can no longer be considered as a mere grating. A source

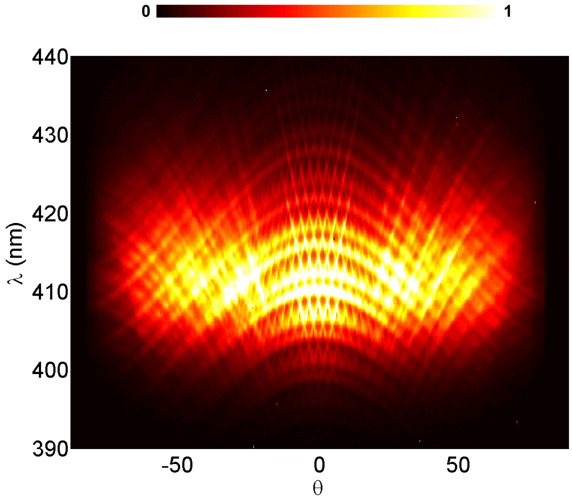

Figure 4.60: Angle-resolved PL spectrum of a GaN sample with a square lattice PhC etched through the active layer (ΓX direction, TE polarization). The photonic bands differs slightly from those of other angular measurements found in this thesis, because of the different lattice.

embedded in a PhC directly feels a modified local density of states (DOS), which modifies its emission properties. Besides, the photonic strength of the PhC is now too strong to retain a nearly-free photon approximation.

On the other hand, the simple picture of a complete bandgap does not hold either. Of course, some band gap effects are definitely expected for such high air filling factors. As a reference, Fig. 4.61 gives the gap map for a 2D GaN/air PhC and shows that large gaps should open *for in-plane propagation*, for air filling factors around $f = 50\%$.

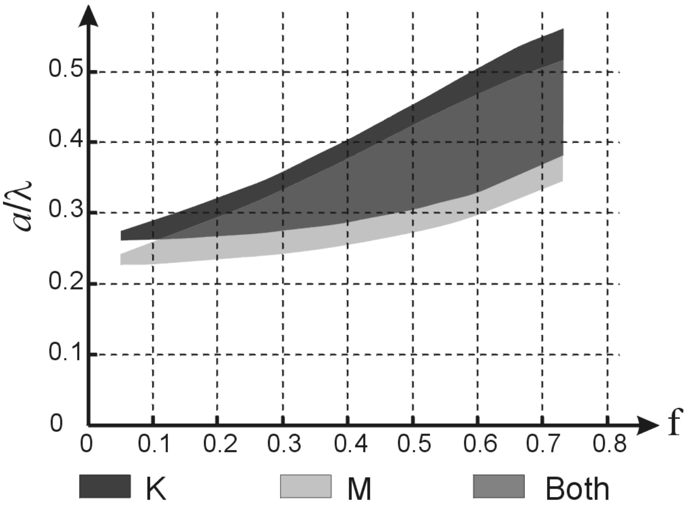

Figure 4.61: Gap map for a 2D PhC made of air holes in a GaN matrix ($n = 2.55$, triangular lattice) in H polarization, as a function of the air filling factor. Although the structures of interest here are inverted (GaN rods embedded in air), gaps with similar magnitude can be expected in one or the other polarization.

This calculation gives a fair idea of the magnitude of gaps in a thin membrane, which is optically close to a 2D PhC. However, the present structure is very different from a membrane: the PhC region lies on a GaN buffer layer, which still carries a large density of modes. These modes can to some extent be excited by the source, either by propagative or evanescent coupling. In other words, all polar angles have to be taken into account because, unlike in a membrane, there is no index confinement by air in the vertical direction. It is therefore hard to guess to what extent emission at non-glancing angles will be quenched.

However, even if light is emitted beyond the critical angle, the diffraction effect of the PhC is expected to be strong and one can hope that leaky modes will be efficiently extracted.

Let us here summarize the various photonic effects likely to occur in this structure:

- Lowering of the *average index* in the vicinity of the emitting source, leading to a lower density of states (DOS)
- Further suppression of the photonic DOS, either because band gaps open, or more generally because the dispersion of the remaining photonic modes is affected by the PhC
- Scattering of leaky modes (propagating at $n_{eff} > 1.7$) by the PhC, to the sapphire substrate and to air

4.5.2 Patterned emitting region: modeling / quantitative discussion

In this section, we attempt a quantitative discussion of the mentioned photonic effects. A convenient way to investigate these is to compute the emission diagram of a dipole in the structure, which gives access to relevant quantities such as light extraction and radiative lifetime.[18]

As such calculations are time-intensive, we are led to restrict ourselves to a simple case where results can be interpreted easily. In practice, we consider a structure made of a sapphire substrate, a 1μm thick GaN buffer (this value is rather thin but should not significantly alter physical insight), a 400 nm thick PhC (triangular lattice of *circular GaN columns in air* with $a = 200$ nm and $f = 0.5$), and an air superstrate (Fig. 4.62).

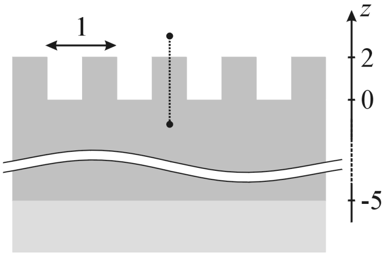

Figure 4.62: Geometry of the structure considered in the calculations (distances in units of a). (Dotted line) The source is moved from GaN to air through the center of a GaN column

We investigate the emission of a dipole source whose vertical direction is varied between $z = -1$ (embedded in the GaN buffer) and $z = 3$ (in air). The source is made of a sheet of dipoles with in-plane alignment. This choice corresponds to emission from delocalized excitons. Alternately, one could consider emission from point-like dipole sources, but the position of the source would introduce an additional parameter (see Annex C for a more complete discussion).

Besides, the normalized frequency of the dipole is taken as $u = 0.58$, which corresponds to a favorable situation in the ΓM direction. As seen on the Ewald construction of Fig. 4.63, in this case, there is always at least one diffraction channel to air (either the ΓM or $2\Gamma M$ order), and the ΓK diffractions do not enter the sapphire circle. On the other hand, extraction is not omnidirectional in this case: there is no diffraction channel to air in the ΓK direction.

---

[18] One may also consider computing the Bloch modes of the structure instead. However, it is more difficult to draw direct conclusions from the sole knowledge of Bloch modes: in this intricate case, it is unclear which modes will be excited by a source. Direct calculation of emission diagrams seems a more straightforward approach.

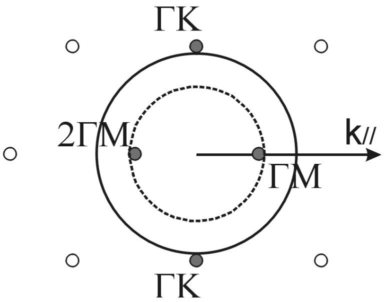

Figure 4.63: Ewald construction ($u = 0.58$) for a Bloch mode with the parameters considered in calculations: the second ΓM diffraction enters the light cone while the first ΓM diffraction still lies inside of it, so that all light emitted in the ΓM direction is extracted to air.

We are interested in the emission lifetime of the dipole and in the extraction efficiency to air of the light it emits. Here, we define the Purcell effect of the dipole with respect to a dipole in bulk GaN:

$$F_p = \frac{\tau_{GaN}}{\tau} \tag{4.11}$$

F_p is simply the inverse lifetime of the dipole, normalized so that $F_p = 1$ for a dipole in GaN.

Purcell effect: average index approximation

First, let us discuss the simple effect of the average index on the source emission. A dipole embedded in a medium of index n has a radiative rate proportional to n.This is a very simple form of Purcell effect, linked to the increased bulk density of modes in a medium of higher index.[19] Here, we discuss this simple effect of average index, disregarding all effects due to in-plane Bragg scattering (in practice, we ignore all terms others than $\mathbf{G} = 0$ in Maxwell's equations).

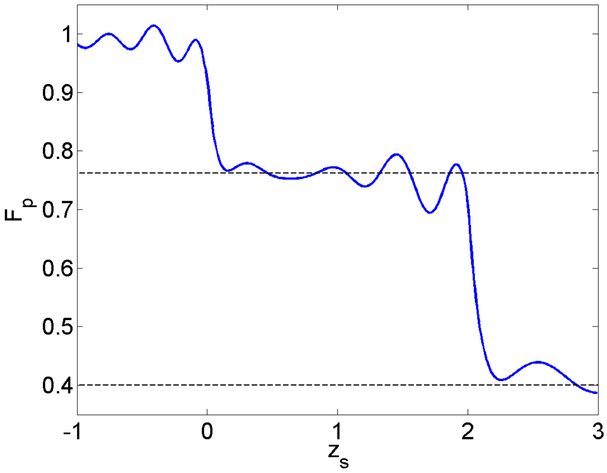

Figure 4.64: Purcell effect for a dipole moved through the PhC along the path of Fig. 4.62, in the effective index approximation. The dashed lines represent the values of F_p in bulk media of indices $n = 1.9$ (average index in the PhC) and $n = 1$ (i.e. in air).

When the source is embedded in the PhC, it feels a lower average index than in bulk GaN. Therefore, we can expect that its radiative lifetime decreases. This effect can be estimated by computing the

---

[19] The photonic DOS actually scales like n^3. However, in the case of bound charges of interest here, screening of the dipole by ϵ removes a n^2 contribution, leading to an enhancement factor by only n.

emission diagram in a multilayer structure, where the source is moved through the structure as in Fig. 4.62. This 1-dimensional calculation has the advantage of being very light on computation time. In the average index approach, the PhC region is a medium of index $\langle n \rangle = 1.9$.

The result of the calculation, shown on Fig. 4.64, confirms the expected result. Apart from some small oscillations due to reflections at the various interfaces, the Purcell effect is equal to 1 in GaN, $1.9/2.5 = 0.76$ in the PhC and $1/2.5 = 0.4$ in air. This means that spontaneous emission has a longer lifetime in the PhC than in bulk GaN. On the one hand, this means that the relative effect of non-radiative losses will be stronger. On the other hand, it also indicates that the dipole 'sees' a medium of index 1.9, which is advantageous in terms of light extraction: the weigh of guided modes is much smaller than in GaN.

In the following we denote this 'average index' Purcell effect as $\bar{F}_p$.

Purcell effect: inclusion of scattering terms

The previous results need to be confronted against a 3D approach which takes scattering effects into account, e.g. retaining **G** harmonics.[20] In presence of the PhC, azimuthal directions φ are no longer equivalent. Therefore, we introduce the emission rate in a given azimuthal direction:

$$f_p(\varphi) = \int I(\theta, \varphi) sin(\theta) d\theta \tag{4.12}$$

Where $I(\theta, \varphi)$ is the intensity emitted by the source in a given direction, and the term $sin(\theta)$ accounts for solid angles; f_p represents the radiative rate in direction φ and is sometimes called the *partial Purcell factor* in the direction φ. It is related to the total Purcell factor by:

$$F_p = \int f_p d\varphi \tag{4.13}$$

First, let us consider the impact of scattering effects in the ΓM direction only, by computing $f_p^{\Gamma M} = f_p(\varphi = 0^o)$. As can be seen on Fig. 4.65, the result is rather close to the average index result when the source is not located inside the PhC, because scattering effects do not significantly affect the emission pattern. Inside the PhC on the other hand, $f_p^{\Gamma M}$ is *smaller* than $\bar{F}_p$. For instance, for $z \sim 1.5$, the lifetime is twice as large. As will be seen next, this effect is due to a partial suppression of the photonic DOS along ΓM, e.g. to partial band gaps.

Let us now compute the overall Purcell effect F_p and compare it to $f_p^{\Gamma M}$. Note that this calculation is rather tedious because sharp resonances appear in the spectra, so that a fine mesh is needed both along θ and φ. Therefore, the calculation is only performed for source positions inside the PhC region, where interesting effects can be expected. The result is shown on Fig. 4.65.

Interestingly, the overall F_p is in general closer to $\bar{F}_p$ than $f_p^{\Gamma M}$ was: part of the emission which is inhibited along ΓM is thus *redistributed* in other directions − a phenomenon reminiscent of intensity redistribution in interference fringes. This is best seen on Fig. 4.66, where f_p is detailed as a function of φ: the DOS is indeed reduced along ΓM, but is also increased in other directions, which limits the Purcell effect.

---

[20] The parameters of the calculation are as follows. Only 37 plane wave harmonics are considered, and an imaginary part $n'' = 0.005i$ is added to the refractive index of the GaN buffer in order to add absorption and to resolve all modes properly (see the discussion on this subject in Chapter 6). It has been carefully checked that this modest plane wave cutoff leads to numerical errors of the order of 1% or less. It has also been ckecked extraction efficiency to air could still be estimated in the presence of absorption, provided energy calculations were renormalized to remove the effect of absorption. In all cases, a dipole along x and a dipole along y are added incoherently to simulate an average distribution of in-plane dipoles.

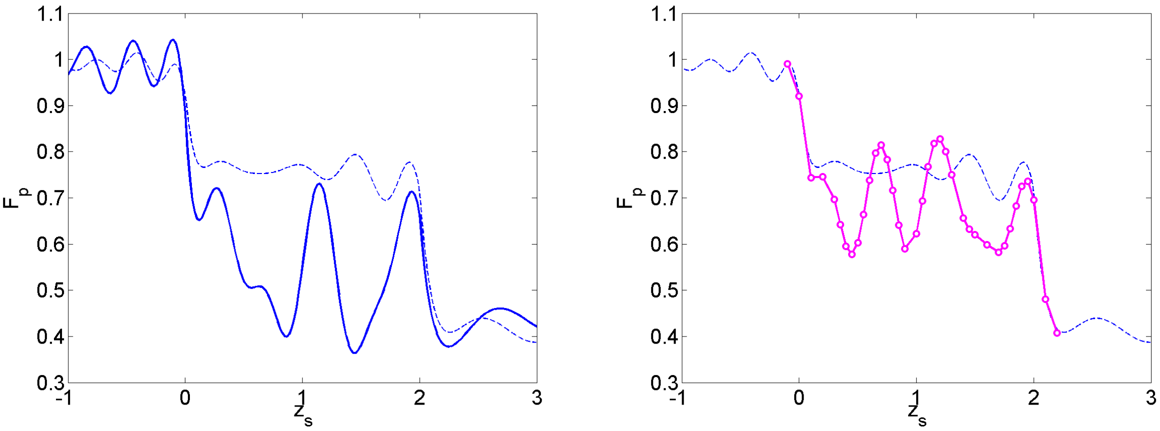

Figure 4.65: (Left) Partial Purcell factor $f_p^{\Gamma M}$ in the ΓM direction for the same structure as previously, taking scattering effects into account. (Right) Purcell factor F_p (properly integrated over φ). In both plots, the dashed line is the average index result $\bar{F}_p$.

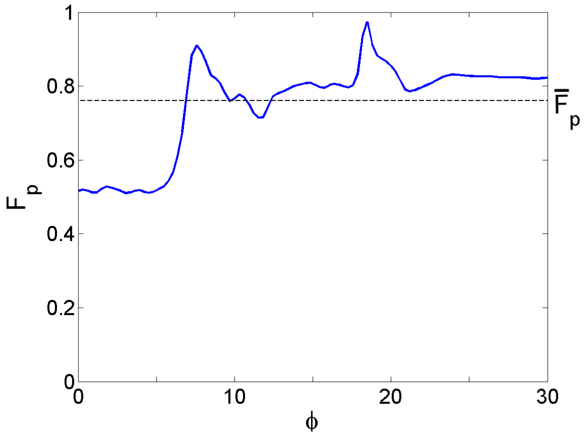

Figure 4.66: Partial Purcell factor as a function of φ, for a source located at $z_s = 1.3$. Close to ΓM (e.g. $\varphi = 0$) the photonic DOS is reduced and emission is inhibited. At larger values of φ however, the DOS increases over the $\bar{F}_p$ value (dashed horizontal line). In this case the integrated Purcell factor is $F_p = 0.75$, very close to $\bar{F}_p = 0.76$

In the context of light emission, this result lifts some of our worries: the inhibition of spontaneous emission lifetime can be quite limited. Especially, at the best points of Fig. 4.65, $F_p = 0.80$ and the radiative lifetime is modified by only 20% with respect to bulk GaN. In this case, and assuming an original internal quantum efficiency of 50%, the new quantum efficiency is $0.8/1.8 = 45\%$ which is still reasonable – especially if the emitted light is efficiently extracted, as can be hoped in a well-designed structure.

Extraction efficiency

Let us now evoke the extraction efficiency of this structure. A thorough exploration is out of the scope of this short discussion. From a qualitative point of view, the detrimental effect of guided light is expected to be limited because emission should be quenched at effective indices over 1.9: thus a large part of the guided modes emission is simply avoided. Besides, if the remaining guided light

($1 < n_{eff} < 1.9$) is well-diffracted, extraction should be very high. Especially, in the case of extraction to epoxy, only modes with ($1.5 < n_{eff} < 1.9$) need to be diffracted.

For a quick quantitative perspective, we restrict ourselves to giving the extraction efficiency to air in the ΓM direction (Fig. 4.67).

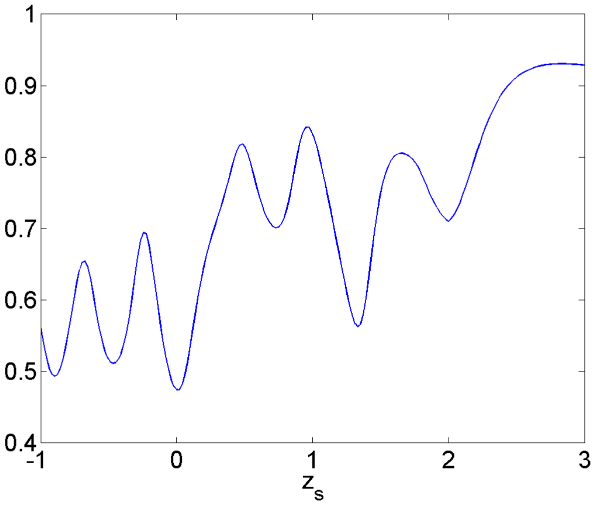

Figure 4.67: Light extraction efficiency to air in the ΓM direction as a function of dipole position.

When the dipole is in GaN, the extraction efficiency is mainly limited by diffraction losses to the sapphire substrate. However, when the dipole is moved in the PhC, regions of high extraction efficiency appear in the ΓM direction (for instance when z_s =1). This effect may be linked to resonant emission in a well-extracted leaky mode. One may also wonder why the extraction efficiency does not reach unity when the dipole is largely placed in air ($z = 3$): instead, it saturates around 90 %. It can be checked that this is because a sizable part of the light emitted downward is scattered by the PhC at angles where it is trapped in the sapphire.

Again, let us stress that only a full integration would determine the total efficiency. Because we consider a high frequency in the model structure, substrate losses would probably be strong in our case. A well-designed structure with extraction to epoxy would be more suitable for an assessment of the extraction efficiency performance.

4.5.3 Analysis of emission in a patterned layer by source emission diagrams

The previous discussion presents global results on the emission properties of patterned QW layers, but limited insight on the detailed emission behavior at the source level. A convenient way to access the latter is through study of the source emission diagram, which underlies all the properties studied above. The source emission diagram $I(\theta, \varphi) = I(\mathbf{k}_{//})$ indicates the intensity emitted by a quantum well in a given direction. In order to introduce such a diagram, let us first consider the emission diagram of a simpler structure: a PhC membrane without a substrate or GaN buffer layer.

Emission in a PhC membrane

For now, we consider a simple GaN membrane of thickness 1 (in units of a), etched by a triangular PhC of air holes with $f = 0.5$, and surrounded by air. Figure 4.68 presents the emission diagram of a source located in the middle of this membrane, at a frequency $u = 0.6$. Here, directions are characterized by their in-plane wavevectors $k_x = k_{//}cos\varphi$ and $k_y = k_{//}sin\varphi$ (expressed in units of k_0). Therefore, the air cone corresponds to $k_{//} < 1$ (i.e. $n_{eff} < 1$ with our units).

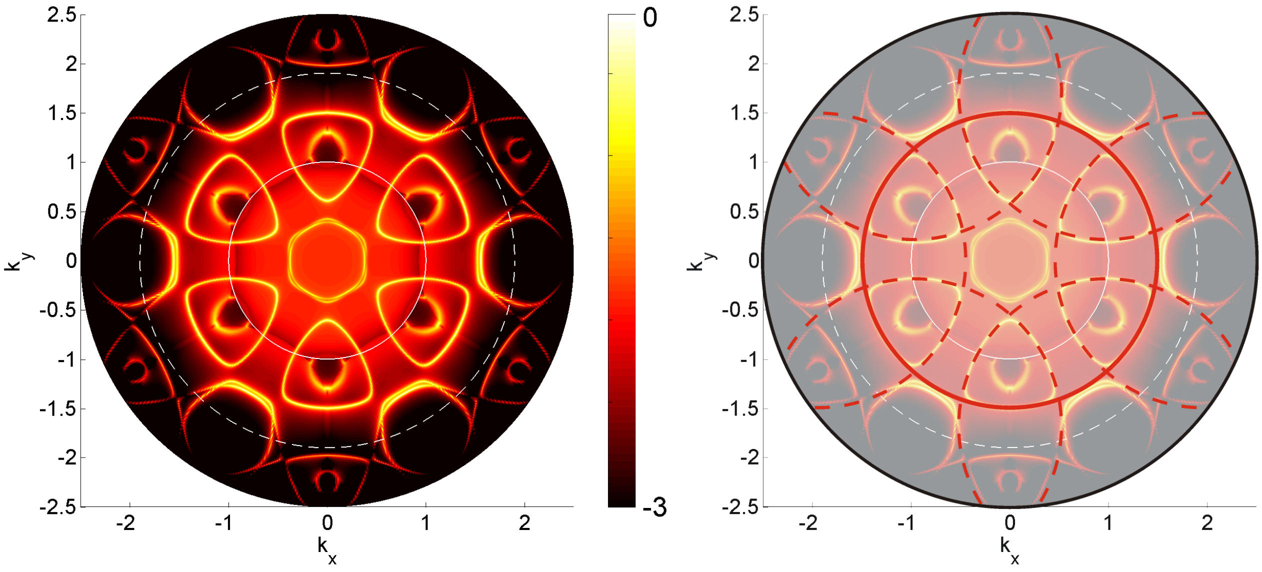

Figure 4.68: PhC membrane emission diagram. (Left) Emission diagram of a quantum well in a GaN PhC membrane (log scale). k_x and k_y are the components of the wavevector, in units of k_0. The small full circle is the air cone ($n_{eff} = 1$), and the large dashed circle corresponds to the average index of the membrane ($n_{eff} = 1.9$): emission is strongly suppressed beyond this circle. (Right) Emission diagram with the equifrequency contours of a mode ($n_{eff} = 1.6$) superimposed as red lines. The full red circle is the dispersion of a guided mode with $n_{eff} = 1.6$, and the dashed circles correspond to periodization by the reciprocal lattice.

As can be seen, the emission diagram is mainly composed of a somehow uniform background for $k_{//} < 1.9$, and of additional shield-shaped sharp features with a sixfold symmetry. The background simply corresponds to direct light emission to air. Let us note that at $u = 0.6$, all directions (θ, φ) fall within the light cone due to periodicity (Apart from six small zones around the K points). Therefore, emission to air is possible in all these directions, hence the uniformity of the background everywhere (apart from the K points). However, this background is seen to collapse when $k_{//} \sim 1.9$. Indeed, the average index of the membrane is 1.9, so that light with a higher effective index is evanescent in the membrane (and still more of course in the surrounding air). Therefore, light emission is strongly frustrated for effective indices over 1.9.[21]

Let us now come to the sharp lines appearing over the background. These correspond to emission in a resonant Bloch mode of the PhC slab, with an effective index $n_{eff} = 1.6$. This is apparent on Fig. 4.68 (right), where the simplified isofrequency curve of a Bloch mode with $n_{eff} = 1.6$ is superimposed on the emission diagram. This curve corresponds to a nearly-free photon: zero photonic strength is assumed, so that the isofrequency is only made of periodized circles of radius 1.6. As can be seen, the sharp lines of the actual emission diagram very closely follow this curve, apart from some gaps openings occurring when different circles intersect. This Bloch mode, although leaky, is well confined inside the PhC membrane so that it couples well to the quantum well (roughly as much as a classic guided mode would).

This kind of emission diagram is typical of thin PhC membranes: light emission occurs through

---

[21] Emission is not completely suppressed however: this is because light emitted in modes evanescent everywhere ($n_{eff} > 1.9$) can still be diffracted back to propagative modes by the grating.

two channels, a continuous background (direct emission in the air cone) and a 'discrete' component corresponding to the Bloch modes supported by the membrane. Of course, if no Bloch mode is supported (as happens when the frequency falls in an omnidirectional band gap) only the first channel remains. This is the basis of the 'band gap approach' to light extraction described above.

Emission in a realistic structure

We now come back to the problem of emission in our structure of interest, including the unetched GaN buffer and sapphire substrate. In this case, the distribution of guided modes is expected to change drastically. Indeed, in the absence of total internal reflection at the PhC/GaN interface, there is no more well-defined guided mode in the vertical direction on which highly resonant PhC Bloch modes can build up. Rather, we can expect the presence of low-order modes localized in the GaN buffer (with an effective index larger than the average index $\langle n \rangle$ of the PhC layer), and of high-order modes which can penetrate the PhC. Possibly, some of these modes may be resonant in the PhC layer. Fig. 4.69 describes this guided modes distribution.

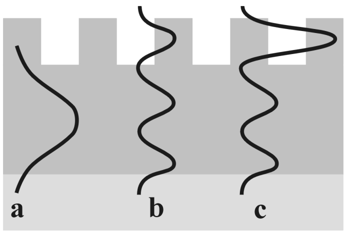

Figure 4.69: Expected guided modes distribution in the structure. (a) Low-order mode with $n_{eff} > \langle n \rangle$ (b) High-order mode (c) High-order mode with high localization in the PhC layer, due to a vertical resonance.

In addition, modes may be suppressed in some directions due to band gap effects. More specifically in our structure, $u = 0.58$ so that a band gap is expected at the second Bragg order, around an effective index $n_{eff} = 2/\sqrt{3}u \sim 2$.

After this preliminary discussion, let us now study the emission diagrams in the structure. Fig. 4.70 depicts the source emission for various source positions, starting in the GaN buffer and moving in the PhC.

When the source is located at the interface between the unetched GaN buffer and the PhC ($z_s = 0$), the emission is very close to that in a regular waveguide. Light is collected in circular rings corresponding to the guided modes of the GaN buffer, and the influence of the PhC is very weak: it only acts as a diffraction grating but does not modify the source's behavior. We are thus in the same regime as in all other PhC structures previously studied in this chapter. For any given azimuthal angle φ, the intensity $I(\theta)$ is composed of a series of peaks corresponding to the propagation angles of guided modes.

On the other hand, when the source is placed at the entrance of the PhC ($z_s = 0.2$), the spontaneous emission itself suffers some alterations. The most obvious is a strong quenching of light emission for effective indices larger than $\langle n \rangle$. This effect was anticipated: in the PhC, the source 'sees' an effective medium of index $\langle n \rangle$. This leads to the average index Purcell effect $\bar{F}_p$ already evoked: indeed $F_p = 0.75$, very close to $\bar{F}_p = 0.76$. Clearly, scattering by the PhC has little to do with this Purcell effect: the emission diagram barely depends on the azimuthal direction φ.

When the source is placed deep in the PhC ($z_s = 0.7$), the scattering effects of the PhC become predominant. The emission diagram now shows a strong φ-dependence, with a sixfold symmetry stemming from the triangular lattice of the PhC. Emission occurs in bands which interact well with

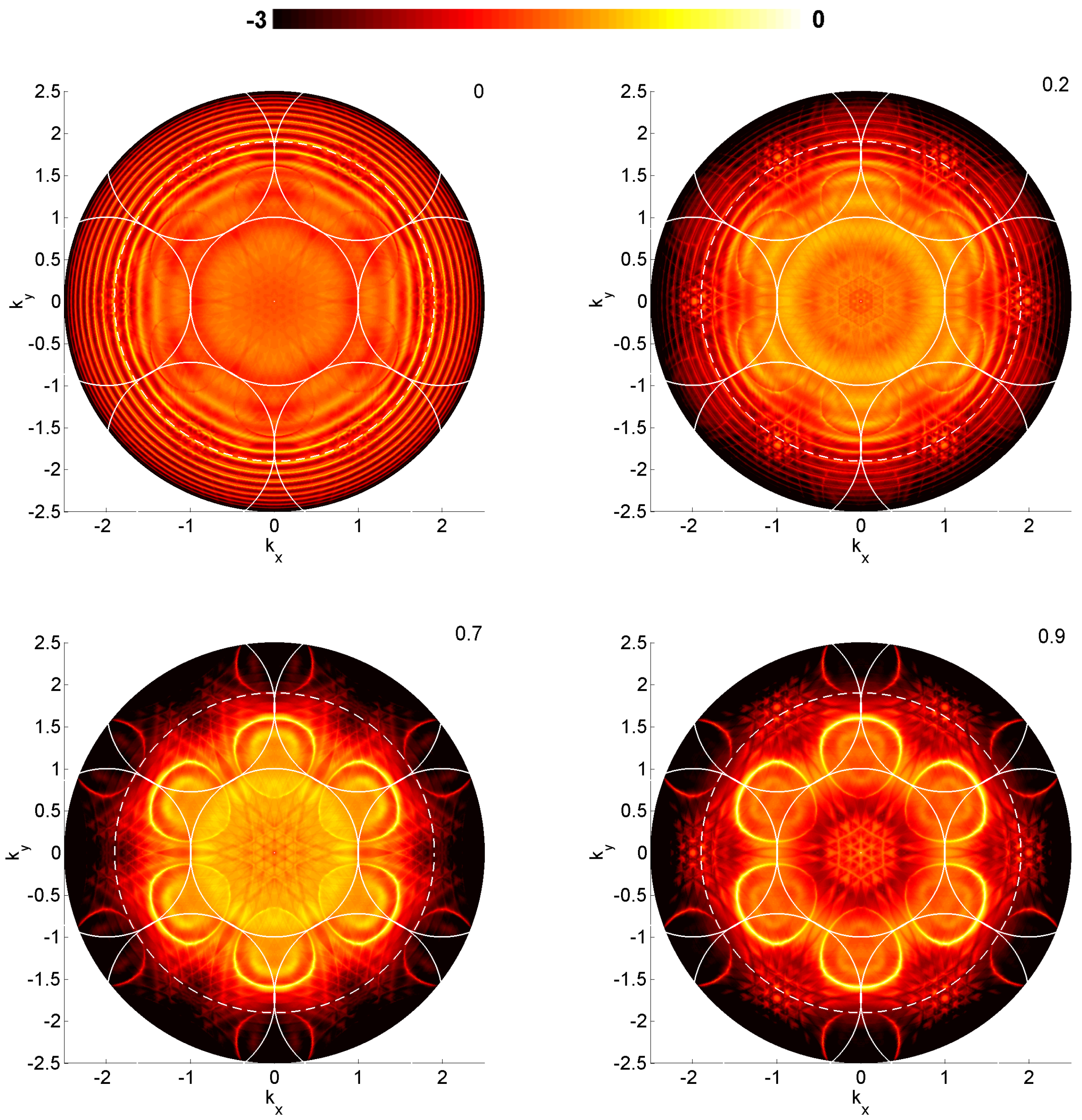

Figure 4.70: Emission diagram for a light source in a 'realistic' PhC structure (with GaN buffer and sapphire substrate), for different positions z_s of the source (log_{10} scale, all figures have the same scale), the PhC layer's thickness being 2. The full white circles are the folded air cones. (Top left) $z_s = 0$: the source is at the interface between the PhC and the GaN buffer, emission is distributed in regular guided modes and does not depend on φ. (Top right) $z_s = 0.2$: the average index felt by the source decreases from 2.5 to 1.9. Emission at effective indices beyond 1.9 is quenched. (Bottom left) $z_s = 0.7$: the source is deep within the PhC, where the photonic density of states is strongly altered. Most of the emission is collected in a sharp peak reminiscent of a Bloch mode's equifrequency contours. (Bottom right) $z_s = 0.9$: when the source is moved through the PhC, vertical resonances modify the overall emission, leading to modifications of the Purcell effect. The Purcell factor drops from 0.8 at $z_s = 0.7$ to 0.6 at $z_s = 0.9$.

the PhC, and are thus observed intensely in the FBZ.[22]

The most striking feature of this third diagram is the presence of very intense resonances in the emission diagram. This sharp emission peak has an egg-like shape centered around point K in the reciprocal space, and is reminiscent of the shield-shaped isofrequency curves observed in the case of a PhC membrane. The intensity and dispersion of this peak allow us to understand Fig. 4.66: the peak is present around K but not around M, and represents a large fraction of the emitted light. Therefore, emission is weaker along M and larger around K, which explains the behavior of $f_p(\varphi)$. Notably, the peak of f_p for $\varphi \sim 7^o$ is caused by the inflexion of the egg at the corresponding angle. The presence of this feature is surprising since we do not expect this PhC structure on a high-index substrate to support well-defined resonant modes (more precisely, resonant modes in a large range of directions $k_{//}$ for a given ω). We will comment further on its origin in the next section.

Finally, when the source is moved between various positions within the PhC region ($z_s = 0.9$), the emission diagram keeps most of the characteristics described above, but the relative intensity of some regions of the diagram varies. While the resonant peak is always intense, the emission in the quasi-continuum of the other modes strongly depends on z_s. For instance, light emission in the central air cone is much stronger for $z_s = 0.7$ than for $z_s = 0.9$.

Quasi-guided modes of a PhC

As we will see, the intense features of the emission diagram are indeed caused by the existence of a resonant Bloch mode which is strongly localized in the PhC. This is quite unexpected because the effective index of this mode is ~ 1.6, *inside the light cone of the sapphire substrate.*

Therefore, such a mode is in principle propagative in the GaN buffer layer *and* in the sapphire substrate, and one could assume that its energy will not localize in the PhC layer under most circumstances. In other words, this mode should be very lossy (due to direct leakage in the GaN and sapphire), and unable to 'build up' in the PhC region − which would require multiple reflections with moderate losses.

The existence of this mode can however be checked by a direct Bloch mode calculation: one indeed finds a leaky mode whose isofrequency curve exactly follows the sharp feature of the emission diagram (Fig. 4.71). As expected, this mode is rather strongly localized in the PhC region. Its unfolded wavevector is $k = 5.8 + 0.027i$.[23]

To appreciate this value of k'',let us consider light propagating at the same effective index n_{eff} in a 1D multilayer system (i.e. in the average index approximation where scattering effects are neglected). In the following, we denote modes in the 1D approximation as guided modes and actual modes of the PhC as Bloch modes. For simplicity, we ignore the sapphire substrate − this is legitimate since the effective index considered is smaller than the sapphire's index. As shown on Fig. 4.72, light rays are perfectly reflected at the PhC/air interface, and reflected at the PhC/GaN interface with a Fresnel coefficient:

$$r = \frac{n_1 cos\theta_1 - n_2 cos\theta_2}{n_1 cos\theta_1 + n_2 cos\theta_2} \tag{4.14}$$

Where θ_1 (resp. θ_2) is the propagation angle in the PhC (resp. GaN) layer corresponding to n_{eff}, and L the thickness of the PhC layer. In a round-trip in the PhC layer, light travels a distance $2Ltan\theta_1$ in the x direction, so that the loss coefficient for this light ray is:

---

[22] More precisely, the harmonic of these modes which is folded in the FBZ has a rather strong weight in the total Bloch mode, so that the mode can couple efficiently to dipole emission. In contrast, a vanishingly weak harmonic would collect very little dipole emission.

[23] In units of a^{-1}. The corresponding effective index is thus $k/2\pi u = 1.6$.

$$k''_{1D} = -\frac{ln(-r)}{2Ltan\theta_1} \tag{4.15}$$

In our case, we obtain $k''_{1D} = 0.38$ (corresponding to a decay length of $1.3a$), whereas the actual loss coefficient of the Bloch mode is only $k'' = 0.027$ (corresponding to a decay length of $20a$)! The value of k'' for the Bloch mode is indeed unexpectedly small and explains why the mode is able to localize in the PhC.

Let us now try to justify how this low-loss mode is built. As we have seen, propagation in the 1D system at $n_{eff} = 1.6$ is very lossy, because the Fresnel coefficient is low ($r = -0.3$). On the other hand, r increases quickly when $n_{eff} \rightarrow 1.9$: light propagating close to glancing angles can actually be well reflected at the PhC/GaN interface. When the angle of propagation enables *phase-matching* of the light bouncing in the PhC layer, light can localize in this low-index layer and form a *quasi-guided mode* (QGM). Phase-matching is expected to occur around:

$$k_z = \frac{\pi}{L} \rightarrow cos\theta_1 = \frac{1}{2Ln_1u} \tag{4.16}$$

In our case ($L = 2a$), this yields $\theta_1 = 77.3^o$ (this value neglects the small phase shift at the PhC/air interface). A 1D numerical calculation confirms the existence of a resonant solution of Maxwell's equations at an angle $\theta_1 = 78^o$, very close to the above value.[24] This QGM has an effective index $n_{eff} = 1.86$ and losses $k'' = 0.025$. The vertical profile of this QGM is shown on Fig. 4.73.

---

[24] This calculation is performed with the hybrid method: this method does converge to a resonant solution, although it is not a proper Bloch mode.

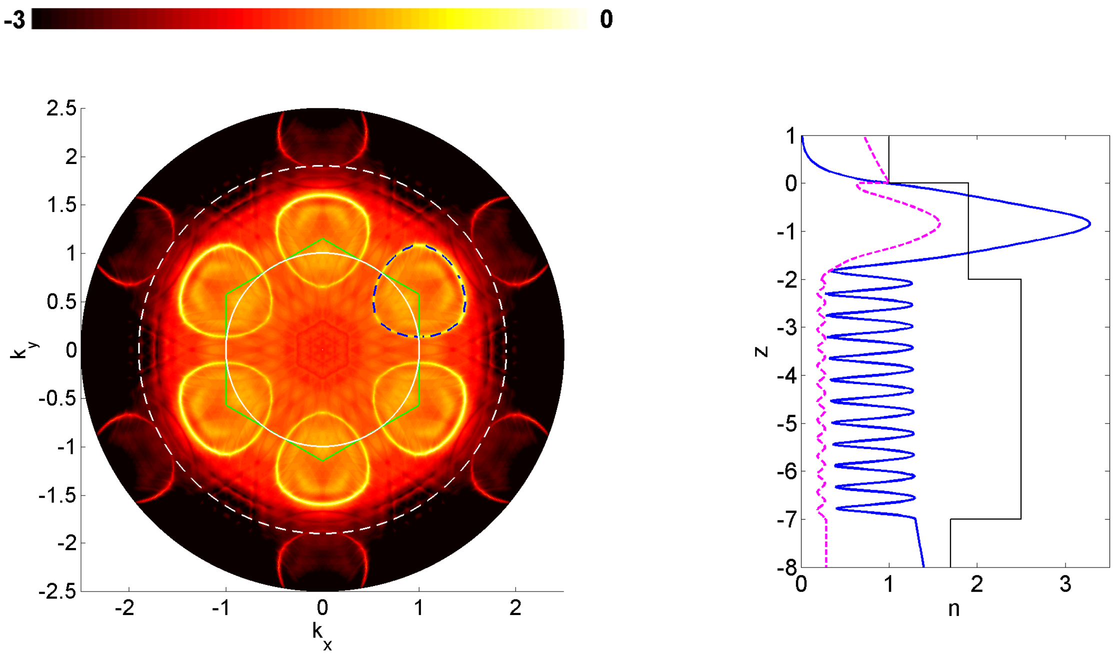

Figure 4.71: (Left) Emission diagram for $z_s = 1.45$ (same scale as Fig. 4.70). The isofrequency of the Bloch mode localized in the PhC region is superimposed as a blue dashed line: it follows exactly the emission peak of the diagram. The green lines correspond to the boundary of the first Brillouin zone. (Right) Modulus of the electric field ($|E|$) along z for the localized Bloch mode, in the ΓK direction. Blue line: fundamental harmonic. Magenta line: second-largest harmonic. The average index profile is represented by the black line.

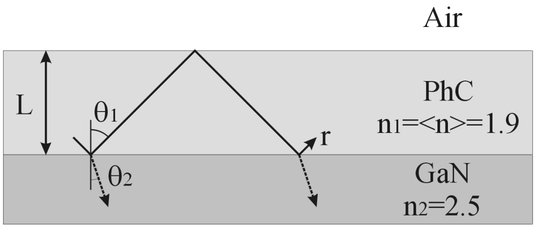

Figure 4.72: Light ray bouncing in a 1D structure made of a low-index 'PhC' layer between GaN and air. The ray loses energy at each bounce due to its imperfect reflection at the PhC/GaN interface.

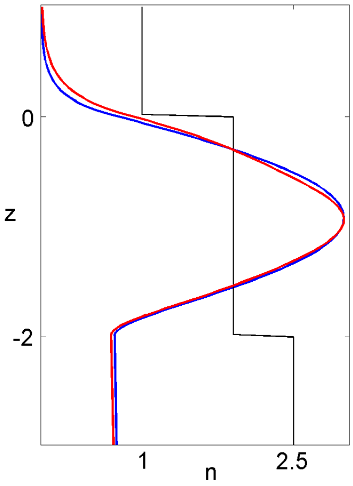

Figure 4.73: Blue: $|E|$ for the 1D GM propagating at $n_{eff} = 1.86$. Red: $|E|$ for the fundamental harmonic of the corresponding Bloch QGM (taking scattering by the PhC into account), propagating at $n_{eff} = 1.6$. The profile of both modes is nearly identical.

This 1D QGM is the basis on which the quasi-guided Bloch mode is built in the PhC. To see this, let us compute the Bloch mode numerically, taking scattering effects into account. Fig. 4.73 compares the electric field profile of the 1D QGM with that of the fundamental harmonic of the Bloch QGM. Both are nearly identical, confirming the origin of the quasi-guided Bloch mode: light is confined in the PhC layer due to a strong enough reflectivity at the PhC/GaN interface.

We still have to understand how this strong reflectivity can be obtained at such a low effective index in the case of the Bloch QGM. To this effect, let us use a simple coupled-wave model with two waves, where a 1D quasi-guided mode E^+ can coupled to a counter-propagating harmonic E^- through a reciprocal vector G. In this simple case, Maxwell's equations become:[25]

$$\omega^2 \begin{pmatrix} \epsilon_0 & \epsilon_1 \\ \epsilon_1 & \epsilon_0 \end{pmatrix} \begin{vmatrix} E^+ \\ E^- \end{vmatrix} = \begin{vmatrix} k_\parallel^2 + k_z^2 \\ (k_\parallel - G)^2 + k_z^2 \end{vmatrix} \cdot \begin{vmatrix} E^+ \\ E^- \end{vmatrix} \tag{4.17}$$

Here, ϵ_0 is the dielectric constant of the propagation medium, $k_\parallel$ and k_z are the in-plane and vertical wavevectors of the mode. G is the reciprocal vector coupling the waves, and ϵ_1 the strength of the coupling.

This system can of course be solved numerically, but we will also look for an analytical solution. Let us call $k_{\parallel 1D}$ the in-plane wavevector in the absence of coupling, and $k_\parallel = G/2 + K$ the in-plane wavevector in the presence of coupling. To obtain a simple analytical solution, let us assume that,

---

[25] With $c = 1$, implying $\omega = k_0 = 2\pi a/\lambda$.

at a given frequency, the vertical wavevector k_z is imposed by the phase matching condition and is therefore unchanged by the presence of the coupling, i.e.:

$$k_z^2 = \epsilon_0\omega^2 - k_{\|1D} \tag{4.18}$$

The solution of Eq. 4.17 is then:

$$\begin{aligned} K^2 &= \frac{G^2 + 2(k_{\|1D}^2 - G^2/4) - \sqrt{\left(G^2 + 2(k_{\|1D}^2 - G^2/4)\right)^2 + 4\omega^4\epsilon_1^2 - (k_{\|1D}^2 - G^2/4)^2}}{2} \\ &\approx \frac{1}{2}\frac{(k_{\|1D}^2 - G^2/4)^2 - \omega^4\epsilon_1^2}{k_{\|1D}^2 + G^2/4} \end{aligned} \tag{4.19}$$

Where the approximation of the second line is valid in the region $k_{\|1D} \sim G/2$. To study the properties of Eq. 4.19, let us neglect the small losses of the mode and assume that $k_{\|1D}$ is real. In this case, three regions of interest appear:

$$\begin{aligned} &k_{\|1D}^2 - G^2/4 < -\omega^2|\epsilon_1| && \rightarrow \quad K \in \mathbb{R}, K < 0 \quad \text{(dielectric band)} \\ &-\omega^2|\epsilon_1| < k_{\|1D}^2 - G^2/4 < \omega^2|\epsilon_1| && \rightarrow \quad K \in i\mathbb{R} \quad \text{(gap)} \\ &\omega^2|\epsilon_1| < k_{\|1D}^2 - G^2/4 && \rightarrow \quad K \in \mathbb{R}, K > 0 \quad \text{(air band)} \end{aligned} \tag{4.20}$$

Where the sign of K has been deduced from its asymptotic behavior.[26] We recover the well-known opening of a band gap at $k_\| = G/2$. The band located below the band gap is bent 'down', corresponding to a higher effective index (i.e. a stronger localization of the mode in the dielectric) and is therefore termed *dielectric band*. Likewise, the band above the band gap corresponds to localization in the air and is called the *air band*. These results are exemplified on Fig. 4.74, where the parameters correspond to a PhC membrane of GaN rods in air with $f = 0.5$ and only two coupled waves (air superstrate, GaN substrate).

Notably, it appears that although the coupling significantly modifies the effective index, it has little impact on the loss coefficient (except in the gap region of course) because losses are dominated by the leakage of the fundamental harmonic, whose vertical phase-matching condition (Eq. 4.16) is not modified by the coupling.

The nature of the QGM Bloch mode can thus be understood as follows: the 1-dimensional QGM supported in the low-index region gets preferentially localized in air due to the scattering of the PhC. This lowers its effective index, while keeping the loss coefficient low. The resulting Bloch mode displays low losses at an 'anomalously low' effective index, i.e. in spite of its ability to leak in the GaN buffer.

Let us note that, while we ignored the presence of the sapphire substrate when justifying the existence of this mode, our arguments still hold in its presence – although additional reflections at the GaN/sapphire interface may somehow modify the loss coefficient of the mode.

---

[26] Namely, $K < 0$ when $\omega \rightarrow 0$ and $K > 0$ when $\omega \rightarrow \infty$.

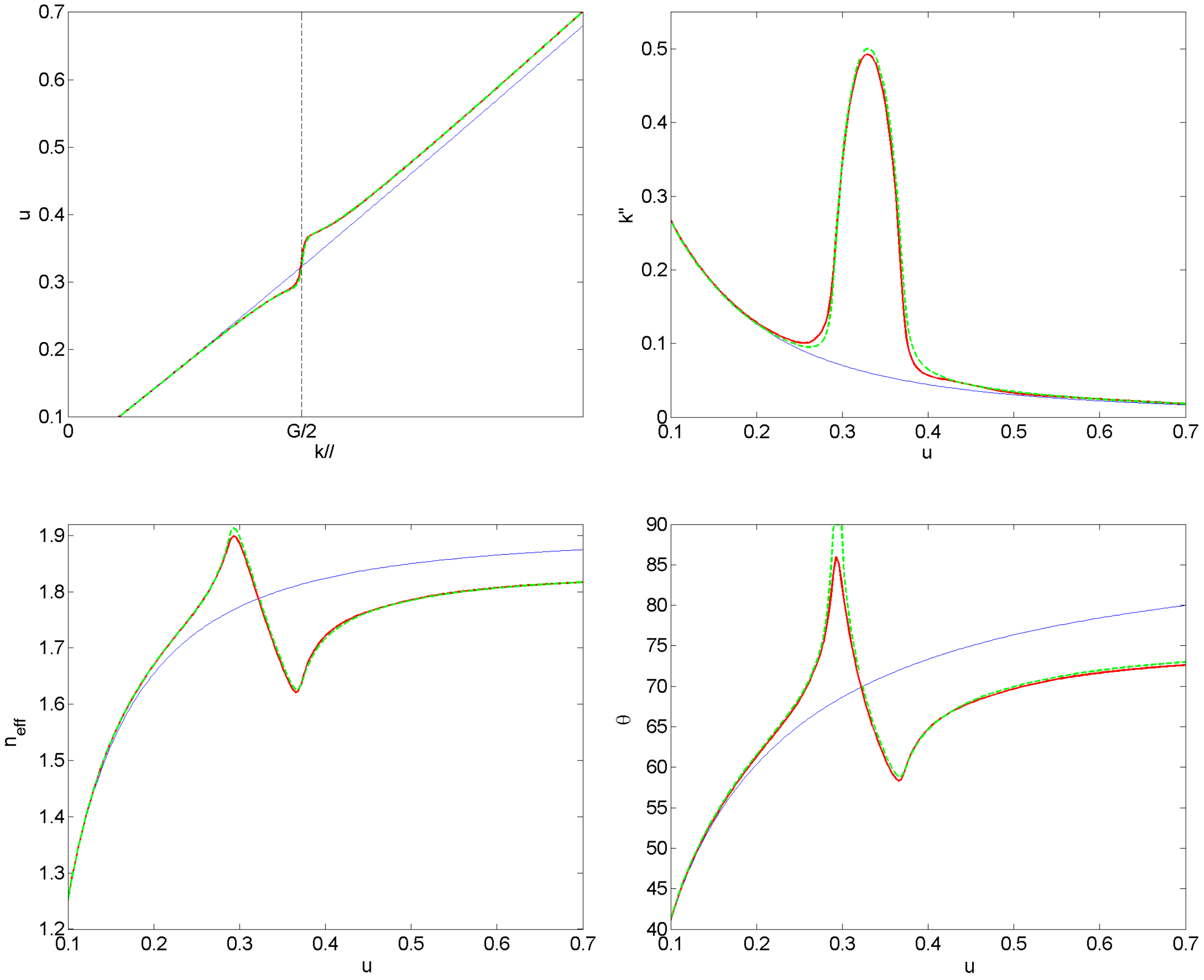

Figure 4.74: Propagation properties of the uncoupled 1D QGM (thin blue line), and the coupled Bloch QGM (red thick line: numerical result, magenta dashed line: analytical result of Eq 4.19). As can be seen, the analytical solution is in general very close to the numerical solution. (Top left) Dispersion relation. The coupling causes a gap opening at G/2 (dashed vertical line). (Top right) Loss coefficient k''. In the presence of coupling, k'' is high in the gap due to reflection. Outside of the gap, losses are dictated by the leakage of the fundamental harmonic and barely modified by the coupling. (Bottom left) Effective index n_{eff}. Below the gap, the mode localizes in the dielectric and n_{eff} increases with respect to the 1D value. Above the gap on the other hand, the mode localizes in air and n_{eff} decreases. Notice the *rigid shift* of n_{eff} caused by the coupling at high frequency: its asymptotic value is not $\langle n \rangle$ but $\langle n \rangle \sqrt{1-(\epsilon_1/\langle n \rangle)^4}$. (Bottom right) Corresponding angle of propagation.

Emission in a patterned layer: consequences

Several conclusions may be drawn from the existence of such a mode.

First, this mode might play a role in practical applications. Diffractive filters, for instance, may make use of such a resonance (in contrast to the common view that optical confinement by a substrate is necessary to obtain sharp Fano resonances in a filter). Besides, the existence of this QGM holds even if GaN is present on both sides of the PhC region, instead of an air superstrate (the mode's losses are simply doubled). Current is easy to inject in such a structure (Fig. 4.75). Thus, we obtain a photonic structure which keeps some properties of a PhC membrane (such as a vertically-localized mode with band gaps, which collects most of the light emission) but is easy to inject, in contrast to usual membranes. Such a structure may be considered for a PhC-based laser: current injection is easy, and the mode is naturally confined vertically in the low-index region.

Figure 4.75: (Left) QGM in a GaN/PhC/GaN structure: the mode is trapped in the low-index region, and constitutes an easily injectable photonic crystal membrane. (Right) Generalization of the QGM to higher-order quasi-guided resonances in the PhC region. Here, the first and second resonances are depicted.

Second, it is tempting to generalize the existence of the QGM and assume the presence of other, higher-order quasi-guided resonances (Fig. 4.75). Obviously, such higher order resonances are more lossy, and less well confined in the PhC region, than the QGM we just studied. Nevertheless, if we assume that these resonances dominate the optical properties in the PhC layer, we obtain a very simple picture of the spontaneous emission properties: the active region can couple to a few vertical resonances, much as it does in a thin microcavity supporting a few guided modes.

Of course, computing the precise profile and k_z of each resonance would be necessary for an accurate evaluation of spontaneous emission. However, we can simply assume that these resonances are those of a simple Fabry-Pérot of thickness L:

$$k_z^p = \frac{p\pi}{L}, E^p \sim cos(k_z^p z) \text{ in the PhC region.} \tag{4.21}$$

As in a microcavity, the spontaneous emission rate at position z is then proportional to the coupling to each mode:

$$F_p(z) \sim \sum_p sin(k_z^p z)^2 \tag{4.22}$$

In the structure considered so far, four vertical resonances are supported in the PhC region.[27] The Purcell effect obtained with this heuristic approach is compared with the previous rigorous numerical results on Fig. 4.76. As can be seen, the fit is acceptable. The amplitude of the oscillations of F_p are of the right order. The position of the first and last peaks, on the other hand, are not well reproduced – which is not surprising since they correspond to the fourth and last resonance, for which Eq. 4.21 is least valid.

In conclusion, our assumption that spontaneous emission takes place in a few quasi-guided vertical resonances gives at least a qualitative and intuitive picture of emission in a patterned region. From a practical point of view, it gives us a first hint of the optimal quantum well position (highest F_p) without resorting to lengthy calculations.

---

[27] The cutoff condition being $k_z < \langle n \rangle k_0$.

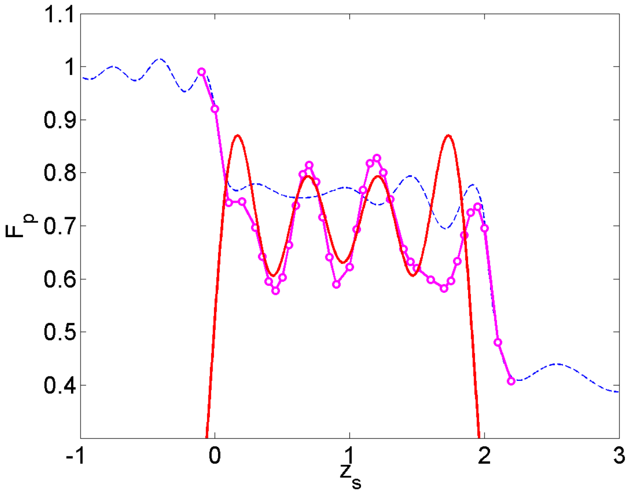

Figure 4.76: (Dashed line) Average index Purcell Factor $\bar{F}_p$. (Line with circles) Purcell factor F_p (rigorous numerical result). (Full line) Fit of F_p using Eq. 4.22 – to account for the slight leakage of the resonances in air and GaN, the Fabry-Pérot cavity has been assumed to extend in the range $z \in [-0.2, 2.1]$ rather than $[0, 2]$. The fit yields a reasonable qualitative approximation of the actual Purcell factor, although the position of the most extreme peaks is largely off.

4.5.4 Conclusion

Overall, the emission properties of a light source embedded in a patterned region are complex and depart from the simple case of planar multilayer structures. The source feels a lower average index, which decreases the emission of guided light. Additional modifications to the photonic DOS further impact the lifetime and extraction efficiency. Unexpected quasi-guided Bloch modes are localized in the patterned region in spite of the high index buffer, and seem to dominate the spontaneous emission properties. While the current analysis is insufficient to estimate the potential of such sources, their peculiar behavior leaves good prospects that such strong photonic effects may be used in favor of efficient light extraction.

4.6 Photonic crystal LEDs: conclusions

In this Chapter, we explored several strategies aimed at enhancing the efficiency of PhC-LEDs. The most important questions to address are:

- How much of the emitted light can be diffracted to air by the PhC ?
- How *efficient* is this phenomenon ?
- What are the optical properties of the resulting source ?

These questions can mostly be addressed by decoupling the two in-plane directions (*choice of the crystal lattice*) and the vertical direction (*vertical structuration*).

According to our discussion of crystal lattices, a triangular lattice (operating at the second Bragg order) is in general a suitable solution, while Archimedean tilings may eventually prove more efficient.

Vertical structuration is necessary to ensure a good extraction efficiency for all leaky modes – especially in thick, multimode GaN structures. Our first approach –insertion of a low-index layer in the structure– proved efficient in spite of its simplicity. To control more tightly the properties of spontaneous emission, other schemes with stronger photonic interaction were introduced: LLO-PhC LEDs, where metal losses are currently challenging, and LEO-PhC LEDs, whose high potential efficiency comes at the cost of a complex growth. Finally, our study of light emission in patterned layers evidenced the unusual properties of these structures. In addition to ensuring extraction on a short scale, all these approaches alter the angular pattern of spontaneous emission in different fashions, and offer as many possible ways to control the far-field pattern of the resulting light source.

It is difficult at this point to determine which PhC-based approach will prove the most efficient. All schemes face specific technical challenges, and overcoming these will eventually decide if any of these strategies can beat 'classic' light extraction schemes.

Bibliography

[1] L. Chen and A. V. Nurmikko. Fabrication and performance of efficient blue light emitting III-nitride photonic crystals. *Applied Physics Letters*, 85(17):3663–3665, 2004.

[2] M. Palamaru and P. Lalanne. Photonic crystal waveguides: Out-of-plane losses and adiabatic modal conversion. *Applied Physics Letters*, 78(11):1466–1468, 2001.

[3] D. Marcuse. *Theory of Dielectric Optical Waveguides.* Academic Press, New York, second edition, 1991.

[4] P. Sanchis, P. Bienstman, B. Luyssaert, R. Baets, and J. Marti. Analysis of butt coupling in photonic crystals. *IEEE Journal of Quantum Electronics*, 40(5):541–550, 2004.

[5] P. Sanchis, J. Marti, B. Luyssaert, P. Dumon, P. Bienstman, and R. Baets. Analysis and design of efficient coupling in photonic crystal circuits. *Optical and Quantum Electronics*, 37(1-3):133–147, 2005.

[6] G. Bottger, C. Liguda, M. Schmidt, and M. Eich. Improved transmission characteristics of moderate refractive index contrast photonic crystal slabs. *Applied Physics Letters*, 81(14):2517–2519, 2002.

[7] H. Benisty, R. Stanley, and M. Mayer. Method of source terms for dipole emission modification in modes of arbitrary planar structures. *Journal of the Optical Society of America a-Optics Image Science and Vision*, 15(5):1192–1201, 1998.

[8] R. Sink. *Cleaved-Facet Group-III Nitride Lasers.* PhD thesis, University of California, Santa Barbara, 2000.

[9] M. Rattier, T. F. Krauss, J. F. Carlin, R. Stanley, U. Oesterle, R. Houdre, C. J. M. Smith, R. M. De La Rue, H. Benisty, and C. Weisbuch. High extraction efficiency, laterally injected, light emitting diodes combining microcavities and photonic crystals. *Optical and Quantum Electronics*, 34(1-3):79–89, 2002.

[10] M. Rattier, H. Benisty, R. P. Stanley, J. F. Carlin, R. Houdre, U. Oesterle, C. J. M. Smith, C. Weisbuch, and T. F. Krauss. Toward ultrahigh-efficiency aluminum oxide microcavity light-emitting diodes: Guided mode extraction by photonic crystals. *IEEE Journal of Selected Topics in Quantum Electronics*, 8(2):238–247, 2002.

[11] J. J. Wierer, M. R. Krames, J. E. Epler, N. F. Gardner, M. G. Craford, J. R. Wendt, J. A. Simmons, and M. M. Sigalas. InGaN/GaN quantum-well heterostructure light-emitting diodes employing photonic crystal structures. *Applied Physics Letters*, 84(19):3885–3887, 2004.

[12] P. L. Hagelstein and D. R. Denison. Nearly isotropic photonic bandgap structures in two dimensions. *Optics Letters*, 24(11):708–710, 1999.

[13] J. F. Carlin, J. Dorsaz, E. Feltin, R. Butte, N. Grandjean, M. Ilegems, and M. Laugt. Crack-free fully epitaxial nitride microcavity using highly reflective AllnN/GaN Bragg mirrors. *Applied Physics Letters*, 86(3), 2005. 031107.

[14] M. Notomi, H. Suzuki, T. Tamamura, and K. Edagawa. Lasing action due to the two-dimensional quasiperiodicity of photonic quasicrystals with a penrose lattice. *Physical Review Letters*, 92(12), 2004. 123906.

[15] A. Della Villa, S. Enoch, G. Tayeb, V. Pierro, V. Galdi, and F. Capolino. Band gap formation and multiple scattering in photonic quasicrystals with a Penrose-type lattice. *Physical Review Letters*, 94(18), 2005. 183903.

[16] S. David, A. Chelnokov, and J. M. Lourtioz. Wide angularly isotropic photonic bandgaps obtained from two-dimensional photonic crystals with Archimedean-like tilings. *Optics Letters*, 25(14):1001–1003, 2000.

[17] S. David, A. Chelnokov, and J. M. Lourtioz. Isotropic photonic structures: Archimedean-like tilings and quasi-crystals. *IEEE Journal of Quantum Electronics*, 37(11):1427–1434, 2001.

[18] M. Rattier, H. Benisty, E. Schwoob, C. Weisbuch, T. F. Krauss, C. J. M. Smith, R. Houdre, and U. Oesterle. Omnidirectional and compact guided light extraction from archimedean photonic lattices. *Applied Physics Letters*, 83(7):1283–1285, 2003.

[19] Y. C. Zhong, S. A. Zhu, H. M. Su, H. Z. Wang, J. M. Chen, Z. H. Zeng, and Y. L. Chen. Photonic crystal with diamondlike structure fabricated by holographic lithography. *Applied Physics Letters*, 87(6), 2005. 061103.

[20] P. B. Johnson and R. W. Christy. Optical-constants of noble-metals. *Physical Review B*, 6(12):4370–4379, 1972.

[21] S. Olivier, M. Rattier, H. Benisty, C. Weisbuch, C. J. M. Smith, R. M. De la Rue, T. F. Krauss, U. Oesterle, and R. Houdre. Mini-stopbands of a one-dimensional system: The channel waveguide in a two-dimensional photonic crystal. *Physical Review B*, 63(11):art. no.–113311, 2001. 113311.

[22] P. Gibart. Metal organic vapour phase epitaxy of GaN and lateral overgrowth. *Reports on Progress in Physics*, 67(5):667–715, 2004.

[23] Y. Kato, S. Kitamura, K. Hiramatsu, and N. Sawaki. Selective growth of wurtzite GaN and AlxGa1-xN on GaN sapphire substrates by metalorganic vapor-phase epitaxy. *Journal of Crystal Growth*, 144(3-4):133–140, 1994.

[24] O. H. Nam, M. D. Bremser, B. L. Ward, R. J. Nemanich, and R. F. Davis. Growth of GaN and Al0.2Ga0.8Non patterened substrates via organometallic vapor phase epitaxy. *Japanese Journal of Applied Physics Part 2-Letters*, 36(5A):L532–L535, 1997.

[25] S. H. Fan, P. R. Villeneuve, J. D. Joannopoulos, and E. F. Schubert. High extraction efficiency of spontaneous emission from slabs of photonic crystals. *Physical Review Letters*, 78(17):3294–3297, 1997.

[26] R. K. Lee, Y. Xu, and A. Yariv. Modified spontaneous emission from a two-dimensional photonic bandgap crystal slab. *Journal of the Optical Society of America B-Optical Physics*, 17(8):1438–1442, 2000.

[27] M. Fujita, S. Takahashi, Y. Tanaka, T. Asano, and S. Noda. Simultaneous inhibition and redistribution of spontaneous light emission in photonic crystals. *Science*, 308(5726):1296–1298, 2005.

[28] S. Keller, C. Schaake, N. A. Fichtenbaum, C. J. Neufeld, Y. Wu, K. McGroddy, A. David, S. P. DenBaars, C. Weisbuch, J. S. Speck, and U. K. Mishra. Optical and structural properties of gan nanopillar and nanostripe arrays with embedded InGaN/GaN multi-quantum wells. *Journal of Applied Physics*, 100(5):054314, 2006.

Chapter 5

2D Simulation of photonic structures

5.1 Aims of Photonic crystal modeling

In the field of Photonic crystals, there has been a widespread interest in a variety of new optical effects, much beyond the quest for large bandgaps of the early 90's. It is possible to classify the modeling and theory efforts along the kind of effects sought rather than with reference to a particular method. This is because few effects have their single distinctive method, to date. A reasonable classification follows the way optical waves are managed at least in a linear regime. According to this view, we may distinguish:

- Dispersive effects
- Confinement and extraction effects
- Signal routing/filtering studies

For now, we shall intersperse the methods of interest, assumed for brevity to be known by the reader, along this description. The following Chapter presents a more thorough description of some of these methods.

5.1.1 Dispersion

Dispersion is a basic property of a photonic band. As such it can essentially be captured by any photonic band calculation, such as the plane-wave expansion method. In a broad sense, it may encompass the low-frequency effective medium behavior of PhC's, their birefringence in 2D for example. Similar methods are adapted to waveguides and or any periodic system (e.g. coupled cavities) by the use of supercell. 'Bulk' PhC bands are also of interest for phenomena such as the superprism and the supercollimator, taking advantage of singular region of the dispersion relation $\omega(\mathbf{k})$. Dispersion studies of uniform objects are also a preferred validation means for further more sophisticated studies. Just as in semiconductors, the bands should be set before novel effects can be sought. The idea to develop a gradient of photonic crystal parameters, mimicking the 'GRIN' (GRaded INdex) systems, opens the perspective of even richer and more functional behavior. It may for example include the issue of in-and outcoupling by transition regions. In this area, one would expect an 'envelope' method to be relevant. However, there have been few attempts which are really widespread in this direction. The work by Johnson *et al.* unravels some of the conceptual difficulties along this path.[1] The work performed during this thesis could be classified in this area. However, the account given of losses or coupling to extended modes is generally secondary in the many available dispersion studies, whereas dispersion in our case is not a primary concern (or only in a broad sense of depicting the phase space of photons we want to extract) and *losses* are clearly the main concern.

5.1.2 Confinement and extraction

The quest for fully confined modes has been relatively simple as long as lossless systems were concern. The basic method involves a superperiodic defect mode using the plane-wave expansion or the Finite-Difference-Time-Domain method.

However, leakage in real system is the main property of interest as no dispersion is sought here. In this framework, the FDTD method has been a workhorse of many research groups, with a clear success when it comes to the last generation of ultra-high Q cavities (Q >100,000 and up to 1,000,000) by e.g. Japanese teams.[2] The conceptual efforts that led to this particular design are however based on dispersion consideration, indicating that no single tool can serve all purposes. The topic of waveguides is naturally at a crossroad in this game : good propagation also means good confinement in the concerned directions. Several approaches (FTDT, numerous scattering matrix and modal methods, AndreaniŠs...) have been applied to the understanding of losses in waveguide modes that couple to the continuum for intrinsic or extrinsic reasons. Recently, the approaches by Hugues *et al.* have revived the potential of the Green function as a central tool to establish this property, a tool that was rather common in the near-field studies community. This shows that nanophotonics is a field that naturally fosters transverse use of several tools. Extraction has been studied more for enhanced light collection (e.g. in micropillars, or from PhC nanocavities in a quantum optics perspective) than for high-efficiency LEDs. In this sense, we believe the present work is rather original. An exception worth quoting is the work by Ghent university on chip-to-fiber vertical coupling by gratings.([3])

5.1.3 Routing and filtering

A broad class of modeling studies has been performed with the aim of applying photonic crystals to the routing of optical signals, in the spirit of telecoms applications (wavelength domain multiplexing, dispersion compensation...). Cavities in interaction with waveguides have been at the heart of many of these studies, the more classic microrings being known to perform very well in integrated optics for decades, be it with stringent requirements on the coupling geometry. FDTD has been the preferred tool for these studies. Other basic functions include splitters, bends, etc. The trial-and-error procedure has been the basic method in the first studies, e.g. adding or removing holes here and there, followed by shifts or changes in diameters of these holes for finer control. A Danish team has introduced a more thorough search in terms of inverse problem, letting the dielectric map vary toward more arbitrary shapes.[4, 5] This has proved efficient at the simulation level in 2D, and successful in 3D. Yablonovitch also touts the merits of the inverse problem approach to get the best grip on the delicate design issues facing the engineer when it comes to fulfill predetermined functions with a tight tolerance, to take into account fabrication tolerances, etc.[6] Commercial optimization packages (PhotonDesign) indeed implement some complex multiparametric approach, indicating that this topic is gradually maturing. This kind of investigation methods could also be of some use in the future of extraction researches, either for ultimate light emitters, or to manage sources that would emit a predetermined arbitrary radiation pattern.

After this tour, it is worth saying that the methods we have chosen are dictated by the basic physics of extraction of quasi-guided modes. No efficient recognized methods existed when I started this effort, especially in the atypical case where numerous bands have to be considered in the presence of a substrate.

With this introduction in mind, we now open a more detailed study of 2D and 3D modeling of PhCs. In this chapter and the following, we describe the numerical methods used in the thesis for calculations on photonic structures. This chapter is devoted to 2D calculations. We begin by introducing the well-known plane-wave expansion. We then derive and exemplify Fourier factorization rules ensuring faster numerical convergence. Finally, we discuss the extension to off-axis propagation.

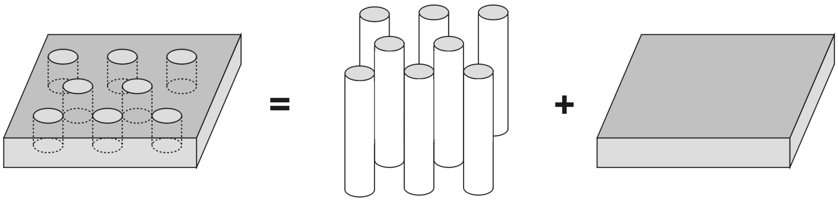

Figure 5.1: In the 2D+1D approximation, the effects of the photonic crystal and of the vertical waveguide are separated.

5.2 Plane wave expansion

5.2.1 Regular Plane wave expansion

Historically, 2D calculations have played an important role in the development of PhCs, especially at earlier stages when 3D calculations were prohibitive. They still constitute a powerful tool, well adapted to numerous situations. Their applicability to actual problems stems from the fact that most deterministic PhC structures use a '2D+1D' confinement approach: light is guided in the vertical direction by index contrast, and its dispersion is controlled in-plane by photonic crystal effects (Fig. 5.1). Such problems are then approximately separable[Benisty], so that calculations of the photonic effects can be handled as a 2D problem, that is, considering that the PhC is made of infinitely high rods.

Several methods can be considered when looking for eigenmodes of a 2D periodic structure, but the plane wave expansion (PWE) is probably the most straightforward. Fields are decomposed on a plane wave basis which is naturally adapted to the periodicity of the problem. Maxwell's equations then take the form of an eigenvalue problem, which can readily be solved numerically.

Due to the symmetry of the problem, modes can be classified in two categories corresponding to their polarization. For E (or TM) polarized modes the electric field is along the invariance direction z (and the magnetic field is in the $x-y$ plane), while for H (or TE) polarized modes the magnetic field is along z. For each polarization Maxwell's equation can then be reduced to one equation, on the z component of the field, for E and H polarization respectively:

$$\frac{1}{\epsilon}\left(\partial_x^2 E_z + \partial_y^2 E_z\right) = -\mu_0 \omega^2 E_z \tag{5.1}$$

$$\partial_x\left(\frac{1}{\epsilon}\partial_x H_z\right) + \partial_y\left(\frac{1}{\epsilon}\partial_y H_z\right) = -\mu_0 \omega^2 H_z \tag{5.2}$$

We now Fourier transform these equations. Let us introduce the following notations: if A is a real-space column vector, $[A]$ is the vector column of its Fourier transform. If B is a matrix, $[\![B]\!]$ is the Matrix of its Fourier transform (more precisely, the Toeplitz matrix whose (n,m) element is the Fourier coefficient B_{n-m}).[1]

According to the Bloch-Floquet theorem, the fields can be written:

$$\begin{aligned} E_z &= \left(\textstyle\sum_G [E_z]_G e^{i\mathbf{G}.\mathbf{r}}\right) e^{i\mathbf{k}_{//}.\mathbf{r}} \\ H_z &= \left(\textstyle\sum_G [H_z]_G e^{i\mathbf{G}.\mathbf{r}}\right) e^{i\mathbf{k}_{//}.\mathbf{r}} \end{aligned} \tag{5.3}$$

---

[1] A few remarks can be made on these notations. First, $[A]$ and $[\![B]\!]$ are *a priori* infinite since an infinity of harmonics appear in Fourier transforms. However, they will later be truncated to a finite number of harmonics for numerical computation – say, N_x terms in the x direction and N_y terms in the y direction. Second, we are working on 2D periodic functions (depending on both in-plane coordinates x and y) so that their Fourier transforms are initially characterized by two coefficients, say n_x and n_y. In order to use the present notations, these coefficients need to be reindexed along one dimension, for instance by letting $n = n_x + N_x n_y$.

Here, $\mathbf{k}_{//}$ is the in-plane wavevector of the Bloch mode and $\mathbf{G}$ are the reciprocal lattice vectors. By introducing this in Maxwell's equations (5.1, 5.2) we obtain:

$$\begin{array}{c} \sum_{G'}(\mathbf{k}_{//} + \mathbf{G'})^2[\![1/\epsilon]\!]_{G-G'}[E_z]_{G'} = \mu_0\omega^2[E_z]_G \\ \sum_{G'}(\mathbf{k}_{//} + \mathbf{G}) \cdot (\mathbf{k}_{//} + \mathbf{G'})[\![1/\epsilon]\!]_{G-G'}[H_z]_{G'} = \mu_0\omega^2[H_z]_G \end{array} \tag{5.4}$$

This is a standard eigenvalue problem, whose solutions yield the Bloch modes of the PhC. Other Fourier forms of Maxwell's equations can also be written, as will be discussed later. The above form is that of the original article by Plihal and Maradudin.[7]

In order to solve the eigenproblem numerically, one has to truncate the infinite sums over the reciprocal lattice to a finite number N of harmonics. Obviously, the accuracy of the calculation increases with N. Usually, only a few eigenvalues are needed (those of lowest-energy), even though $N \sim 10^3$ is sometimes needed for good precision. Therefore, it is often advantageous to use numerical packages (such as Lapack) which only look for a few eigenvalues and are much less time-consuming than a full diagonalization.

5.2.2 Inversion of the eigenvalue equation

In the form (5.4) of the eigenvalue problem, it is straightforward to impose a value of $k_{//}$ and look for a value of ω. This is inherited from band structure calculations methods in semiconductors, where the energy and momentum of electrons are equally "good" unknowns. However, in photonic structure, the frequency of light is usually imposed, so that it can be more useful to set ω and look for the corresponding $k_{//}$ values. In order to do this, we introduce the following notations: G_x, G_y are the coordinates of a reciprocal lattice vector $\mathbf{G}$. $\mathbf{k}_{//}$ can be decomposed as $\mathbf{k}_{//} = k_{//}(c\mathbf{u}_x + s\mathbf{u}_y)$, where $\mathbf{u}_x$ and $\mathbf{u}_y$ are unitary vectors. The Fourier transform of Maxwell's equation can then be written:

$$\sum_{G'} \left((G'^2_x + G'^2_y) + 2k_{//}(cG'_x + sG'_y)) + k^2_{//} \right) [\![1/\epsilon]\!]_{G-G'}[E_z]_{G'} = \mu_0\omega^2[E_z]_G \tag{5.5}$$

$$\sum_{G'} \left((G_xG'_x + G_yG'_y) + k_{//}(cG_x + cG'_x + sG_y + sG'_y) + k^2_{//} \right) [\![1/\epsilon]\!]_{G-G'}[H_z]_{G'} = \mu_0\omega^2[H_z]_G \tag{5.6}$$

The above equations are now generalized eigenvalue problems, as both $k_{//}$ and $k^2_{//}$ intervene. In order to get back to conventional eigenvalue problems, one can use the following canonical method. Both equations are of the form:

$$A_0X + k_{//}A_1X = k^2_{//}BX \tag{5.7}$$

Where X is the unknown field (respectively, E_z or H_z). By letting:

$$\mathbb{A} = \begin{pmatrix} A_1 & A_0 \\ \mathbb{1} & 0 \end{pmatrix}, \mathbb{B} = \begin{pmatrix} B & 0 \\ 0 & \mathbb{1} \end{pmatrix}, Y = \left| \begin{array}{l} k_{//}X \\ X \end{array} \right. \tag{5.8}$$

The initial problem can be rewritten as:

$$\mathbb{A}Y = k_{//}\mathbb{B}Y \tag{5.9}$$

This results in a regular (first-order) eigenvalue problem, at the cost of doubling the size of the problem – as matrices scale as N^2, memory requirements are multiplied by 4. In this new form however, it is not possible to compute only a few of the eigenvalues because matrix $\mathbb{B}$ is not definite positive. This results in long computation times, especially when the truncation order N is large. It is possible to avoid this by writing Maxwell's equations differently. For E polarization, one just has to multiply Eq. (5.1) by ϵ before the Fourier transform, thus getting:

$$\mu_0\omega^2\sum_{G'}[\![\epsilon]\!]_{G,G'}[E_z]_{G'} - (G_x^2+G_y^2)[E_z]_G - 2k_{//}(cG_x+sG_y))[E_z]_G = k_{//}^2[E_z]_G \tag{5.10}$$

Then, using the same procedure as above, one can get back to a conventional eigenvalue problem where $\mathbb{B}$ is an identity matrix.

For the case of H polarization, such a simple trick is not possible: ϵ appears in derivative terms in Eq. (5.2). One has to work on fields E_x and E_y rather than on H_z, yielding the following system:

$$\left\{\begin{array}{rl} k_{//}^2(s^2[E_x]_G + cs[E_y]_G) = & \mu_0\omega^2\sum_{G'}[\![\epsilon]\!]_{G,G'}[E_x]_{G'} - G_y^2[E_x]_G + G_xG_y[E_y]_G \\ & \quad +k_{//}(-2sG_y[E_x]_G + (cG_y+sG_x)[E_y]_G) \\ k_{//}^2(c^2[E_y]_G - cs[E_x]_G) = & \mu_0\omega^2\sum_{G'}[\![\epsilon]\!]_{G,G'}[E_y]_{G'} - G_x^2[E_y]_G + G_xG_y[E_x]_G \\ & \quad +k_{//}(-2cG_x[E_y]_G + (cG_y+sG_x)[E_x]_G) \end{array}\right. \tag{5.11}$$

Once again, using (5.8), one is then led to an eigenvalue problem with a definite positive $\mathbb{B}$, which can be solved for a few eigenvalues.

When comparing the new expressions (5.10-5.11) to the more conventional PWE form (5.4), memory demands are multiplied by 4 in order to get back to an eigenvalue problem, and by an additional factor 4 in H polarization in order to work on two fields instead of one.

In spite of the additional computational task, this form presents several advantages over the conventional formulation. First, index dispersion can be readily included, since a calculation is performed for each value of ω. Second, bands can also naturally be investigated inside the band gaps, where $k_{//}$ acquires an imaginary part. The eigenvalue is then of the form $k_{//} = k'_{//} + ik''_{//}$, and $k''_{//}$ characterizes the exponential decay of Bloch modes. Finally, isofrequency contours (e.g. Fermi surfaces) can be easily calculated. This is especially interesting for local density of states (LDOS) calculations, where one otherwise has to interpolate a mesh in $k_{//}$-space in order to find the Fermi surfaces.[8] Fig. 5.2 presents examples of such calculations.

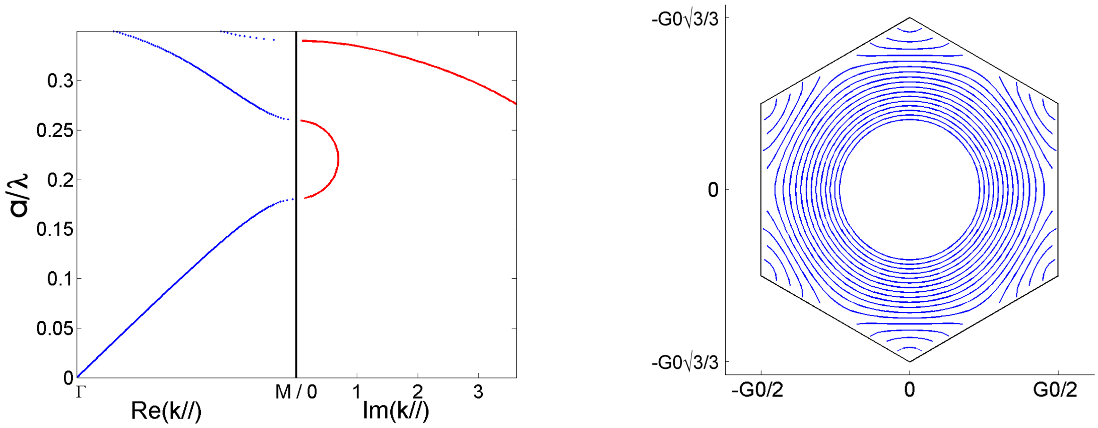

Figure 5.2: Applications of the inverted eigenvalue problem. (left) Real and imaginary branches of the dispersion of a triangular PhC ($\epsilon_{core} = 12, \epsilon_{rods} = 1, f = 0.3$, H polarization). Im($k_{//}$) is in a^{-1} units. (right) Isofrequencies of the same PhC, for a/λ ranging from 0.1 to 0.22. G_0 is the norm of the basis vector of the reciprocal space.

5.2.3 Supercell calculations

The PWE is limited to periodic structure. However, more complex objects can also be studied by using a supercell provided the fields are decaying far enough from such objects. For instance, PhC waveguides or cavities fall in this category because their guided or defect modes have localized fields which are evanescent in the PhC cladding. In this case, the object can be artificially periodized, as will be illustrated in Fig. 5.8. If the PhC cladding separating the instances of the object is large enough, the fields in each supercell do not contaminate each other.

5.3 Fourier rules for fast convergence

5.3.1 A history of Fourier rules

In the above, depending on the PWE form used, the dielectric map appeared in two ways: the "simple" Fourier transform $[\![\epsilon]\!]$ (as in the article by Ho Ref. [9]) and the Fourier transform of the inverse dielectric map $[\![1/\epsilon]\!]$ (as in Ref. [7]). This simply stemmed from the way Maxwell's equation were written before the Fourier transform was performed. Both forms are mathematically equivalent, because the infinite Toeplitz matrices involved commute, so that $[\![\epsilon]\!]^{-1} = [\![1/\epsilon]\!]$.

However, this commutation no longer holds when the matrices are truncated to a finite number of harmonics. As was soon realized, numerical convergence (that is, the number of harmonics needed to reach a given accuracy) actually strongly depends on the way the Fourier transform of ϵ is performed.

Several years were needed before this problem was properly solved. After Lalanne introduced semi-empirical expressions for enhancing numerical convergence,[10] Li finally derived general mathematical rules which govern proper factorization of the Fourier transform of functions products.[11] He showed that they stem from the discontinuities of the electromagnetic field at dielectric interfaces. The key results are summarized below.

In general, when considering the Fourier transform h of a product of functions f and g, it is natural to write Laurent's rule:

$$h_n = \sum_{m=-\infty}^{\infty} f_{n-m} g_m \tag{5.12}$$

Here h_n is the n^{th} Fourier coefficient of h. In matrix notation, this becomes:

$$[h] = [\![fg]\!] = [\![f]\!]\,[g] \tag{5.13}$$

However, according to Li, when the sums are truncated to a finite number of harmonics N, Laurent's rule is no longer true if both f and g are discontinuous at the same point while the product fg remains continuous at that point. In this case, the discontinuities prevent uniform convergence of the partial sums toward the series. Rather, one should use the so-called inverse rule:

$$h_n = \sum_{m=-M}^{M} \left(\frac{1}{f}\right)^{-1}_{n-m} g_m \tag{5.14}$$

Or, in matrix notations:

$$[h] = [\![fg]\!] = [\![1/f]\!]^{-1}\,[g] \tag{5.15}$$

While both (5.13) and (5.15) are mathematically equivalent when $N \to \infty$, the convergence speed is significantly enhanced using the inverse rule. The cutoff M in the sums is related to the total number of harmonics by:

$$M = 2N + 1 \tag{5.16}$$

This result was first applied to 1D gratings, and then generalized to 2D and 3D periodic structures. [12, 13, 14] At that point, focus was only brought onto structures with piecewise-straight dielectric boundaries along the crystal axes, such as square holes, but it was argued that any boundary can be approximated by a piecewise-smooth boundary – this is the so-called staircase approximation (Fig. 5.3). In Ref. [14], Lalanne detailed the use of these rules in the context of PWE. Shortly after, Nevière and Popov noted that for 1D gratings with smooth boundaries, such as sine gratings, the staircase approximation was actually not valid [15], a fact that they attributed to the appearance of electric field divergences at the corners of the stairs. They showed that the expression of the rules had to be modified to ensure fast convergence, yielding the so-called "fast Fourier factorization" (FFF) [16]. At this point, the theoretical background governing efficient Fourier factorization was essentially complete.

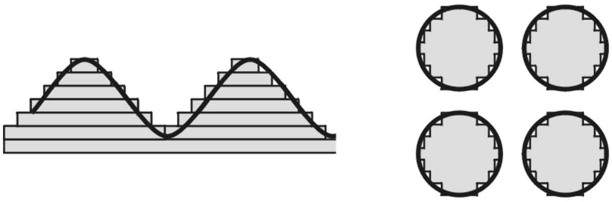

Figure 5.3: Staircase approximation of a sine grating (left) and an array of circular rods (right)

5.3.2 FFF implementation for 2D PhCs with arbitrary hole shape

During this thesis, the analogous problem for 2D PhC was tackled. It was first checked that the staircase approximation does not enhance convergence for circular holes. The FFF rules were then adapted to the case of 2D PhCs with curvilinear boundaries. Of course, this includes the important case of a PhC with circular holes, which is by far the most frequently studied structure, both in theory and experimentally. Other interesting applications include the case of elliptic holes (which are sometimes considered in order to lift degeneracy in a structure [17] and also appear as an effect of imperfect fabrication), and the application to supercell calculations, where the computation task is heavy and fast convergence is welcome. Here, we only present the main results; a more complete discussion can be found in [18].

In order to express these rules, we now consider a Fourier transform of the most general form:

$$\begin{aligned} [\![\epsilon E_x]\!] &= \epsilon^{xx}\,[E_x] + \epsilon^{xy}\,[E_y] \\ [\![\epsilon E_y]\!] &= \epsilon^{yx}\,[E_x] + \epsilon^{yy}\,[E_y] \\ [\![\epsilon E_z]\!] &= \epsilon^{zz}\,[E_z] \end{aligned} \tag{5.17}$$

In this framework, the so-called Ho's method corresponds to the simple choice:

$$\begin{aligned} &\epsilon^{xx} = \epsilon^{yy} = \epsilon^{zz} = [\![\epsilon]\!] \\ &\epsilon^{xy} = \epsilon^{yx} = 0 \end{aligned} \tag{5.18}$$

while in the method of Plihal and Maradudin, also called E-method, we have

$$\begin{aligned} &\epsilon^{xx} = \epsilon^{yy} = \epsilon_{zz} = [\![1/\epsilon]\!]^{-1} \\ &\epsilon^{xy} = \epsilon^{yx} = 0 \end{aligned} \tag{5.19}$$

Let us now express the FFF rules. In the above expressions, the possibility is left to *mix* both coordinates x and y during the Fourier transform. Intuitively, this is justified by the fact that, at a curved dielectric boundary, neither x nor y is a relevant direction regarding the field discontinuities. Rather, one should consider the (local) normal and tangential coordinates. On the other hand, z is along the PhC rods and constitutes a "good" direction for discontinuity properties.

Namely, across any dielectric boundary, the vertical component E_z and the tangential component E_T of the electric field are continuous, and the normal component E_N is discontinuous, while the product ϵE_N remains continuous. According to Li's theorem, a correct factorization is then:

$$\begin{aligned} [\![\epsilon E_N]\!] &= [\![1/\epsilon]\!]^{-1}\,[E_N] \\ [\![\epsilon E_T]\!] &= [\![\epsilon]\!]\,[E_T] \\ [\![\epsilon E_z]\!] &= [\![\epsilon]\!]\,[E_z] \end{aligned} \tag{5.20}$$

Following this principle, let us define two adequate functions $c(x, y)$ and $s(x, y)$ and two vector fields associated with them (see Fig. 5.4):

$$\begin{aligned} E_x &= cE_N - sE_T \\ E_y &= cE_T + sE_N \end{aligned} \tag{5.21}$$

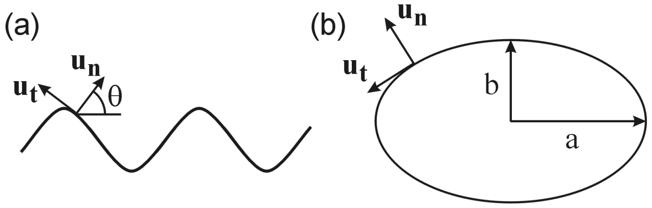

Figure 5.4: Definition of local normal and tangential vectors at the dielectric boundaries for : (a) a sine grating (b) an elliptic hole

The functions c and s must be continuous (at least at the discontinuities of ϵ) and such that at the discontinuities of ϵ, E_N be normal to the profile of the discontinuity, and E_T tangent to it. Moreover, one must have:

$$c^2 + s^2 = 1 \;\forall (x, y) \tag{5.22}$$

The above relation can be inversed as:

$$\begin{aligned} E_T &= cE_y - sE_x \\ E_N &= cE_x + sE_y \end{aligned} \tag{5.23}$$

Therefore, we obtain:

$$\epsilon E_x = \epsilon(cE_N - sE_T) \tag{5.24}$$

so that, according to Laurent's rule and the inverse rule:

$$[\![\epsilon E_x]\!] = [\![1/\epsilon]\!]^{-1}[\![cE_N]\!] - [\![\epsilon]\!][\![sE_T]\!] \tag{5.25}$$

We then get back to E_x and E_y using Eq. 5.23, and get:

$$[\![\epsilon E_x]\!] = \left([\![1/\epsilon]\!]^{-1}[\![c^2]\!] + [\![\epsilon]\!][\![s^2]\!]\right)[E_x] + \left([\![1/\epsilon]\!]^{-1} - [\![\epsilon]\!]\right)[\![cs]\!]\,[E_y] \tag{5.26}$$

Using similar arguments for the y coordinate, we finally find:

$$\epsilon_{FFF} = \begin{pmatrix} \epsilon^{xx} & \epsilon^{xy} & \\ \epsilon^{yx} & \epsilon^{yy} & \\ & & \epsilon^{zz} \end{pmatrix} = \begin{pmatrix} [\![1/\epsilon]\!]^{-1}[\![c^2]\!] + [\![\epsilon]\!][\![s^2]\!] & \left([\![1/\epsilon]\!]^{-1} - [\![\epsilon]\!]\right)[\![cs]\!] & \\ \left([\![1/\epsilon]\!]^{-1} - [\![\epsilon]\!]\right)[\![cs]\!] & [\![1/\epsilon]\!]^{-1}[\![s^2]\!] + [\![\epsilon]\!][\![c^2]\!] & \\ & & [\![\epsilon]\!] \end{pmatrix} \tag{5.27}$$

As expected, ϵ_{xy} and ϵ_{yx} no longer vanish, because the continuity conditions mix the fields E_x and E_y. We will now express the eigenvalue equations using this dielectric tensor. Let us define:

$$M = \begin{pmatrix} \epsilon^{xx} & \epsilon^{xy} \\ \epsilon^{yx} & \epsilon^{yy} \end{pmatrix} \tag{5.28}$$

and

$$M^{-1} = \begin{pmatrix} \alpha & \beta \\ \gamma & \delta \end{pmatrix} \tag{5.29}$$

Maxwell's equations can then be brought down to second-order equations on $[E_z]$ and $[H_z]$ only:

$$\partial_x^2[E_z] + \partial_y^2[E_z] = -\mu_0\epsilon\omega^2[E_z] \tag{5.30}$$

$$\left(-\partial_x\delta\partial_x + \partial_x\gamma\partial_y + \partial_y\beta\partial_x - \partial_y\alpha\partial_y\right)[H_z] = \mu\omega^2\,[H_z] \tag{5.31}$$

Under this form, $[E_z]$ and $[H_z]$ can be developed according to Floquet's theorem and Maxwell's equations take the form of an eigenvalue problem. As above, various forms can be considered, depending whether one wants to compute $k_{//}(\omega)$ or $\omega(k_{//})$. The general recipe for implementation, independent of the precise way the eigenproblem is derived, is given by Eq. 5.17.

It is worth noticing that, for E polarization, *the correct Fourier factorization is just that given by Ho's method.*[2] This explains why, even at the early stages of PhC calculations, good convergence was reached in E polarization while H polarization remained problematic.[19]

5.3.3 Applications of the FFF rules

In order to get M, one needs to compute the 2D Fourier transform of functions c^2, s^2 and $c.s$ over the unit cell. This can easily be done numerically using an FFT algorithm (the fact that the functions are not defined at the origin of the plane and the cell boundaries can just be ignored numerically) - and taking advantage of the fact that:

$$[\![c^2]\!] + [\![s^2]\!] = 1 \tag{5.32}$$

For a given PhC geometry, it is generally easy to find suitable functions c and s, either analytically or numerically (if the profile of the holes is arbitrary). Of course, the choice of c and s is not unique away from the dielectric interfaces. However a "canonical" form generally exists. In the following, we illustrate this by three examples.

---

[2] In his article [9], Ho used the PWE to compute the band structure of a 3D PhC made of spheres: in this case, of course, the simple use of $[\![\epsilon]\!]$ does not provide good convergence. However, this factorization choice was called Ho's method in general, and does provide fast convergence when applied to 2D PhCs in E polarization !

Circular holes We simply define $c = cos(\theta)$ and $s = sin(\theta)$, where θ is the angle between the x-axis and the radial unit vector $\mathbf{u}_r$. This defines c and s everywhere in space. The convergence of the FFF and Ho's method is compared on Fig. 5.5, for a square lattice PhC with circular holes. The FFF clearly performs better, with a relative error below 10^{-3} as soon as $M \geq 5$.

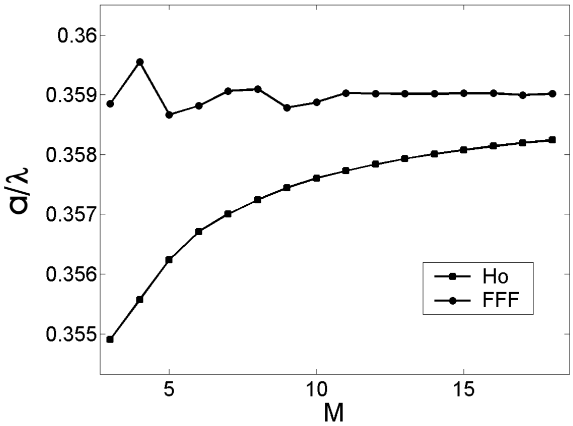

Figure 5.5: Normalized frequency of the second band at the X point for a square PhC lattice with circular holes, made of a dielectric matrix ($\epsilon = 12$) and air holes with $f = 0.4$. Ho's method (squares) converges more slowly than the FFF (circles).

Elliptic holes In the case of elliptic holes of half-axis parameters a and b (Fig. 5.4), we define the parameter t by:

$$tan(t) = \frac{a}{b} tan(\theta) \tag{5.33}$$

One can then define normal and tangent vectors at the boundaries of the ellipse using:

$$\begin{aligned} c &= b.cos(t)/\sqrt{b^2cos^2(t) + a^2sin^2(t)} \\ s &= a.sin(t)/\sqrt{b^2cos^2(t) + a^2sin^2(t)} \end{aligned} \tag{5.34}$$

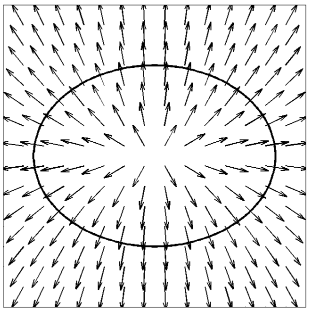

Figure 5.6: Vector field of the normal vectors for an elliptic hole. The bold line indicates the dielectric boundary.

If we extend this definition to the whole (x, y) plane, we obtain functions c and s which fulfill the above conditions. As an example, we consider the case of a square lattice of elliptic air holes (with parameters $a = 0.3$ and $b = 0.4$ in units of the crystal lattice, corresponding to a filling factor $f \approx 0.38$) in a dielectric material ($\epsilon = 12$). For reference, the vector field corresponding to the normal vectors is shown on Fig. 5.6. As before, we choose $N_x = N_y = 2M + 1$. Convergence is shown on Fig. 5.7. Here again, convergence is much faster with the new method: the relative error is below 10^{-3} for M=7 (225 plane waves), a precision which is not reached by Ho's method even for M=21 (1849 plane waves).

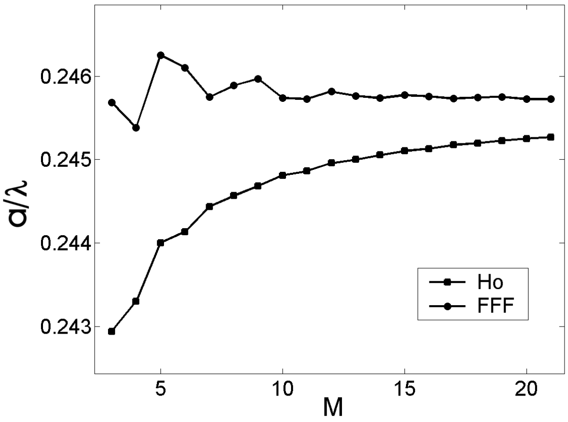

Figure 5.7: Normalized frequency of the second band at the X point for a square PhC lattice with elliptic holes, as obtained with Ho's method and with the FFF.

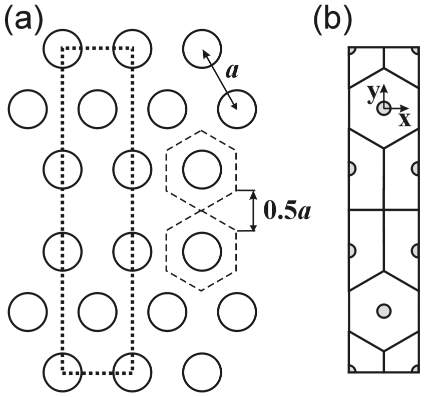

Figure 5.8: (a) Geometry of the defect waveguide. The supercell boundaries are indicated by the dotted line. (b) Definition of the subcells of the supercell.

Supercell calculations Functions c and s can be defined piecewise in subcells of the supercell. Choice of the subcells is arbitrary as long as their boundaries do not coincide with a discontinuity of ϵ. For instance, one can define the subcells as the closest points to the center of each PhC hole (Fig. 5.8), and then define c and s as previously, by centering the (x, y) coordinates at the center of the hole in each cell. Functions c and s are plotted on Fig. 5.9.

Here, we consider a waveguide displaying an ultra-flat band dispersion. Such bands display low group velocity and have aroused much interest lately because they open new perspectives for efficient manipulation of 'slow' light. Namely, we study a W-0.7 defect waveguide in a triangular PhC of air holes of radius 0.33 in a medium of index $n = 3$ (a typical effective index value for a silicon membrane). We use a cladding of 7 holes to avoid interaction between supercells, so that we choose $N_x = 2M + 1$

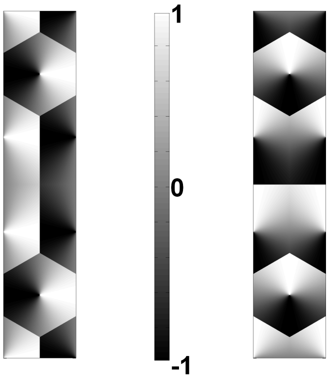

Figure 5.9: Functions c (left) and s (right) for the supercell calculation

and $N_y = 14M + 1$. Rather than the frequency, we focus on the effective mass of photons at the edge of the Brillouin zone, which characterizes the flatness of the band. A good precision can be essential since some phenomena (such as the penetration of evanescent waves) vary exponentially with m_{eff}. We choose the convenient following definition for m_{eff} (getting rid of prefactors):

$$m_{eff}^{-1} = \frac{d^2u}{dk^2}$$

The results of calculations, displayed on Fig. 5.10, evidence the difficulty of convergence. With the FFF, the value of m_{eff}^{-1} stabilizes around 3.10^{-4}, and oscillations around this value are still as high as $\sim$ 10%. Even though the relative error is rather high, the value of m_{eff} can be reasonably inferred. For reference, a typical value for a usual photonic band is two orders of magnitude higher −for instance, the other (non-flat) guided mode of this waveguide yields $m_{eff}^{-1} \sim 4.10^{-2}$. With Ho's method, the inverse effective mass is strongly over-estimated (notice the scale), typically more than twice the value obtained above.

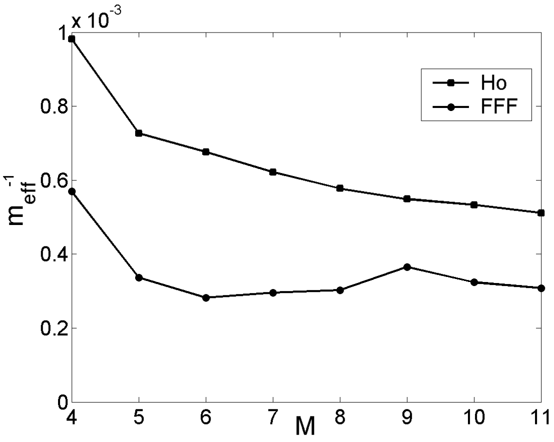

Figure 5.10: Inverse effective mass ($\partial^2 u/\partial^2 k$) at the edge of the Brillouin zone for the guided mode of a W-0.7 waveguide with ultra-flat dispersion.

5.4 Generalization to off-plane propagation

In all of the previous, the wavevector of the Bloch mode has been taken in-plane, e.g. perpendicular to the PhC rods. We now consider the case of off-plane propagation, and write the wavevector as $\mathbf{k} = \mathbf{k}_{//} + \mathbf{k}_z$. The interest of this situation goes beyond the frame of 2D calculations, as it provides the ground for 3D scattering matrix calculations. For the problem to be well-defined, one needs to specify two of the three quantities $\left\{\mathbf{k}_{//}, \mathbf{k}_{\perp}, \omega\right\}$ and look for the third quantity as an eigenvalue of Maxwell's equation.

E and H polarizations are not defined anymore, so that one may no longer work on one field. It is still possible to eliminate $\mathbf{H}$ and E_z, and work on E_x and E_y. Usually, derivation of the eigenproblem is rather tedious. It can be easily found in various forms in the literature [20, 21, 22], although without an FFF implementation for arbitrary holes shapes. The difference between these forms simply stems from the order in which one gets rids of the fields of Maxwell's equations to keep only E_x and E_y. In the following, we explicit the FFF implementation for two popular forms found in literature (keeping the same notations as in the original articles), and maintain details of the derivation to a minimum.

5.4.1 Moharam form

This form is found in many works using the rigorous coupled-wave analysis (RCWA) method, first introduced by Moharam (see Chapter 6). It can for instance be found in [21] and slight variations exist,[10, 23, 24] mainly depending on the Fourier factorization rules used. From Maxwell's equations, one starts by getting rid of the vertical field components E_z, H_z, yielding four first-order equations on E_x, E_y, H_x, H_y:

$$1/k_0 \left| \begin{matrix} \partial_z E_x \\ \partial_z E_y \end{matrix} \right. = \begin{pmatrix} -K_x \epsilon^{-1} K_y & K_x \epsilon^{-1} K_x - \mathbb{1} \\ \mathbb{1} - K_y \epsilon^{-1} K_y & K_y \epsilon^{-1} K_x \end{pmatrix} \left| \begin{matrix} H_x \\ H_y \end{matrix} \right. \tag{5.35}$$

$$1/k_0 \left| \begin{matrix} \partial_z H_x \\ \partial_z H_y \end{matrix} \right. = \begin{pmatrix} -K_x K_y - \epsilon^{yx} & K_x^2 - \epsilon^{yy} \\ -K_y^2 + \epsilon^{xx} & K_y K_x + \epsilon^{xy} \end{pmatrix} \left| \begin{matrix} E_x \\ E_y \end{matrix} \right. \tag{5.36}$$

The above are matrix notations. K_x is a diagonal matrix whose (n, n) coefficient is $(k_x + G_{x,n})^2$ − where $\mathbf{G}_n$ is the n^{th} reciprocal lattice vector. ϵ^{xx} and others are the components of the FFF dielectric tensor (5.17), and $\epsilon^{-1} = (\epsilon^{zz})^{-1}$ (we omit the zz indices for clarity). The only difference with respect to the standard (non-FFF) formulation found in literature lies in the ϵ coefficients of Eq. 5.36. As expected, all terms of Eq. (5.27) are used in this formulation: since polarizations are no longer defined, all the terms of the FFF dielectric tensor intervene. The FFF form leads to similar convergence enhancement as in previous sections.

Both equations can then be reduced to a second-order set of equations on E_x, E_y only, yielding:

$$\omega^2 \begin{pmatrix} \epsilon^{xx} & \epsilon^{xy} \\ \epsilon^{yx} & \epsilon^{yy} \end{pmatrix} \left| \begin{matrix} E_x \\ E_y \end{matrix} \right. = \tag{5.37}$$

$$\begin{pmatrix} k_z^2 + K_y^2 + K_x \epsilon^{-1} K_x \epsilon^{xx} + K_x \epsilon^{-1} K_y \epsilon^{yx} & -K_y K_x + K_x \epsilon^{-1} K_y \epsilon^{yy} + K_x \epsilon^{-1} K_x \epsilon^{xy} \\ -K_y K_x + K_y \epsilon^{-1} K_x \epsilon^{xx} + K_y \epsilon^{-1} K_y \epsilon^{yx} & k_z^2 + K_x^2 + K_y \epsilon^{-1} K_y \epsilon^{yy} + K_y \epsilon^{-1} K_x \epsilon^{xy} \end{pmatrix} \left| \begin{matrix} E_x \\ E_y \end{matrix} \right.$$

We label this form of the eigenproblem as the Moharam form. It is here written to obtain ω as a function of $\{k_x, k_y, k_z\}$. However, as k_0 and k_z are independent of other terms, it can also easily be reordered in order to obtain k_z as a function of $\{k_x, k_y, \omega\}$.

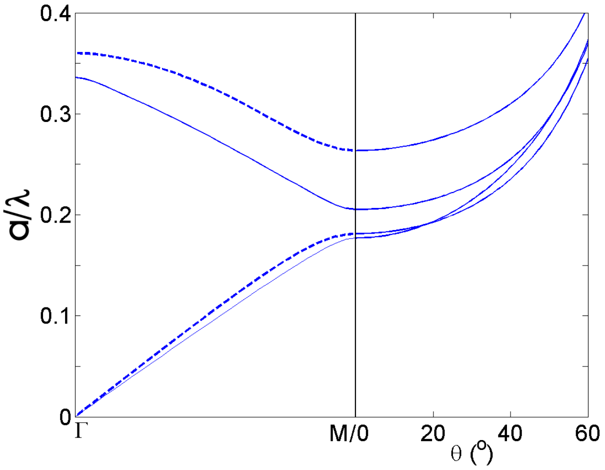

Figure 5.11: (left) In-plane band structure of a triangular lattice PhC ($\epsilon_{core} = 12, \epsilon_{rods} = 1, f = 0.3$) in the ΓM direction for $k_z = 0$. Dashed=H polarization, full=E polarization. (right) Band structure at the M point (e.g. $k_{//} = G_0/2$) as a function of the off-plane angle $\theta = tan(k_z/k_{//})$. The gap narrows for off-plane propagation.

As an application of this formula, Fig. 5.11 displays the evolution of the band gap at the edge of the Brillouin zone (point M) when k_z differs from 0. For all bands, the frequency increases with k_z because the total wavevector is larger. In addition, the gaps get narrower; for $\theta > 52^o$ the gap closes. This is best seen by looking at the distance between consecutive bands (Fig. 5.12).

5.4.2 Tikhodeev form

Another derivation of the eigenvalue problem can be found in [22], using only Laurent's rule. This form, which we call the Tikhodeev form, will be used in the next chapter for construction of the scattering matrix. In the Tikhodeev approach, one first gets rid of **H** and works only on **E**. Then, one expresses E_z as a function of E_x and E_y. This derivation is slightly different from that of Moharam, hence the different form of the final equations. Including the FFF is straightforward and does not modify the derivation method, so that we restrict ourselves to giving the resulting eigenproblem with the FFF rules.

We first define the $2N$-dimensional column vector of the electric field components,

$$\vec{\mathcal{E}} = \left| \begin{array}{c} E_{x,G_1} \\ \vdots \\ E_{x,G_N} \\ E_{y,G_1} \\ \vdots \\ E_{y,G_N} \end{array} \right. \tag{5.38}$$

and $2N \times 2N$ matrices

$$\mathcal{M} = \begin{pmatrix} M_{11} & M_{12} \\ M_{21} & M_{22} \end{pmatrix}, \quad \mathcal{N} = \begin{pmatrix} N_{11} & N_{12} \\ N_{21} & N_{22} \end{pmatrix} \tag{5.39}$$

whose components are:

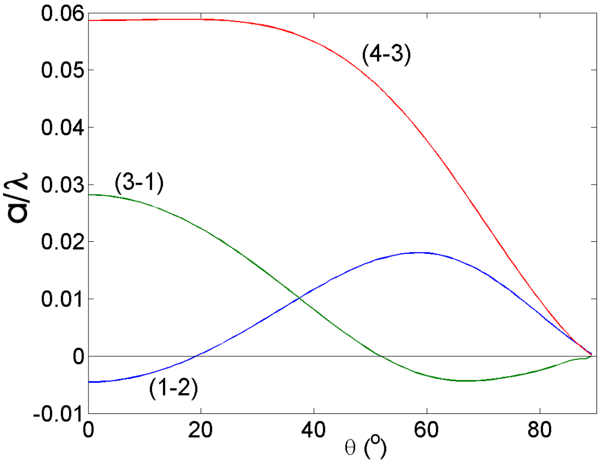

Figure 5.12: Magnitude of the band gaps (e.g. distance between photonic bands) as a function of k_z for the same structure as previously. The bands are sorted from 1 to 4 by increasing frequency at the M point. When $\theta \sim 52^o$, the second band crosses the third band and the gap closes.

$$\begin{aligned}
M_{11} &= \mu_0\omega^2\epsilon^{xx} - (k_y + G_y)^2\mathbb{1} \\
M_{22} &= \mu_0\omega^2\epsilon^{yy} - (k_x + G_x)^2\mathbb{1} \\
M_{12} &= \mu_0\omega^2\epsilon^{xy} + (k_x + G_x)(k_y + G_y)\mathbb{1} \\
M_{21} &= \mu_0\omega^2\epsilon^{yx} + (k_x + G_x)(k_y + G_y)\mathbb{1} \\
N_{11} &= \mathbb{1} - (k_x + G_x)Z^{-1}(k_x + G_x) \\
N_{22} &= \mathbb{1} - (k_y + G_y)Z^{-1}(k_y + G_y) \\
N_{12} &= -(k_x + G_x)Z^{-1}(k_y + G_y) \\
N_{21} &= -(k_y + G_y)Z^{-1}(k_x + G_x)
\end{aligned} \tag{5.40}$$

All the above notations should be understood in a matrix sense: $\mathbb{1}$ is the $N \times N$ identity matrix, $(k_x + G_x)^2$ is a diagonal matrix whose (n, n) coefficient is $(k_x + G_{x,n})^2$, and Z is:

$$Z = -\mu_0\omega^2\epsilon^{zz} + \left((k_x + G_x)^2 + (k_y + G_y)^2\right)\mathbb{1} \tag{5.41}$$

The eigenproblem then takes the form:

$$\mathcal{M}\,\vec{\mathcal{E}} = k_z^2\mathcal{N}\,\vec{\mathcal{E}} \tag{5.42}$$

In this form, one has to set the value of $\{k_x, k_y, \omega\}$ and look for the corresponding k_z. Unlike the Moharam form, it can not easily be reordered to look for ω as a function of $\{k_x, k_y, k_z\}$ because ω appears in the definition of Z.

5.4.3 Comment on the various forms of the eigenproblem

As can be seen, many equivalent forms of the eigenproblem can be derived. One may wonder whether they all perform equally as regards numerical convergence. From various trials, it appears that all forms display similar convergence for a given dielectric tensor. In other words, the choice of factorization

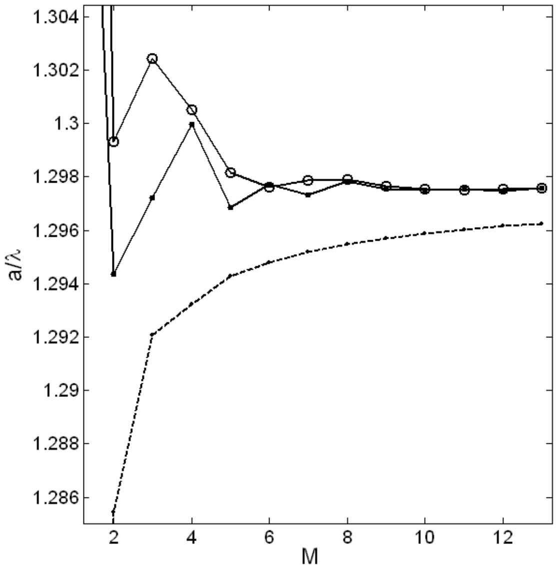

Figure 5.13: Frequency of the first H-polarized band at the M point of a triangular lattice PhC ($\epsilon_{core} = 12, \epsilon_{rods} = 1, f = 0.5$), as a function of plane-wave truncation order M. Dashed line: Ho's method. Full line, points: original PWE with FFF. Full line, circles: Moharam form with FFF.

rules (Ho's method, FFF...) sets the convergence behavior, and the precise form of the eigenproblem only adds small fluctuations around this convergence curve.

As an illustration, we compare in Fig. 5.13 the original PWE expressed on H_z (Eq. 5.31) to the form of Moharam (Eq.5.37) restricted to $k_z = 0$. As can be seen, Ho's method identical slow-converging result with the original and the Moharam forms, while the FFF gives fast-converging and very similar results for both forms.

A potential advantage of the Tikhodeev form over the Moharam form is that the eigenproblem is hermitian (when the hermitian form of the FFF is used, see below), which is sometimes a useful property in numerical implementations. This is not the case of the Moharam form.

5.4.4 FFF and hermiticity

While the FFF provides enhanced convergence, it is worth noticing that it transforms a Hermitian problem into a non-Hermitian one: the dielectric tensor ϵ_{FFF} of Eq. (5.27) is no longer symmetric because it involves products of non-commuting matrices.

Some algorithms can take advantage of the symmetry of matrices for faster diagonalization; therefore, in some cases it is desirable to recover the hermiticity of the problem. This can be done simply, by noticing that the arguments used above to obtain ϵ_{FFF} can also lead to its transpose ${}^t\epsilon_{FFF}$. It is easily checked that, numerically, using ϵ_{FFF} and ${}^t\epsilon_{FFF}$ is equivalent. Therefore, and since Maxwell's equations are linear with ϵ, hermiticity is straightforwardly recovered by using the following dielectric tensor:

$$\frac{1}{2}\left(\epsilon_{FFF} +^t \epsilon_{FFF}\right) \tag{5.43}$$

This hermitian dielectric tensor can be used with the Moharam and Tikhodeev formulations. It conserves the fast-converging property of the FFF. It will also be of interest in Chapter 6, when checking for energy conservation.

5.5 Conclusion

The 2D plane wave expansion is a simple method for band structure computation. Depending on its formulation, it can yield the frequency ω or the wavevector $k_{//}$ of Bloch modes. Numerical convergence of the PWE strongly depends on the form of the dielectric tensor (the Fourier transform of the dielectric map), and using the FFF form ensures fast convergence. The PWE method can also handle off-axis propagation, which will be of interest for 3D calculations.

Bibliography

[1] S. G. Johnson, P. Bienstman, M. A. Skorobogatiy, M. Ibanescu, E. Lidorikis, and J. D. Joannopoulos. Adiabatic theorem and continuous coupled-mode theory for efficient taper transitions in photonic crystals. *Physical Review E*, 66(6), 2002. Part 2 066608.

[2] B. S. Song, S. Noda, T. Asano, and Y. Akahane. Ultra-high-q photonic double-heterostructure nanocavity. *Nature Materials*, 4(3):207–210, 2005.

[3] D. Taillaert, W. Bogaerts, P. Bienstman, T. F. Krauss, P. Van Daele, I. Moerman, S. Verstuyft, K. De Mesel, and R. Baets. An out-of-plane grating coupler for efficient butt-coupling between compact planar waveguides and single-mode fibers. *IEEE Journal of Quantum Electronics*, 38(7):949–955, 2002.

[4] L. H. Frandsen, A. Harpoth, P. I. Borel, M. Kristensen, J. S. Jensen, and O. Sigmund. Broadband photonic crystal waveguide 60 degrees bend obtained utilizing topology optimization. *Optics Express*, 12(24):5916–5921, 2004.

[5] J. Smajic, C. Hafner, and D. Erni. Design and optimization of an achromatic photonic crystal bend. *Optics Express*, 11(12):1378–1384, 2003.

[6] M. Burger, S. J. Osher, and E. Yablonovitch. Inverse problem techniques for the design of photonic crystals. *Ieice Transactions on Electronics*, E87C(3):258–265, 2004.

[7] M. Plihal and A. A. Maradudin. Photonic band-structure of 2-dimensional systems - the triangular lattice. *Physical Review B*, 44(16):8565–8571, 1991.

[8] K. Busch, S. Lolkes, R. B. Wehrspohn, and H. Foll. *Photonic Crystals - Advances in Design, Fabrication, and Characterization*. Wiley, New York, 2004.

[9] K. M. Ho, C. T. Chan, and C. M. Soukoulis. Existence of a photonic gap in periodic dielectric structures. *Physical Review Letters*, 65(25):3152–3155, 1990.

[10] P. Lalanne and G. M. Morris. Highly improved convergence of the coupled-wave method for TM polarization. *Journal of the Optical Society of America a-Optics Image Science and Vision*, 13(4):779–784, 1996.

[11] L. F. Li. Use of fourier series in the analysis of discontinuous periodic structures. *Journal of the Optical Society of America a-Optics Image Science and Vision*, 13(9):1870–1876, 1996.

[12] L. F. Li. New formulation of the fourier modal method for crossed surface-relief gratings. *Journal of the Optical Society of America a-Optics Image Science and Vision*, 14(10):2758–2767, 1997.

[13] P. Lalanne. Improved formulation of the coupled-wave method for two-dimensional gratings. *Journal of the Optical Society of America a-Optics Image Science and Vision*, 14(7):1592–1598, 1997.

[14] P. Lalanne. Effective properties and band structures of lamellar subwavelength crystals: Plane-wave method revisited. *Physical Review B*, 58(15):9801–9807, 1998.

[15] E. Popov, M. Neviere, B. Gralak, and G. Tayeb. Staircase approximation validity for arbitrary-shaped gratings. *Journal of the Optical Society of America a-Optics Image Science and Vision*, 19(1):33–42, 2002.

[16] E. Popov and M. Neviere. Grating theory: new equations in fourier space leading to fast converging results for TM polarization. *Journal of the Optical Society of America a-Optics Image Science and Vision*, 17(10):1773–1784, 2000.

[17] S. Noda, M. Yokoyama, M. Imada, A. Chutinan, and M. Mochizuki. Polarization mode control of two-dimensional photonic crystal laser by unit cell structure design. *Science*, 293(5532):1123–1125, 2001.

[18] A. David, H. Benisty, and C. Weisbuch. Fast factorization rule and plane-wave expansion method for two-dimensional photonic crystals with arbitrary hole-shape. *Physical Review B*, 73(7), 2006. 075107.

[19] P. R. Villeneuve and M. Piche. Photonic bandgaps - what is the best numerical representation of periodic structures. *Journal of Modern Optics*, 41(2):241–256, 1994.

[20] X. P. Feng and Y. Arakawa. Off-plane angle dependence of photonic band gap in a two-dimensional photonic crystal. *IEEE Journal of Quantum Electronics*, 32(3):535–542, 1996.

[21] M. G. Moharam, E. B. Grann, D. A. Pommet, and T. K. Gaylord. Formulation for stable and efficient implementation of the rigorous coupled-wave analysis of binary gratings. *Journal of the Optical Society of America a-Optics Image Science and Vision*, 12(5):1068–1076, 1995.

[22] S. G. Tikhodeev, A. L. Yablonskii, E. A. Muljarov, N. A. Gippius, and T. Ishihara. Quasiguided modes and optical properties of photonic crystal slabs. *Physical Review B*, 66(4), 2002. 045102.

[23] S. Peng and G. M. Morris. Resonant scattering from two-dimensional gratings. *Journal of the Optical Society of America a-Optics Image Science and Vision*, 13(5):993–1005, 1996.

[24] D. Delbeke. *Design and fabrication of a highly efficient light-emitting diode: the Grating-Assisted Resonant-Cavity Light-Emitting Diode.* PhD thesis, University of Ghent, 2003.

Chapter 6

3D Simulation of photonic structures

In this chapter, we discuss three-dimensional calculations on photonic structures. We first present an overview of various photonics methods, both in 2D and 3D. Then, we introduce an original method suited for 3D calculations of diffraction losses, which is used throughout the thesis. Finally, a Fourier modal method is implemented for comparison and validation of the previous method.

6.1 Photonic calculation methods: a quick overview

It is quite delicate to sort the multitude of numerical methods for photonics calculations, since many criteria can be considered. For instance, one can sort them according to the mathematical tools they use (finite differences, expansion on a function basis such as a Fourier basis...), to the kind of problems they can handle (simulation of finite structures, eigenmodes...), to the kind of objects they use to solve the equations (total electromagnetic field in real space, eigenmodes of sub-structures...) and so on. Neither of these criteria is ideal or universal.

The following is a personal view of how the most popular methods can be sorted. Needless to say, it does not claim to be comprehensive, were it only because many groups use personal methods which do not fall exactly in any category. However, I believe it gives a reasonable overview of the main popular approaches at solving Maxwell's equations. I restricted this review to *rigorous* methods, which solve Maxwell's equations exactly (apart from numerical approximations). Of course, a multitude of approximate methods also exist, which can perform very well in their domain of validity.

Fig.6.1 gives a schematic view of the classification of methods described below.

6.1.1 Time-domain method - FDTD

Since the 2000's, the **Finite Difference Time Domain (FDTD)** method is by far the most popular calculation method in the time domain – that is, using Maxwell's equations as a function of time rather than frequency.

The differentials in Maxwell's equations are approximated by finite differences operators. Both the electric and the magnetic fields are used, with interlocked discretization grids (both in time and space). The magnetic field at time $(t+1/2)$ is deduced from the electric field at time (t), then the electric field at time $(t+1)$ is deduced from the magnetic field at time $(t+1/2)$, and so on. This initial scheme was introduced by Yee[1] – numerous refinements have since then been introduced. In the FDTD, fields are excited by placing dipole sources in the structure. For boundary conditions, the structure is usually surrounded by a region of Perfectly Matched Layers (PMLs).[2] These are numerical material regions (with either complex refractive index, complex distances, or both) which have the property

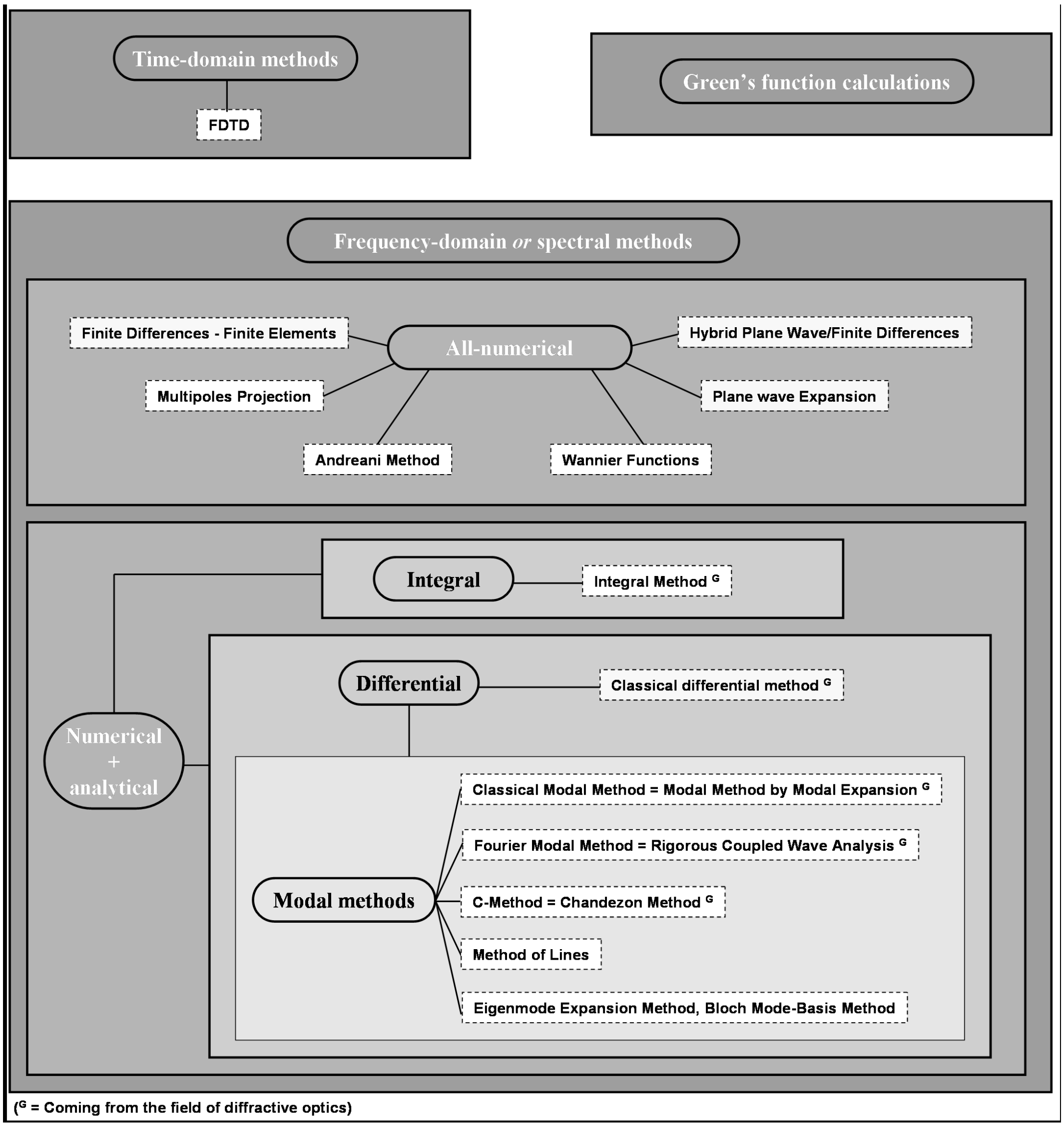

Figure 6.1: Overview of numerical methods.

of absorbing any incoming field and hence simulate an infinite open region. Efficient PMLs are more demanding to implement but yield less parasitic reflections of the field.

The great advantage of the FDTD is that it can handle any object, with no restriction of shape. One simply needs to define the object in space and let the code run long enough to reach good numerical convergence. The FDTD can readily treat propagation problems (such as a wave incoming on a PhC structure). It can also be used to determine band structures or cavity modes. Currently, it is the only method suited for calculation of critical phenomena which require very accurate convergence, such as ultra-high quality factor cavities.

However, the FDTD suffers from drawbacks. First, implementation of an efficient 3D FDTD code is reputedly difficult. Second, the method is very demanding in terms of calculation power, especially for 3D calculations of large objects where computer clusters are necessary. Third, while the method gives access to the value of the field, the insight it provides is debatable – for instance, there is no universal way to distinguish different diffracted orders. In some cases, a description in terms of Bloch modes is much preferable.

It is worth noting that the FTDT scheme is quite clever and efficient: in spite of a discretization in *four dimensions*, it is capable of treating extremely complex systems. As will be seen below, "brute force" discretization in only three dimensions is often prohibitive for spectral methods. While 3D FDTD calculations are reputed to be time-and resources-consuming, it may be argued that their demands are after all reasonable considering the basic paradigm of discretization.

In the context of my research, the FDTD seems of limited use. First, large structures should be simulated since diffraction occurs over long scales. This would probably lead to unacceptable computation demands – the few simulations of PhC-LEDs that can be found in literature are limited to a few crystal periods, which is not even sufficient to obtain a coherent behavior. Second, I believe modal approach gives precious insight for optimization strategies.

For reference, other hybrid time-domain methods also exist, such as the time-domain moments method (which works on the current density **J** rather than on the fields), although they are not widespread.

6.1.2 Spectral methods

Nearly all methods except the FDTD operate in the frequency domain, assuming an $e^{i\omega t}$ time-dependence for the fields. The time derivative in Maxwell's equation is then changed to a scalar multiplication, which makes them easier to handle. Spectral domain methods can be divided according to their basic strategy for solving Maxwell's equations: either all-numerically or semi-analytically.

A) All-numerical methods

All-numerical (or "brute force") methods discretize the problem in *all directions at the same time* and solve the resulting equation. For instance, the 2D plane wave expansion exposed in the previous chapter falls within this category, as the Maxwell's equations are expanded along x and y at the same time. This approach typically results in a straightforward formulation at the expense of a heavier computation burden.

a) Finite Differences and others It is of course possible to solve Maxwell's equations in real space directly, for instance by finite differences. Finite differences approximate differential operators by discrete differences. For PhCs, this approach is not very popular because it makes no use of the periodicity of the problem. Some results have been reported for fast-converging band structure calculations in 2D PhCs, but they require an adaptive mesh (finer close to the dielectric boundaries) which limits their versatility. For non-periodic structures, such as a random set of dielectric rods, finite differences are sometimes used and have the advantage of being very simple to implement.

Other conventional methods for solving differential equations can also be used: Finite Elements, Method of Moments... They are traditionally more complex and more efficient numerically than finite differences. However, in the context of photonics, if one can afford complexity, one is usually better off with more specific methods than these generic approaches.

b) Plane Wave Expansion The Plane Wave Expansion (PWE) is described in detail in the previous Chapter. It consists in expanding the field in a Fourier basis and solving the eigenproblem corresponding to Maxwell's equations. It is therefore a straightforward method for band structure calculations in strictly periodic structures – both in 2D, as in the previous chapter, and for 3D crystals such as woodpiles or inverted opals. 2D PWE is also often used by 3D modal methods for calculation of 2D eigenmodes (see below). Moreover, use of the FFF rules significantly enhances the convergence properties of the PWE.

For non-periodic 2D problems such as defect problems (PhC waveguides or cavities), the PWE can be used with a supercell approach (see previous chapter). This is easily implemented, and reasonably efficient.

3D problems which are only periodic in 2 dimensions (typically, 2D PhCs embedded in planar waveguides) can also be treated with a supercell, by stacking the object vertically (Fig. 6.2). For instance, the popular software package **MIT-PBG** uses this approach, and solves the eigenproblem efficiently using optimized algorithms for finding a few eigenvalues.[3] However, this assumes that all fields are decaying far enough from the waveguide in the vertical direction, so that all supercells are independent. Calculations of leaky modes above the light cone are therefore not possible (or at least not accurate), because the modes become propagative outside of the waveguide and leak though supercells. It has also been suggested to introduce perfectly matched layers to isolate the supercells.[4] However, this introduces serious complications, such as the appearance of spurious modes localized in the PMLs which have to be discriminated from actual modes.

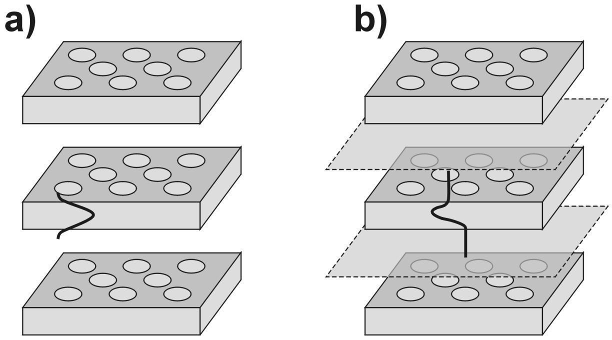

Figure 6.2: a) A supercell enables treatment of 2D PhCs embedded in planar waveguides. b) If the fields are leaky outside the waveguide, PMLs can be inserted to isolate the supercells.

c) Multipole Expansion While the PWE is a good general-purpose method, its main strength (a straightforward decomposition in a Fourier basis) can also be a weakness. Plane waves are not well suited to increase accuracy in a specific region of space, which can be necessary for objects with a complex geometry (either because of a complex non-circular shape or a non-periodic arrangement). Therefore, other basis functions can be considered for expansion of the field. A efficient choice, found in the literature under the names **Multiple Multipole Expansion**, **Generalized Multipole Expansion**, **Multiple-Scattering Method** or **Discrete Sources Method**, consists in choosing a basis of spatial Bessel and Hankel functions. Many functions with multiple origins can be used to increase the accuracy, and the origins can be localized close to the regions where accuracy is needed. This is definitely a more complex method which requires far more programming involvement than the PWE, but it proves efficient for difficult calculation such as plasmonic modes in metallic PhCs [5].

Another implementation using a Hankel-Bessel basis is detailed in [6], where the structure is made of rods with arbitrary shape and position. In [7] it is applied to the study defect modes in 2D PhCs of finite extension *without using a supercell.*

Variations of the multipole expansion also use other functions analogous to Bessel/Hankel functions, for instance spherical harmonics. The principle is the same as above, but spherical symmetry is privileged over cylindrical symmetry. This choice is well suited for scattering by random 3D particles, in the context of light scattering for instance.[8]

d) Wannier Functions Wannier functions are yet another projection basis for Bloch-modes, inspired by their equivalent in electronic structures. Their main feature is their localization in space. They have been proposed for calculations in 2D PhC circuits incorporating waveguides, bends and cavities. In order to build the Wannier functions, one first finds the Bloch modes of an infinite PhC (for instance with the PWE or another of the above methods). From these, a basis of Wannier function is built. This basis is subsequently used to compute the fields of more complex PhC systems, such as defects, waveguides and PhC circuits in general. As the Wannier functions are localized in space, they constitute an efficient basis for these systems where the field is localized in the defect regions. They claim to compete with multipole expansions in the case of objects with complex shape. A thorough review of photonic Wannier functions can be found in Ref. [9].

e) Andreani Method This method, introduced by Andreani *et al.*, is adapted to 3D Bloch modes calculations of 2D PhCs in planar waveguides.[10] It uses a plane-wave expansion in the two periodic (horizontal, x and y) directions and a basis of guided modes in the vertical (z) direction. More precisely, the actual PhC waveguide is first approximated by an effective waveguide whose index depends only on z and is averaged along x and y. The guided modes of this waveguide are computed −this is a simple 1D problem− and are then used as a basis for the decomposition of Bloch modes. As noted by Andreani, *"The guided modes of the 'effective' waveguide represent an orthonormal set of states, however the basis set is not complete since the leaky modes of the waveguide are not included."* Because of this, this method is actually not strictly rigorous. Notably, losses above the light line are not obtained immediately, but can be deduced as a perturbation by coupling the obtained solutions to the continuum of radiative modes through Fermi's golden rule. This approximation is obviously only valid if the loss of the modes is small − this is not a problem for most propagative modes, but calculation of purely evanescent modes in gaps is impossible.

On the other hand, the basis of "effective guided modes" is well suited to expand the vertical profile of Bloch modes, since it is naturally adapted to the vertical profile of the waveguide. Therefore, only a few terms are needed to expand the fields, and computations are fast. A supercell can be used in the horizontal directions to treat the case of defects (PhC waveguides or cavities). The good computation speed of the method enabled Gerace and Andreani to investigate the effect of disorder on loss in PhC waveguides, by averaging their calculations over numerous configurations with random disorder. [11]

f) Hybrid Plane Wave/Finite Differences Method During this thesis, I developed a 3D method adapted to calculation of leaky Bloch modes in 2D PhCs embedded in planar waveguides. It consists in a plane-wave expansion in the two periodic (horizontal) directions, and a finite difference expansion in the non-periodic (vertical) direction. Its main originality is to naturally take into account radiation losses thanks to transparent boundary conditions, without resorting to a supercell or perfectly matched layers. This method will be exposed in greater details in section 6.2. It suffers from the main drawback of 3D all-numerical methods, their need for computation power. On the other hand, it has proved quite efficient in treating the strongly multimode structures investigated in this thesis.

B) Semi-analytical methods

Unlike all-numerical methods, semi-analytical methods partially solve the problems along some directions, and then "integrate" the resulting solutions along the remaining direction (which we shall call *analytical direction*). This last integration is usually performed numerically as well, but deserves the "analytical" qualification in the sense that one takes advantage of the propagation properties specific to the electromagnetic field − rather than considering Maxwell's equations as any standard set of partial differential equation. Semi-analytical methods are usually more sophisticated to implement than all-numerical methods, but less demanding in terms of computation power.

Most of these methods originate from the field of diffractive optics, or grating theory. A more thorough presentation of grating theories can be found in [12], and an up-to-date review including the latest developments of the theory in [13]. Following a well-established tradition in this field, there have been numerous heated debates between proponents of each grating method to impose its supremacy.[14] There is now a consensus that each method can be the best for a particular set of problems – it is however true that some are more versatile than others.

a) Integral Method The integral method, introduced in the 1960s by Maystre and others, differs from other spectral methods because, instead of using Maxwell's equations in the form of partial differential equations, it recasts them as a system of coupled linear integral equations.[15, 12] In other words, rather than numerically integrating the equations in the vertical direction, they are directly expressed in integral form. This method is reputedly powerful, but its mathematical background and implementation are heavier than that of differential methods. For instance, it was used by Popov and Neviere as a reference to assess the fast convergence of the FFF (see Chapter 5) in their original paper [16].

Stemming from the field of diffractive optics, it is mostly used in 1D grating calculations. However, adaptation to 2D PhCs has been proposed to access the transmission of a *finite* PhC.[17] In this case, the PhC is periodic (infinite) in the horizontal direction and can be non-periodic in the vertical direction, for instance because it is made of a finite number of periods. Actually, this just consists in viewing the PhC as a 1D grating with a complicated vertical profile made of the PhC rods (see Fig. 6.3b). This approach was later extended to compute the Bloch modes of an *infinite* 2D PhC: in that case, the integral method is used to obtain the scattering matrix (see below for a general definition of scattering matrices) of one PhC layer, and the poles of this matrix correspond to the Bloch modes of the infinite PhC.[18]

To my knowledge, 3D problems such as 2D PhCs in a planar structure have not been tackled.

b) Classical Differential Method The classical differential method is essentially used in the context of grating theory, to compute the diffraction efficiency of 1D gratings. Unlike other differential methods, it does not "slice" the grating in the vertical direction, but considers its actual profile. Quoting Popov *et al.* [19], *"The classical differential method uses Fourier basis in x with numerical integration of a finite set of ordinary differential equations in z"*. These differential equations in z correspond to the vertical profile of the grating and are integrated numerically (typically, using a Runge-Kutta algorithm). This is an advantage for gratings with smooth boundaries, because the actual shape can be considered. It also allows use of the FFF rules for smooth gratings, as in [16]. On the other hand, numerical integration along z requires heavier calculations than other methods.

The classical differential method has also been proposed for calculations in 2D photonic crystals.[20] As for the integral method, the principle is to consider the PhC as complex grating. Likewise, 3D PhCs and 2D PhCs in planar structures can be treated, using a Fourier basis in the $x - y$ directions and numerical integration along z.[13] Again, due to the numerical integration, this approach is characterized by a heavier numerical burden than some other semi-analytical methods – such as the FMM (see below). On the other hand, it enables use of the FFF in any geometry (even for anisotropic materials [21]) whereas the FMM is limited by the staircase approximation.

A very complete review of the classical differential method can be found in [13].

All remaining semi-analytical methods can be classified as **Modal Methods** (or **Eigenmode Expansion Methods**, or **Mode Matching Methods**). Their basic principle is to *slice* the object (for instance by using the staircase approximation) along the analytical direction, obtain a basis of the electromagnetic field in each slice, and match the boundary conditions between different slices to express Maxwell's equation for the whole object. This usually results in a description of the object by a matrix such as a Scattering matrix (see section 6.3 for more details). Depending on the method, there can be differences in the choice of slices, in the basis in each slice, and in the way this basis is computed. Fig. 6.3 illustrates possible slicing of objects in the particular case of the Fourier Modal Method described below – other methods use similar slicing.

c) Fourier Modal Method The Fourier Modal Method (FMM) is very popular, probably thanks to its great versatility. Historically, the method is hard to trace but some of the first implementations date back from the mid-1960s ([22], see also [23]). It proceeds as follows:

i) The object is divided in slices along the analytical direction –say z– and approximated by a staircase profile so that the index profile is constant along z in each slice. The index profile can still depend on x (for instance, if one studies a 1D grating) or on x and y (if one studies a 2D PhC or another complex object). Usually, one chooses the "longest" dimension of the object for the z direction, so that determination of the eigenmodes in the other direction(s) is fast.

ii) The eigenmodes of each slice are found in a Fourier basis – hence the name of the method. The field in the total object can now be described as a superposition of the eigenmodes in each slice.

iii) Matching the continuity conditions at the interface between slices imposes linear equations on the coefficients of the eigenmodes in each slice. This set of equations is cast in the form of a matrix (usually a Scattering matrix). All the properties of the object are then contained in the matrix. For instance, reflectivity/transmission properties can be derived immediately, and the poles of the matrix correspond to the eigenmodes of the object.

In a sense, the FMM can be seen as a restriction of the Classical Differential Method to gratings with staircase profiles, in which case solving the differential equation along z amounts to finding the eigenmodes in each slice.

The FMM is also often called **Rigorous Coupled Wave Analysis (RCWA)**, a name introduced by Moharam and Gaylord, [24, 25, 26] and **Coupled Wave Method**. In addition, many groups use the same method but give it other (and sometimes inaccurate) names. It is sometimes designated as a **Scattering Matrix** algorithm (for instance by Whittaker and Culshaw), although in principle a S-matrix can make use of other bases than a Fourier basis, and can be derived by other methods than the FMM (Classical Differential and Integral methods for instance [18]).[1] It has even been called a Transfer Matrix algorithm, even though a scattering matrix was used (see the distinction between S-matrix, T-matrix and others in section 6.3 below).[27] The name RCWA is the most widespread in the field of grating optics, while the term S-matrix can be found more frequently for multilayer structure with photonic crystals.

The efficiency of the FMM has sometimes been debated in the past, notably because of its convergence difficulties for certain polarizations compared to other semi-analytical methods. However, implementation of the FFF rules seems to have solved most of these difficulties. Use of the staircase approximation can still represent a limitation of this method, as shown in [19].

The main strength of the FMM is that it can treat a great variety of problems efficiently (see Fig. 6.3 for a sketch of the slices definition in various situations). It was initially used to study diffraction gratings; in which case the eigenmode problem is cast in one dimension (Fig 6.3a). Just as for the integral method and the classical differential method, 2D PhCs can also be treated this way (considering the PhC as a complex grating). 3D problems, such as a 2D PhCs in a planar structure, can also be treated; the eigenmode problem is then cast in 2 dimensions.

---

[1] One may argue that, for lamellar geometries, there is no difference between the Classical Differential Method and the FMM, so that the name S-matrix should be preferred over those.

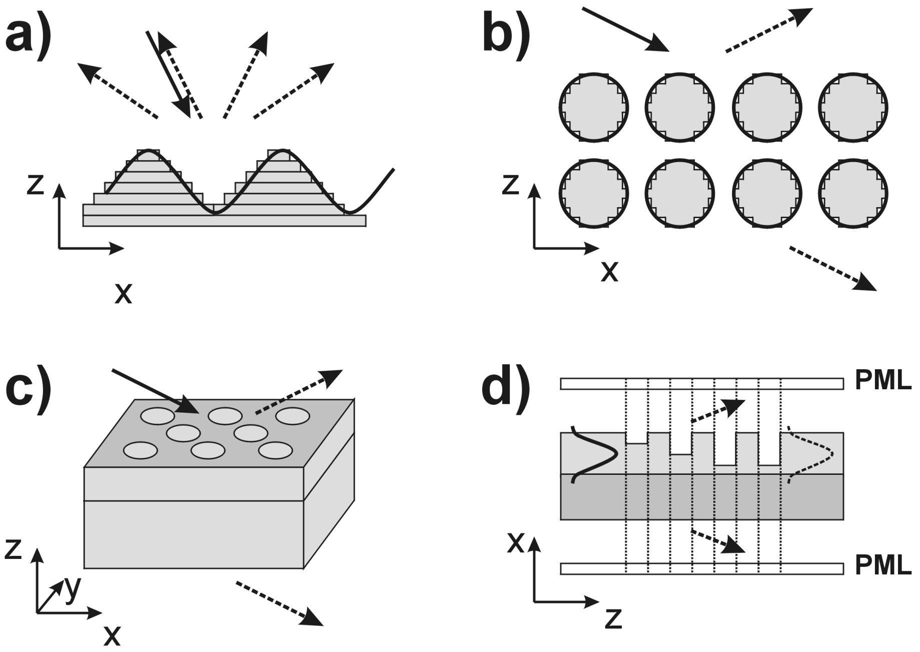

Figure 6.3: Slices definition in the FMM for various objects. In each case, z is the analytical direction. a) a sine grating is decomposed using a staircase approximation, each of the stairs is a slice where eigenmodes are computed by a 1D PWE. Typical boundary conditions consist in one incoming plane wave (full line arrow). The calculation gives access to the diffraction efficiencies in various orders (dashed arrows). b) In the same way, a 2D PhC (here, infinite along x and made of two rows along z) can be seen as a 1D grating and treated as previously. c) A 2D PhC embedded in a planar waveguide can be treated as above, using 4 slices in the present case (air, patterned region, substrate region, air). The only change is that the PWE in each slice is now 2-dimensional. d) A non-periodic object needs introduction of PMLs and use of a supercell (the object is periodized vertically). The analytic direction is now along the "horizontal" direction: the vertical dotted lines correspond to the slices. The incoming boundary condition is here a guided mode, and the computation gives access to the scattering losses (dashed arrows) and transmission (dashed guided mode). Of course, each slice can also be y-dependent in the case of a fully 3D object.

Finally, the FMM can also deal with *strictly non-periodic* problems like a finite PhC structure (see Fig.6.3 d).[28] This is done by use of a supercell and perfectly matched layers, like in some all-numerical methods, but the lower computation demands of the FMM enable treatment of very complex objects with good convergence. At this time, the FMM is probably the only method which may claim to compete with the FDTD for very accurate calculations on such objects, such as optical cavities with ultra-high quality factor. On the other hand, it must be acknowledged that the introduction of PMLs greatly increases the complexity of implementation – especially for *efficient* PMLs, which are a field of study by themselves.[29] Another remarkable advantage of this formulation of the FMM is that determination of eigenmodes takes the form of an eigenvalue problem – whereas usually, one has to find the pole of a scattering matrix, which is way more tedious and less systematic.

d) Classical Modal Method In the Classical Modal Method, or **Modal Method by Modal Expansion** (MMME), one *avoids* use of a Fourier basis in each slice. Rather, one directly uses the exact, analytical basis of eigenmodes in each slice (e.g. the solution of Maxwell's equations in the slice if it is considered infinitely high in the analytical direction). Of course, this is not always possible since the exact basis of eigenstates is only known for a few geometries – namely, lamellar gratings and gratings with sinusoidally-varying index. Use of the staircase approximation somehow extends the domain of validity of this method, but it still remains limited to a few 1D gratings. When it can be used, the classical modal method has a better convergence than the FMM – see [30] for a comparison of the two methods, and [19] for a comparison with the classical differential method with FFF rules.

e) C-method The C-method, or **Method of Chandezon** after its author, is a coordinate transformation method.[31] It uses a nonorthogonal curvilinear system in which the surface of the grating is 'planar'. Quoting Granet, Chandezon and Coudert[32]: *"Everything happens as if the interface was plane, but the media become nonhomogeneous and nonisotropic"*. This greatly simplifies the formulation of boundary conditions at the grating interface, but writing Maxwell's equations in this coordinate system becomes complicated. Maxwell's equations are developed in a Fourier basis and a scattering matrix is built, like in the FMM. Obviously, this method is especially well suited for some grating geometries, such as multicoated conformal surfaces.

Other coordinate transformation methods also exist, such as the Conformal Mapping technique.[33]

f) Method of lines In the Method of Lines, the eigenmodes in each slice are simply found by finite differences. Each slice is characterized by a matrix called impedance matrix (analogous to a scattering matrix), and combination of these matrices gives the total impedance matrix of the structure.[34] This method is mainly adapted to waveguide calculations where the cross-section of the waveguide varies piecewise along the propagation direction. It was also used for grating calculations by Lalanne and Hugonin who showed that good convergence can be reached for metallic gratings, when using a specific form of the finite difference operators.[35]. Finally, Ref. [36] presents the result of the COST268 coordinate action and presents a numerical comparison of the method of lines, the FDTD and several modal method implementations (FMM and Eigenmode expansion method, see below), where a Bragg grating in a planar waveguide is studied. The main conclusion of this benchmark is the consistency between the results obtained by all methods.

g) Eigenmodes Expansion Method / Bloch Mode basis method The Eigenmodes expansion method is rather close in its concept to the FMM. The structure of interest is again divided in slices of constant profile, perpendicular to the analytical direction. The eigenmodes of each slice are then found, and connection between the slices yields the scattering matrix of the structure, as for the FMM. However the eigenmodes of each layer are *not* projected in a Fourier basis. Rather, in each layer, they are found by solving the transcendent equation of the relation dispersion of this layer. In very simple cases (when the structure of each slice is very simple) this transcendent relation can be expressed explicitly. Otherwise, one can resort to a Transfer (or Scattering) matrix *in each slice*[2] to solve the transcendent equation and find the eigenmodes. In general, PMLs have to be placed around the structure to properly account for radiated fields, which makes implementation more complex.

This method is well adapted for structures of finite size such as VCSELs or finite Bragg gratings as in Fig. 6.3d. The freely available software package **CamFR** uses this approach (Refs. [37, 38]).

The Bloch mode basis method is a rather recent method which deals specifically with photonic crystals, and can be seen as an extension of the Eigenmode Expansion Method. It emerges from the realization that Bloch modes are a relevant object to describe propagation in photonic crystals. Its main goal is to deal with complicated 2D photonic circuits. First, the circuit is divided in elementary PhC objects (such as waveguides, bends...). The Bloch modes of each object are then computed by one of the numerical methods already described, which is not a heavy task since the object is basic. Then, the elementary objects are connected. Propagation in each object and interface between objects are

---

[2] This matrix then has a reduced dimensionality with respect to the S-matrix of the total structure, and its analytical direction is *perpendicular* to that of the total structure.

described by Scattering matrices expressed *in the Bloch modes bases.* In other word, this method is a Scattering matrix method where the elementary objects are simple PhC structures – rather than the slices used in other modal methods – and where the projection basis is made of Bloch modes.[39, 40]

6.1.3 Green's function

In general, Green's functions are a mathematical tool which can be used to obtain analytical expressions of quantities related to differential equations. In the context of photonics, they are usually not used to solve Maxwell's equations themselves, but rather to obtain useful quantities which derive from the electromagnetic field.

Typically, the electromagnetic field (or a basis of fields) is first computed by another method – for instance the FDTD. Then, this field is used to obtain Green's functions which give access to derived quantities. Alternately, the differential equation defining the Green's function can be solved directly using one of the methods above, but this is less frequent.[41]

Green's functions can be used to compute the local density of states or the spontaneous emission rate of dipoles (Purcell effect), which are immediately given by the unperturbed Green's functions.[42] Moreover, the unperturbed Green's function can serve as a basis to obtain Green's functions of perturbed systems (due to disorder, defects in PhCs...). Hughes *et al.* recently applied this approach to the calculation of cavity electrodynamics effects (strong coupling) [43, 44] and disorder-related scattering and losses in PhC waveguides[44]. Remarkably, this last result *explicitly* gives the effect of group velocity on losses.

In summary, Green's functions methods are most useful to study photon propagation in complex structured dielectrics and quantum optics effects, and usually come in combination with one of the previous calculation methods.

6.1.4 Choice of a method

In summary, the choice of a method should be dictated by two criteria : the problem of interest and the intended involvement in implementation. A specific problem is usually best tackled by a given method; on the other hand, a versatile method which will perform reasonably well in a wide range of problems may be preferable. Moreover, the most efficient methods require more implementation effort, especially if one wants to include additional refinement (very efficient PMLs, FFF rules...). One should keep in mind this tradeoff between the convergence speed, versatility and ease of implementation of a code.

6.2 Hybrid Plane Wave/Finite Differences method

6.2.1 Principle of the hybrid method

The basic motivation behind my developing this hybrid method is the fact that, while 3D plane-wave expansions (such as the MIT-PBG toolbox) are simple and powerful enough for Bloch modes calculations of 2D PhCs embedded in planar waveguides, they fail to describe diffraction losses above the light line because of the boundary conditions they assume, namely decaying fields far from the waveguide. Attempts at dodging this difficulty by introducing PMLs raise other difficulties, such as spurious modes.[4]

The alternative is then to avoid the use of the supercell approach in the z direction. However, this imposes giving up the use of a plane wave basis. In the hybrid method, Bloch modes are therefore Fourier transformed in the x and y directions, while their z dependence remains in real space and is treated with finite differences. Maxwell's equations take the form of an eigenproblem on a large but sparse matrix. In order to take into account diffraction losses, *transparent* boundary conditions are introduced.

6.2.2 Implementation of the hybrid method

Basic implementation

According to the Floquet-Bloch theorem, the Bloch modes of a multilayer structure with a 2D PhC are of the form:

$$\mathbf{E}(z,\mathbf{r}) = \sum_{\mathbf{G}\in RL} \mathbf{E}_{\mathbf{G}}(z) exp\left(i\left(\mathbf{k}_{//}+\mathbf{G}\right)\cdot\mathbf{r}\right) = \sum_{\mathbf{G}} e^{i(k_x+G_x)x} e^{i(k_y+G_y)y} \left| \begin{array}{l} E_x^G(z) \\ E_y^G(z) \\ E_z^G(z) \end{array} \right. \tag{6.1}$$

We also introduce c and s as:

$$c = k_x/k_{//} \quad s = k_y/k_{//} \tag{6.2}$$

The dielectric permittivity of the material can be written:

$$\epsilon(z) = \epsilon_0(z) + \sum_{\mathbf{G}} \epsilon_G(z).e^{i(G_x x + G_y y)} \tag{6.3}$$

Starting from Maxwell's equations:

$$\nabla \times \mathbf{H} = -i\omega\epsilon\mathbf{E} \tag{6.4}$$

$$\nabla \times \mathbf{E} = i\omega\mu_0\mathbf{H} \tag{6.5}$$

We get rid of $\mathbf{H}$ to get a system of second-order equations on $\mathbf{E}$ only:

$$\nabla \times \nabla \times \mathbf{E} = \left| \begin{array}{l} -\partial_y^2 E_x - \partial_z^2 E_x + \partial_x\partial_y E_y + \partial_x\partial_z E_z \\ -\partial_x^2 E_y - \partial_z^2 E_y + \partial_y\partial_x E_x + \partial_y\partial_z E_z \\ -\partial_x^2 E_x - \partial_y^2 E_x + \partial_z\partial_x E_x + \partial_z\partial_y E_y \end{array} \right. = \mu_0\epsilon\omega^2 \left| \begin{array}{l} E_x \\ E_y \\ E_z \end{array} \right. \tag{6.6}$$

We now perform the Fourier expansion, and approximate derivatives in the z direction by finite differences. Therefore, for a given reciprocal lattice vector $\mathbf{G}$, differential operators on a function f become:

$$\begin{aligned} \partial_x f &\rightarrow i(k_x + G_x)f \\ \partial_y f &\rightarrow i(k_x + G_x)f \\ \partial_z f &\rightarrow (f_{n+1} - f_n)/\Delta z \end{aligned} \tag{6.7}$$

After inserting these forms of ϵ and E in Eq. 6.6, and collecting terms with the same exponential factor, we are led to a system of 3 equations for each value of G:

$$\begin{aligned} (-(k_y + G_y)^2 + \partial_z^2)E_x^G + (k_x + G_x)(k_y + G_y)E_y^G - i(k_x + G_x)\partial_z E_z^G + k_0^2 \sum_{\mathbf{G'}} \epsilon_{\mathbf{G}-\mathbf{G'}} E_x^{G'} &= 0 \\ (k_x + G_x)(k_y + G_y)E_x^G + (-(k_x + G_x)^2 + \partial_z^2)E_y^G - i(k_y + G_y)\partial_z E_z^G + k_0^2 \sum_{\mathbf{G'}} \epsilon_{\mathbf{G}-\mathbf{G'}} E_y^{G'} &= 0 \\ -i(k_x + G_x)\partial_z E_x^G - i(k_y + G_y)\partial_z E_y^G - ((k_x + G_x)^2 + (k_y + G_y)^2)E_z^G + k_0^2 \sum_{\mathbf{G'}} \epsilon_{\mathbf{G}-\mathbf{G'}} E_z^{G'} &= 0 \end{aligned} \tag{6.8}$$

Each of these terms ∂_z, ∂_z^2 is written in finite differences form: we discretize the vertical direction with N_z points. We also retain an arbitrary number of terms in the series - say N_x (resp. N_y) terms in the x (y) direction. We define the total number of plane wave harmonics $N_{PW} = 2M + 1 = N_x N_y$. Factorizing the terms of Eq. 6.8 by $k_{//}$, the system can be expressed in matrix form as:

$$A_0 X + k_{//} A_1 X = k_{//}^2 A_3 X \quad \text{where} \quad X = \left| \begin{matrix} E_x \\ E_y \\ E_z \end{matrix} \right. \tag{6.9}$$

Here A_0, A_1 and A_2 are matrices containing the coefficients of 6.8. Making use of Eq. 6.2, their expression is:

$$\begin{aligned} A_0 &= \begin{pmatrix} -\mathbb{G}_y^2 + \partial_z^2 + \epsilon & \mathbb{G}_x\mathbb{G}_y & -i.\mathbb{G}_x\partial_z \\ \mathbb{G}_x\mathbb{G}_y & -\mathbb{G}_x^2 + \partial_z^2 + \epsilon & -i.\mathbb{G}_y\partial_z \\ -i.\mathbb{G}_x\partial_z & -i.\mathbb{G}_y\partial_z & \epsilon \end{pmatrix} \\ A_1 &= \begin{pmatrix} -2s\mathbb{G}_y & c\mathbb{G}_y + s\mathbb{G}_x & -ic\partial_z \\ c\mathbb{G}_y + s\mathbb{G}_x & -2c\mathbb{G}_x & -is\partial_z \\ -ic\partial_z & -is\partial_z & -2c\mathbb{G}_x - 2s\mathbb{G}_y \end{pmatrix} \\ A_2 &= \begin{pmatrix} s^2 & -c.s & 0 \\ -c.s & c^2 & 0 \\ 0 & 0 & \mathbb{1} \end{pmatrix} \end{aligned} \tag{6.10}$$

In the above, each element is a $N_{PW}N_z$ by $N_{PW}N_z$ matrix. For instance, $\mathbb{G}_x\mathbb{G}_y$ is a diagonal matrix, where each diagonal N_zxN_z sub-block corresponds to a given $\mathbf{G}$ and is a diagonal matrix with a constant coefficient G_xG_y:

$$\mathbb{G}_x\mathbb{G}_y = \begin{pmatrix} \ddots & & & & \\ & G_xG_y & & & \\ & & \ddots & & \\ & & & G'_xG'_y & \\ & & & & \ddots \end{pmatrix} \tag{6.11}$$

Likewise, ϵ is roughly a Toeplitz matrix. Each sub-block of size N_zxN_z corresponds to two RL vectors **G** and**G'**, and is a diagonal matrix with coefficient $\epsilon(\mathbf{G}-\mathbf{G'})$. This coefficient gives the z-profile of the harmonic $\mathbf{G}-\mathbf{G}'$ of ϵ and varies along the diagonal for a given sub-block:

$$\epsilon = \begin{pmatrix} \ddots & & & & \\ & \epsilon(0) & \dots & \epsilon(\mathbf{G}-\mathbf{G'}) & \\ & & \ddots & & \\ & \epsilon(\mathbf{G'}-\mathbf{G}) & \dots & \epsilon(0) & \\ & & & & \ddots \end{pmatrix} \quad \text{with} \quad \epsilon(\mathbf{G}-\mathbf{G'}) = \begin{pmatrix} \epsilon^{\mathbf{G}-\mathbf{G'}}_{n_z=1} & & \\ & \ddots & \\ & & \epsilon^{\mathbf{G}-\mathbf{G'}}_{n_z=N_z} \end{pmatrix} \tag{6.12}$$

Finally, ∂_z and ∂_z^2 represent the finite differences operator which discretize derivative. In our case however, choice of the discretization scheme is not arbitrary. In general, it is well known that derivative operators can be written in several ways with finite differences (two- or three-points derivatives...). Three-point derivatives are usually considered to lead to faster convergence, even though this is not a systematic result. In our case however, numerical convergence requires that the problem be cast in hermitian form. For this reason, we have to use two-points derivatives for the ∂_z terms. These must be ***backward*** derivatives for upper terms of A_0 (e.g. terms located above the diagonal of A_0) and ***forward*** derivatives for lower terms of A_0.[3] With this choice, A_0 remains hermitian. On the other hand, ∂_z^2 is naturally symmetric. In summary, we have:

$$\begin{aligned} \partial_z^2 &= \frac{1}{dz^2}\begin{pmatrix} -2 & 1 & & & \\ 1 & -2 & 1 & & \\ & \ddots & \ddots & \ddots & \\ & & 1 & -2 & 1 \\ & & & 1 & -2 \end{pmatrix} \\ \text{upper} \quad \rightarrow \qquad \partial_z &= \frac{1}{dz}\begin{pmatrix} 1 & & & \\ -1 & 1 & & \\ & \ddots & \ddots & \\ & & -1 & 1 \end{pmatrix} \\ \text{lower} \quad \rightarrow \qquad \partial_z &= \frac{1}{dz}\begin{pmatrix} -1 & 1 & & \\ & \ddots & \ddots & \\ & & -1 & 1 \\ & & & -1 \end{pmatrix} \end{aligned} \tag{6.13}$$

---

[3] Or the contrary: forward for upper terms and backward for lower terms. The goal is to obtain a hermitian matrix.

We still have to solve Eq. 6.9, which is a Quadratic Eigenvalue Problem. As has already been done in Chapter 5 in the context of 2D plane wave expansion, it can be rewritten in the form of a usual eigenvalue problem using a canonical transformation. We define:

$$A = \begin{pmatrix} A_1 & A_0 \\ \mathbb{1} & 0 \end{pmatrix}, \quad B = \begin{pmatrix} A_2 & 0 \\ 0 & \mathbb{1} \end{pmatrix}, \quad Y = \left| \begin{array}{c} k_{//}X \\ X \end{array} \right. \tag{6.14}$$

The problem then takes the form of a standard eigenvalue problem with doubled size:

$$AY = k_{//}BY \tag{6.15}$$

Solving this problem yields the Bloch modes of the structure. Its final size is $(6N_{PW}N_z)^2$.

Transparent boundary conditions

In the above discussion, we have postponed the issue of boundary conditions. In a finite differences scheme, they are carried by the outer points of the vertical mesh (say $z = 0$ at the bottom of the structure, and $z = L$ at the top of the structure). They are typically of a Dirichlet or Von Neumann form, which are both easy to implement. However, in our case, such a choice is not possible. Of course, for strictly guided Bloch modes, it would be possible to approximate the exponential decay of the field by taking a large enough computation box and letting $E(0) = E(L) = 0$. This is routinely done for simple FD calculations, such as computation of a guided mode in a slab or of an electronic level in a quantum well. The small error introduced by approximating the BCs is acceptable − it amounts to embedding the actual quantum well in a wide quantum well of infinite height.

However, we are mainly interested in leaky modes for which at least one harmonic is propagative and thus does not decay away from the structure. We introduce the z-wavevector of the harmonic in the substrate of index n_s:

$$k_z^G = \sqrt{n_s^2 k_0^2 - \left|\mathbf{k}_{//} + \mathbf{G}\right|^2} \tag{6.16}$$

In general, the actual z-dependence of harmonic G is then:

$$E_G \sim exp(i \cdot z \cdot k_z^G) \tag{6.17}$$

Which translates into the following boundary condition at $z = 0$:

$$E_G(z = dz) = E_G(z = 0) \cdot exp(i \cdot dz \cdot k_z^G) \tag{6.18}$$

Similar boundary conditions hold in the superstrate at $z = L$. In the above definition, the sign of k_z^G is such that all leaky harmonics decay away from the structure. For propagative harmonics, the sign should correspond to outgoing waves, e.g. $Re(k_z^G) > 0$ in the superstrate and $Re(k_z^G) < 0$ in the substrate. This sign convention is naturally met if $k_{//}$ is real, but generally needs to be enforced 'manually' when the square root of an imaginary number is taken.

The difficulty here is that these BC depend on $k_{//}$, which we are precisely trying to determine as a solution of the eigenproblem. In order to solve this last hurdle, we introduce an iterative scheme. We start from a trial value of $k_{//}$. We write the BC given by Eq. 6.18 corresponding to this trial value; thus, these BC are only approximate. We can then solve the eigenproblem of Eq. 6.15, which yields a corrected value of $k_{//}$. We reinject this value in the boundary conditions, and iterate until the correction to $k_{//}$ is close enough to zero. At this point, the BC are correct because they incorporate the correct value of $k_{//}$: the solution of Maxwell's equations is then rigorous.

In practice, this iterative scheme is fortunately efficient. Starting from some trial value of $k_{//}$ inside the first Brillouin zone, the first iteration gives us a choice of several possible solutions of Eq. 6.15, in the vicinity of this trial value. Several criteria can be used to pick one of these (value of $k_{//}$, symmetry properties of the mode...). The subsequent iterative scheme typically leads to corrections smaller than 10^{-5} on $k_{//}$ within 3 to 5 iterations.

The main drawback of these boundary conditions is that they can only be applied to one mode at a time. In other words, although Eq. 6.15 in principle applies to all Bloch modes, the iterative procedure can only be followed for one value of $k_{//}$ at a time. Therefore, when convergence is reached, only one solution of Eq. 6.15 has proper boundary conditions and is correct. However, the inaccuracy of the other solutions turns out to be rather small in many cases of interest. This property will be discussed in more details below.

Introduction of the FFF

Introducing the FFF in this method is straightforward, because ϵE appears directly in the final equation (it is simply the last term of Eq. 6.6). Following the prescriptions of Chapter 5, we simply replace the dielectric tensor:

$$\epsilon = \begin{pmatrix} \epsilon^{zz} & & \\ & \epsilon^{zz} & \\ & & \epsilon^{zz} \end{pmatrix} \longrightarrow \epsilon_{FFF} = \begin{pmatrix} \epsilon^{xx} & \epsilon^{xy} & \\ \epsilon^{yx} & \epsilon^{yy} & \\ & & \epsilon^{zz} \end{pmatrix} \tag{6.19}$$

This simply modifies matrix A_0 to:

$$A_0 = \begin{pmatrix} -\mathbb{G}_y^2 + \partial_z^2 + \epsilon^{xx} & \mathbb{G}_x\mathbb{G}_y + \epsilon^{xy} & -i.\mathbb{G}_x\partial_z \\ \mathbb{G}_x\mathbb{G}_y + \epsilon^{yx} & -\mathbb{G}_x^2 + \partial_z^2 + \epsilon^{yy} & -i.\mathbb{G}_y\partial_z \\ -i.\mathbb{G}_x\partial_z & -i.\mathbb{G}_y\partial_z & \epsilon^{zz} \end{pmatrix} \tag{6.20}$$

Summary

The procedure of the hybrid method is now fully described. It can be summarized as follows:

- Obtain ϵ with the FFF, and write A_0, A_1 and A_2
- Pick a trial value of $k_{//}$ and use it to express the (approximate) boundary conditions at the extremities of A_0, A_1 and A_2
- Form the double-sized matrices A and B and solve the resulting eigenvalue problem (Eq.6.15)
- Deduce the correction to the trial value of $k_{//}$, and reiterate the procedure with the new boundary conditions imposed by this correction

6.2.3 Applications

Multimode calculations

Many examples of Bloch mode calculations using the hybrid method can be found in this thesis. Whenever a strongly multimode system is investigated, the method proves convenient. Indeed, the general procedure to obtain the band structure of a 3D multimode system consists in finding each band individually (for instance, by looking for all the poles of the scattering matrix of the system). In principle, this is also true with the hybrid method because the transparent boundary conditions are only valid for one Bloch mode at a time.

However, it is well-known that finite differences are in general robust with respect to boundary conditions. For instance, when solving for guided modes $E(x)$ of a dielectric slab (or electronic wavefunctions $\Psi(x)$ of a quantum well), the proper BCs in a computation box of finite size are of the form $E(x_{lim}) \sim exp(-kx)$. However, one often approximates these by Dirichlet conditions of the type $E(x_{lim}) = 0$. The eigenvalue problem nevertheless converges, with a minute error on the eigenvalue (wavevector or energy) if the computation box is large enough. This is often considered as legitimate because the field decays exponentially, so that a small error on the BCs 'should not matter'. However, the same argument clearly fails with other methods such as the shooting method: on the contrary, the BCs completely determine the field and even a small error in these leads to wrong field profiles (this is precisely how shooting methods work).

The reason is that in the latter case, the field is built by propagating the BCs. On the other hand, for finite differences, the differential equation has to be met at all points in space simultaneously: intuitively, points far enough from the boundaries 'forget' their effect and are more immune to an error in BCs. Of course, this property comes at a cost in terms of computational burden: in our example, the memory occupancy for a discretization of size N would be $O(N)$ with finite differences, against $O(1)$ for a shooting method or a transfer matrix.

This property is conserved in the hybrid method: in principle, only the eigenvalue of Eq. 6.15 closest to the desired solution should be considered during the iterative scheme. However, a few other eigenvalues can be computed at the same time: in general, they are very close to the actual eigenvalue of other Bloch modes. This means that, when a strongly multimode structure is computed, one can get a good estimate of the total band structure with only one or a few calculations, each of which yields the dispersion of several Bloch modes. In practice, the position of these bands in the dispersion diagrams zone is usually within one to a few percents of the converged value. As regards their loss rate, the conservation of energy is met with a precision in the order of 10% in all the light cone. Of course, if one wants to know precisely the properties of a given band, the full calculation for this band has to be performed.

Convergence

As regards convergence against the number of plane wave, the hybrid method's behavior is set by the Fourier factorization used in the plane wave expansion. The convergence therefore benefits from the use of the FFF. This is fortunate, because the 3D discretization of the problem clearly puts a severe limit on the plane waves cutoff. Use of the FFF enables a good accuracy with relatively low plane-wave cutoffs. Besides, the structures generally considered in this thesis are of weak to moderate photonic strength: the PhC usually isn't etched through the whole structure. In this regime, the cutoff can typically be lower than in the case of strong photonic interaction (as for instance in a membrane completely perforated by a PhC).

Figure 6.4 compares the convergence with plane-wave cutoff M (defined as $2M+1 = N_x N_y$), using the method of Ho and the FFF in the PWE, for a structure of moderate photonic strength. The usual trends of Chapter 5 can be observed. With the FFF, the relative error on n_{eff} is less than 5.10^{-5} for $M \geq 5$ and the relative error on k'' is less than 3.10^{-3} for $M \geq 3$. This result is rather general, and most calculations on light-extracting structures are well described using $M = 3$ e.g. 49 plane waves.

The convergence also depends on discretization in the z direction. In this case, the error decreases monotonously with finer vertical step dz, as is usual with finite differences. Fig. 6.5 shows the convergence with respect to dz, on the same vertical scale as Fig. 6.4 for easier comparison. Ideally, the values of M and dz should be matched so that both imprecisions are of the same orders. In our case, taking $M = 3$, the error brought by the vertical discretization is comparable to the PW error for $dz \sim a/50$. This rather fine mesh is in part needed because the PhC is quite shallow and needs enough points to

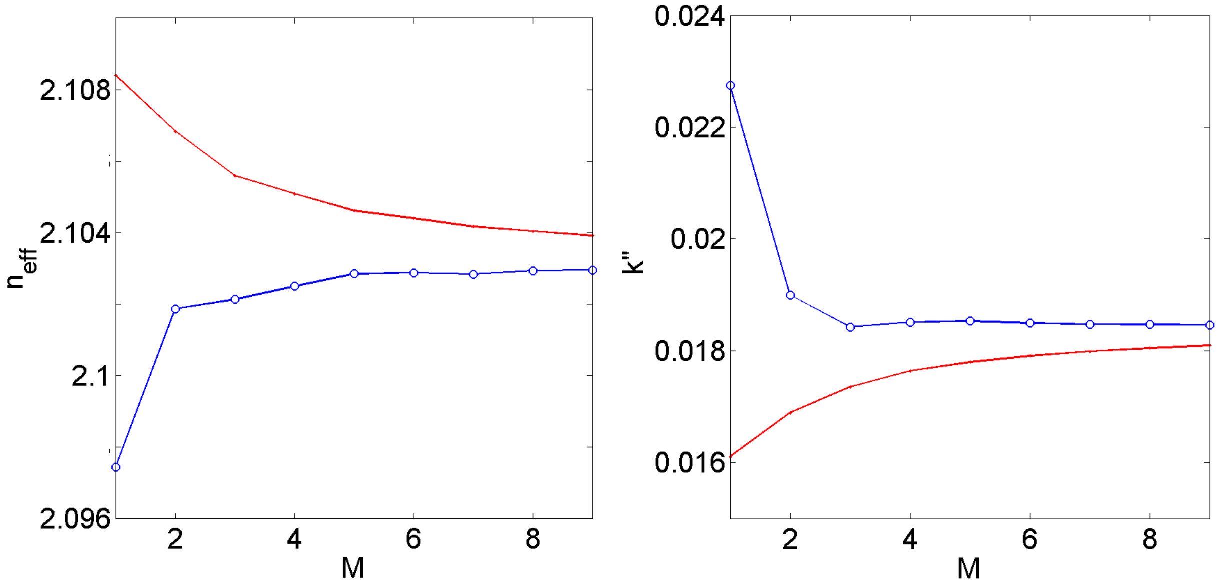

Figure 6.4: Convergence of the hybrid method against plane wave cutoff M with the method of Ho (line) and the FFF (circles). (Left) Effective index n_{eff}. (Right) Imaginary part of the wavevector k''. The structure considered is that of Fig. 3.18: a waveguide of index 2.5 and total thickness $0.6a$, surrounded by air and pierced to a depth $0.2a$ by a triangular lattice PhC of period a, with circular air holes of filling factor 0.3. The frequency of the fundamental Bloch mode is computed at a reduced frequency $a/\lambda = 0.45$, above the light line. As the core of the waveguide is rather thin, the Bloch mode leaks in the PhC region and the photonic interaction is moderate.

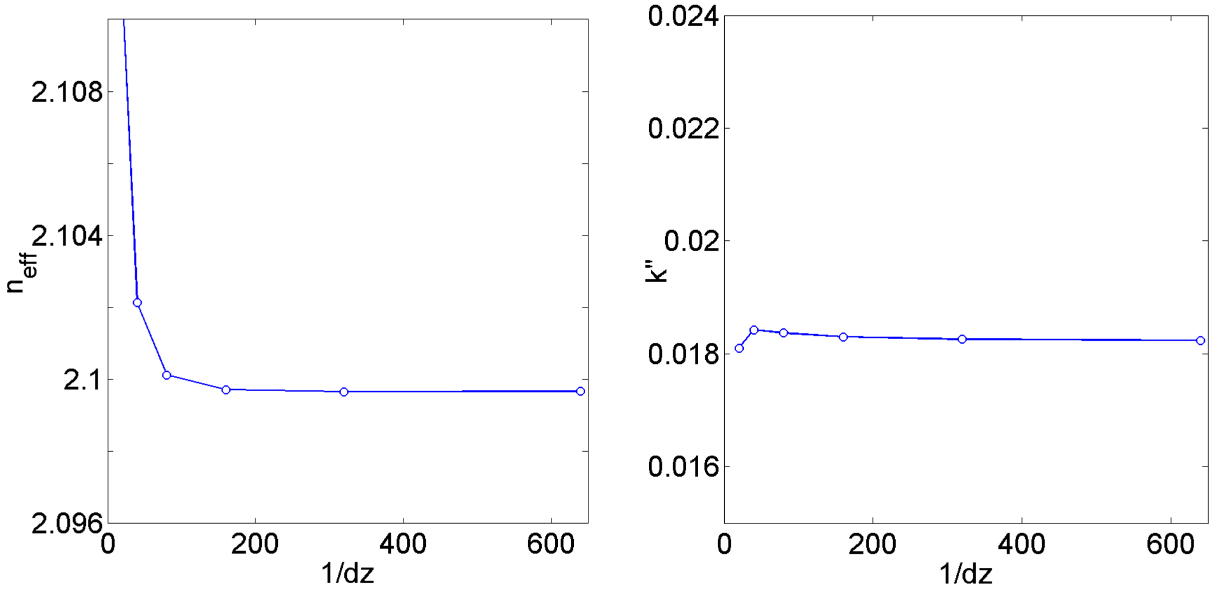

Figure 6.5: Convergence of the hybrid method against vertical step dz (in units of a) with the FFF. (Left) Effective index n_{eff}. (Right) Imaginary part of the wavevector k''. The plane wave cutoff is $M = 3$, and the vertical scale is the same as for Fig. 6.4.

be resolved. In structures where all thicknesses are $\sim a$, the finite differences converge slightly faster.

It is interesting to note that the memory requirements of the method are actually not proportional to the *total* vertical size of the system, but rather to the vertical size of the *patterned region*. Indeed, looking back at the form of the sparse matrices of Eq. 6.10, it appears that all values of z outside of the PhC region lead to nearly diagonal submatrices with only a few nonzero terms − this is because the dielectric tensor is diagonal. In contrast, inside the PhC the dielectric tensor is a full matrix and leads to numerous nonzero coefficients. These generally dominate the total number of nonzero coefficients in the final matrices, so that most of the memory storage is due to the points inside the PhC. As a consequence, structures with a very deep PhC ($d >> a$) are calculation-intensive with the hybrid method.

Finally, it should be emphasized that the simple finite differences scheme used (two-point derivatives) is clearly not optimal from the point of view of numerical efficiency. Although I have not explored this direction, it is likely that more elaborate schemes would enhance convergence.[4]

---

[4] However, one should keep in mind the difficulty evoked previously: not all schemes can be used because the matrices need to be Hermitian for numerical convergence.

6.3 Implementation of a Fourier Modal method

In addition to the hybrid method introduced above, I also implemented a Fourier Modal Method for 3D calculations. This was done for several reasons. The first is the validation of the hybrid method. Second, besides Bloch modes calculations, the FMM can treat other kinds of problems. Its ability to compute the emission of a dipole source was useful for Chapter 4, section 4.5. Finally, the FMM is in general able to treat systems where the computation task is too heavy for the hybrid method, but this turned out not to be a limitation in this thesis.

In this section, the FMM is first quickly introduced, then implemented, and some of its applications are presented.

6.3.1 Scattering matrix: principle

The principle of the FMM has already been exposed. The system is separated in layers which are invariant along z, the eigenmodes of each layer are computed by a 2D PWE, and the continuity conditions linking the eigenmodes of adjacent layers are cast as a matrix which connects the amplitudes of the fields outside the structure. Once this matrix is built, it can be used for several tasks, such as reflectivity/transmission measurements (or, in terms of diffractive optics, diffraction efficiencies) and Bloch modes computation. Therefore, the system can be seen as a quadrupole, whose ports are the incoming and outgoing fields on each side of the structure.

In the following, we assume that the system is made of $N+1$ layers. The layers are characterized by their thickness and optical parameters (refractive index or more parameters if the layer is patterned). Layers 0 and N are semi-infinite. The regions of interest are the layers themselves, and the interfaces between layers.

The fields are decomposed in a plane wave basis in each layer. To describe the field, we use column vectors of field amplitudes $\mathcal{A}$, which represent the amplitudes of plane waves propagating along the z-axis. These amplitudes will be related formally to the electromagnetic field in the next section. We assign the superscript $+$ to plane waves going in the $+z$ direction, and $-$ to waves going in the $-z$ direction.

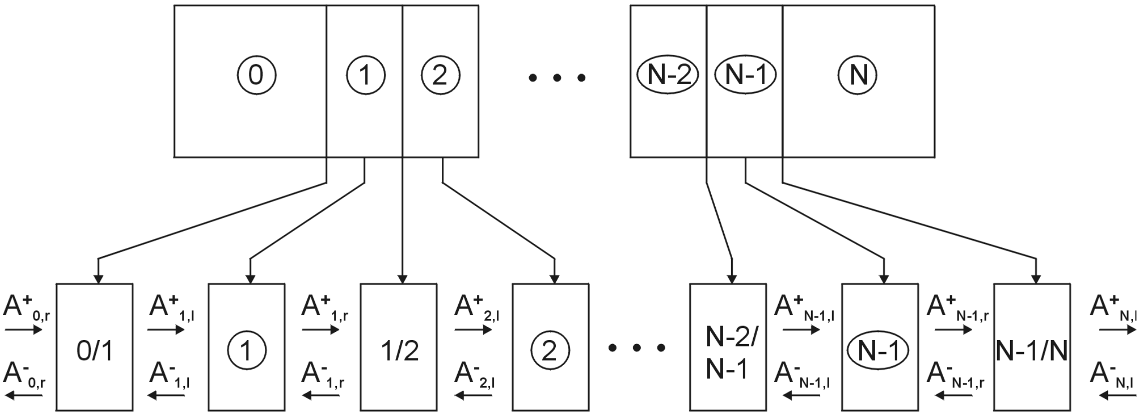

Figure 6.6: Notations for construction of the $\mathbb{S}$-matrix. The system is made of $N+1$ layers, and of N interfaces between layers. Amplitudes are indexed by their layer, direction of propagation and position in the layer (left or right). For instance $\mathcal{A}^+_{2,l}$ corresponds to the amplitude of fields propagating in the $+z$ direction, at the left side of the 2^{nd} layer.

We now index these amplitudes as described in Fig. 6.6. The boundary fields (i.e. the fields outside the structure) are then $\mathcal{A}^+_{0,r}$ and $\mathcal{A}^-_{0,r}$ at the left of the structure, and $\mathcal{A}^+_{N,r}$ and $\mathcal{A}^-_{N,r}$ at the right of the structure.

Several matrices can be built to characterize the structure. The easiest to implement is the Transfer matrix ($\mathbb{T}$-matrix), which connects the fields on one side to the fields on the other side:

$$\left| \begin{array}{c} \mathcal{A}^{+}_{N,l} \\ \mathcal{A}^{-}_{N,l} \end{array} \right. = \mathbb{T} \left| \begin{array}{c} \mathcal{A}^{+}_{0,r} \\ \mathcal{A}^{-}_{0,r} \end{array} \right. \tag{6.21}$$

For instance, with this matrix, one can impose the fields incoming and outgoing on the left side of the structure, and deduce the fields on the right side. While the $\mathbb{T}$-matrix formalism is mathematically exact, it suffers from numerical instabilities which make it unusable for nearly any practical use. Namely, when building the $\mathbb{T}$-matrix, one has to deal with growing and decaying exponential terms. Due to unavoidable numerical roundoffs in the computation of the matrix coefficients, the growing exponential terms rapidly diverge and dominate all other matrix coefficients.[5]

For this reason, one rather uses a Scattering-matrix ($\mathbb{S}$-matrix), which connects the incoming fields to the outgoing fields:

$$\left| \begin{array}{c} \mathcal{A}^{+}_{N,l} \\ \mathcal{A}^{-}_{0,r} \end{array} \right. = \mathbb{S} \left| \begin{array}{c} \mathcal{A}^{+}_{0,r} \\ \mathcal{A}^{-}_{N,l} \end{array} \right. \tag{6.22}$$

This can simply be expressed as:

$$\mathcal{A}_{out} = \mathbb{S}\mathcal{A}_{in} \tag{6.23}$$

This form is convenient in terms of boundary conditions, since one typically imposes incoming fields and looks for outgoing fields. The major advantage of the $\mathbb{S}$-matrix is that no growing exponentials appear in its construction, so that the numerical divergences of the $\mathbb{T}$-matrix are avoided, no matter what the thickness of the structure is.

It should be noted that in some cases (determination of diffraction efficiency for instance) one still needs to work on the corresponding $\mathbb{T}$-matrix rather than on $\mathbb{S}$ directly. This should be done carefully to avoid numerical instabilities, for instance by using $(\mathbb{T} - 1)^{-1}$ instead of $\mathbb{T}$.[13]

For the sake of completeness, let us mention another quadrupole matrix which can described a multilayer system: the $\mathbb{R}$-matrix, which is similar to the $\mathbb{S}$-matrix but uses a sinusoidal basis rather than an exponential basis in each layer. This does not especially improve the algorithm and makes implementation slightly more complicated.[45]

6.3.2 Scattering matrix: implementation

The implementation of the $\mathbb{S}$-matrix is vastly detailed in literature. While it is described in many articles related to grating theory, some articles focus on multilayer photonic crystal structures and are more closely related to the subject of this thesis. A classic reference is the article by Whittaker.[46]. A discussion of the various algorithms which can be used to build the $\mathbb{S}$-matrix can be found in Ref. [45], which also discusses some interesting properties of $\mathbb{S}$-matrices. Another good and detailed reference for practical implementation of the $\mathbb{S}$-matrix is [47]. In the following, I use the notations of the latter reference, where derivation of the formalism is detailed in depth. Therefore, only the key steps of the implementation are presented here.

---

[5] This happens more rapidly for strongly evanescent harmonics, which correspond to large reciprocal vectors. Therefore we obtain a paradoxical behavior: the $\mathbb{T}$-matrix becomes *more unstable* as one tries to increase accuracy by adding reciprocal vectors. On the other hand, this means that $\mathbb{T}$-matrices can safely be used in the case of thin unpatterned layers, where only one harmonic is involved.

Eigenmodes of a layer - Homogeneous problem

The first step consists in finding the eigenmodes of each layer, considered infinitely high in the z direction. This is the so-called homogeneous problem, which we simply solve using the 2D PWE exposed in Chapter 5. The input parameters in this case are the values of ω and $k_{//}$, and one now looks for the values of k_z corresponding to eigenmodes in the layer. As was seen in section 5.4 of Chapter 5, the homogeneous problem can be cast in various form. Here, we retain that of section 5.4.2 (the so-called Tikhodeev form).

Let us introduce the following notations: $\{\mathbf{G}\}$ are the reciprocal lattice vectors, which are truncated to a number N_G. The in-plane wavevector $k_{//}$ has coordinates k_x and k_y. The electric field in each layer is written as:

$$\vec{\mathcal{E}} = \left| \begin{array}{c} E_{x,\mathbf{G}_1} \\ \vdots \\ E_{x,\mathbf{G}_{N_G}} \\ E_{y,\mathbf{G}_1} \\ \vdots \\ E_{y,\mathbf{G}_{N_G}} \end{array} \right. \tag{6.24}$$

As seen in Chapter 5, Maxwell's equations then take the form:

$$\mathcal{M}\,\vec{\mathcal{E}} = k_z^2 \mathcal{N}\,\vec{\mathcal{E}} \tag{6.25}$$

Where $\mathcal{M}$ and $\mathcal{N}$ have been defined in section 5.4.2 of Chapter 5, and include the FFF implementation. Since this equation admits $2N_G$ solutions, the eigenproblem can be rewritten by stacking all the solutions into a matrix:

$$\mathcal{M}\mathcal{E} = \mathcal{K}^2 \mathcal{N}\mathcal{E} \tag{6.26}$$

Under this form, $\mathcal{E}$ is a matrix whose columns are the vectors $\vec{\mathcal{E}}$, and $\mathcal{K}$ is a diagonal matrix whose elements are the corresponding eigenvalues k_z. As can be seen, the eigenvalues of Eq. 6.26 are the *squares* of k_z. This is because the structure is symmetric vertically, so that each eigenvalue corresponds to a pair of eigenmodes (one mode propagating in the $+z$ direction and one in the $-z$ direction). Here, we choose to take the square roots of *positive* imaginary part in the definition of $\mathcal{K}$ – this convention is important for the numerical stability of the algorithm.

Definition of the field amplitudes $\mathcal{A}$

Coming back to the 3D structure, we can now formally define the column vector of amplitudes $\mathcal{A}$ already introduced earlier. It is related to the *total* in-plane electric field in the structure $\mathbf{E}_{//}$ as follows:

$$\mathbf{E}_{//}(z) = \left| \begin{array}{c} E_x \\ E_y \end{array} \right. = \left(\begin{array}{cc} \mathcal{E} & \mathcal{E} \end{array} \right) \left| \begin{array}{c} \mathcal{A}^+(z) \\ \mathcal{A}^-(z) \end{array} \right. \tag{6.27}$$

In other words, at each point z, $\mathcal{A}(z)$ just contains the coefficients of the electric field projected on the basis of eigenmodes. Matrices $\mathcal{E}$ only depend on the layer, whereas the coefficients in $\mathcal{A}$ vary with z. The fact that the same matrix $\mathcal{E}$ can be used for modes propagating to the right $(+)$ and left $(-)$

is just due to the vertical symmetry in each layer. The indexing $\mathcal{A}^{+}_{j,r}$ introduced earlier corresponds to particular values of z (namely, at the extremities of a layer).

The $\mathbb{S}$-matrix is built iteratively. We initiate the recursion with $\mathbb{S}_0 = \mathbb{1}$. We assume that we know matrix $\mathbb{S}_{j-1}$ corresponding to propagation through layers 0 to $j-1$. More precisely, $\mathbb{S}_{j-1}$ connects the fields $\mathcal{A}_{0,r}$ on the left of the 0/1 interface to the fields $\mathcal{A}_{j-1,r}$ on the left of the $(j-1)/j$ interface:

$$\begin{pmatrix} \mathcal{A}^{+}_{j-1,l} \\ \mathcal{A}^{-}_{0,r} \end{pmatrix} = \mathbb{S}_{j-1} \begin{pmatrix} \mathcal{A}^{+}_{0,r} \\ \mathcal{A}^{-}_{j-1,l} \end{pmatrix} \tag{6.28}$$

We look for $\mathbb{S}_j$. The effect of the structure on the field can be described in terms of two phenomena: connection between layers and propagation inside a layer.

Connection between layers

We first consider the interface between layers $j-1$ and j. In order to express the field continuity conditions in matrix form, let us first decompose $\mathbb{S}_{j-1}$ as:

$$\mathbb{S}_{j-1} = \begin{pmatrix} S_{11} & S_{12} \\ S_{21} & S_{22} \end{pmatrix} \tag{6.29}$$

In each layer j we define the following matrices:

$$\mathcal{C} = \begin{pmatrix} -N_{21} & -N_{22} \\ N_{11} & N_{12} \end{pmatrix} \tag{6.30}$$

$$\mathbb{F}_j = \begin{pmatrix} \mathcal{E} & \mathcal{E} \\ \frac{1}{\omega}\mathcal{C}\mathcal{E}\mathcal{K} & -\frac{1}{\omega}\mathcal{C}\mathcal{E}\mathcal{K} \end{pmatrix} \tag{6.31}$$

The components N of matrix $\mathcal{C}$ are those defined in the PWE (see Chapter 5, section 5.4.2).[6] Matrix $\mathbb{F}_j$ is called the *material matrix* for layer j. It has the important property of converting the field amplitudes $\mathcal{A}$ into electric and magnetic fields (as shown in Ref. [47]):

$$\mathbb{F}_j \left| \begin{matrix} \mathcal{A}^{+}_{j} \\ \mathcal{A}^{-}_{j} \end{matrix} \right. = \left| \begin{matrix} \mathbf{E}_{//} \\ \mathbf{H}_{//} \end{matrix} \right. \tag{6.32}$$

This is useful because the continuity of the tangential fields $\mathbf{E}_{//}$ and $\mathbf{H}_{//}$ between layers $j-1$ and j can now be expressed on $\mathcal{A}$:

$$\mathbb{F}_j \left| \begin{matrix} \mathcal{A}^{+}_{j} \\ \mathcal{A}^{-}_{j} \end{matrix} \right. = \mathbb{F}_{j+1} \left| \begin{matrix} \mathcal{A}^{+}_{j+1} \\ \mathcal{A}^{-}_{j+1} \end{matrix} \right. \tag{6.33}$$

To rewrite these continuity conditions, we define the *interface matrix* between layers $j-1$ and j:

$$\mathbb{T}_{j-1,j} = \begin{pmatrix} T_{11} & T_{12} \\ T_{21} & T_{22} \end{pmatrix} = \mathbb{F}^{-1}_{j-1}\mathbb{F}_j \tag{6.34}$$

The interface matrix then links fields on the left and the right of the interface as follows:

---

[6] Note that $\mathcal{C}$ is a 'skewed' form of matrix N introduced in Chapter 5. This skewing of matrix blocks is characteristic of the transition from the formalism of transfer matrices to that of scattering matrices

$$\left|\begin{matrix} \mathcal{A}^+_{j-1,r} \\ \mathcal{A}^-_{j-1,r} \end{matrix}\right. = \mathbb{T}_{j-1,j} \left|\begin{matrix} \mathcal{A}^+_{j,l} \\ \mathcal{A}^-_{j,l} \end{matrix}\right. \tag{6.35}$$

However, the above amplitudes are sorted for a Transfer-matrix algorithm. This relation can not be used directly for the Scattering-matrix formalism where the amplitudes needs to be reordered. We have to define:

$$\mathcal{D} = (T_{11} - S_{12}T_{21})^{-1} \quad , \quad \mathcal{F} = (S_{12}T_{22} - T_{12}) \tag{6.36}$$

The continuity conditions of Eq. 6.35 can finally be expressed in a scattering matrix form. We obtain:

$$\hat{\mathbb{S}} = \begin{pmatrix} \mathcal{D}S_{11} & \mathcal{D}\mathcal{F} \\ S_{21} + S_{22}T_{21}\mathcal{D}S_{11} & S_{22}T_{21}\mathcal{D}\mathcal{F} + S_{22}T_{22} \end{pmatrix} \tag{6.37}$$

The new matrix $\hat{\mathbb{S}}$ connects $\mathcal{A}_{0,r}$ to the fields on the *right* of the $(j-1)/j$ interface, $\mathcal{A}_{j,l}$.

Propagation inside a layer

Let us now consider propagation through layer j, of thickness L and whose eigenvalues of the homogeneous problem are stacked in matrix $\mathcal{K}^{(j)}$. For each of the layer's eigenvectors $\overrightarrow{\mathcal{E}}$ with a corresponding eigenvalue k_z, the z-dependence is just $e^{ik_z z}$. This can be put in matrix form:

$$\left|\begin{matrix} \mathcal{A}^+_{j,r} \\ \mathcal{A}^-_{j,r} \end{matrix}\right. = \begin{pmatrix} \phi^+_j & 0 \\ 0 & \phi^-_j \end{pmatrix} \left|\begin{matrix} \mathcal{A}^+_{j,l} \\ \mathcal{A}^-_{j,l} \end{matrix}\right. \tag{6.38}$$

Where matrices ϕ are defined as:

$$\phi^+_j = e^{i\mathcal{K}^{(j)}L} \quad , \quad \phi^-_j = e^{-i\mathcal{K}^{(j)}L} \tag{6.39}$$

Matrix ϕ^- is responsible for the numerical instabilities evoked earlier, because it contains growing exponentials.[7] However, it needs not be used if one only propagates (+) fields from left to right, and (−) fields from right to left. This is precisely the principle of the $\mathbb{S}$-matrix algorithm, where propagation is described by:

$$\mathbb{S}_j = \begin{pmatrix} \phi^+_j & 0 \\ 0 & \mathbb{1} \end{pmatrix} \hat{\mathbb{S}} \begin{pmatrix} \mathbb{1} & 0 \\ 0 & \phi^+_j \end{pmatrix} \tag{6.40}$$

Thus, we obtain $\mathbb{S}_j$, which connects $\mathcal{A}_{0,r}$ to $\mathcal{A}_{j,r}$. By repeating the iteration until layer N, we build the total $\mathbb{S}$-matrix of the system.

6.3.3 Applications of the $\mathbb{S}$-matrix

Reflectivity calculations

Once the $\mathbb{S}$-matrix of the system is known, it is straightforward to obtain the system's reflectivity and transmission, by using Eq. 6.23. One simply has to impose an incoming field $\mathcal{A}_{in}$. As an example, Fig. 6.7 gives the reflectivity of a membrane etched by a PhC and illuminated by TM light. Sharp dips and peaks in the reflectivity (Wood anomalies) are present, some of which manifest coupling with leaky modes of the structure.

---

[7] This is due to our convention on the sign of $Im(\mathcal{K})$.

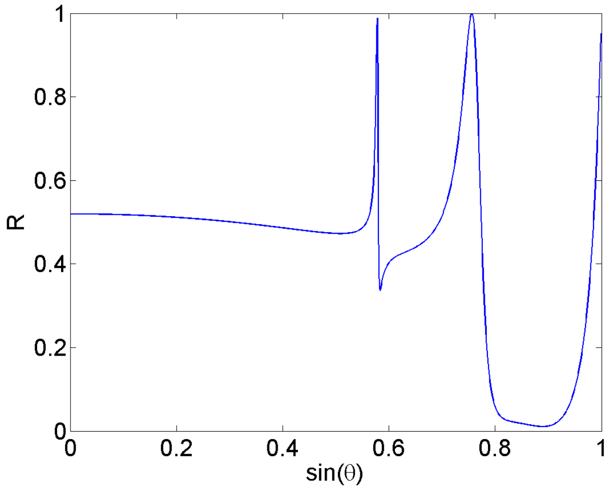

Figure 6.7: Reflectivity of a membrane with index $n = 3$ and total thickness 0.7 embedded in air, with a triangular lattice ($f = 0.5$) etched to a depth 0.2. The structure is illuminated along ΓM by a TM-polarized plane wave at a normalized frequency 0.4.

Bloch modes calculations

The Bloch modes of the structure correspond to self-sustained excitations, able to exist without energy feed from the outside. They are characterized by the condition $\mathcal{A}_{in} = 0, \mathcal{A}_{out} \neq 0$. Therefore, one should have:

$$\mathbb{S}^{-1}\mathcal{A}_{out} = \mathcal{A}_{in} = 0 \tag{6.41}$$

For this to admit non-trivial solutions, one must have $det(\mathbb{S}^{-1}) = 0$. Therefore, Bloch modes can be obtained by looking for the poles of $\mathbb{R} = \mathbb{S}^{-1}$. This can be done either by setting $k_{//}$ and varying ω, or the contrary. In practice, searching for poles in the complex plane is no easy task: one is looking for the complex roots of $det(\mathbb{S}^{-1})$ as a function of the complex variable ω, which requires several costly computations of $\mathbb{S}$. Another difficulty is that many poles can exist, so that one should usually start 'close enough' to a given pole to reach it. Typically, this is solved by starting from a trivial problem (holes of vanishing depth or filling factor...) and 'following' the pole in the complex plane as the parameter varies.

Anyway, one must still choose a mathematical method to find the pole. Mapping systematically a region of the complex plane, as was shown in Fig. 3.5 of Chapter 3 is inefficient and prohibitive in terms of calculation time as soon as a reasonable number of plane waves is kept. Usually, one rather uses an iterative method such as a gradient method, which follows the steepest descent path in the surface defined by $|det(\mathbb{S}^{-1})|$.

In this thesis, I used an iterative scheme introduced by Gippius *et al.* [48] which I found efficient and simple to implement: once the $\mathbb{S}$-matrix building algorithm is written, it only requires a few additional lines of code. Let us look for a given pole ω_0 of $\mathbb{S}$. One first assumes a trial value for ω, and computes $\mathbb{R}(\omega)$ and $\partial_\omega \mathbb{R}(\omega)$.[8] Eq. (6.41) can then be linearized as:

$$\mathbb{R}(\omega_0)\mathcal{A}_{out} = 0 \Rightarrow (\mathbb{R}(\omega) + \partial_\omega \mathbb{R}\delta\omega)\mathcal{A}_{out} = 0 \tag{6.42}$$

---

[8] This is done numerically by computing $\mathbb{R}(\omega + \Delta\omega)$ with $\Delta\omega$ small enough with respect to ω. Hence, *two* $\mathbb{S}$-matrices have to be built, which doubles the computational time. On the other hand, the ensuing iterative scheme converges rapidly.

This last equation takes the form of an eigenproblem:

$$-(\partial_\omega \mathbb{R})^{-1}\mathbb{R}(\omega)\mathcal{A}_{out} = \delta\omega\mathcal{A}_{out} \tag{6.43}$$

Only the smallest (or the few smallest) eigenvalues are of interest, which relieves the computational effort. The eigenvalue provides a correction to the trial value of ω: $\omega \leftarrow \omega + \delta\omega$. One then repeats the calculation of $\mathbb{S}$ and the procedure, until convergence of ω to ω_0.

This method turns out to be efficient for pole-searching. Usually, a few (less than ten) iterations give an accuracy better than 10^{-5} on $\delta\omega$. I haven't faced cases where the iteration would fail (bouncing between two poles), *except* for some calculations at the edge of the Brillouin zones. In that case, the issue was solved by first looking for poles very close to the edge of the Brillouin zone, and then following the desired pole at the edge.

The same iterative procedure can be applied with inverting the roles of $k_{//}$ and ω, if one wants to look for the eigenmodes at a given frequency. As pointed earlier, this is very useful for implementation of index dispersion.

Source terms

Previous work An interesting feature of Transfer and Scattering matrices is the possibility to insert a source term in the structure, in order to simulate the emission of a point dipole. Mathematically, dipole emission translates into a discontinuity of the fields across the dipole, which can easily be imposed in matrix form. The first implementation of this principle was introduced by Benisty *et. al.* ([49]) in the context of 1D planar structures, based on initial work at EPFL. It made use of transfer matrices. Since then, the formalism has been adapted to 3D structures, which actually requests little change with respect to the 1D case.

The first 3D implementation of dipole emission is proposed by Whittaker and Culshaw (Ref. [46]). Here, the source is treated exactly as in the 1D case of Ref. [49]. The partial S-matrices for the left and right halves of the structure (on each side of the source) are computed, and the field emitted by the source is expressed as a function of these and the discontinuity brought by the source. This field can then be propagated everywhere to obtain the emission of the source. This method is straightforward. On the other hand, the authors do not comment on the precise form of the source, and more precisely on the angular normalization factors which should be used in order to model a horizontal or vertical dipole.

A second implementation, proposed by Rigneault *et. al.* (Ref. [50]), follows the same approach. The article describes the mathematical formalism in greater details. Moreover, in order to build the $\mathbb{S}$-matrices of the system, the differential method is used instead of the FMM.

A third implementation is introduced by Delbeke *et al.* (Ref. [51]). In this paper, the authors treat the effect of the source by expressing the fields outside of the structure in a closed form which involves the discontinuity and partial reflection/transmission matrices (corresponding to each half of the structure around the source layer). In my opinion, this offers the slight disadvantage that these reflection and transmission matrices are not directly given by the S-matrix algorithm and have to be built. However, the authors discuss angular normalization factors in greater details and comment on important aspects, such as the position of the source and its refractive index.

In this section, I follow the treatment of Whittaker and Culshaw and adapt it to the notations of this thesis. I also indicate the proper normalization coefficients for in-plane dipoles in this formalism.

Insertion of a dipole source Let us assume that a dipole is located in layer p, at position z_s. We assume for now that the source is embedded in a layer with thickness 0 and refractive index n_s (Fig. 6.8).

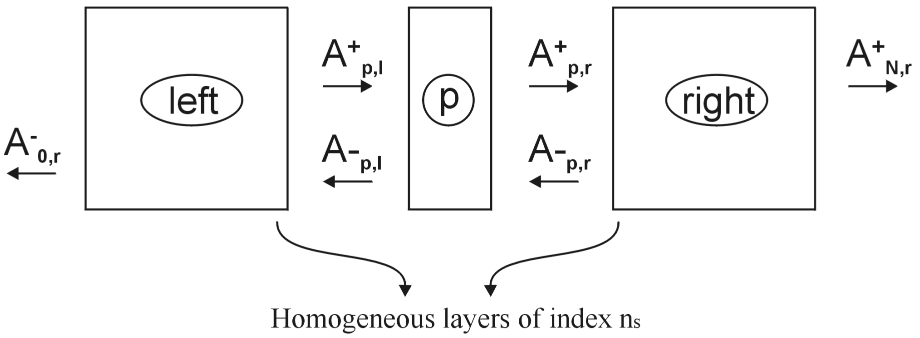

Figure 6.8: Structure with a source at layer p. The structures to the left and right of the source should end with an homogeneous layer of index n_s, the index of the source layer.

This dipole a discontinuity of the electromagnetic field, whose details depend on the orientation of the dipole. For now, let us consider that the dipole has general coordinates:[9]

$$\tilde{\mathbf{p}} = \left| \begin{array}{l} p_x \\ p_y \\ p_z \end{array} \right. \tag{6.44}$$

Let us note that the above are Fourier-transform coordinates: p_x itself is a column vector of height M, whose coefficients are the Fourier coefficients of p_x. Their precise form will be clarified later. As explained in Ref. [46], the presence of the dipole translates into the following discontinuities for the in-plane electric and magnetic fields:

$$\mathbf{E}_{//}(z^+) - \mathbf{E}_{//}(z^-) \quad = \quad \left| \begin{array}{l} p_z \\ p_z \end{array} \right. \qquad \mathbf{H}_{//}(z^+) - \mathbf{H}_{//}(z^-) \quad = \quad \left| \begin{array}{c} p_y \\ -p_x \end{array} \right. \tag{6.45}$$

These can be summarized by:

$$\left| \begin{array}{l} \mathbf{E}_{//}(z^+) \\ \mathbf{H}_{//}(z^+) \end{array} \right. - \left| \begin{array}{l} \mathbf{E}_{//}(z^-) \\ \mathbf{H}_{//}(z^-) \end{array} \right. = \Delta \qquad \text{with} \qquad \Delta = \left| \begin{array}{c} p_z \\ p_z \\ p_y \\ -p_x \end{array} \right. \tag{6.46}$$

We introduce $\mathbb{S}^{left}$ and $\mathbb{S}^{right}$, the scattering matrices for the left and right sides of the structure (i.e. on each side of the source). At this point, let us mention that $\mathbb{S}^{left}$ should end (and $\mathbb{S}^{right}$ should start) with a layer of index n_s (and of thickness 0 if so desired), for proper continuity.[10] We also introduce $\mathcal{E}_p$, $\mathcal{C}_p$, $\mathcal{K}_p$ and $\mathbb{F}_p$ which are defined as previously, for a homogeneous medium of index n_s. Eq. 6.46 takes the form:

$$\mathbb{F}_p \left| \begin{array}{l} \mathcal{A}^+_{p,r} \\ \mathcal{A}^-_{p,r} \end{array} \right. - \mathbb{F}_p \left| \begin{array}{l} \mathcal{A}^+_{p,l} \\ \mathcal{A}^-_{p,l} \end{array} \right. = \Delta \tag{6.47}$$

Moreover, the boundary conditions of this problem state that no field should be incoming on the structure from outside, e.g. $\mathcal{A}^+_{0,r} = \mathcal{A}^-_{N,l} = 0$. Thus, the definition of $\mathbb{S}^{left}$ and $\mathbb{S}^{right}$ leads us to:

---

[9] For reference, in the case of GaN heterostructures grown along the c-axis, the dipoles are usually assumed horizontal.

[10] More precisely, the field discontinuity should only be due to the presence of the source. Therefore the source must be embedded in a medium of index n_s to avoid discontinuities due to dielectric boundaries.

$$\begin{array}{rcl} \mathcal{A}^{+}_{p,l} & = & \mathbb{S}^{left}_{12}\mathcal{A}^{-}_{p,l} \\ \mathcal{A}^{-}_{0,r} & = & \mathbb{S}^{left}_{22}\mathcal{A}^{-}_{p,l} \\ \mathcal{A}^{-}_{p,r} & = & \mathbb{S}^{right}_{21}\mathcal{A}^{-}_{p,r} \\ \mathcal{A}^{+}_{N,l} & = & \mathbb{S}^{right}_{11}\mathcal{A}^{+}_{p,r} \end{array} \tag{6.48}$$

This and the definition of $\mathbb{F}_p$ leads to the following equation for the outgoing field on the left and the right of the structure:

$$\begin{pmatrix} \mathcal{E}_p(\mathbb{1}+\mathbb{S}^{right}_{21}) & -\mathcal{E}_p(\mathbb{1}+\mathbb{S}^{left}_{12}) \\ \frac{1}{\omega}\mathcal{C}_p\mathcal{E}_p\mathcal{K}_p(-\mathbb{S}^{right}_{21}+\mathbb{1}) & \frac{1}{\omega}\mathcal{C}_p\mathcal{E}_p\mathcal{K}_p(-\mathbb{S}^{left}_{12}+\mathbb{1}) \end{pmatrix} \left| \begin{array}{l} \mathcal{A}^{+}_{p,r} \\ \mathcal{A}^{-}_{p,l} \end{array} \right. = \Delta \tag{6.49}$$

Solving this equation yields the outgoing fields on each side of the source. From these, all other fields can be computed by applying the partial scattering matrices. The most interesting fields in our problem are the fields around the source, and the outgoing fields outside of the structure: all of these can be obtained directly from Eq. 6.48. Once the fields around the source are obtained, the power emitted at the source can be computed. Thanks to the outgoing fields, the power radiated outside of the structure can be computed.

Simple source or folded source As has been said, $\tilde{\mathbf{p}}$ is the Fourier transform of the dipole $\mathbf{p}$. For a dipole localized at point $(\mathbf{r}_0, z_0)$, we have:

$$\mathbf{p}(\mathbf{r}, z) = \mathbf{p}_0\delta(\mathbf{r}-\mathbf{r}_0)\delta(z-z_0) \tag{6.50}$$

Its Fourier transform can thus be expressed in two ways:

$$\begin{array}{ll} (1) & \mathbf{p} = \mathbf{p}_0\delta(z-z_0)\displaystyle\int_{\mathbf{k}_{//}} exp\left(-i\mathbf{k}_{//}\cdot(\mathbf{r}-\mathbf{r}_0)\right)d\mathbf{k}_{//} \\ (2) & \mathbf{p} = \mathbf{p}_0\delta(z-z_0)\displaystyle\int_{\mathbf{k}_{//}\in FBZ}\sum_{\mathbf{G}} exp\left(-i(\mathbf{k}_{//}+\mathbf{G})\cdot(\mathbf{r}-\mathbf{r}_0)\right)d\mathbf{k}_{//} \end{array} \tag{6.51}$$

The first form should be understood with caution. At first glance, it could be seen as a point dipole localized in space, which can hence couple to any value of $k_{//}$. However, this is not quite true because here, emission at wavevectors $k_{//}$ and $k_{//}+G$ occurs *incoherently*. This form actually describes a collection of *delocalized* dipole sheet sources, incoherently emitting light in all directions (see Annex C for a short discussion of this question). We then have:

$$p_x = \left| \begin{array}{c} 0 \\ \vdots \\ 0 \\ p_x exp\left(-i\mathbf{k}_{//}\cdot(\mathbf{r}-\mathbf{r}_0)\right) \\ 0 \\ \vdots \\ 0 \end{array} \right. \tag{6.52}$$

Where the only nonzero coefficient corresponds to $\mathbf{G} = 0$; p_y and p_z have similar forms.

The second form may seem equivalent to the first, but the integral on $k_{//}$ is cut in parts, each of which is folded back in the FBZ. There is a subtle difference in this case: emission in directions $k_{//}$ and $k_{//} + G$ is *coherent*. As explained in Annex C, this correspond to a point-like source which emits coherently in all space directions. In this case:

$$p_x = \left| \begin{array}{c} \vdots \\ p_x exp\left(-i(\mathbf{k}_{//} + \mathbf{G}) \cdot (\mathbf{r} - \mathbf{r}_0)\right) \\ \vdots \end{array} \right. \tag{6.53}$$

Note that in principle, both forms *do not yield* the same results for the dipole emission. Therefore, the choice of the source term depends whether the emitter (exciton or electron-hole pair) is localized in the horizontal direction or not.

The first form is easy to interpret, because the source only couples to the harmonic $\mathbf{G} = 0$, and the field carried by other harmonics is generated by scattering in the patterned regions. Therefore, it is easy to determine the contribution of the PhC to light extraction when considering the field outside of the structure. The main disadvantage of this choice is that in principle the integral runs from $-\infty$ to ∞, which is rather unpractical for numerical implementation. In practice, the maximum value of $k_{//}$ supported in the source layer is $n_s k_0$, so that the integral is bounded through the choice of n_s. This calls for a discussion. In the case where there is no PhC, n_s can just be taken equal to the largest index in the multilayer structure, so that even tunnel emission through evanescent waves is taken into account.[11]. When there is a PhC, n_s should in principle be taken infinite so that all light emission events can be accounted for: any value of $k_{//}$ can be scattered by a large enough $\mathbf{G}$ vector, and brought back to a propagative $k_{//} + G$. However, the strength of such coupling is determined by $\epsilon(\mathbf{G})$ and thus becomes very small for large G. In most cases of interest, it is thus reasonable to ignore these events and to take n_s large enough to couple the source only to the strongest reciprocal lattice points. Of course, these vary with the crystal lattice: for a typical triangular lattice, only the smallest $\mathbf{G}$ vectors are strong, whereas for an Archimedean tiling the photonic strength spreads further in the reciprocal lattice (see Chapter 4 for a detailed discussion) .

The second form has the advantage that the values of $k_{//}$ to be considered are bounded by the FBZ. On the other hand, the source couples directly to all harmonics, which makes physical interpretation less intuitive.

In our case, it is not clear whether excitons (or electron-hole pairs) are localized horizontally in InGaN quantum wells: the choice of the source term is thus not determined. Therefore, we generally opt for the first form because it offers easier physical insight, and because it avoids introducing the horizontal position of the source as an additional parameter (in a sense, the source 'feels' the total density of states in the horizontal direction, rather than the local density of states).

Fig. 6.9 illustrates a few of these remarks.

Normalization of source terms In the above treatment, each value of $k_{//}$ (e.g. each angle of emission) is treated separately. However, if one wants to simulate the effect of a dipole source (or equivalently an exciton recombination), the proper angular dependence of emission has to be inserted in the source's normalization. This factor should be such that the emission in a bulk medium corresponds to the theoretical emission of a dipole in bulk.

In practice, as explained in Ref. [49] and depicted in Fig. 6.10, a dipole oriented along y emits a TE-polarized field, whose amplitude is constant at all angles. A dipole oriented along x emits a TM-polarized field, whose amplitude varies like $\cos(\theta)$. In conclusion, the proper source term normalization

---

[11] In the case of a metal, a larger value has to be taken to account for possible coupling to surface plasmons.

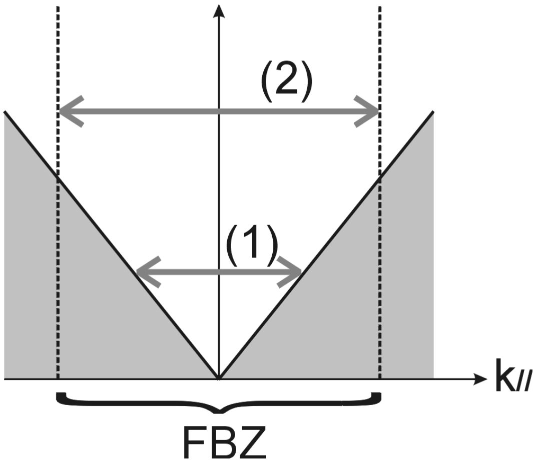

Figure 6.9: Integration intervals for the two forms of the source dipole. (1) If n_s is too small, the light cone of the source is inside the FBZ and some emission channels are neglected . (2) With the second form the integral is restricted to the FBZ, even if the light cone of the source is large.

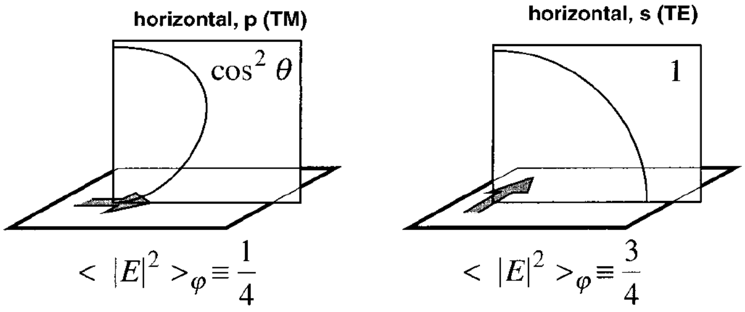

Figure 6.10: (After Ref. [49]) Angular dependence of the emission patterns of horizontal dipoles oriented along x and y.

factors *for the electric field emitted by a dipole* are:

$$\begin{array}{rcl} \text{dipole along } y \text{ (TE source)} & \rightarrow & E_y \sim 1 \\ \text{dipole along } x \text{ (TM source)} & \rightarrow & |E| \sim \cos(\theta) \end{array} \tag{6.54}$$

This normalization is commented in greater details in Ref. [49], where they are straightforwardly applied because the authors work directly on the amplitude of the electric field. A possible caveat in our case is that for horizontal dipoles (terms p_x and p_y), the discontinuity conditions we introduced concern the *magnetic* field. Therefore, the above normalization can not be applied blindly. Rather, we notice that the angular relationship between **E** and **H** for plane waves is:

$$\begin{array}{rcl} \text{TE} & \rightarrow & H_x \sim \cos(\theta) E_y \\ \text{TM} & \rightarrow & H_y \sim |E| \end{array} \tag{6.55}$$

Therefore, for the electric field's angular dependence to vary as prescribed, the normalization of discontinuities in Eq. 6.46 should finally be:

$$\begin{aligned} p_y &= \cos(\theta)\sqrt{\frac{3}{4\pi}} \\ p_x &= \cos(\theta)\sqrt{\frac{3}{4\pi}} \end{aligned} \tag{6.56}$$

In addition to the angular dependence, the above expression also includes the proper multiplying constants to normalize the emission so that the total power (integrated over all directions) emitted by a dipole in a bulk material of index n_s is:

$$\begin{aligned} \text{TE} &\rightarrow \mathcal{P} = 3n_s/4 \\ \text{TM} &\rightarrow \mathcal{P} = n_s/4 \end{aligned} \tag{6.57}$$

This normalization is convenient because both contributions (TE and TM) can then be summed incoherently in order to obtain the emission of a dipole averaged in all in-plane directions. The convention we chose is that an average in-plane dipole emits a power n_s in a bulk material of index n_s: this reflects the change in radiative lifetime with respect to the same dipole in air.[12]

Calculation of emitted power Once the fields in the structure are known, we have to obtain the far-field power emission of the dipole outside of the structure. One approach consists in integrating emission over $k_{//}$ in the FBZ. This approach, well suited to the case of a 'folded source' (e.g. using the second Fourier transform of the dipole described above), is well described in Ref. [51].

The second option is to describe the emission in terms of power emitted per solid angle. This method is more directly suited to the choice of an 'unfolded source' where the polar angle of emission at the source θ is a natural variable. In my opinion, it also offers easier interpretation. Unfortunately, using solid angles is not a trivial task. Indeed, we need to switch from the plane-wave formalism, well adapted to infinite in-plane structures, to that of solid angle which is suited for spherical symmetry and hence for the far field of the dipole.

A detailed discussion of the transformation can be found in Ref. [49] and Ref. [52] in the case of a 1D multilayer structure. Here, I give the corresponding form in the case of patterned layers. Note that in the case of an unfolded source, all the power emitted at the source is carried by harmonic $\mathbf{G} = 0$.

Using the normalization conventions of Eq. 6.56, the power emitted at the source to the right and the left in the infinitesimal angle $d\varphi$ is simply expressed as:

$$\begin{aligned} \text{right} \rightarrow \quad d\mathcal{P}_{p,r} &= \int_{\theta=0}^{\pi/2} \left(|E^{+}_{G=0,p,r}|^2 - |E^{-}_{G=0,p,r}|^2\right) \sin(\theta) d\theta d\varphi \\ \text{left} \rightarrow \quad d\mathcal{P}_{p,l} &= \int_{\theta=0}^{\pi/2} \left(|E^{-}_{G=0,p,l}|^2 - |E^{+}_{G=0,p,l}|^2\right) \sin(\theta) d\theta d\varphi \end{aligned} \tag{6.58}$$

The total emission at the source in $d\varphi$ is the sum of both contributions, $d\mathcal{P}_{p,r} + d\mathcal{P}_{p,l}$. The total power emitted at the source is obtained by integrating this value over φ (in practice, by summing over a discrete number of calculations):[13]

---

[12] Neglecting possible local field effects... This point would certainly call for a longer discussion but is out of the context of the present work. Fortunately, in our case, in-plane dipoles do not lead to a direct paradox when they are moved across horizontal interfaces. On the other hand, when vertical dipoles are included, their emitted power is *discontinuous* at such interfaces. The key to this paradox probably lies in the way the polar field screens the charges in the vicinity of the dipole.

[13] One should be careful in this integration: in a triangular lattice PhC, the additional presence of a dipole breaks the sixfold symmetry of the PhC: for instance all ΓM directions are not equivalent, so that the calculation can not simply be reduced to $\varphi \in [0; \pi/6]$.

$$\mathcal{P}_{source} = \int_{\varphi=0}^{2\pi} d\mathcal{P}_{p,r} + d\mathcal{P}_{p,l} \tag{6.59}$$

As already stated, an important property of the normalisation taken in Eq. 6.56 is that the value of $\mathcal{P}_{source}$ is equal to n_s in bulk (when one sums the contributions of horizontal dipoles along x and y, in order to obtain an averaged horizontal dipole). This means that, in general, $\mathcal{P}_{source}$ is simply *equal* to the inverse of the spontaneous emission lifetime modification of the dipole with respect to air, or *Purcell effect*:

$$\mathcal{P}_{source} = \tau_0/\tau = F_p \tag{6.60}$$

Here τ_0 is the lifetime of a dipole in air. Of course, this Purcell effect should be used with caution: emission in air is taken as a reference. Therefore, F_p is composed of two effects: change of the index of the source (which increases the 'bulk density of modes', and contributes to F_p by a factor n_s) *and* modification of the photonic density of states by the structuration (multilayers, patterning...). In general, one is rather interested in the modification of lifetime between an dipole in bulk of index n_s and a multilayer structure with a PhC patterning. In this case, the relevant reference is the emission in bulk, and F_p should be divided by n_s:

$$F_p^{ref=bulk} = \frac{F_p^{ref=air}}{n_s} \tag{6.61}$$

As regards the power emitted by the source outside of the structure to the right (similar expressions hold to the left), the contribution of each harmonic can be distinguished. We introduce the polar angle of each harmonic in the right medium:

$$\sin(\theta_{G,right}) = \frac{\left|\mathbf{k}_{//} + \mathbf{G}\right|}{n_{right} k_0} \tag{6.62}$$

We can then define the power emitted to the right (corresponding to layer N), in the infinitesimal angle $d\varphi$, by harmonic $\mathbf{G}$:

$$d\mathcal{P}_{G,right} = \int_{\theta_{G,right}=0}^{\pi/2} \left(\frac{n_{right}}{n_s}\right)^3 \left(\frac{cos(\theta_{G,right})}{cos\theta_s}\right)^2 |E^+_{G,N,r}|^2 \sin(\theta_{G,right}) d\theta_{G,right} d\varphi \tag{6.63}$$

Note that the coefficient intervening in this expression is not trivial. As already mentioned, it stems from the transition between plane-wave formalism and solid angle formalism − the reader is referred to Refs. [49, 52] for its demonstration in a 1D case, which is here generalized to a periodic medium.

The form of Eq. 6.63 is not very convenient, because each harmonic has to be integrated over its specific angle $\theta_{G,right}$. Besides, the infinitesimal integrand d$\theta_{G,right}$ needs to be found, and it is not constant even in the case where $d\theta$ is (that is, when θ is discretized on a uniform mesh). It is therefore more convenient to come back to an integration over the inner angle θ. To this effect, we differentiate Snell's law and obtain:

$$n_{right} d\theta_{G,right} \cos(\theta_{G,right}) = n_s d\theta \cos(\theta) \tag{6.64}$$

Eq. 6.63 can then be recast as:

$$d\mathcal{P}_{G,right} = \int_{\theta=0}^{\pi/2} |E^+_{G,N,r}|^2 \frac{n_{right} \cos(\theta_{G,right})}{n_s \cos(\theta)} \sin(\theta) d\varphi \tag{6.65}$$

This integration runs over solid angles of the inner angle, and is more convenient. For instance, for a given angle θ, one can compare this value to the power emitted by the source to determine what fraction of the emitted power is extracted to the right by a given harmonic.

The power emitted to the right in $d\varphi$ is the sum over the harmonics:

$$d\mathcal{P}_{right} = \sum_G d\mathcal{P}_{G,right} \tag{6.66}$$

Finally, the total power emitted to the right is the sum over φ:

$$\mathcal{P}_{right} = \int_{\varphi=0}^{2\pi} d\mathcal{P}_{right} \tag{6.67}$$

The light extraction efficiency of the structure is simply given by

$$\eta_{right} = \frac{P_{right}}{P_{source}} \tag{6.68}$$

It should be noted that even for an omnidirectional light extractor (e.g. when the whole FBZ is in the air cone), P_{source} can be different from $P_{left} + P_{right}$ if absorption is present in the materials. In this case, the missing power is lost by absorption.

Introduction of artificial absorption In some situations, light emitted at an angle θ remains trapped in the structure. This is the case if no PhC is present (true guided modes) but also in the presence of a PhC, if some Bloch modes are under the light lines of air and substrate. Such modes correspond to a discrete real value of θ and cause a numerical difficulty: their density of state is a Dirac function which can't be resolved by a discrete meshing of θ.

In 1D multilayer structures, this problem is routinely dodged by a simple trick: a very small imaginary part n'' is added to the refractive index of some guiding layers. In this case, guided modes acquire a finite lifetime and the delta function is broadened into a Lorentzian, as described in Chapter 3, section 3.1.1. They can then be treated numerically. Provided the broadening is small compared to the separation between guided modes, the emitted power does not depend on the value of n'', and does represent the actual power emitted in the limit of non-absorbing material.

When a PhC is present, the same trick can be used, but with some care. Especially, in the case of a PhC with small extraction efficiency, this artificial absorption may dominate the extraction effect of the PhC for some leaky modes. This has two consequences. First, the angular width of the corresponding peaks is then set by absorption rather than by the extraction efficiency of the PhC. Second, the value of $\mathcal{P}_{right}$ and $\mathcal{P}_{left}$ obtained in this case is wrong: some modes are counted as absorbed rather than extracted. One may still estimate the extraction efficiency by integrating the power at the source over the angles where extraction is possible.

On the other hand, introduction of a small n'' can be convenient because it broadens peaks, so that a coarser mesh can be used when discretizing θ, leading to faster calculations. Moreover, taking the mere value of the extraction efficiency, one sometimes misses a crucial fact: the extraction length of the modes. In some cases, the extraction is close to 1, but with a PhC of infinite extent. This is especially the case in some structures studied in this thesis, where low-order Bloch modes are extracted over an unacceptable distance. In this case, one can use n'' to artificially introduce a limit extraction length. Modes whose extraction is too large are absorbed, and no longer counted as extracted.

Fig. 6.11 gives an example of dipole emission calculation in the following structure: a GaN waveguide ($n = 2.5$) of total thickness a embedded in air, etched to a depth $0.5a$ by a triangular lattice PhC ($f = 0.5$). A horizontal dipole sheet polarized along y is placed midway in the unetched

GaN core, and emits light at a frequency $u = 0.4$.[14] The calculation is performed along the ΓM direction perpendicular to the dipole, e.g. along x.

Beyond the critical angle, the source emits in two guided modes (narrow and sharp peaks, observed because a small imaginary part $n'' = i.10^{-4}$ is added to the index of GaN) and in a leaky mode (broader peak close to $\theta = 60^o$). The leaky mode is extracted to air by harmonic (-1) along ΓM, as can be seen on the outer emission diagram. Moreover, it is interesting to notice that there is a small cusp in the *direct* emission (e.g. light emitted directly in the light cone) at the angle of extraction of the leaky mode. This feature can be seen as an analogous to a Wood anomaly for light emission.

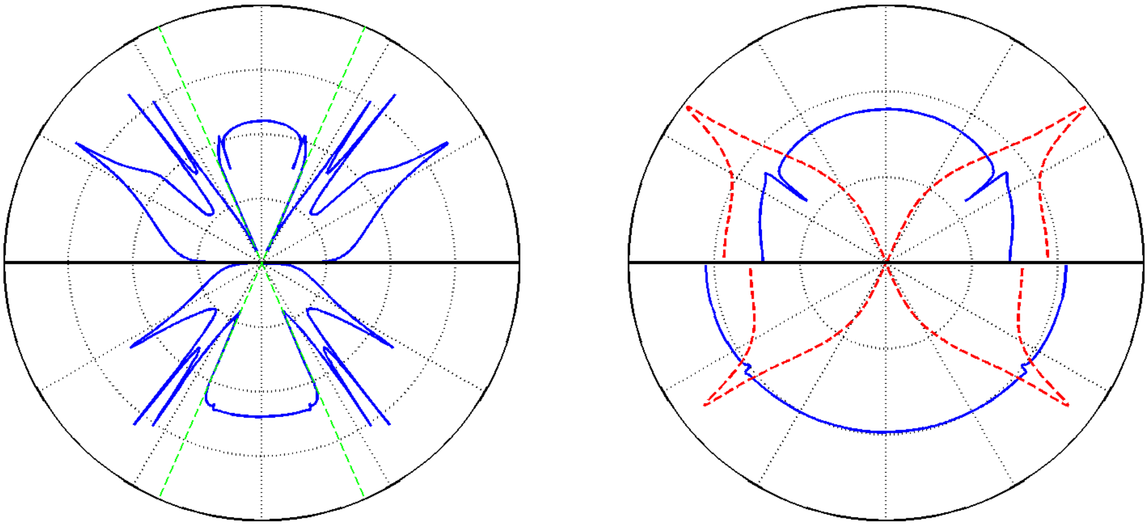

Figure 6.11: Power emission of a point dipole in a patterned multilayer (log scale). (Left) Emission at the source (the top corresponds to the side etched by the PhC, the horizontal line to the x axis). Dotted lines: critical angle of the GaN/air interface. Two guided modes and a leaky mode are present beyond the critical angle. (Right) Emission outside the structure, to top and bottom respectively. Full lines: direct emission by the harmonic $G = 0$. This is very similar to the emission in an unpatterned structure, except for the cusp at the position of the leaky mode. Dashed lines: extraction by the harmonic $G = 1$ along ΓM. The leaky mode is extracted around $\theta = 50^o$.

This closes our discussion of applications of the FMM.

---

[14] As already mentioned, modeling a dipole sheet (rather than a point dipole) corresponds to the unfolded form of the source term, Eq. 6.51.

6.3.4 A note on energy conservation:

It is often argued in literature that energy is analytically conserved by the FMM, regardless of the number of harmonics involved.[53] For instance, in the case of a reflectivity calculation, the sum of all scattered efficiencies is always equal to one. In the case of a Bloch mode calculation, the sum of outgoing and reflected power is equal to the incoming power. This is usually convenient because energy balance can be estimated even with a small number of harmonics, but it also implies that energy conservation cannot be used as a criterion for numerical convergence.

However when the FFF is used, the matrices lose their hermiticity, as argued in Chapter 5, section 5.4.4. This means that energy balance is no longer verified: for instance, the sum of all scattered efficiencies may be smaller or larger than one. This can be circumvented by using the hermitian form of the FFF described in Chapter. 5. Alternately, one may take advantage of this and use energy conservation to estimate numerical convergence, because violations to energy conservation tend to zero when the number of harmonics is increased.

This effect is illustrated on Fig. 6.12 for a reflectivity calculation. The energy conservation reads $R+T=1$, but this is not exactly verified with the 'original', non-hermitian FFF form. More specifically, violations to energy conservation are stronger when the incoming wave is nearly resonant with a leaky mode – this is the case on Fig. 6.12.

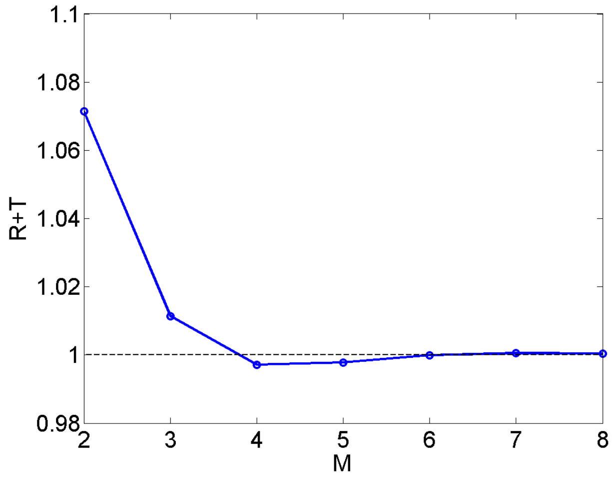

Figure 6.12: Energy conservation (R+T) with the 'original' FFF expression (full line) and with the symmetrized FFF (dashed line) as a function of truncation order. The calculation is performed for the same structure as in Fig. 6.7, and for $sin(\theta) = 0.583$, which corresponds to the excitation of a leaky mode of the structure.

6.3.5 Computation of the electromagnetic fields in the structure

In all of the above calculations (either when computing reflectivity or eigenmodes), one only gets access to the amplitude of the fields at the boundaries of the structure, $\mathcal{A}_{in}$ and $\mathcal{A}_{out}$, with:

$$\mathbb{S}^{-1}\mathcal{A}_{out} = \mathcal{A}_{in} \tag{6.69}$$

If one wants to obtain the fields everywhere inside the system, one has to use again the partial $\mathbb{S}$-matrices of the system. As this procedure is not described in [47], I will explicit it here.[15] As

---

[15] Of course, one could also consider using $\mathbb{T}$-matrices, in which case the fields can be built immediately from the boundary fields. However, the numerical stability issues evoked earlier cause the same difficulties, and the resulting fields diverge rapidly, even for a very accurate value of the boundary fields.

above, the principle consists in avoiding matrices where growing exponentials intervene and using their inverses instead.

Amplitudes

First, starting from the field amplitudes on the right of the last $(N-1/N)$ interface, one gets the amplitudes on the left of this interface by using the interface matrix $\mathbb{T}_{N-1,N}$:

$$\left| \begin{array}{l} \mathcal{A}^+_{N-1,r} \\ \mathcal{A}^-_{N-1,r} \end{array} \right. = \mathbb{T}_{N-1,N} \left| \begin{array}{l} \mathcal{A}^+_{N,l} \\ \mathcal{A}^-_{N,l} \end{array} \right. \tag{6.70}$$

One can then propagate $\mathcal{A}^-_{N-1,r}$ to the left until interface $(N-2)/(N-1)$, because only decaying exponentials are involved in this propagation:

$$\mathcal{A}^-_{N-1,l} = \phi^+_{N-1}\mathcal{A}^-_{N-1,r} \tag{6.71}$$

One then deduces $\mathcal{A}^+_{N-1,l}$ by using $\mathbb{S}_{N-1}$ (which has already been computed when building the total $\mathbb{S}$-matrix) :

$$\left| \begin{array}{l} \mathcal{A}^+_{N-1,l} \\ \mathcal{A}^-_{0,l} \end{array} \right. = \mathbb{S}_{N-1} \left| \begin{array}{l} \mathcal{A}^+_{0,l} \\ \mathcal{A}^-_{N-1,l} \end{array} \right. \tag{6.72}$$

Thus, one went from the amplitudes $\mathcal{A}_{N,l}$ to $\mathcal{A}_{N-1,l}$, without using any unstable ϕ^- matrix. By iterating this procedure, one gets $\mathcal{A}$ at all the interfaces of the system. Finally, one gets the amplitudes at any point z *inside* layer n (of thickness L) by using:

$$\begin{array}{rcl} \mathcal{A}^+_n(z) & = & \hat{\phi}^+_n\mathcal{A}^+_{n,l} \\ \mathcal{A}^-_n(L-z) & = & \hat{\phi}^+_n\mathcal{A}^-_{n,r} \end{array} \tag{6.73}$$

Where $\hat{\phi}^+$ is the analogous of ϕ^+ for a propagation over a distance z:

$$\hat{\phi}^+ = e^{i\mathcal{K}z} \tag{6.74}$$

Fields

Once the amplitudes are known at any point z, one deduces the fields $E_{//}$ and $H_{//}$ by using the material matrix $\mathbb{F}$ in the corresponding layer:

$$\left| \begin{array}{l} E_{//}(z) \\ H_{//}(z) \end{array} \right. = \mathbb{F} \left| \begin{array}{l} \mathcal{A}^+(z) \\ \mathcal{A}^-(z) \end{array} \right. \tag{6.75}$$

Finally, one gets E_z et H_z. There are several ways to obtain E_z: from $E_{//}$ or $H_{//}$. Here, we make the first choice. For this, E_z is first decomposed as $E_z = E^+_z + E^-_z$. For a given k_z, the link between E^+_z and $E^+_{//}$ is (Ref. [47]):

$$E^+_{z,\mathbf{G}} = \sum_{\mathbf{G'}} Z^{-1}_{\mathbf{GG'}} k_z[(k_x + G'_x)E^+_{x,\mathbf{G'}} + (k_y + G'_y)E^+_{y,\mathbf{G'}}] \tag{6.76}$$

A similar relation links E^-_z to $E^-_{//}$. Let us now introduce the matrix:

$$\mathcal{C}_z = \left(\begin{array}{cc} Z^{-1}(k_x + G'_x) & Z^{-1}(k_y + G'_y) \end{array} \right) \tag{6.77}$$

Eq. 6.76 takes the matrix form:

$$E_z^+(z) = \mathcal{C}_z \mathcal{E} \mathcal{K} \mathcal{A}^+(z) \tag{6.78}$$

And similarly for E_z^-. Therefore, E_z can be linked to $\mathcal{A}$:

$$\left| \begin{array}{c} E_z^+(z) \\ E_z^-(z) \end{array} \right. = \left(\begin{array}{cc} \mathcal{C}_z \mathcal{E} \mathcal{K} & -\mathcal{C}_z \mathcal{E} \mathcal{K} \end{array} \right) \left| \begin{array}{c} \mathcal{A}^+(z) \\ \mathcal{A}^-(z) \end{array} \right. \tag{6.79}$$

As regards H_z, it is simply linked to $E_{//}$ by Maxwell's equations:

$$\partial_x E_y - \partial_y E_x = i\omega\mu_0 H_z \tag{6.80}$$

Therefore, the plane wave coefficients directly verify:

$$H_z = \frac{1}{k_0} \left(\begin{array}{cc} -(k_y + G_y) & (k_x + G_x) \end{array} \right) \left| \begin{array}{c} E_x \\ E_y \end{array} \right. \tag{6.81}$$

6.3.6 Comparison with the hybrid method

The main goal of this implementation was to check the accuracy of the hybrid method I developed during the thesis. To exemplify the comparison between both methods let us consider a structure made of a $1.5a$-thick GaN membrane in air, etched to a depth $0.5a$ by a triangular PhC of filling factor 0.3. The fundamental pseudo-TE mode of this structure is studied by both the FMM and the hybrid method, using the same plane-wave cutoff $N_G = 81$ and the FFF implementation (for the hybrid method, the vertical step is $0.02a$). As can be seen on Fig. 6.13, the real part of the wavevector (k') is nearly identical for both methods (the relative error on the effective index is less than 10^{-5}). The imaginary part of the wavevector (k'') is also very similar for both methods: here, the relative error is about 10^{-3}. This is very satisfying considering that k'' is already a correction to k', by three orders of magnitude. The residual disagreement is likely to be due to the spatial discretization of the hybrid method.

As regards numerical efficiency, the FMM is clearly less demanding: as any semi-analytical method, its computational burden is greatly relieved by the fact that only two dimensions are discretized at the same time. However, this advantage is somehow limited by two points. First, the 2D PWE in each layer requires *all* the eigenvalues to be found (whereas in the hybrid method only a few eigenvalues of the very large and sparse matrix are needed). Second, construction of the $\mathbb{S}$-matrix requires numerous matrix inversions, an expensive operation in terms of memory and computation time. In the end, the number of discretization points which can be used in the FMM is certainly superior than for the hybrid method, but not by a power 3/2 as could naively be expected.

The main advantage I found in using the hybrid method lies in its *insensitivity to boundary conditions.* This has already been discussed: even though only one Bloch mode is accurately computed at a time, the other eigenvalues of the large matrix are usually reasonably close to actual Bloch modes. This is very useful for the strongly multimode structures studied in this thesis: it means that one can obtain a good idea of the overall dispersion for dozens of mode in one calculation. This proved to be very convenient when fitting the experimental results, because the fits had to account for the dispersion of all modes at the same time. Of course, if better convergence is requested for a given mode, it still has to be computed individually.

One could hope that the FMM displays a similar property: indeed, in the pole-tracking method described earlier, the correction to the pole's frequency (or wavevector) is the smallest eigenvalue of a matrix. Therefore, one could expect that other small eigenvalues of this matrix lead to other Bloch

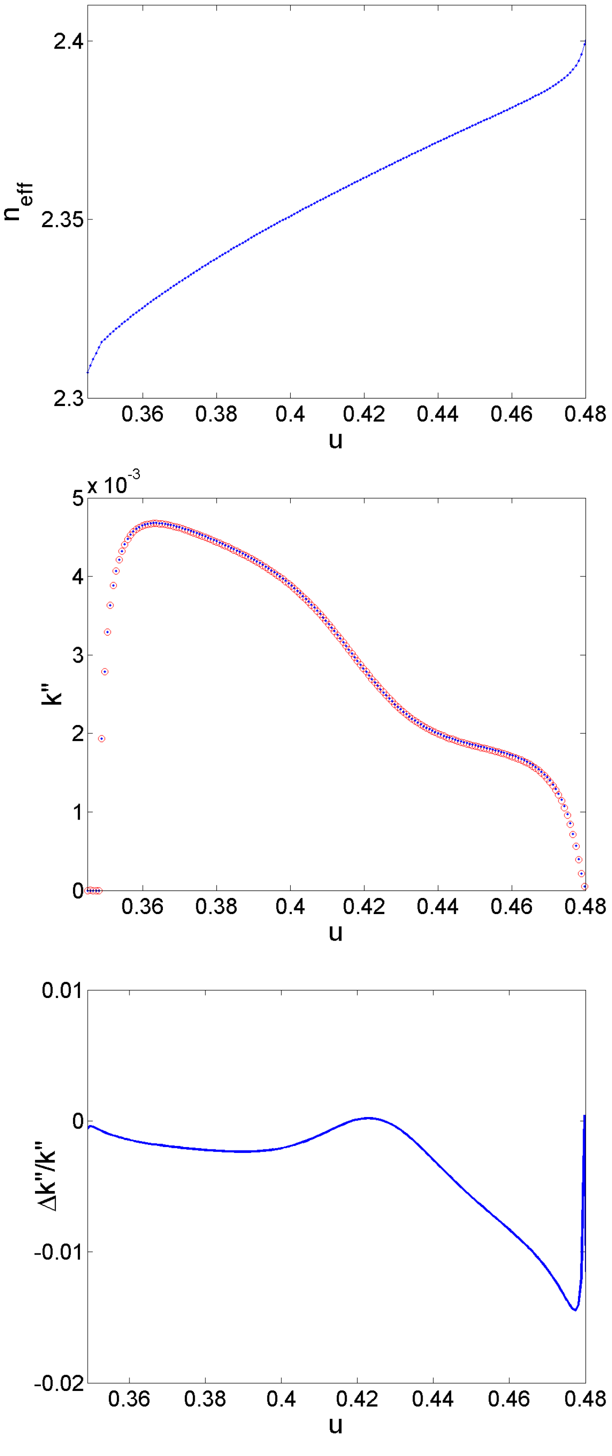

Figure 6.13: (Top) Effective index of the fundamental TE mode obtained by the hybrid method (full line) and the FMM (dots): the difference is indistinguishable. (Middle) Imaginary part of the wavevector. The mode enters the light cone at $u \sim 0.345$ and reaches the end of the Brillouin zone at $u = 0.48$. Dots: hybrid method, Circles: FMM. (Bottom) Relative error between the two methods on k''.

modes. Unfortunately, this is not the case. This is evidenced on Fig. 6.14, where the FMM is used to

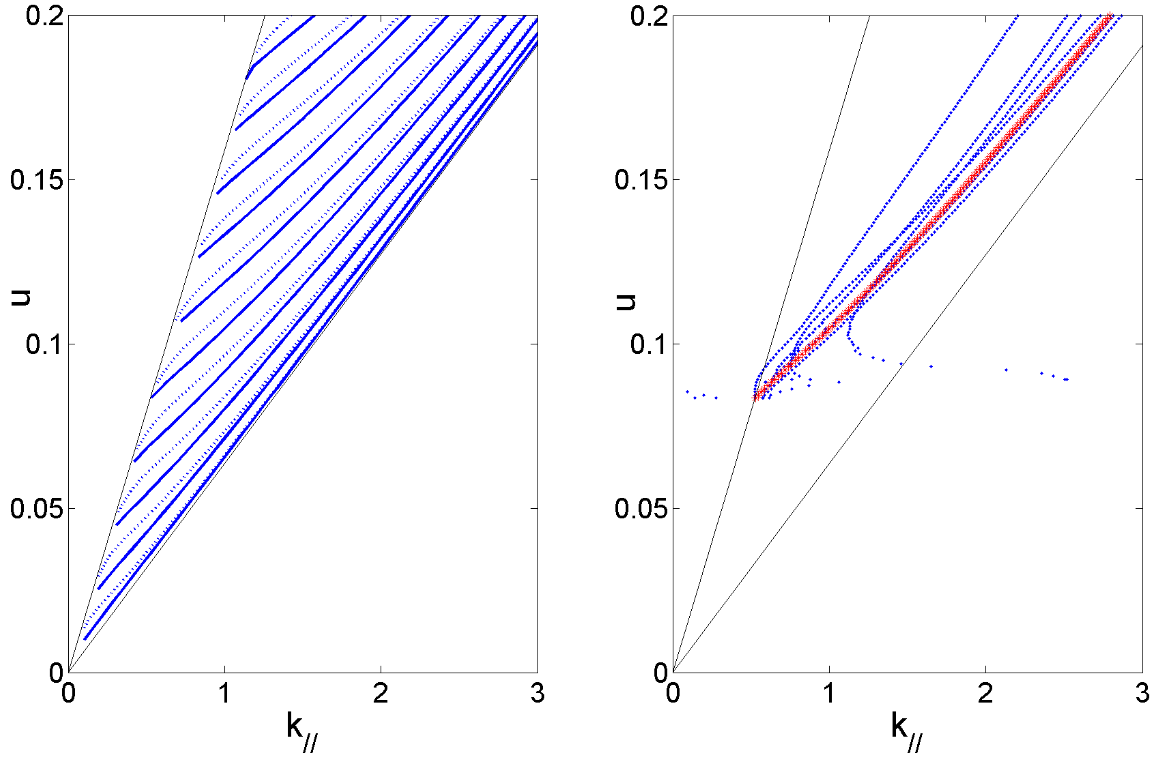

Figure 6.14: Modeling of a thick GaN PhC structure using the FMM. The structure consists of a GaN layer of thickness $6a$ etched to a depth a by a triangular lattice PhC of filling factor 0.3, with air substrate and superstrate. (left) Actual dispersion of the Bloch modes: the structure supports up to 10 TE modes (full lines) and 10 TM modes (dotted lines). A computation is needed for each Bloch mode. (right) Computation of only one mode (mode TE5, plotted as red stars) where the other eigenvalues of Eq. 6.43 are also plotted (blue dots): these do not correspond to any other Bloch mode.

model a thick GaN layer. If one plots several of the eigenvalues of Eq. 6.43, they do not correspond to any of the Bloch modes supported by the structure. This may be due to the fact that in the FMM the fields are propagated exponentially in the analytic direction, which would account for the sensitivity to the input value of ω. This limitation of the FMM is not just a matter of convenience: all modes of Fig. 6.14 could easily be obtained "manually" because there was no anticrossing at such low frequencies. However, above the light cone where many anticrossings occur, it becomes very difficult to follow a given band at a time, and therefore account for the total band structure.

As a conclusion, the hybrid method is a precious tool for analysis of multimode structures. Its accuracy was confirmed by comparison with the FMM. Due to its memory requirements, it is limited to structures with somewhat limited photonic effects where few plane waves (in the range of 100-200) are required for good convergence. It was thus efficient for modeling the structures studied during this thesis. For structures which demand many harmonics −such as PhC waveguides which request a supercell and display strong photonic interactions− a semi-analytic method such as the FMM is preferable.

Bibliography

[1] K. S. Yee. Numerical solution of initial boundary value problems involving Maxwells equations in isotropic media. *IEEE Transactions on Antennas and Propagation*, AP14(3):302–307, 1966.

[2] J. P. Berenger. A perfectly matched layer for the absorption of electromagnetic-waves. *Journal of Computational Physics*, 114(2):185–200, 1994.

[3] S. G. Johnson and J. D. Joannopoulos. Block-iterative frequency-domain methods for maxwell's equations in a planewave basis. *Optics Express*, 8(3):173–190, 2001.

[4] S. Y. Shi, C. H. Chen, and D. W. Prather. Plane-wave expansion method for calculating band structure of photonic crystal slabs with perfectly matched layers. *Journal of the Optical Society of America a-Optics Image Science and Vision*, 21(9):1769–1775, 2004.

[5] E. Moreno, D. Erni, and C. Hafner. Band structure computations of metallic photonic crystals with the multiple multipole method. *Physical Review B*, 65(15), 2002. 155120.

[6] D. Felbacq, G. Tayeb, and D. Maystre. Scattering by a random set of parallel cylinders. *Journal of the Optical Society of America a-Optics Image Science and Vision*, 11(9):2526–2538, 1994.

[7] G. Tayeb and D. Maystre. Rigorous theoretical study of finite-size two-dimensional photonic crystals doped by microcavities. *Journal of the Optical Society of America a-Optics Image Science and Vision*, 14(12):3323–3332, 1997.

[8] T. Wriedt. A review of elastic light scattering theories. *Particle and Particle Systems Characterization*, 15(2):67–74, 1998.

[9] K. Busch, S. F. Mingaleev, A. Garcia-Martin, M. Schillinger, and D. Hermann. The Wannier function approach to photonic crystal circuits. *Journal of Physics-Condensed Matter*, 15(30):R1233–R1256, 2003.

[10] L. C. Andreani and M. Agio. Photonic bands and gap maps in a photonic crystal slab. *IEEE Journal of Quantum Electronics*, 38(7):891–898, 2002.

[11] D. Gerace and L. C. Andreani. Disorder-induced losses in photonic crystal waveguides with line defects. *Optics Letters*, 29(16):1897–1899, 2004.

[12] R. Petit. *Electromagnetic Theory of Gratings*, volume 22 of *Topics in Current Physics*. Springer-Verlag, 1980.

[13] M. Neviere and E. Popov. *Light propagation in periodic media - Differential theory and design.* Optical Engineering. Marcel Dekker, New York, 2003.

[14] M. Neviere and P. Vincent. Differential-theory of gratings - answer to an objection on its validity for TM polarization. *Journal of the Optical Society of America a-Optics Image Science and Vision*, 5(9):1523–1524, 1988.

[15] D. Maystre. New general integral theory for dielectric coated gratings. *Journal of the Optical Society of America*, 68(4):490–495, 1978.

[16] E. Popov and M. Neviere. Grating theory: new equations in fourier space leading to fast converging results for TM polarization. *Journal of the Optical Society of America a-Optics Image Science and Vision*, 17(10):1773–1784, 2000.

[17] D. Maystre. Electromagnetic study of photonic band gaps. *Pure and Applied Optics*, 3(6):975–993, 1994.

[18] B. Gralak, S. Enoch, and G. Tayeb. Anomalous refractive properties of photonic crystals. *Journal of the Optical Society of America a-Optics Image Science and Vision*, 17(6):1012–1020, 2000.

[19] E. Popov, M. Neviere, B. Gralak, and G. Tayeb. Staircase approximation validity for arbitrary-shaped gratings. *Journal of the Optical Society of America a-Optics Image Science and Vision*, 19(1):33–42, 2002.

[20] E. Popov and B. Bozhkov. Differential method applied for photonic crystals. *Applied Optics*, 39(27):4926–4932, 2000.

[21] E. Popov and M. Neviere. Maxwell equations in fourier space: A fast-converging formulation for diffraction by arbitrary shaped, periodic, anisotropic media. *Journal of the Optical Society of America a-Optics Image Science and Vision*, 18(11):2886–2894, 2001.

[22] T. Tamir, A. A. Oliner, and H. C. Wang. Wave propagation in sinusoidally stratified dielectric media. *IEEE Transactions on Microwave Theory and Techniques*, MT12(3):323–335, 1964.

[23] L. F. Li. Justification of matrix truncation in the modal methods of diffraction gratings. *Journal of Optics a-Pure and Applied Optics*, 1(4):531–536, 1999.

[24] M. G. Moharam and T. K. Gaylord. Rigorous coupled wave analysis of surface gratings with arbitrary profiles. *Journal of the Optical Society of America*, 71(12):1573–1573, 1981.

[25] M. G. Moharam and T. K. Gaylord. Diffraction analysis of dielectric surface-relief gratings. *Journal of the Optical Society of America*, 72(10):1385–1392, 1982.

[26] M. G. Moharam and T. K. Gaylord. 3-dimensional vector coupled-wave analysis of planar-grating diffraction. *Journal of the Optical Society of America*, 73(9):1105–1112, 1983.

[27] Z. Y. Li and L. L. Lin. Photonic band structures solved by a plane-wave-based transfer-matrix method. *Physical Review E*, 67(4), 2003. Part 2 046607.

[28] Q. Cao, P. Lalanne, and J. P. Hugonin. Stable and efficient Bloch-mode computational method for one-dimensional grating waveguides. *Journal of the Optical Society of America a-Optics Image Science and Vision*, 19(2):335–338, 2002.

[29] J. P. Hugonin and P. Lalanne. Perfectly matched layers as nonlinear coordinate transforms: a generalized formalization. *Journal of the Optical Society of America a-Optics Image Science and Vision*, 22(9):1844–1849, 2005.

[30] L. F. Li and C. W. Haggans. Convergence of the coupled-wave method for metallic lamellar diffraction gratings. *Journal of the Optical Society of America a-Optics Image Science and Vision*, 10(6):1184–1189, 1993.

[31] J. Chandezon, M. T. Dupuis, G. Cornet, and D. Maystre. Multicoated gratings - a differential formalism applicable in the entire optical-region. *Journal of the Optical Society of America*, 72(7):839–846, 1982.

[32] G. Granet, J. Chandezon, and O. Coudert. Extension of the c method to nonhomogeneous media: Application to nonhomogeneous layers with parallel modulated faces and to inclined lamellar gratings. *Journal of the Optical Society of America a-Optics Image Science and Vision*, 14(7):1576–1582, 1997.

[33] M. Neviere, M. Cadilhac, and R. Petit. Applications of conformal mappings to diffraction of electromagnetic waves by a grating. *IEEE Transactions on Antennas and Propagation*, AP21(1):37–46, 1973.

[34] R. Scarmozzino, A. Gopinath, R. Pregla, and S. Helfert. Numerical techniques for modeling guided-wave photonic devices. *IEEE Journal of Selected Topics in Quantum Electronics*, 6(1):150–162, 2000.

[35] P. Lalanne and J. P. Hugonin. Numerical performance of finite-difference modal methods for the electromagnetic analysis of one-dimensional lamellar gratings. *Journal of the Optical Society of America a-Optics Image Science and Vision*, 17(6):1033–1042, 2000.

[36] J. Ctyroky, S. Helfert, R. Pregla, P. Bienstman, R. Baets, R. De Ridder, R. Stoffer, G. Klaasse, J. Petracek, P. Lalanne, J. P. Hugonin, and R. M. De La Rue. Bragg waveguide grating as a 1d photonic band gap structure: Cost 268 modelling task. *Optical and Quantum Electronics*, 34(5):455–470, 2002.

[37] P. Bienstman and R. Baets. Optical modelling of photonic crystals and VCSELs using eigenmode expansion and perfectly matched layers. *Optical and Quantum Electronics*, 33(4-5):327–341, 2001.

[38] P. Bienstman and R. Baets. Advanced boundary conditions for eigenmode expansion models. *Optical and Quantum Electronics*, 34(5):523–540, 2002.

[39] S. F. Mingaleev and K. Busch. Scattering matrix approach to large-scale photonic crystal circuits. *Optics Letters*, 28(8):619–621, 2003.

[40] L. C. Botten, T. P. White, A. A. Asatryan, T. N. Langtry, C. M. de Sterke, and R. C. McPhedran. Bloch mode scattering matrix methods for modeling extended photonic crystal structures. i. theory. *Physical Review E*, 70(5), 2004. Part 2 056606.

[41] A. A. Asatryan, K. Busch, R. C. McPhedran, L. C. Botten, C. M. de Sterke, and N. A. Nicorovici. Two-dimensional Green's function and local density of states in photonic crystals consisting of a finite number of cylinders of infinite length. *Physical Review E*, 63(4), 2001. Part 2 046612.

[42] Y. Xu, R. K. Lee, and A. Yariv. Quantum analysis and the classical analysis of spontaneous emission in a microcavity. *Physical Review A*, 61(3):art. no.–033807, 2000. 033807.

[43] S. Hughes and H. Kamada. Single-quantum-dot strong coupling in a semiconductor photonic crystal nanocavity side coupled to a waveguide. *Physical Review B*, 70(19), 2004. 195313.

[44] S. Hughes, L. Ramunno, J. F. Young, and J. E. Sipe. Extrinsic optical scattering loss in photonic crystal waveguides: Role of fabrication disorder and photon group velocity. *Physical Review Letters*, 94(3), 2005. 033903.

[45] L. F. Li. Formulation and comparison of two recursive matrix algorithms for modeling layered diffraction gratings. *Journal of the Optical Society of America a-Optics Image Science and Vision*, 13(5):1024–1035, 1996.

[46] D. M. Whittaker and I. S. Culshaw. Scattering-matrix treatment of patterned multilayer photonic structures. *Physical Review B*, 60(4):2610–2618, 1999.

[47] S. G. Tikhodeev, A. L. Yablonskii, E. A. Muljarov, N. A. Gippius, and T. Ishihara. Quasiguided modes and optical properties of photonic crystal slabs. *Physical Review B*, 66(4), 2002. 045102.

[48] N. A. Gippius and S. G. Tikhodeev. Efficient computational technique for resonances in photonic crystal slabs (poster presentation at PECS VI, Aghia Pelagia, Crete), 2005.

[49] H. Benisty, R. Stanley, and M. Mayer. Method of source terms for dipole emission modification in modes of arbitrary planar structures. *Journal of the Optical Society of America a-Optics Image Science and Vision*, 15(5):1192–1201, 1998.

[50] H. Rigneault, F. Lemarchand, and A. Sentenac. Dipole radiation into grating structures. *Journal of the Optical Society of America a-Optics Image Science and Vision*, 17(6):1048–1058, 2000.

[51] D. Delbeke, P. Bienstman, R. Bockstaele, and R. Baets. Rigorous electromagnetic analysis of dipole emission in periodically corrugated layers: the grating-assisted resonant-cavity light-emitting diode. *Journal of the Optical Society of America a-Optics Image Science and Vision*, 19(5):871–880, 2002.

[52] D. Ochoa. *Diodes electroluminescentes planaires a haut rendement d'extraction lumineuse*. PhD thesis, EPFL, 2001.

[53] P. S. Russell. Power conservation and field structures in uniform dielectric gratings. *Journal of the Optical Society of America a-Optics Image Science and Vision*, 1(3):293–299, 1984.

Conclusion

During this thesis, I explored several *deterministic* strategies to obtain high-efficiency LEDs in GaN-based materials. The peculiarities of AlInGaN compounds, and especially of their epitaxial requirements, appeared as determining and led to different optimal solutions than in conventional III-V semiconductors.

The first path I considered was that of Microcavity LEDs, because of the solid theoretical framework already developed to describe these light sources over the two past decades. Here, the rather low refractive index of GaN proves to be beneficial to performances. On the other hand, in part because of the absence of good DBRs, MCLEDs with an ultimate efficiency request a complex fabrication process which involves bonding to a new substrate and removal of the initial sapphire substrate. Very thin MCLEDs obtained by this method could be characterized, and evidenced the peculiar emission properties of thin-film LEDs. However, the complexity and low yield of the process – especially the need for a very high precision on layers thickness – prevented a quantitative demonstration of high efficiency MCLEDs. These difficulties lead me to conclude that a new fabrication strategy is necessary if MCLEDs GaN are to be considered as a viable option. In any case, even the best structure would still not fully address the issued of light extraction because at least 50% of the light remains guided in the GaN layer.

Faced with the unavoidable strong light emission into these guided modes, I then considered the use of photonic crystals to diffract these modes into air. While this phenomenon had already been studied quite extensively in the past, quantitative description of the approach was still rather scarce – especially in the context of optimizing a light emitter. Moreover, application of the concept to GaN-based structures was still in its infancy, with very little existing work discussing the possible specificities of photonic crystal extraction in GaN: most of the published results consisted in experimental demonstrations of PhC-LEDs which lacked an analysis of the underlying mechanisms.

The first experimental results obtained during this thesis outlined the peculiarities linked to the thickness of GaN LEDs: the conventional shallow-etch approach which is successfully used in other materials can not straightforwardly be applied in GaN, because such photonic crystals interact poorly with a large fraction of the guided light. It appeared that a multimode view was relevant to describe the behavior of the PhC and tackle its optimization.

I then explored several possible strategies to optimize the efficiency of a PhC extractor. As regards the crystal lattice, the study of Archimedean tilings confirmed their potential as an omnidirectional light extractor. Other efforts were rather devoted to the 'vertical' (or epitaxial) direction, where the need for optimization is most stringent due to the multimode nature of the problem. First, the distribution of guided modes was tailored by modifying the epitaxial layers, so that all guided modes could interact well with the PhC. The proof of concept of this approach was demonstrated, although full optimization was hindered by the difficulty to grow the desired structures. Second, I considered more advanced structures where the microcavity and the PhC approach were combined. The regime of strong photonic interaction reached in these thin devices opens promising perspectives because it moves away from the loose optical confinement of previous schemes, where photonic interaction is barely sufficient to extract light efficiently. However, in this case as well, fabrication difficulties still remain a challenge.

More recently, I was also involved in two other projects which push this principle further, and strongly modify the optical environment of the LEDs. Lateral Epitaxial Overgrowth LEDs combine the modification of guided modes distribution with a structure which is well adapted to large-scale, high-power LEDs. However, the fabrication limitations which will eventually set the efficiency of such devices still need to be assessed. Efficient luminescence from deeply patterned layers is a surprising result which adds to the unusual properties of GaN. It opens new perspectives for very strong photonic interaction, where the PhC serves not only as a grating but also to modify the emission lifetime and strongly alter the photonic density of states. Here, the experimental and theoretical work are just beginning.

Throughout this thesis, the experimental work was sustained and guided by rigorous modeling of the optical properties of photonic structures. Various tools were implemented to this effect, and a specific method was developed to treat the case of thick GaN structures, whose study is challenging with conventional methods. Important efforts were also directed to alleviate the computational burden of photonic calculations. The efficient interplay between modeling and experiments confirm the soundness of a deterministic approach: it may eventually yield light sources which not only efficiently emit light, but emit it in a controlled and tailored fashion.

Overall, the general trend suggested by the results of this thesis is that light extraction from GaN is hindered by the poor control one initially has on light generation, mainly because of the thickness of the layers. Therefore, a need appears to control more strongly the photonic behavior of the structures. This regime of strong photonic interaction enables a more direct influence on light emission, but it also relies on more complex physical phenomena and more advanced fabrication. The challenges, both theoretical and technological, increase accordingly. Therefore, the commercial potential of the methods presented in this thesis still remains as an open question, but with good prospects in my opinion. In particular, the efficient use of modeling as a diagnosis and design tool opens promising perspectives toward ultimately controlled light sources, which may eventually be designed to emit light efficiently with a predetermined radiation pattern.

Appendix A

Power flow of a Bloch mode

Here, we derive various quantities which enable us to describe the power flow and loss channels of a Bloch mode. The electric field of the Bloch mode is of the form:

$$\mathbf{E} = \sum_G \mathbf{E}_G(z) e^{i(\mathbf{k}_{//}+\mathbf{G})\cdot\mathbf{r}} \tag{A.1}$$

For simplicity, we assume that the Bloch mode is propagating along x (e.g. $k_{//}$ is parallel to x). We look for the various power flows of the Bloch mode through a plane yz located at $x = 0$. This corresponds either to a problem where the PhC is infinite and we look for power flows at an arbitrary value of x, or to a problem where the medium for $x < 0$ is a 'black box' where the field continuity conditions are matched, so that the Bloch mode can be fed in the $x > 0$ region. This has the interest of giving us access to intrinsic quantities of the Bloch mode, rather than coupling efficiencies which necessarily depend on the incoming field.

First, let us notice that whenever one considers a Poynting vector related to the Bloch mode, all crossed terms involving two different harmonics $\mathbf{G}$ and $\mathbf{G}'$ contain a term of the form:

$$e^{i(\mathbf{G}-\mathbf{G}')\cdot\mathbf{r}} \tag{A.2}$$

Which averages out to zero when the Poynting vector is integrated over y. Therefore, each harmonic can be considered as independent in power-related calculations. We now divide the harmonics of the Bloch mode into three categories: forward, backward, and leaky. Forward and backward harmonics are defined by the sign of their wavevector along x:

$$\begin{aligned} k_{//} + Gx > 0 &\quad \rightarrow \quad \text{Forward} \\ k_{//} + Gx < 0 &\quad \rightarrow \quad \text{Backward} \end{aligned} \tag{A.3}$$

Leaky harmonics are those whose vertical wavevector k_z is propagative, either in the substrate or the superstrate. Fig. A.1 depicts the three kinds of modes, and the integration box used for power calculations. This box starts at $x = 0$ and extends to $x = \infty$. It extends to all space in the y and z direction.

First, let us consider a non-leaky harmonic (p). We call ϕ_p^x the flow of the Poynting vector through an infinite vertical cross-section located at $x = 0$, with a sign convention such that ϕ_p^x is always positive:

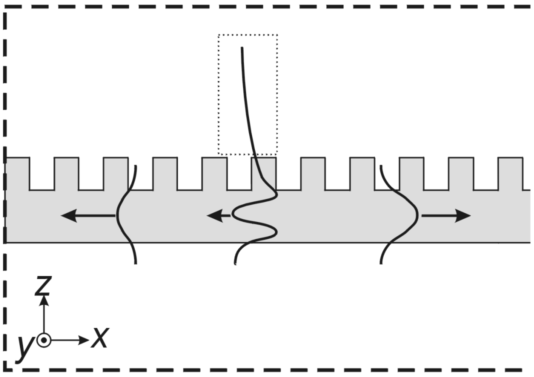

Figure A.1: From left to right, backward, leaky-backward, and forward harmonics of a Bloch mode. The large dashed box is the integration box.

$$\begin{aligned}
\text{Forward} \quad &\rightarrow \quad \phi_p^x = +\int_{-\infty}^{\infty} \Pi_{p,x} dydz \\
\text{Backward} \quad &\rightarrow \quad \phi_p^x = -\int_{-\infty}^{\infty} \Pi_{p,x} dydz \\
\text{With:} \quad \Pi_{p,x} = &\quad Re(\mathbf{E}_{p,y} \cdot \mathbf{H}^*_{p,z} - \mathbf{H}_{p,y} \cdot \mathbf{E}^*_{p,z})
\end{aligned} \tag{A.4}$$

Let us now come to leaky harmonics. Firts, it is worth commenting on their exponential decay outside of the structure in the z direction (dotted box in Fig. A.1). As shown on Fig. A.2, the energy of the Bloch mode decays exponentially in the x direction, with a decay constant $1/2k''$. Moreover, *at a given time and x position*, the power radiated outside through a vertical cross-section Σ_1 stems from the power radiated *at an earlier time* through a horizontal cross-section Σ_2. This explains the exponential decay of leaky harmonics outside of the structure. In this example, the leaky harmonic propagates backward. If it propagated forward on the other hand, the profile of the leaky harmonic would *increase* exponentially with z because power emitted at an earlier time would propagate forward. Such diverging exponential are not unphysical, they simply corresponds to energy emitted by the Bloch mode in an infinite time.

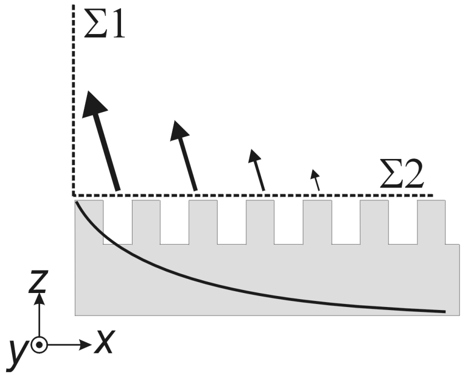

Figure A.2: Inside the structure, the power of the Bloch mode decays along x like $exp(-x/2k'')$. Therefore, the power radiated at a given time by a leaky harmonic through the horizontal section Σ_2 also decays along x. This power then propagates backwards in the $-x$ direction and reaches the vertical section Σ_1 at a later time. Hence, the intensity of the leaky harmonic along Σ_1 decreases with z, because it stems from power radiated at a larger x.

This discussion also shows that for a leaky harmonic, power flows can be calculated by taking the flow of the Poynting vector through Σ_1 and Σ_2. Since we are interested in vertical radiation, it is more intuitive to use horizontal sections like Σ_2 in the case of leaky harmonics. More precisely, we consider sections as depicted on Fig. A.3.

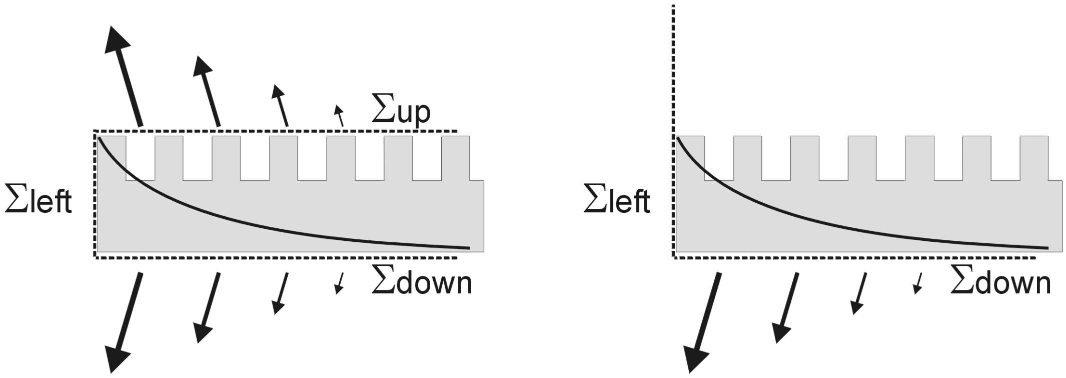

Figure A.3: Sections used for energy flow calculations for a leaky mode. (Left) If the mode is leaky both in the substrate and superstrate, three sections are used. (Right) If the mode is only leaky in the substrate, only two sections are needed: the evanescent half of the leaky mode is treated in Σ_{left}.

We can then define ϕ_p^x, $d\phi_{up}^x$ and $d\phi_{down}^x$ for a leaky mode:

$$\begin{aligned}
\phi_p^x &= \pm\int_{\Sigma_{left}} \Pi_{p,x}\, dydz \\
d\phi_p^{up} &= \int_{\Sigma_{up},x=0} \Pi_{p,z}\, dy \\
d\phi_p^{down} &= \int_{\Sigma_{down},x=0} \Pi_{p,z}\, dy
\end{aligned} \tag{A.5}$$

Again, the sign of ϕ_p^x is always positive. We can now introduce $\mathcal{P}_{in}$, $\mathcal{P}_{ref}$, $d\mathcal{P}_{up}$ and $d\mathcal{P}_{down}$:

$$\begin{aligned}
\mathcal{P}_{in} &= \sum_{p|Forward} \phi_p^x \\
\mathcal{P}_{ref} &= \sum_{p|Backward} \phi_p^x \\
d\mathcal{P}_{up} &= \sum_{p|Leaky} d\phi_p^{up} \\
d\mathcal{P}_{down} &= \sum_{p|Leaky} d\phi_p^{down}
\end{aligned} \tag{A.6}$$

$\mathcal{P}_{in}$ is the flow of *incoming* power on the integration box from the left, and $\mathcal{P}_{ref}$ is the flow of *outgoing* power, or in other words the *reflected* power. Therefore, the reflexion coefficient R of a Bloch mode is given by:

$$R = \mathcal{P}_{out}/\mathcal{P}_{in} \tag{A.7}$$

For instance, for a non-leaky Bloch mode inside a band gap (and in the absence of absorption), we have $R = 1$ which is simply an expression of energy conservation.

The fraction of the Bloch mode's power which is radiated upwards (resp. downwards) per unit length (e.g. per period a) is:

$$\begin{aligned} u &= d\mathcal{P}_{up}/\mathcal{P}_{in} \\ d &= d\mathcal{P}_{down}/\mathcal{P}_{in} \end{aligned} \tag{A.8}$$

The *total* fraction of the Bloch mode's power which is radiated upwards (resp. downwards) is then obtained by integrating this quantity along x, which just yields a factor $1/2k''$ because all harmonics have the same amplitude dependence $\sim exp(-x/2k'')$. If we call U (resp D) this quantity, we have:

$$\begin{aligned} U &= \int_x u.dx = \frac{d\mathcal{P}_{up}}{2k''\mathcal{P}_{in}} \\ D &= \int_x d.dx = \frac{d\mathcal{P}_{down}}{2k''\mathcal{P}_{in}} \end{aligned} \tag{A.9}$$

When the Bloch mode is lossy, no energy can escape of the box (even at $x = \infty$). Energy conservation then simply reads:

$$R + U + D = 1 \tag{A.10}$$

In principle, this is always verified in a coupled-wave approach, because the numerical problem is haermitian and hence conserves energy (even when the infinite plane wave basis is truncated). Therefore, energy conservation can't be used as a check for energy balance, only as a check for possible errors in the code. There is a possible exception when the FFF is written in a non-hermitian way. In this case, energy balance is not analytically verified, and can inddeed be used as a convergence criterion.

As an example, we reproduce here Fig. 3.10. It is interesting to note that the reflexion coefficient rises just before the reaching the light line, and then collapses. This is due to the fact that, around the light line, harmonic (-1) is always strong.[1] Therefore, as long as it is not leaky, its power is counted as reflected power. Once the light line is reached, the same power is counted as radiated and R goes down.

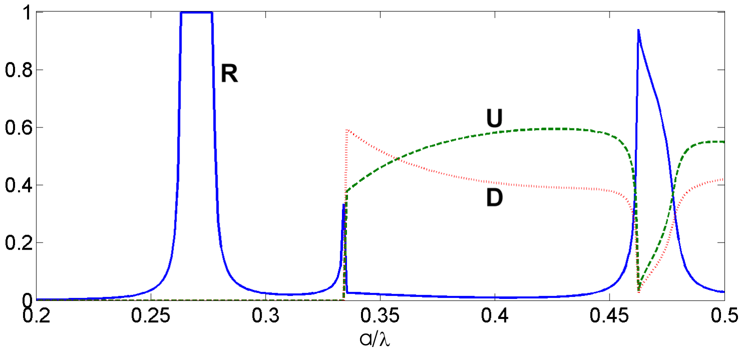

Figure A.4: Balance of power a Bloch mode in a 1D grating. For $a/\lambda > 0.25$, the reflection coefficient increases and reaches 1 in the band gap. For $a/\lambda \sim 0.33$, the Bloch mode crosses the light line and becomes lossy. We then have R+U+D=1.

---

[1] Indeed, harmonic (-1) crosses the light line precisely when a new Bloch mode reaches cutoff and becomes propagative inside the PhC. There is always a mini-stop band, of varying strength, at this point.

When R is very small (in practice, everywhere outside of band gaps), the energy balance also takes an interesting form:

$$k'' = \frac{1}{2\mathcal{P}_{in}} \sum_p d\phi_p^{up} + d\phi_p^{down} \tag{A.11}$$

This equation gives the contribution of each radiative channel (e.g. each harmonic (p) which radiates upwards and/or downwards) to the total decay constant of the Bloch mode k''.

In the case where the refractive index in the structure has an imaginary part, the Bloch mode experiences material absorption upon propagating. Again, it is possible to give a modal expression of this absorption ([1, 2]). We denote the complex refractive index as $n = n' + in''$, and introduce $d\mathcal{P}_{abs}$:

$$d\mathcal{P}_{abs} = 2k_0 \int n'.n''.|\mathbf{E}_p|^2 \tag{A.12}$$

$d\mathcal{P}_{abs}$ is then the equivalent of $d\mathcal{P}_{up}$ for absorption: the fraction of the Bloch mode's power which is absorbed per unit length is:

$$\mathrm{a} \;=\; d\mathcal{P}_{abs}/\mathcal{P}_{in} \tag{A.13}$$

Likewise, the *total* fraction of the Bloch mode's power which is absorbed upwards (resp. downwards) is obtained by integrating a along x:

$$A \;=\; \int_x \mathrm{a}.dx = \frac{d\mathcal{P}_{abs}}{2k''\mathcal{P}_{in}} \tag{A.14}$$

The conservation of energy then reads:

$$R + U + D + A = 1 \tag{A.15}$$

An example of energy balance in the case of absorption in metal is given in Fig. 4.51 of Chapter 4.

Appendix B

Wurtzite and zinc-blende Hamiltonians

In this annex, we discuss the electronic band structures of semiconductors and their consequences for optical properties. We begin with a simple presentation of general properties. We then study the well-known case of zinc-blende crystals and derive the corresponding emission diagrams for optical transitions. Finally, we come to the case of wurtzite crystals (which applies to AlInGaN compounds); we compare their properties with those of zinc-blende crystals and discuss the peculiar case of nonpolar GaN.

B.1 Band structure and optical properties: basic discussion

B.1.1 Energy bands of a crystal

The electron wavefunctions in the bands of a semiconductor crystal are solutions of Schrödinger's equation:

$$H\psi = \left(\frac{\mathbf{p}^2}{2m} + V\right)\psi = E\psi \tag{B.1}$$

In a bulk semiconductor, the solutions are simply Bloch modes:

$$\psi = e^{i\mathbf{k}\cdot\mathbf{r}}u(\mathbf{k},\mathbf{r}) \tag{B.2}$$

Where $\mathbf{k}$ is the electron's wavevector and u is the *periodic part of the Bloch function* (PPBF). In most semiconductor heterostructures, one makes the assumption that u is a slowly varying function of $\mathbf{k}$ (at least in the vicinity of $\mathbf{k}$=0, where electrons are usually located) and hence lets $u(\mathbf{k},\mathbf{r}) \approx u(0,\mathbf{r}) \approx u(\mathbf{r})$. In this approximation, it can be shown that solutions of Eq. B.1 are of the form:

$$\psi = F(r)u(\mathbf{r}) \tag{B.3}$$

$F(r)$ is the so-called *envelope function* and the corresponding approximation is called the envelope approximation.

In the energy range of interest in a semiconductor (i.e. around the band gap), the solutions of Eq. B.1 have the following general properties:

- They are divided in distinct energy bands. There exist an energy range (the band gap) where no solution exists, and hence no electron can propagate in the crystal at such energies (Fig. B.1).
- At zero temperature, the bands located below the gap (*valence bands*, VB) are fully filled with electrons while the bands located above the band gap (*valence bands*, CB) are empty.

- Electrons can hop from the VB to the CB (leaving holes behind them), for instance due to finite temperature or to the absorption of a photon. Likewise, they can fall back in th VB by emitting a photon.

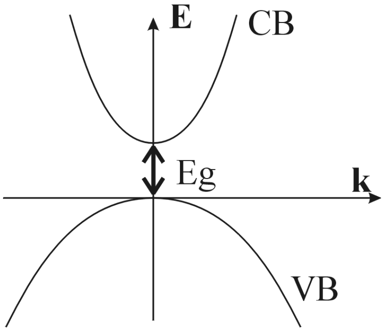

Figure B.1: Schematic dispersion of a semiconductor. **k** is the total electron's wavevector and E_g the gap. Close to the Γ point, the dispersion of the bands is roughly parabolic. In realistic cases, the valence band is usually composed of several degenerate bands.

In order to fully determine the band structure of a realistic semiconductor, one needs to fully diagonalize the corresponding Hamiltonian. This leads to heavy calculations as the Hamiltonian is large (typically 6 × 6 or 8 × 8) in order to account for all bands couplings, and all the material parameters of the semiconductor must be used. While calculations for the CB are usually simple (thanks to the use of an effective mass approximation), the VB is more complex to treat. This is because one usually starts from a 'simple' semiconductor without interactions where the valence band is made of several degenerate bands; when interactions are subsequently 'plugged in', the degeneracy is lifted (see below) and the formerly degenerate bands interact strongly.

B.1.2 Optical transitions in a semiconductor

Let us consider the interaction between an electron in a semiconductor crystal and a photon. This corresponds to the absorption of a photon with energy $\hbar\omega$ and the transition of an electron from the VB to the CB, or to the symmetric process (i.e. spontaneous emission). The matrix element for this process can be obtained from Fermi's golden rule and is (Ref. [3]):

$$\left|H'\right|^2 = \left(\frac{q\mathcal{A}}{2m_0}\right)^2 \left|\langle u_c|\,\mathbf{e}\cdot\mathbf{p}\,|u_v\rangle\right|^2 \left|\langle F_c|F_v\rangle\right|^2 \tag{B.4}$$

In this expression, $\mathcal{A}$ is the amplitude of the photon's vector potential and **e** its unit polarisation vector; m_0 is the free electron mass, and **p** the momentum operator of the electron. F_c and F_v are the envelope functions of the electron in the conduction and valence bands (in the case of a bulk semiconductor, these are just plane waves as in Eq. B.2); u_c and u_v are the corresponding PPBF.

Thus, it appears that several factors govern the strength of an optical transition: the polarization of the photon, the overlap properties of the PPBF (coupled by the momentum operator) and the overlap of the envelope functions.

B.1.3 Basis for the periodic part of the Bloch functions

As has been said, full determination of a semiconductor's band structure is a complex task. However, it appears from Eq. B.4 that a number of useful trends can be obtained from the symmetry properties of the periodic part of the Bloch functions at the Γ point (i.e. $\mathbf{k} = 0$). We will follow this approach here.

To his effect, let us for now consider a bulk semiconductor in the absence of either spin-orbit coupling or built-in electric field. In general, the various bands of the semiconductor can be characterized by their symmetry at the Γ point ($\mathbf{k} = 0$). Because crystal bands can be interpreted as originating from atomic orbitals (in a LCOA approach), one often describes their symmetry properties in analogy with those of atomic orbitals.

If we quantize the orbital momentum along an arbitrary axis z, the conduction band corresponds to a state with total agular momentum J=1/2 (Γ_6 group symmetry). Therefore, it is not degenerate (apart from a twofold spin degeneracy), and the PPBF possess s-like symmetry (that is, it is even with respect to x, y and z).

The valence band, on the other hand, corresponds to a total momentum J=3/2 and is threefold symmetric (sixfold including spin). In analogy with the p orbital atomics of a hydrogen atom, one can choose a *basis* of PPBF with p_x, p_y and p_z symmetries respectively. Here, we denote these states as $|X\rangle$, $|Y\rangle$ and $|Z\rangle$. Besides, if we include spin, each of these states is twofold-degenerate: the basis becomes $\left\{|X\rangle, |Y\rangle, |Z\rangle, |\bar{X}\rangle, |\bar{Y}\rangle, |\bar{Z}\rangle\right\}$ where the first three states have spin up and the three last states have spin down.

When the specific details (interactions) of the Hamiltonian are 'plugged in', the degeneracy of the valence band is lifted. The eigenstate of the Hamiltonian can then be expressed in the former basis. Group theory enables us to deduce useful properties, depending on the symmetry of the new hamiltonian. In the following, we will apply this approach to two specific cases: the zinc-blende and wurtzite hamiltonians.

B.2 Zinc-blende structure

The results and notations of this section summarize those of Refs. [3, 4]. Historically, the zinc-blende valence band structure was first solved by Luttinger (Ref. [5]). The corresponding Hamiltonian is called the Luttinger-Kohn Hamiltonian.

B.2.1 Bulk

For a bulk semiconductor with cubic zinc-blende structure, the spin-orbit coupling lifts the degeneracy of the valence band: instead of a triplet, the states split in a singlet and a doublet state, in analogy with the atomic singlet $|J=1/2\rangle$ and doublet $|J=3/2\rangle$.

The eigenstates of the Hamiltonian in presence of spin-orbit coupling become:

$$\begin{array}{lll}
\text{Heavy holes} & |u_{hh}\rangle = \left|\frac{3}{2},\frac{3}{2}\right\rangle = -\frac{1}{\sqrt{2}}\left(|X\rangle + i\,|Y\rangle\right) & |\bar{u}_{hh}\rangle = \left|\frac{3}{2},-\frac{3}{2}\right\rangle = \frac{1}{\sqrt{2}}\left(|\bar{X}\rangle - i\,|\bar{Y}\rangle\right) \\
\text{Light holes} & |u_{lh}\rangle = \left|\frac{3}{2},\frac{1}{2}\right\rangle = -\frac{1}{\sqrt{6}}\left(|\bar{X}\rangle + i\,|\bar{Y}\rangle - 2\,|Z\rangle\right) & |\bar{u}_{lh}\rangle = \left|\frac{3}{2},-\frac{1}{2}\right\rangle = \frac{1}{\sqrt{6}}\left(|X\rangle - i\,|Y\rangle + 2\,|\bar{Z}\rangle\right) \\
\text{Spin-Orbit} & |u_{so}\rangle = \left|\frac{1}{2},\frac{1}{2}\right\rangle = -\frac{1}{\sqrt{3}}\left(|\bar{X}\rangle + i\,|\bar{Y}\rangle + |Z\rangle\right) & |\bar{u}_{lh}\rangle = \left|\frac{1}{2},-\frac{1}{2}\right\rangle = \frac{1}{\sqrt{3}}\left(|X\rangle - i\,|Y\rangle - |\bar{Z}\rangle\right)
\end{array} \tag{B.5}$$

The first four states are degenerate at the Γ point. They are called heavy and light hole states respectively. The two last states are degenerate and are called spin-orbit holes. To each kind of hole corresponds a given effective mass, which can be obtained by fully diagonalizing the Hamiltonian.[1] The dispersion relation of a typical zinc-blende semiconductor is depicted in Fig. B.2.

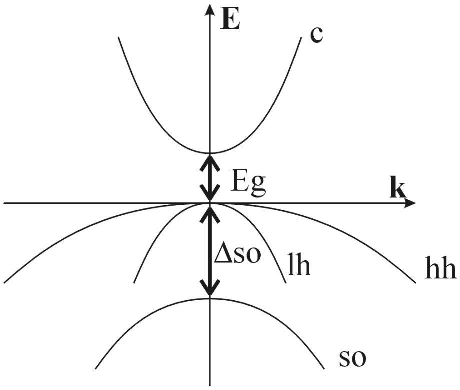

Figure B.2: Typical dispersion of a bulk zinc-blende semiconductor. **k** is the total electron's wavevector, E_g the gap and Δ_{so} the spin-orbit splitting.

From this figure, the meaning of 'heavy' and 'light' holes become clear: this refers to the effective mass of the holes around the Γ point. In GaAs for instance, $m_{hh} = 0.5 m_0$ and $m_{lh} = 0.08 m_0$ (m_0 being the free electron's mass). The spin-orbit band is shifted to a lower energy than the HH and LH bands. This spin-orbit splitting Δ_{so} is usually quite large (0.34 eV in GaAs). Therefore, only the top

---

[1] Actually, in realistic semiconductors the effective mass is not isotropic but this simple assumption is sufficient for the present discussion.

of the HH and LH bands are populated at usual temperatures and optical transitions involving the SO bands can be neglected, as we will do in the following.

B.2.2 Quantum Wells

Let us now come to the case of a quantum well heterostructure. Due to confinement in the quantum well, each energy band is shifted from its original level by an amount corresponding to its ground state energy level (Fig. B.3). Because of its higher effective mass, the shift (ϵ_{hh}) of the HH band is much smaller than that (ϵ_{lh}) of the LH band. Therefore, *the lowest energy transition in a quantum well corresponds to a conduction band to heavy hole band transition.* The energy of this transition is $E_g + \epsilon_c + \epsilon_{hh}$.

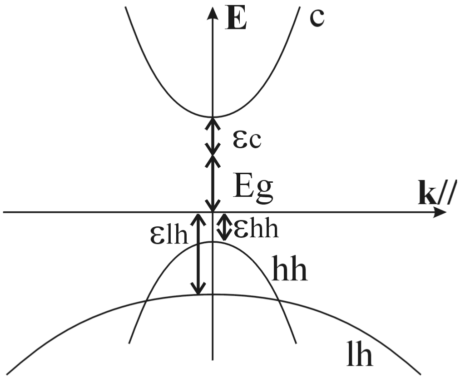

Figure B.3: Typical dispersion of the first confined levels in a zinc-blende quantum well: the degeneracy of the HH and LH bands is lifted. $\mathbf{k}_{||}$ is the in-plane electron's wavevector. ϵ_c, ϵ_{hh} and ϵ_{lh} are the confinement energies (i.e. the fundamental energy levels of the quantum well) for the conduction, HH and LH bands. Note that in a QW, the *in-plane* masses of the HH and LH are *light and heavy*, respectively! This leads to an anticrossing of these bands at $k \neq 0$.

It follows that, in first approximation, one can consider only these transition in optics experiments – of course, the accuracy of this approximation depends on the magnitude of the quantum well's energy shifts, and on the temperature (at high temperature, lower valence bands become populated). Below, we will study the angular dependence of this transition and see how it can be incorporated in electromagnetic modeling.

In addition, it should be noted that growth of a quantum well may be cause strain because of the lattice mismatch between the matrix and the well. This strains can further break the crystal symmetry, and therefore slightly mix the HH and LH PPBF at the Γ point. However, this phenomenon depends on the details of the semiconductor and is out of the scope of this general discussion.

B.2.3 Electromagnetic modeling of an electron-heavy hole transition

Periodic part of the transition matrix element

Let us now come back to Eq. B.4 and evaluate it in the case of an C-HH transition. We can write:

$$\mathbf{e} \cdot \mathbf{p} = -i\hbar \left(e_x \partial_x + e_y \partial_y + e_z \partial_z \right) \tag{B.6}$$

Due to the s-symmetry of u_c and to p-symmetry of $\{|X\rangle, |Y\rangle, |Z\rangle\}$, most components of $\langle u_c| \mathbf{p} |u_v\rangle$ vanish, except for three terms:

$$|\langle u_c| i\hbar\partial_x |X\rangle|^2 = |\langle u_c| i\hbar\partial_y |Y\rangle|^2 = |\langle u_c| i\hbar\partial_z |Z\rangle|^2 = \Pi \tag{B.7}$$

All three terms are equal, and are denoted (in absolute value) as Π, the *interband matrix element* of the semiconductor. The numerical value of Π can be determined experimentally. We are now ready to evaluate the periodic part of Eq. B.4:[2]

$$\begin{aligned} |\langle u_c|\,\mathbf{e}\cdot\mathbf{p}\,|u_{hh}\rangle|^2 &= \left|-\frac{1}{\sqrt{2}}\langle u_c|-i\hbar\,(e_x\partial_x+e_y\partial_y+e_z\partial_z)\,|X+iY\rangle\right|^2 \\ &= \frac{\Pi}{2}(e_x^2+e_y^2) \end{aligned} \tag{B.8}$$

Thus, we obtain the angular dependence of light emission (or absorption), which is a function of polarization. It is convenient to decompose it on the basis of TE and TM polarizations:

$$\begin{aligned} |\langle u_c|\,\mathbf{e}_{TE}\cdot\mathbf{p}\,|u_{hh}\rangle|^2 &= \frac{\Pi}{2} \\ |\langle u_c|\,\mathbf{e}_{TM}\cdot\mathbf{p}\,|u_{hh}\rangle|^2 &= \frac{\Pi}{2}cos(\theta)^2 \end{aligned} \tag{B.9}$$

Conveniently, these angular dependencies can easily be reproduced by those of in-plane electromagnetic dipole emitters.[6, 7] Namely, let us consider emission in a given direction (θ,φ). It can be verified that an in-plane dipole parallel to the unit vector u_φ emits TE-polarized light with an intensity which does not depend on θ (Fig. B.4). Likewise, an in-plane dipole perpendicular to the unit vector u_φ emits TM-polarized light with an intensity varying like $cos(\theta)^2$.

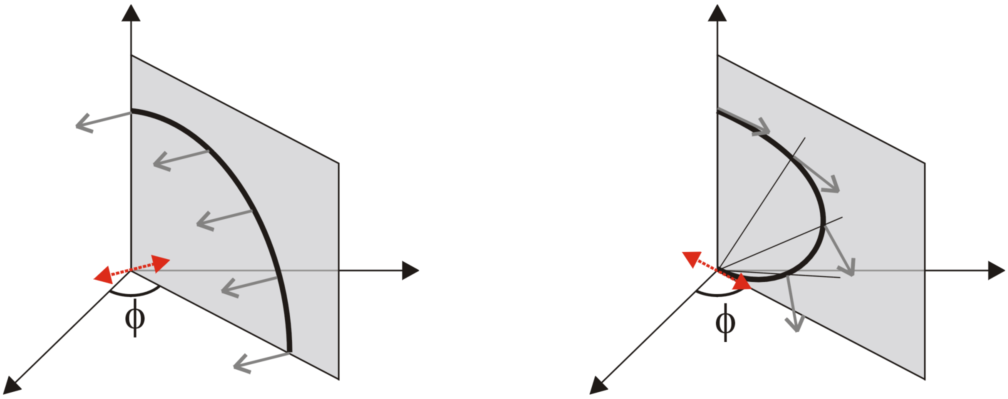

Figure B.4: Emission diagrams of dipoles (dotted arrows). The thick line represents the intensity of emission in a given direction, and the gray arrows the polarization of light. (Left) An in-plane dipole perpendicular to the plane of emission emits TE light with a constant intensity. (Right) An in-plane dipole parallel to the plane of emission emits TM light with an intensity $\sim cos(\theta)^2$.

The modeling of electron-hole recombinations by dipole source terms in $\mathbb{S}$-matrix calculations is based on this correspondence.

---

[2] Actually, we need to sum over transitions between spin up and spin down PPBF, but in the current case this simply leads to a factor of 2 which is included in the present result. Things are more subtle for C-LH transitions. See Ref. [3] p.518-519 for an accurate discussion.

Envelope part of the transition matrix element

For transitions in a quantum well, the term $\langle F_c|F_{hh}\rangle$ of H' also needs to be evaluated.[3] This overlap simply consists in an integral of the envelope wavefunctions in the z directions. As sketched in Fig. B.5, both wavefunctions are generally quite similar so that this overlap is close to 1.

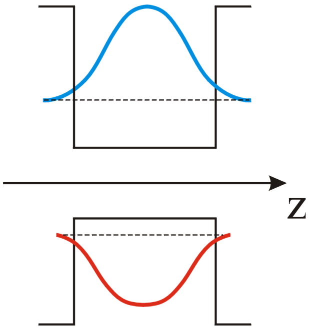

Figure B.5: Envelope wavefunctions of the fundamental levels of the conduction and heavy hole bands. Both functions are quite similar, leading to an overlap close to 1 (although their different penetrations in the barriers of the well make the overlap slightly smaller than 1).

---

[3] In general, the envelope function F_{hh} can be mixed with light holes terms when $\mathbf{k}_{\|} \neq 0$. However, this effect is neglectable for optical transitions because the in-plane wavevector of photons is very small, so that we always have $\mathbf{k}_{\|} \approx 0$.

B.3 Wurtzite structure

The wurtzite lattice corresponds to the stable structure of GaN under usual conditions. It is depicted on Fig. B.6. The Hamiltonian describing the wurtzite structure was established by Bir and Pikus, and is thus called the Bir-Pikus Hamiltonian.[8]

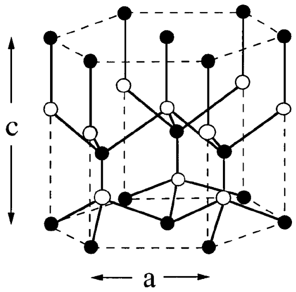

Figure B.6: [After Ref. [9]] Wurtzite crystal lattice, composed of two hexagonal closely packed lattices. Usually, GaN is grown along the c(0001) axis.

B.3.1 Bulk

There is a significant difference between zinc-blende and wurtzite lattices. In zinc-blende crystals, the three crystallographic axes x, y and z are equivalent whereas in wurtzite crystals the c-axis (the 'vertical' axis of the hexagon) is not equivalent to the 'in-plane' axes. This symmetry breaking, called *crystal field*, leads to a strong anisotropy in the band structure. One of the valence bands (the crystal field holes, or CH) is split from the two others by an amount Δ_{CF}. In bulk GaN $\Delta_{CF} \sim 10meV$ (Ref. [10]).

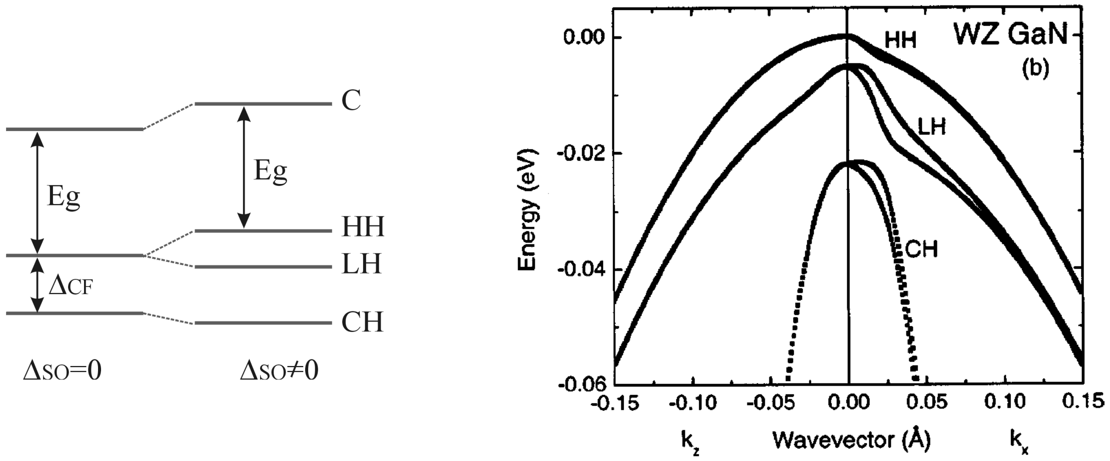

Figure B.7: (Left) [After Ref. [9]] The crystal field splits one of the valence bands. The spin-orbit interaction further splits the two remaining valence bands, yielding the three valence bands HH, LH and SH. (Right) [After Ref. [10]] Actual valence band structure of wurtzite GaN. Dispersions are different along z and the in-plane direction x because of the anisotropy of the lattice. Besides, note that the spin-degeneracy of each valence band is lifted: because of the crystal field, spins up and down are no longer equivalent. However, this effect is weak for the HH band and close to $\mathbf{k} = 0$.

The spin-orbit interaction further splits the two remaining bands in a heavy hole (HH) and a light hole (LH) bands (Fig. B.7). As for zinc-blende, since we are mainly interested in the lowest energy optical transitions, it will be sufficient for us to investigate the properties of the C-HH transition.

Let us insist on the difference with the zinc-blende case. In bulk zinc-blende crystals, the choice of the z-axis (the axis of quantification for the orbital momentum and spin) is arbitrary and the heavy and light hole bands are degenerate. In presence of a quantum well, the symmetry is broken. The z-axis is imposed as that perpendicular to the quantum well, and the degeneracy between heavy and light holes is lifted. In wurtzite crystals on the other hand, the symmetry is broken even in bulk and the z-axis is the c axis. This difference will be reflected in the polarization of luminescence in GaN.

As regards the PPBF in the valence band, they are of the following form (Ref. [9]):

$$\begin{array}{lll} \text{Heavy holes} & |u_{hh}\rangle = -\frac{1}{\sqrt{2}}\left(|X\rangle + i\,|Y\rangle\right) & |\bar{u}_{hh}\rangle = \frac{1}{\sqrt{2}}\left(|\bar{X}\rangle - i\,|\bar{Y}\rangle\right) \\ \text{Light holes} & |u_{lh}\rangle = -a\left(|\bar{X}\rangle + i\,|\bar{Y}\rangle\right) + b\,|Z\rangle & |\bar{u}_{lh}\rangle = a\left(|X\rangle - i\,|Y\rangle\right) + b\,|\bar{Z}\rangle \\ \text{Crystal holes} & |u_{so}\rangle = -b\left(|\bar{X}\rangle + i\,|\bar{Y}\rangle\right) - a\,|Z\rangle & |\bar{u}_{lh}\rangle = b\left(|X\rangle - i\,|Y\rangle\right) - a\,|\bar{Z}\rangle \end{array} \tag{B.10}$$

The precise form of coefficients a and b depends on the crystal's parameters and can be found in Ref. [9]. The most important point for us is to note that the PPBF for heavy holes are identical to those of the zinc-blende Hamiltonian (note that this is not the case for the LH and CH bands).

B.3.2 C-axis quantum wells, effect of built-in electric fields

Let us now consider the optical properties of a quantum well grown along the c-axis. Since the PPBF of the HH band is similar to that of zinc-blende, the periodic part of Eq. B.4 is unchanged. In other terms, the polarization properties of light emission depicted in Fig. B.4 still holds.

This result is often used during this thesis to argue that guided modes are mainly TE-polarized. This is also compatible with the experimental results obtained in the thesis. It is worth noting, however, that the LH band may mix with the HH band and contribute to optical transitions in the presence of strain, or if emitting regions of InGaN quantum wells are actually not fully planar.[4] Thus more accurate measurements would be desirable to estimate this mixing, although it is likely to be small at best.

Specifically, wurtzite Its existence leads to a strong anisotropy in the band structure.

On the other hand, the envelope part of Eq. B.4 deserves some attention. Again, the anisotropy of the Wurtzite structure along the c axis has a consequence here: the crystal is polar (the Ga and N atoms are partially charged) so that a macroscopic *spontaneous polarizationn field* appears. This bult-in polarization field is aligned with the c-axis. In addition, a piezoelectric polarization field may be caused by strain in the crystal.[11] This modifies the band structure as depicted on Fig. B.8.

As can be seen, the existence of this field strongly decreases the overlap integral $\langle F_c|F_{hh}\rangle$ because the electron and hole wavefunctions are confined to different sides of the quantum well. Incidentally, the energy of the optical transition is also significantly reduced with respect to what one would deduce in a flat band situation.

This low overlap integral implies a low radiative recombination rate. This is all the more true in wide quantum wells, a fact which is considered responsible for the collapsing internal quantum efficiency

---

[4] Indeed, the existence of In-rich clusters in InGaN quantum well is often suggested in literature to account for their high quantum efficiency in spite of their high dislocations density.

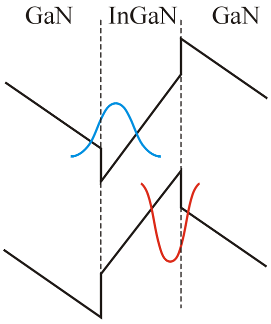

Figure B.8: Effect of the polarization fields on the bands of a heterostructure. Note that the sign of the field is opposite in the GaN and InGaN regions.

in low-energy (green) InGaN LEDs. Let us note that the strength of this effect is not fully assessed and may be mitigated by some phenomena, such as localization of carriers in In-rich clusters of the quantum well. Besides, current injection in an LED modifies the bands and may bring them closer to a flat-band situation (this is compatible with the experimental observation that the internal quantum efficiency initially *increases* with current density, before decreasing when the 'efficient' localized states are saturated).

B.3.3 Nonpolar quantum wells

Nonpolar GaN for increased quantum efficiency

In any case, it seems desirable to get rid of these piezoelectric fields which reduce the wavefunctions overlap, at least to some extent. For this reason, a number of teams actively pursue the growth of *nonpolar* GaN, e.g. GaN structures grown along other axes than the c-axis. Indeed, in this case the piezoelectric field is no longer perpendicular to the quantum well and the overlap of electron and hole wavefunctions is restored.

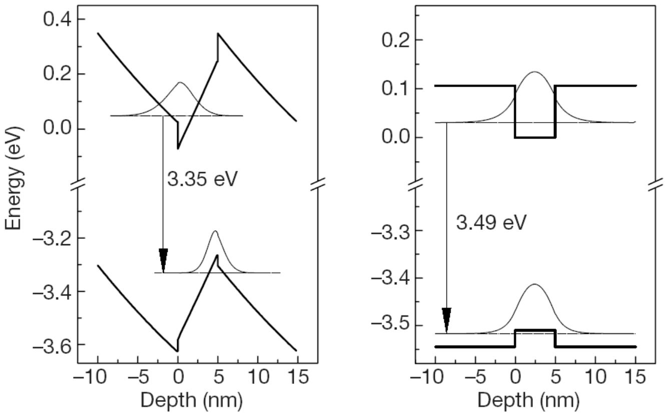

Figure B.9: [After Ref. [12]] Actual calculations of electron and hole wavefunctions in a c-plane quantum well (left) and an m-plane quantum well (right). In the m-plane quantum well, the wavefunctions overlap is restored and the transition energy is modified.

There have been numerous reports of optical experiments on nonpolar GaN in recent years - first in photoluminescence [12], and more recently in LEDs in a-plane [13] and m-plane [14] structures.

Polarized emission

In addition, nonpolar GaN possesses an unusual property: light emission from its top surface is strongly polarized. At normal incidence, the polarization is orthogonal to the *c*-axis.[15] It has often been argued that this property was desirable because it could lead to efficient, *polarized* light sources – a feature which is necessary in some applications like backlighting of LCD screens – without resorting to an external polarizer, which induces some losses (50% of the light in the worst case).

Let us account for this polarized emission and discuss its interest for a polarized light source. As has been explained, the z axis in the quantification of the PPBF of Eq. B.10 is fixed as the *c*-axis rather than the axis of the quantum well. Therefore, the emission diagram of C-HH transitions now has to be rotated by 90^o. Eq. B.9 becomes:

$$\begin{aligned} |\langle u_c|\,\mathbf{e}_{TE}\cdot\mathbf{p}\,|u_{hh}\rangle|^2 &= \frac{\Pi}{2} sin(\varphi)^2 \\ |\langle u_c|\,\mathbf{e}_{TM}\cdot\mathbf{p}\,|u_{hh}\rangle|^2 &= \frac{\Pi}{2}\left(cos(\theta)^2 cos(\varphi)^2 + sin(\theta)^2\right) \end{aligned} \tag{B.11}$$

The corresponding emission diagrams are depicted on Figs. B.10 and B.11, in two special cases. Again, they can be reproduced by the emission diagrams of two orthogonal dipoles perpendicular to the *c*-axis.

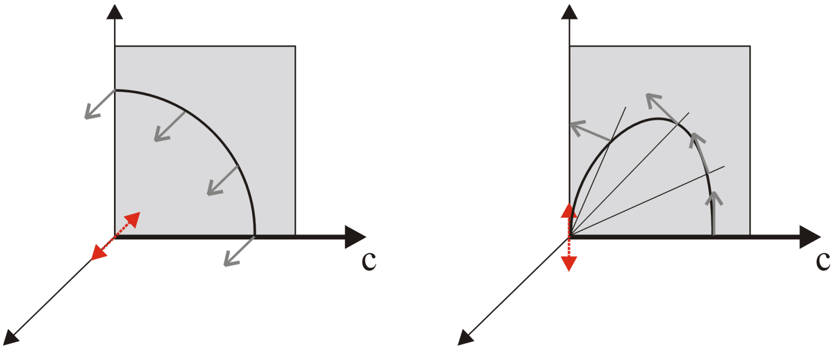

Figure B.10: Emission diagram when $\varphi = \pi/2$. (Left) TE emission corresponds to a dipole perpendicular to the *c*-axis and to the plane of emission. (Right) TM emission corresponds to a dipole perpendicular to the *c*-axis and parallel to the plane of emission.

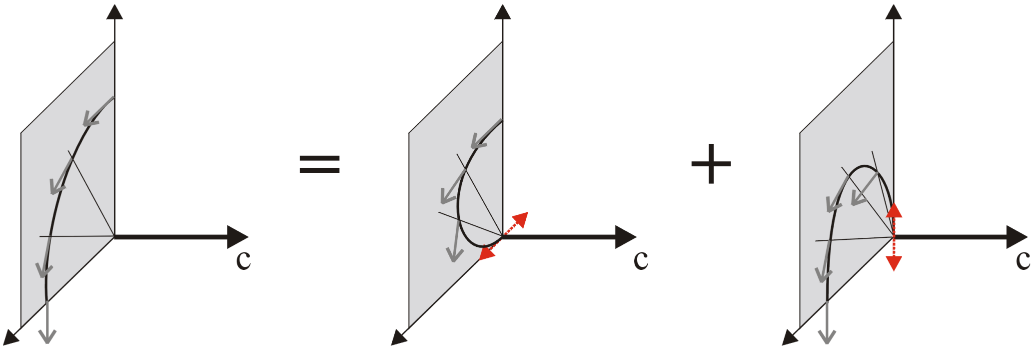

Figure B.11: (Left) Emission diagram when $\varphi = 0$. (Right) This emission diagram is once again the sum of two orthogonal dipoles perpendicular to the *c*-axis.

The polarization of emission in the z direction can be deduced from Eq. B.11 (or from Figs. B.10

and B.11). We find that light emitted at normal incidence has a polarization perpendicular to the c-axis, in agreement with experimental observations.

However, we also realize that *less light is now emitted* in the z direction! In the case of polar GaN, the dipoles responsible for emission lie in the quantum well plane so that they all emit light vertically. Here on the other hand one of the dipoles is perpendicular to the quantum well plane (e.g. vertical), and *does not* radiate any light vertically. Therefore, there is twice less light emitted in the z direction. On the other hand, much more light is now emitted into guided modes by the vertical dipole.[5] This intuitive 'dipole view' is sketched in Fig. B.12

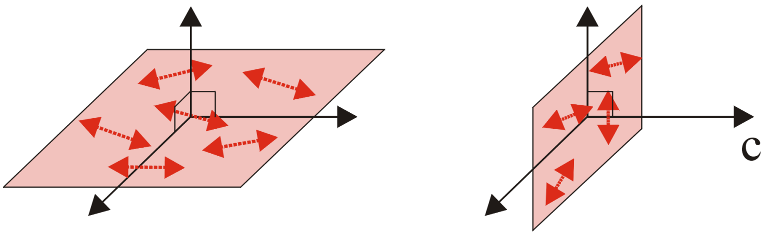

Figure B.12: (Left) In zinc-blende crystal and polar GaN the emitting dipoles all lie in the quantum well plane. (Right) In nonpolar GaN, the dipoles lie in a plane perpendicular to the c-axis.

From this, we conclude that although the internal quantum efficiency may be increased in nonpolar GaN, there is a price to this: the light extraction efficiency is now divided by two. This implies that the use of nonpolar GaN requires even more efforts in strategies for light extraction. Unfortunately, when guided light is extracted it is difficult to control its polarization state (random approaches such as roughening also randomize polarization, and 2D PhCs do not conserve polarization when diffracting light). Therefore, the advantage of nonpolar GaN as a naturally polarized light source seems questionable.

One should note that we have neglected all band-mixing effects (such as HH-LH mixing) which may for instance be produced by strain. Should these occur, their main effect would be to add a $|Z\rangle$ component to the HH PPBF u_{hh}. This in turn would add a dipole component parallel to the c-axis in the emission diagrams, thus mitigating the issue of reduced light extraction while reducing the polarization of vertically-emitted light.

---

[5] Besides, this guided light is now TM-polarized.

Appendix C

Carriers localization and source terms in Maxwell's equations

Here, we shortly discuss the impact of carriers localization on their emission properties. We aim at determining whtther light emitted in different directions $\mathbf{k}_{//}$ is coherent. It is interesting to note that this question has not aroused much interest in the past, probably because light emitted in different directions does not interfere in the far-field (except in experimental schemes like that of Ref. [16], see below), so that the question is irrelevant for simple emission from a semiconductor. In our case however, diffraction by the photonic crystal mixes different $\mathbf{k}_{//}$ so that we have to consider the question.

C.1 Quantum well

Let us first consider the case of carriers localized vertically in a quantum well, but with no in-plane localization (i.e. the quantum well is perfect, with no interface fluctuations). In this case, the in-plane dependence of an electron (or a hole) in the well is a plane wave:

$$\psi_{e,h} \sim e^{i\mathbf{k}_{//}\mathbf{r}} \tag{C.1}$$

For an electron-hole (e-h) pair to recombine radiatively, their wavevector $\mathbf{k}_{//}$ must match, so that a recombining e-h can be characterized by a single $\mathbf{k}_{//}$.

If the electron-hole pair forms an exciton (usually, this effect is only predominant at low temperature) the in-plane delocalization is reflected on the center-of-mass motion (CM) of the excition:

$$\psi_{CM} \sim e^{i\mathbf{k}_{//}\mathbf{r}} \tag{C.2}$$

Therefore, both in the case of a free e-h pair and of an exciton, the in-plane wavevector is well-defined (this simply reflects translation invariance). The photon produced in a radiative recombination carries this wavevector $\mathbf{k}_{//}$. Photons with different $\mathbf{k}_{//}$ are thus produced by different transitions, and are *incoherent.*

Therefore, when modeling emission from a quantum well, the *intensities* emitted at different $\mathbf{k}_{//}$ must be summed, to reflect this incoherence. This implies that source term calculations must be performed for each $\mathbf{k}_{//}$ independently, and their sum constitutes the total emission. Therefore, the 'unfolded' source described in Chapter 6, Section 6.3.3 should be used.

Of course, it may be argued that the in-plane dependence of an e-h pair can not exactly be a plane wave (either because the quantum well is perfect, or because e-h pairs have a finite lifetime anyway), but rather an enveloppe function with a characteristic wavevector K. However, our argument is valid as long as K is much larger than the typical free photon wavevector k_0 (this amounts to comparing the spatial extent of the wavefunction to the photon's wavelength). In other words, since only e-h pairs close to the Γ point can recombine radiatively, we are only interested in delocalization on this scale.

Let us note that an experimental evidence of this effect was reported in Ref. [16], where the authors studied the coherence of light emitted in different directions by a quantum well and showed that only photons with the same $\mathbf{k}_{//}$ interfered.

C.2 Quantum dot

The opposite situation is found in an ideal quantum dot, where the electron and hole (or the exciton center-of-mass) is fully localized at a given position:

$$\psi \sim \delta(\mathbf{r} - \mathbf{r}_0) \tag{C.3}$$

The Fourier transform of this wavefunction is a constant function: ψ contains all wavevectors $\mathbf{k}_{//}$ (the wavevector of the e-h pair is completely undefined). In this case, the emitted photon carries all values of $\mathbf{k}_{//}$, so that light corresponding to different $\mathbf{k}_{//}$ is coherent and can interfere. In the modeling of a source emission, one should use the 'folded' source described in Chapter 6, Section 6.3.3.

Here again, carriers can be considered localized as long as their spatial extent is much smaller than the typical photon scale λ.

Bibliography

[1] A. W. Snyder and J. D. Love. *Optical Waveguide Theory.* Chapman and Hall, New York, 1983.

[2] R. Guobin, W. Zhi, L. Shuqin, L. Yan, and J. Shuisheng. Full-vectorial analysis of complex refractive-index photonic crystal fibers. *Optics Express*, 12(6):1126–1135, 2004.

[3] L. A. Coldren and S. W. Corzine. *Diode lasers and photonic integrated structure.* Wiley Interscience, New York, 1995.

[4] G. Bastard. *Wave Mechanics Applied to Semiconductor Heterostructures.* Les Editions de Physique, Les Ullis, 1992.

[5] J. M. Luttinger. Quantum theory of cyclotron resonances in semiconductors: general theory. *Physical Review*, 102(4):1030, 1955.

[6] H. Benisty, R. Stanley, and M. Mayer. Method of source terms for dipole emission modification in modes of arbitrary planar structures. *Journal of the Optical Society of America a-Optics Image Science and Vision*, 15(5):1192–1201, 1998.

[7] D. Ochoa. *Diodes electroluminescentes planaires a haut rendement d'extraction lumineuse.* PhD thesis, EPFL, 2001.

[8] G. l. Bir and G. E. Pikus. *Symmetry and strain-induced effects in semiconductors.* Wiley, New York, 1974.

[9] S. L. Chuang and C. S. Chang. k.p method for strained wurtzite semiconductors. *Physical Review B*, 54(4):2491–2504, 1996.

[10] I. Vurgaftman and J. R. Meyer. Band parameters for nitrogen-containing semiconductors. *Journal of Applied Physics*, 94(6):3675–3696, 2003.

[11] F. Bernardini, V. Fiorentini, and D. Vanderbilt. Spontaneous polarization and piezoelectric constants of III-V nitrides. *Physical Review B*, 56(16):10024–10027, 1997.

[12] P. Waltereit, O. Brandt, A. Trampert, H. T. Grahn, J. Menniger, M. Ramsteiner, M. Reiche, and K. H. Ploog. Nitride semiconductors free of electrostatic fields for efficient white light-emitting diodes. *Nature*, 406(6798):865–868, 2000.

[13] C. Q. Chen, V. Adivarahan, J. W. Yang, M. Shatalov, E. Kuokstis, and M. A. Khan. Ultraviolet light emitting diodes using non-polar a-plane GaN-AlGaN multiple quantum wells. *Japanese Journal of Applied Physics Part 2-Letters*, 42(9AB):L1039–L1040, 2003.

[14] A. Chakraborty, B. A. Haskell, S. Keller, J. S. Speck, S. P. Denbaars, S. Nakamura, and U. K. Mishra. Demonstration of nonpolar m-plane InGaN/GaN light-emitting diodes on free-standing m-plane GaN substrates. *Japanese Journal of Applied Physics Part 2-Letters and Express Letters*, 44(1-7):L173–L175, 2005.

[15] N. F. Gardner, J. C. Kim, J. J. Wierer, Y. C. Shen, and M. R. Krames. Polarization anisotropy in the electroluminescence of m-plane InGaN-GaN multiple-quantum-well light-emitting diodes. *Applied Physics Letters*, 86(11), 2005. 111101.

[16] W. Hoyer, M. Kira, S. W. Koch, H. Stolz, S. Mosor, J. Sweet, C. Ell, G. Khitrova, and H. M. Gibbs. Entanglement between a photon and a quantum well. *Physical Review Letters*, 93(6), 2004. 067401.